Numerical Modeling and Investigation of Boiling Phenomena

Numerische Modellierung und Analyse von Siedephänomenen
Zur Erlangung des akademischen Grades Doktor-Ingenieur (Dr.-Ing.)
genehmigte Dissertation von Dipl.-Ing. Christian Kunkelmann aus Erbach i. Odw.
September 2011 — Darmstadt — D 17

TECHNISCHE
UNIVERSITÄT
DARMSTADT

TTD
Technische Thermodynamik

Numerical Modeling and Investigation of Boiling Phenomena
Numerische Modellierung und Analyse von Siedephänomenen

Genehmigte Dissertation von Dipl.-Ing. Christian Kunkelmann aus Erbach i. Odw.

1. Gutachten: Prof. Dr.-Ing. Peter Stephan
2. Gutachten: Apl. Prof. Dr.-Ing. Suad Jakirlic

Tag der Einreichung: 30. Mai 2011
Tag der Prüfung: 12. August 2011

Darmstadt — D 17

Meiner Familie

Erklärung zur Dissertation

Hiermit versichere ich, die vorliegende Dissertation ohne Hilfe Dritter nur mit den angegebenen Quellen und Hilfsmitteln angefertigt zu haben. Alle Stellen, die aus Quellen entnommen wurden, sind als solche kenntlich gemacht. Diese Arbeit hat in gleicher oder ähnlicher Form noch keiner Prüfungsbehörde vorgelegen.

Darmstadt, den 30. Mai 2011

(Christian Kunkelmann)

Vorwort

Die vorliegende Arbeit entstand während meiner Anstellung als wissenschaftlicher Mitarbeiter am Fachgebiet für Technische Thermodynamik der Technischen Universität Darmstadt. Dem Leiter des Instituts, Herrn Prof. Dr.-Ing. Peter Stephan, möchte ich ganz herzlich für die Betreuung der Arbeit, die hervorragenden Rahmenbedingungen und das entgegengebrachte Vertrauen danken. Ich konnte die Arbeit in großem Umfang innerhalb der festgelegten Grenzen selbst strukturieren und planen, mir aber auch jederzeit bei ihm fachlichen Rat holen oder mich bezüglich anstehender Entscheidungen mit ihm abstimmen. Aufgrund des von ihm entgegengebrachten Vertrauens, konnten wir fachliche Diskussionen immer auf Augenhöhe führen, wofür ich mich im Besonderen bedanken möchte. Außerdem möchte ich Herrn Apl. Prof. Dr.-Ing. Suad Jakirlic für die Übernahme des Koreferats, die freundliche Unterstützung während meiner Zeit als wissenschaftlicher Mitarbeiter sowie für die Organisation von OpenFOAM Veranstaltungen an der Technischen Universität Darmstadt danken.

Das äußerst angenehme Arbeitsklima am Fachgebiet hat ganz sicher einen großen Anteil zum Gelingen der Arbeit beigetragen. An dieser Stelle möchte ich allen Mitarbeitern des Fachgebiets, gleich welcher Funktion, für ihre Freundlichkeit, Offenheit und Hilfsbereitsschaft danken. Insbesondere bedanke ich mich bei Nils Schweizer und Axel Sielaff für zahlreiche tiefgehende Diskussionen zum Thema Blasensieden sowie Felix Brinckmann, Dr.-Ing. Frank Dammel und Prof. Dr. rer. nat Steffen Hardt für ebenso wertvolle Diskussionen über numerische Methoden und Modellierungsansätze. Desweiteren bedanke ich mich bei Tobias Schulze und Christof Sodtke, die mich vor Promotionsbeginn bei meiner Tätigkeit als Hilfswissenschaftler und Diplomand betreut haben. Beide haben mich in der Entscheidung zu einer Promotion am Fachgebiet für Technische Thermodynamik sicherlich positiv beeinflusst.

Während meiner Zeit als wissenschaftlicher Mitarbeiter hatte ich die Gelegenheit, einige ausgezeichnete Studenten im Rahmen von Bachelor- oder Master-Arbeiten sowie als Hilfswissenschaftler zu betreuen. Auch diesen Studenten gilt mein Dank. Im Besonderen möchte ich mich bei Stefan Herbert für seine umfangreiche Hilfe bei der Implementierung des Siedemodells im Rahmen seiner Tätigkeit als Hilfswissenschaftler sowie für seine ausgezeichnete Master-Arbeit bedanken. Es freut mich außerordentlich, dass er nun selbst wissenschaftlicher Mitarbeiter am Fachgebiet ist und die Arbeit an und mit dem entwickelten Siedemodell fortführen wird. Stefan Herbert sowie Frank Dammel und Nils Schweizer danke ich auch für das Korrekturlesen der Dissertation.

Auch bei meiner Frau Annika möchte ich mich herzlich bedanken. Sie hat meine Entscheidung für eine Promotion voll unterstützt und mir während der zeitweise auch sehr mühsamen Arbeit den notwendigen Rückhalt gegeben. Nicht zuletzt möchte ich auch meinen Eltern und Schwiegereltern danken, die meine Frau und mich bei vielen Entscheidungen und Anlässen sowie auch bei der Betreuung unserer Tochter ausgezeichnet unterstützen.

Mühltal, den 30. Mai 2011

Christian Kunkelmann

Abstract (English, German)

Abstract

The subject of the present thesis is the numerical modeling and investigation of boiling phenomena. The heat transfer during boiling is highly efficient and therefore used for many applications in power generation, process engineering and cooling of high performance electronics.

The precise knowledge of particular boiling processes, their relevant parameters and limitations is of utmost importance for an optimized application. Therefore, the fundamentals of boiling heat transfer have been intensively studied in the last decades and are still subject of many ongoing research activities all over the world. In spite of this effort, many aspects of boiling heat transfer are still not completely understood.

The difficulty is mainly due to the small length and time scales. In addition to highly resolved experiments, the numerical modeling of boiling heat transfer has been established in fundamental research during the last years. However, most of the existing models and methods are limited with respect to their applicability. Thus, 3D simulations of boiling in complex geometries cannot be handled by the existing methods. However, the use of complex heater geometries is one of the possibilities to fulfill the demand for more efficient heat transfer units and its numerical investigation is therefore desirable.

Kurzzusammenfassung

Das Thema der vorliegenden Arbeit ist die numerische Modellierung und Untersuchung von Siedephänomenen. Der Wärmetransport beim Sieden ist äußerst effizient und kommt daher in vielen Anwendungen im Bereich der Kraftwerks- und der Verfahrenstechnik aber auch bei der Kühlung von Hochleistungselektronik zum Einsatz.

Die genaue Kenntnis über bestimmte Siedevorgänge sowie deren relevante Parameter und Grenzen ist unerlässlich für den optimalen Einsatz in einer technischen Anwendung. Aus diesem Grund sind die physikalischen Grundlagen des Siedens in den vergangenen Jahrzehnten intensiv erforscht worden und auch aktuell noch immer Gegenstand vieler Forschungsvorhaben in aller Welt. Trotz dieser Bemühungen sind viele Aspekte des Siedevorgangs noch immer nur unvollständig verstanden.

Vor allem die sehr kleinen Zeit- und Längenskalen stellen hierbei Schwierigkeiten dar. Neben hochauflösenden experimentellen Untersuchungen, hat sich in den letzten Jahren auch die numerische Modellierung von Siedephänomenen in der Grundlagenforschung etabliert. Allerdings sind viele der bestehenden Modelle und Methoden hinsichtlich ihrer Anwendbarkeit sehr stark eingeschränkt, insbesondere hinsichtlich der dreidimensionalen Simulation von Siedevorgängen in komplexer Geometrie. Der Einsatz von komplexer Heizwandgeometrie ist jedoch eine vielversprechende Möglichkeit um die Nachfrage nach immer effizienteren Wärmeübertragern zu erfüllen und sollte daher auch numerisch untersucht werden können.

Within the framework of the present thesis, a numerical model was developed which enables the simulation of boiling processes in arbitrarily complex geometries at a high level of accuracy. The model is based on the Volume-of-Fluid solver of the Computational Fluid Dynamics software OpenFOAM and resolves all relevant length and time scales. The latter particularly applies for the microscopic, but highly relevant, region at the 3-phase contact line where the liquid-vapor interface meets the wall.

The present thesis contains a detailed description of the model and comprehensive information about its validation. Furthermore, several simulations of different boiling phenomena are presented. The simulation results are discussed and compared to mostly experimental data available in literature. Simulations were accomplished for nucleate boiling of single bubbles and merging bubbles, flow boiling in a near-wall shear flow, boiling in a structured micro-channel and film boiling of droplets (Leidenfrost phenomenon). Good agreement to existing data is achieved. Further, the simulation results enable a detailed analysis and a more comprehensive understanding of the transfer mechanisms. Hereby, the knowledge gained during highly resolved experiments can be extended significantly. The formation of an enclosed droplet within a merged bubble which was observed but not understood experimentally is an excellent example. The detailed analysis of the simulation results enable a clarification of the causes for the formation of the droplet and lead to a gain in knowledge which would not have been possible in the experiment.

In summary, the present thesis includes the development, implementation and validation of a boiling model as well as a wide range of simulations on different boiling phenomena. The latter clearly demonstrate the potential of the numerical investigation of boiling phenomena in fundamental research and in the design of small boiling devices.

In der vorliegenden Arbeit wurde ein numerisches Modell entwickelt, mit dem Siedevorgänge in beliebig komplexer Geometrie mit hoher Genauigkeit simuliert werden können. Das Modell basiert auf der Volume-of-Fluid Methode der Computational Fluid Dynamics Software OpenFOAM und löst alle für das Sieden relevanten Zeit- und Längenskalen auf. Letzteres gilt insbesondere für den mikroskopisch kleinen, aber für das Blasensieden äußerst relevanten, Bereich der 3-Phasen-Kontaktlinie, in dem die Dampf-Flüssig-Phasengrenze auf die Wand trifft.

Die vorliegende Dissertationsschrift enthält eine detaillierte Beschreibung des entwickelten Modells sowie ausführliche Informationen zu dessen Validierung. Darüber hinaus werden Simulationen von verschiedenen Siedephänomenen vorgestellt, deren Ergebnisse diskutiert und mit bereits veröffentlichten, vorranging experimentellen Daten verglichen. Die durchgeführten Simulationen umfassen Blasensieden von Einzelblasen und koaleszierenden Blasen, Strömungssieden in einer wandnahen Scherströmung, Sieden in einem strukturierten Mikrokanal sowie Filmsieden von Tropfen (Leidenfrost-Phänomen). Es konnte eine gute Übereinstimmung zu bereits veröffentlichten Ergebnissen erzielt werden. Darüber hinaus ermöglichen die hochaufgelösten Simulationen eine detaillierte Analyse der komplexen Transportvorgänge und damit einen Erkenntnisgewinn, welcher die experimentell gewonnenen Erfahrungen und Erkenntnisse deutlich erweitert. Ein Beispiel hierzu ist die experimentell belegte aber bislang nicht verstandene Entstehung eines eingeschlossenen Tropfens innerhalb einer koaleszierten Blase. Die detaillierte Analyse der Simulationsergebnisse ermöglicht die Klärung der Ursachen für die Tropfenentstehung und führt somit zu einem Erkenntnisgewinn, der rein durch Experimente nicht möglich gewesen wäre.

Zusammenfassend beinhaltet die vorliegende Arbeit die Entwicklung, Implementierung und Validierung des Siedemodells sowie ein breites Spektrum an Simulationen zu unterschiedlichen Siedephänomenen. Letztere zeigen sehr deutlich das Potential der numerischen Untersuchung von Siedephänomenen im Bereich der Grundlagenforschung und bei der Auslegung von kleinen Siedeapparaten.

Contents

Vorwort iv

Abstract (English, German) v

Contents vii

Nomenclature ix

1 Introduction 1
- 1.1 Boiling phenomena . . . 1
- 1.2 State of the art . . . 3
  - 1.2.1 Experimental work . . . 4
  - 1.2.2 Numerical work . . . 6
- 1.3 Goals . . . 8

2 Governing equations 10
- 2.1 Mass, momentum and energy transport . . . 10
- 2.2 2-phase flow and phase change . . . 12
- 2.3 Microscale heat and fluid flow at the 3-phase contact line . . . 14

3 Numerical method 20
- 3.1 Discretization method . . . 20
  - 3.1.1 Spatial and temporal discretization . . . 20
  - 3.1.2 Time and space adaptivity . . . 22
- 3.2 Interface capturing . . . 23
  - 3.2.1 Volume-of-Fluid method . . . 23
  - 3.2.2 Sharp interface reconstruction . . . 24
  - 3.2.3 Surface tension calculation . . . 28
  - 3.2.4 Contact angle treatment . . . 29
- 3.3 Solution procedure . . . 30

4 Model implementation and validation 32
- 4.1 Phase change model . . . 32
  - 4.1.1 Calculation of the local rate of phase change . . . 32
  - 4.1.2 Representation of phase change by a continuous field of source terms . . . 34
- 4.2 Heat and fluid flow at the 3-phase contact line . . . 40
  - 4.2.1 Solution and parameterization of the microscale model . . . 40
  - 4.2.2 Coupling of the microscale model to the CFD simulation . . . 44
- 4.3 Conjugate heat transfer between solid and fluid . . . 46
- 4.4 Validation simulations . . . 49
  - 4.4.1 1D test case (sucking interface problem) . . . 49
  - 4.4.2 2D test case without 3-phase contact line (spherical bubble growth) . . . 51
  - 4.4.3 2D test case with 3-phase contact line (meniscus evaporation) . . . 53

5 Results and discussion **56**
5.1 Single bubble pool boiling 56
5.1.1 Simulation setup, input parameters and post-processing 56
5.1.2 Major findings 60
5.1.3 Influence of mesh resolution, natural convection and contact angle 70
5.1.4 Discussion of simulation and measurement uncertainties 74
5.2 Bubble merger 76
5.2.1 Simulation setup and input parameters 76
5.2.2 Major findings 78
5.2.3 Brief review and relevance of the results 83
5.3 Test simulations for further boiling phenomena 83
5.3.1 Flow boiling in a near-wall shear flow 83
5.3.2 Boiling in a structured microchannel 88
5.3.3 Leidenfrost phenomenon 94

6 Summary and outlook **106**
6.1 Model development, implementation and validation 106
6.2 Numerical simulation and analysis of boiling phenomena 107
6.3 Outlook on ongoing work and potential future projects 108

A Material properties **110**

B Overview of the boiling model **111**

C Correlation coefficients for contact line evaporation model **112**

D Numerical schemes **113**

Bibliography **114**

Nomenclature

Latin symbols

Symbol	Description	Unit
A	Hamaker constant	J
$\boldsymbol{A}$	Matrix of linear algebraic system of equations	various
a	1. Coefficient for contact angle correction	-
	2. Acceleration	m/s^2
$a_{Q,i}$, $a_{\delta,i}$, $a_{\theta,i}$	Correlation coefficients for contact line evaporation model (integrated heat flux, film thickness and contact angle)	various
b	Coefficient for contact angle correction	-
B	Scaling parameter for contact angle hysteresis	s/m
$\vec{b}$	Source term vector, right hand side of linear algebraic system of equations	various
c	Specific heat capacity	J/(kg K)
c_F	Compression coefficient for the transport of the volume fraction field	-
Co	Courant number	-
D	1. Diameter	m
	2. Diffusion constant	various
d	Distance	m
e	Specific energy	J/kg
f	Accomodation coefficient	-
f_{bubble}	Bubble frequency	Hz
$\vec{f}$	Source term in momentum equation	N/m^3
F	Volume fraction of the liquid phase	-
g	Gravitational acceleration	m/s^2
h	Heat transfer coefficient	$W/(m^2 K)$
H	Heaviside function	-
$\boldsymbol{I}$	Identity matrix	-
i	Counter	-
j_{int}	Evaporating mass flux through the liquid-vapor interface	$kg/(m^2 s)$
k	Thermal conductivity	W/(m K)
L	Length	m

L_c	Capillary length	m
L_K	Kolmogorov scale	m
Ma	Mach number	-
$\dot{m}$	Mass flow	kg/s
$\dot{m}^*$	Integrated mass flux evaporating at 3-phase contact line (mass flow per unit contact line length)	kg/(s m)
$\vec{n}$	Normal vector (to interface, unless not otherwise specified by subscript)	-
N	Integer number	-
N_{sub}	Number of subcycles for the transport of the volume fraction field	-
N_l, N_v	Scaling factors for the source term fields in the liquid and vapor phase	-
p	Pressure	Pa
q	Heat flux	W/m^2
Q	1. Heat flow	W
	2. Heat flow per unit contact line length	W/m
r	Radial coordinate	m
R	Radius	m
R_{gas}	Gas constant	J/(kg K)
R_{int}	Interfacial heat resistance	K m^2/W
Re	Reynolds number	-
S, $\vec{S}$	Surface area, surface area vector	m^2
t	Time	s
Δt, Δt_{VOF}	Time step, time step of volume fraction transport	s
Δt_{wait}	Waiting time between two consecutive bubbles	s
T	Temperature	K
u, $\vec{u}$	Velocity, veloctiy vector	m/s
U_{bulk}	Bulk liquid velocity	m/s
V	Volume	m^3
x	Coordinate	m
$\vec{x}$	Solution vector of linear algebraic system of equations	various
y	Coordinate	m
z	Coordinate	m

Greek symbols

Symbol	Description	Unit
δ	1. Thickness of the thermal boundary layer	m
	2. Thickness of the velocity boundary layer	m
	3. Liquid film thickness at the 3-phase contact line	m
	4. Thickness of the vapor layer below a droplet	m
ϵ	Dissipation rate of turbulent kinetic energy	W/kg
η	Local coordinate normal to wall at the 3-phase contact line	m
θ	Contact angle	°
θ_0	Calculated contact angle at the wall which needs to be corrected to the target contact angle	°
θ_A	Advancing contact angle	°
θ_R	Receding contact angle	°
κ	1. Interface curvature	1/m
	2. Isentropic exponent	-
λ	Offset of a plane to the coordinate system	m
μ	Dynamic viscosity	Pa s
ν	Kinematic viscosity	m^2/s
ξ	Local coordinate parallel to the wall at the 3-phase contact line	m
ξ_{mesh}	Local mesh resolution at the 3-phase contact line	m
ρ	Density	kg/m^3
$\dot{\rho}$	Smeared, cropped and scaled mass source term field	$kg/(m^3\,s)$
$\dot{\rho}_0$	Sharp mass source term field	$kg/(m^3\,s)$
$\dot{\rho}_1$	Smeared mass source term field	$kg/(m^3\,s)$
τ	Stress tensor	Pa
σ	Surface tension	N/m
ϕ	Angular coordinate	°
Φ	Generic variable for the transport equation	various
Ψ	Generic material property	various

Subscripts

Subscript	Description
0	Reference quantity
ad	Quantity within the adsorbed film
c	Counter indicating a particular cell of the mesh
cl	Quantity at the 3-phase contact line
cut	Cutoff value
dep	Quantity at the instant of bubble departure
f	Counter indicating a particular face of the mesh
F	Quantity of the fluid (conjugate heat transfer)
heater	Quantity of or at the heater wall
in	Input heat flux or input heat flow
int	Quantity at the interface
l	Quantity of liquid phase
mic	Quantity at the end of the integration domain of the contact line evaporation model
n	Quantity normal to the interface or to a wall
p	Geometric quantity of the cutting polygon created by cutting a cell of the mesh with the interface
rel	Relative quantity
S	Quantity of the solid (conjugate heat transfer)
sat	Quantity at saturation condition
sl	Property of the solid-liquid interface
ST	Quantity related to surface tension
sv	Property of the solid-vapor interface
t	Quantity tangential to the interface or to a wall
trans	Quantity within the transition region at the 3-phase contact line
v	Quantity of the vapor phase
wall	Quantity at the solid heater wall

Superscripts

Superscript	Description
(CFD)	Quantity calculated by CFD simulation
(n), $(n-1)$, ...	Quantity at time step n, $n-1$, ...
T	Transponse of the vector or matrix
’	1. Variation of quantity due to turbulence
	2. First derivative of the quantity

Abbreviations

Abbreviation	Description
ALE	Arbitrary Lagrangian-Eulerian
CFD	Computational Fluid Dynamics
CHF	Critical Heat Flux
CSF	Continuum Surface Force
FVM	Finite-Volume-Method
LS	Level-Set
MAC	Marker And Cell
ODE	Ordinary Differential Equation
ONB	Onset of Nucleate Boiling
PISO	Pressure Implicit with Splitting of Operators
PLIC	Piecewise Linear Interface Calculation
TLC	Thermochromic Liquid Crystals
VOF	Volume-of-Fluid

1 Introduction

Boiling heat transfer is used in a wide field of applications: From rather simplistic cooking activities in everyday life to high-tech solutions for the chemical industry, power generation and cooling applications. While boiling research is, of course, not required for cooking, the exact knowledge of the boiling process, its parameters and limitations is compulsive for the optimized technological application. Besides the wide range of different applications, another very interesting characteristic of boiling heat transfer is the wide range of system scales. Boiling is used to cool tiny high-performance electronic components. On the other hand, boiling is also used on a much larger scale in steam generators for power plants. Due to its intensive use, boiling heat transfer has been intensively studied in the past and still is subject of ongoing research activities in many groups all over the world. In spite of the past research, many aspects of boiling are still not well understood. The demand to transfer higher heat fluxes at the same or even at lower wall superheats and to predict the limits of the boiling process is growing and makes the scientific investigation of boiling phenomena inevitable. In particular, the demand for highly efficient small scale heat transfer is growing. In 1965, Moore [76] has predicted that the performance of computer chips is doubled every 18 months. Although the increase of the computational power has slowed down meanwhile, it still is ever increasing. More and more components are packed on the same area and the dissipated heat flux increases tremendously. Boiling is one of the solutions to overcome this cooling problem. In the past, many correlations have been developed based on a large number of experiments for many different parameter ranges. Boiling heat transfer and its limits can be predicted within these parameter ranges. Of course, these ranges can be extended by new experiments and new correlations. However, as pointed out by Nelson [83], without the comprehensive physical understanding of the whole process and without knowing and resolving its temporal and spatial scales and variations, it will not be possible to significantly ameliorate predictive tools. In particular the use of micro-structured surfaces which are known to enhance boiling heat transfer significantly introduce new geometric parameters which can hardly be covered comprehensively by experiments.

A better physical understanding of the boiling process can be achieved by either highly resolved generic boiling experiments or by highly resolved numerical modeling and simulation. These two approaches should not be considered as separated or even competing. They should rather be used in parallel and in a collaborative way in order to allow quantitative comparison and to make sure that all effort is directed towards a common goal. In the recent years, experiments and numerical modeling have made large progress in terms of temporal and spatial resolution as well as accuracy. In particular, the numerical modeling has been improved thanks to the development and optimization of methods which enable the simulation of 2-phase flows and also thanks to an ever increasing computational power.

The present thesis is one of the many steps towards a better understanding of boiling heat transfer. Within its framework, a numerical model for the simulation of boiling heat transfer has been developed. This model enables highly resolved simulations of various boiling phenomena at a high level of accuracy.

1.1 Boiling phenomena

In this section the boiling phenomena shall be briefly described before an overview of several important experimental and numerical publications on boiling heat transfer is given. This overview mainly contains the aspects of boiling heat transfer that are in close relation to the present thesis and does not claim to be a comprehensive overview of all important publications on boiling heat transfer. For a complete overview,

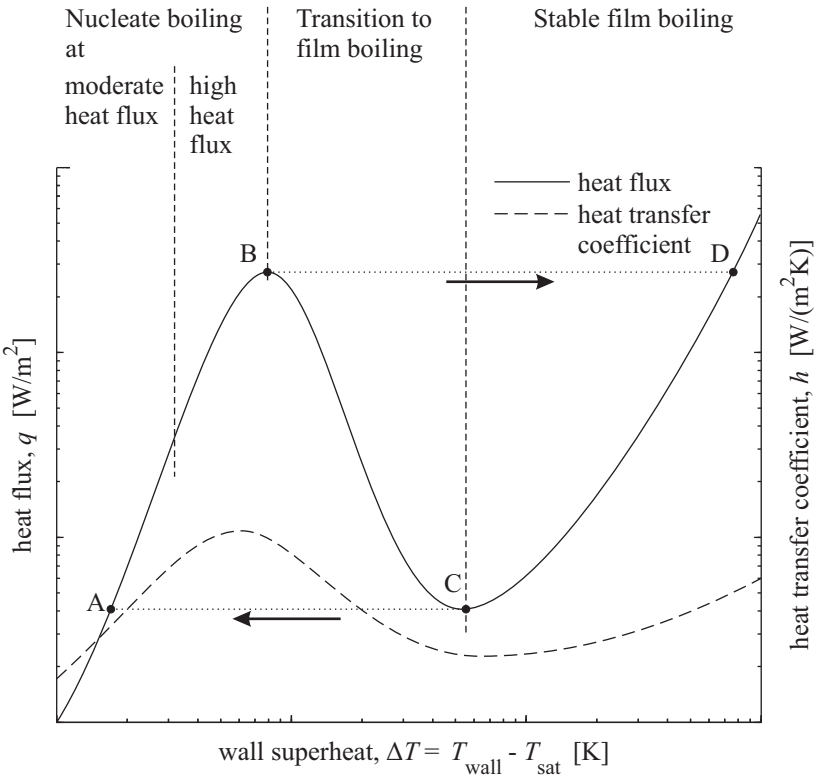

Figure 1.1: The dependence of heat flux and heat transfer coefficient on wall superheat in boiling as proposed by Nukiyama [84]. The regime of natural convection is not shown.

the author would like to refer to review-articles from several authors that have been published on boiling heat transfer, e.g. by Dhir [11] and Manglik [68]. These review articles summarize comprehensively the major research achievements for many aspects of boiling heat transfer.

The heat that is transferred between a heated wall and a bulk liquid can be expressed by the product of the heat transfer coefficient, the heat transfer area and the wall superheat.

$$Q = hS\left(T_{\text{wall}} - T_{\text{liquid}}\right) \tag{1.1}$$

This equation indicates three possiblities to enhance heat transfer: By increasing the heat transfer coefficient h, by increasing the heat transfer area S or by increasing the temperature difference $\left(T_{\text{wall}} - T_{\text{liquid}}\right)$ between wall and fluid. An increase of the heat transfer area is usually limited by constraints on the overall size, weight and cost of the heat transfer unit. Increasing the temperature difference between wall and fluid is typically realizable, but will negatively affect the efficiency of the heat exchanger or even the overall performance of a power generation cycle or a cooling device. Therefore, the most efficient way to increase heat transfer is increasing the heat transfer coefficient. Boiling heat transfer has a significantly higher heat transfer coefficient than single phase heat transfer.

Nukiyama [84] published one of the most cited papers in boiling research. He plotted the heat transferred to boiling water over a wide range of wall superheats and established the boiling curve which is qualitatively shown in Figure 1.1. Still today, the boiling curve of Nukiyama is an important corner stone for all boiling researchers and helps to distinguish different phenomena in pool boiling. Van Stralen and Cole [116] describe the following regimes.

- **Nucleate boiling at moderate heat flux:** In this regime, isolated bubbles grow and detach at the heating wall without interacting with each other. The heat transfer in this regime is characterized

by comparably high heat transfer rates at a moderate wall superheat. This is due to the large amount of heat that can be stored in the vapor phase (latent heat) without heating up the fluid and the agitation of the liquid by the bubbles which positively affects the single phase heat transfer in the vicinity of the bubbles. The range of this regime is limited by the onset of nucleate boiling (ONB) at small wall superheats. Below a minimum wall superheat no bubbles will be generated at the nucleation sites of the heating wall. At higher wall superheats this regime is limited by the onset of interaction between the bubbles which results from an increasing density of active nucleation sites.

- **Nucleate boiling at high heat flux:** At high heat fluxes, more and more nucleation sites become activated and the density of growing bubbles increases. In this regime, the heat transfer rate is higher than in the case of isolated bubbles. However, as more and more area of the heating wall is covered by vapor which has an insulating effect compared to the liquid, the required wall superheat increases, resulting eventually in a decreasing heat transfer coefficient. It should be noted that the maximum of the heat transfer coefficient lies at lower wall superheats than the maximum of the heat flux in Figure 1.1.
- **Transition to film boiling:** If the critical heat flux (CHF) is reached (at point B in Figure 1.1) more and more places on the heater surface become covered with vapor. Eventually, a stable vapor layer can be formed which completely separates the heater surface from the liquid. If the heat flux is kept constant or slightly increased at this point, the transition to a complete vapor layer happens very quickly and the wall temperature jumps to a much higher value (along dashed line between B and D in Figure 1.1). If the local temperature of the heater is controlled rapidly and with a high accuracy, a transition from the partial to the complete vapor layer can be observed and results in a decreasing heat flux (along solid curve between B and C in Figure 1.1). A similar transition in the opposite direction can be observed when the heat flux or the temperature are decreased. If the heat flux is controlled the vapor layer suddenly collapses and the wall superheat drops (dashed line between C and A in Figure 1.1). If the wall temperature is controlled, the vapor film breaks up at more and more places as the temperature decreases resulting in an increasing heat flux (along solid line between C and B in Figure 1.1)
- **Stable film boiling:** As indicated by the naming, this regime is characterized by a stable vapor layer that separates the liquid phase from the heating wall. If the liquid-vapor interface approaches the wall, the vapor generation is intensified and pushes the interface away from the wall until a stable position is reached. In this regime, droplets bounce off or hover above the heating wall without wetting it.

Typically, any industrial application will seek to stay in the nucleate boiling regimes at moderate or high heat fluxes. Nucleate boiling allows to transfer high heat fluxes at moderate wall superheats. Minimizing the wall superheat is generally one measure to optimize the overall performance of a power generation cycle or a cooling device. However, the film boiling regime is also of large interest to certain applications such as quenching of steel or spray cooling of very hot surfaces.

1.2 State of the art

In this section, the major achievements in boiling research are briefly discussed. For the sake of clarity, the section is subdivided into experimental and numerical work. One of the most important achievements of the experimental and numerical research activities, is the identification and distinction of the governing heat transfer mechanisms in boiling. Still today, the transient heat transfer during boiling is not fully understood and subject of ongoing discussions in the scientific community. An early, but very important contribution that distinguished different heat transfer mechanisms during nucleate pool boiling was published by Han and Griffith [25, 26]. The authors state that there are two mechanisms of heat transfer

during nucleate boiling. The bulk convection heat transfer describes the superheated liquid that is sucked away from the wall into the bulk liquid at each bubble departure. The natural convection heat transfer describes the usual natural convection process which transfers heat from the wall into the bulk liquid in a continuous manner. Another heat transfer mechanism is discussed by Cooper and Lloyd [8] who state that there is a microlayer underneath the bubble. The microlayer is characterized by a very thin liquid film which enables tremendously high heat transfer rates. Today, the knowledge about the boiling process has grown significantly. In particular, the highly resolved experiments and numerical simulations that will be discussed below, have led to a more detailed insight into the boiling process. Based on these results, Stephan and Kern [106] as well as Kim [53] describe the following mechanisms for the transport of heat from the wall into the fluid.

- **Enhanced convection:** The liquid in the vicinity of a growing, detaching or rising bubble is submitted to a motion which is induced by the bubble dynamics. The motion results in an augmented convective heat transfer compared to pure natural convection.
- **Transient conduction:** The largest amount of the heat consumed by a bubble is provided by the superheated liquid layer in the vicinity of the heater. During bubble growth, the superheated liquid layer is depleted resulting in a decrease of the liquid temperature. During bubble detachment and after bubble departure, the superheated liquid layer is restored by conductive heat transfer from the heater into the liquid.
- **Microscale heat transfer at the 3-phase contact line:** Very close to the line where the liquid-vapor interface meets the solid wall (3-phase contact line), the heat transfer is governed by one-dimensional heat conduction through a very thin liquid film. On this sub-micrometer scale, intermolecular forces become important which are otherwise negligible. In spite of the different conclusions on the importance of contact line heat transfer, Stephan and Kern [106] as well as Kim [53] state that contact line heat transfer can make up to 20 to 30 % of the total heat consumed by a vapor bubble.

1.2.1 Experimental work

One of the earliest systematic investigations of boiling phenomena was performed by Jakob and Fritz [43] who measured the influence of surface roughness and heat flux on the wall temperature during boiling of water. Some years later, Fritz [20] proposed a theoretical approach to calculate the departure volume of bubbles as a function of the material properties of the boiling fluid and its wetting behavior on the heating wall material. About the same time, Nukiyama [84] established the above mentioned pool boiling curve.

In the last decades, many correlations have been developed to predict bubble departure diameters [7, 20, 134] and frequencies [7, 43, 67] as well as the heat transfer coefficient [103]. Many of the correlations rely heavily on empirical parameters which are only valid for a specific fluid and a certain range of parameters which limits the applicability of these correlations to other fluids and parameter ranges. Nevertheless, in default of more sophisicated predictive models, these correlations are still used for the design of technical applications. The references that are given here respresent only a small part of the scientific work on boiling correlations. A very good and more detailed overview of important correlations is given by Carey [6].

Over the last decades, measurement techniques and experimental methods have developed rapidly and the time and length scales that can be resolved have become smaller and smaller. This enabled the experimental investigation of local and instantaneous quantities such as the local wall temperature underneath a vapor bubble or the instantaneous heat transfer at the bubble foot during the boiling process. In particular the use of thermochromic liquid crystals (TLCs) [49, 50, 98, 118] and high speed infrared thermography [94, 120] permit more detailed insight into the transient heat transfer between

solid and fluid. A different approach that also allows to gain information on the local heat transfer at the bubble foot is the use of micro heater arrays to impose constant temperature or constant heat flux boundary conditions [9, 10, 33, 53, 73, 74, 82]. In this context of local and instantaneous measurements, some research groups perform experiments at reduced gravity [33, 88, 94, 98, 118]. The motivation is the possible application of boiling heat transfer in space on one hand and the slow down and scale up of the boiling phenomena due to the reduced gravity on the other hand. The second effect is due to the smaller buoyancy force in reduced gravity which leads to a longer contact between the bubble and the heating wall and thereby leads to a gain in spatial and temporal resolution.

One of the major outcomes of the local and instantaneous experimental investigations is the importance of the 3-phase contact line for boiling heat transfer. The local heat flux reaches a maximum value at the 3-phase contact line that can be one or even more orders of magnitude higher than the mean input heat flux (see [94, 120]). Even though the different research groups do not necessarily agree on the relative amount of heat that is transferred in the micro region, most publications indicate that around 20 to 30 % of the total heat is transferred in a region very close to the 3-phase contact line. However, not only the timewise integrated heat transfer data is interesting but also the developement of the heat transfer at the 3-phase contact line during the growth and detachment of the bubbles. In particular, the work of Schweizer [93], Moghaddam and Kiger [73, 74], Myers and co-workers [82] and Delgoshaei and Kim [9] indicate that the heat transfer is stronly dependend on the motion direction and speed of the 3-phase contact line. All authors describe an increasing local heat transfer during the advancing motion of the 3-phase contact line at bubble detachment. This has been further confirmed by a generic experiment of Ibrahem an co-workers [38, 39] that aims on a more detailed insight into the local heat transport in vicinity of the 3-phase contact line of an evaporating, moving meniscus. These experiments allow a more precise control of the boundary conditions and of the speed of the 3-phase contact line. The measurements confirm the above mentioned strong dependence of the local heat transfer on the motion of the 3-phase contact line and the increased heat transfer during the advancing motion.

All the above mentioned highly resolved experiments have enabled a much better and more detailed understanding of the transient heat transfer during nucleate boiling. Nevertheless, the spatial and temporal resolution of the different measurement techniques (TLCs, high-speed infrared thermography, micro heater arrays) is still not sufficient to completely understand the microscale heat transfer in the vicinity of the 3-phase contact line. In particular the temperature of the liquid surrounding the vapor bubble could not yet be measured with satisfying resolution. The local wall temperature can be measured within a distance of only several micrometers to the 3-phase contact line while the temperature in the liquid is measured only at a few points in the far-field. The use of micro-thermocouples (e.g. by Wagner [120]) is a promising approach to overcome this problem. However, this technique is under development and the results are not yet reliable enough for a detailed analysis.

Another focus in boiling research besides the highly resolved local measurements is the investigation of boiling on micro-structured surfaces. Wei and Honda [122] investigated the effect of pin-fins on the boiling surface. They observed a significant increase of the heat transfer coefficient in the nucleate boiling regime and an increase of the critical heat flux by a factor of four compared to a smooth surface. Wondra and co-workers [107, 128, 129] investigated the effect of different surface structures on the heat transfer at tube evaporators and also found a tremendous increase of the heat transfer coefficient compared to smooth evaporator walls. Li and Petersen [63] observed a simular increase on microporous coated surfaces. All these investigations show that there is a huge potential to increase the heat transfer coefficient in applications where size and weight are critical and limiting parameters. However, the transfer of the results obtained with a particular fluid at particular conditions to a different fluid or different conditions is not straightforward. Hence, there is need to further investigate and understand how heat transfer can be ameliorated by using micro-structured surfaces. The aim is to reduce the level of empirism and the number of trials to find an optimum surface.

1.2.2 Numerical work

With the growing computing capabilities and the development of new numerical methods for the simulation of 2-phase flow, the numerical simulation of boiling heat transfer has become possible. The numerical simulation of boiling heat transfer is on its way to be established as a tool that can, in addition to experimental investigations, help to gain a better understanding of boiling heat transfer. The major part of the numerical investigations focusses on either nucleate boiling at moderate heat flux (isolated bubbles) or stable film boiling. One of the key problems is the numerical description of the 2-phase flow. Typically, there are four methods which are used for the simulation of boiling heat transfer.

- In the **Marker and Cell (MAC) method** [29] the interface is marked by weightless particles that are convectively transported with the velocity field and can be used to reconstruct the interface position on a fixed mesh.
- The **Arbitrary Lagrangian-Eulerian (ALE) method** [36] is based on a dynamic mesh that follows the motion of the interface. Thus, the interface coincides with a boundary of the computational domain at all times.
- The **Volume-of-Fluid (VOF) method** [37] uses a field that contains information about the volume fraction of one of the phases in a numerical cell and which is convectively transported with the velocity field. The volume fraction field has a step at the position of the interface.
- The **Level-Set (LS) method** [85] uses a field that contains information about the distance of a numerical cell to the interface and which is convectively transported with the velocity field. The interface is represented by the zero isoline of the level-set field.

In Table 1.1 the capabilities of several existing numerical models for the simulation of boiling flows are summarized. The table does not contain all the numerical models on boiling that have been developed but only those on which the authors have frequently published and which aim at goals which are similar to the goals of the present thesis.

The original MAC method has been further developed by Tryggvason and co-workers [110, 113] who applied it to the simulation of boiling flows [17, 18, 19, 46]. The method is very accurate in particular in terms of curvature calculation which is important for the simulation of very small bubbles. Tryggvason and co-workers used the model mainly for the simulation of film boiling. Microscale heat transfer at the 3-phase contact line and the transient heat conduction in the solid wall is not taken into account.

The ALE method is used by Fuchs [21, 22] who simulated the transient heat transfer during pool boiling of binary mixtures. The work of Fuchs is based on the work of Stephan and Hammer [105] and Kern and Stephan [51, 52] who calculated the quasi-steady heat flow at a growing bubble using a boundary-fitted mesh. An important advantage of the ALE method and boundary-fitted meshes in general is the possibility to treat the liquid-vapor interface as a boundary of the computational domain. This facilitates the calculation of the heat flux at the interface and therefore of the evaporation rate. Welch [123, 124] also used a numerical method very similar to ALE to simulate 2-phase flows with phase change. However, microscale heat transfer at the 3-phase contact line is not taken into account in his model.

The LS method is used by Dhir and co-workers for various boiling configurations (a review of the advances is given by Dhir [12]). Already in the late 1990s, Son and Dhir [99, 100] numerically investigated film boiling while Son and co-workers [102] investigated the heat transfer associated with a single bubble during nucleate pool boiling. In the following years, the developers of the model frequently published on bubble mergers [80], flow boiling [63], the effect of contact angle dynamics [81], film boiling on horizontal cyclinders [101] and subcooled pool boiling [130, 131]. The model accounts for the microscale heat and fluid flow at the 3-phase contact line. However, the transient heat conduction

in the solid wall is not modeled and the wall is typically assumed to have a constant and homogeneous temperature.

The VOF method has only rarely been used for the simulation of boiling flows so far. Welch and Wilson [126] implemented a model for phase change in a VOF method and simulated 1D test cases and film boiling. Welch and Rachidi [125] extended the model by the transient heat conduction in the solid wall and simulated film boiling. Aus der Wiesche [3] used the VOF method to simulate nucleate pool boiling of water. More recently, Hardt and Wondra [28] proposed a method for implementing phase change in a VOF or LS approach and performed simulations of film boiling and droplet evaporation using a VOF method. None of the aforementioned models based on the VOF method include any sub-model for the evaporation at the 3-phase contact line.

Shu [96] combined the advantages of the LS and the VOF method to simulate boiling heat transfer using the open-source CFD package *OpenFOAM*[1] [127]. The model takes into account the microscale heat transfer at the 3-phase contact line and the conjugate heat transfer between solid and fluid. The author has performed 2D simulations and states that the extension of the model to 3D simulations is

[1] *OpenFOAM* is an open-source CFD software which is freely available and can be downloaded from the internet (http://www.openfoam.com). *OpenFOAM* version 1.5.x is used in the present thesis.

	interface capturing method	**contact line evaporation**	**transient heat conduction in solid**	**high interface distortion**	**3D simulations**	**unstructured mesh**	**adaptive mesh refinement**
Group of V. K. Dhir [12, 63, 80, 81, 99, 100, 101, 102, 130, 131]	LS	yes	no	yes	yes	no[a]	no[b]
Group of G. Tryggvason [17, 18, 19, 46, 110, 113]	MAC-like	no	no	yes	yes	no	yes
T. Fuchs and predecessors [21, 22, 51, 52, 105]	ALE	yes	yes	no	no	yes	no[c]
B. Shu [96]	LS & VOF	yes	yes	yes	no	no	no
Model of the present thesis [58, 59, 60]	VOF	yes	yes	yes	yes	yes	yes

Table 1.1: Comparison of existing numerical models for the simulation of boiling flows and the model that is the subject of the present thesis with respect to different aspects and capabilities.

[a] This limitation is not explicitely given in the references, but is implied by the use of high-order schemes for the transport and re-distancing of the level-set field.

[b] Adaptive mesh refinement is not used, but the model makes use of a moving mesh method to locally increase the mesh resolution in the vicinity of the vapor bubble.

[c] Adaptive mesh refinement is not used, but the elements at the liquid-vapor interface are chosen very small and follow the interface using the ALE method.

straightforward. However, the calculation of the local evaporation rate and the local coupling between LS and VOF are implemented for structured, orthogonal meshes only. This is highly disadvantageous for the simulation of boiling heat transfer in complex geometries were the generation of a structured, orthogonal mesh is very difficult or even impossible.

In addition to the already mentioned approaches, there is a separate approach for the simulation of hovering droplets above a surface with a temperature higher than the Leidenfrost temperature. In this approach, the droplet dynamics is modelled by an interface capturing method (typically VOF or LS). However, the vapor film which separates the droplet from the superheated wall is not resolved by the mesh but taken into account by a subgrid scale thin film model. This approach is used by Harvie and Fletcher [30, 31] as well as Ge and Fan [23] and Yu and co-workers [132] to simulate droplets impinging on surfaces in the Leidenfrost regime. The approach is highly efficient but has a major disadvantage as it is limited to the simulation of plane or nearly plane surfaces. The generation of a vapor film between a droplet and a structured surface cannot be simulated with this approach.

It should be noted that in addition to the aforementioned methods, the *Lattice-Boltzmann-Method* (e.g. Hazi and Markus [32]) and the *Phase-Field-Method* (e.g. Jamet and co-workers [44]) have to some extend been used for the simulation of boiling flows. However, these methods still seem to be strongly limited to very fundamental research and it will certainly still take some years until they are used as regularly as the aforementioned methods. Therefore, they are only mentioned as an aside within this review of the state of the art.

In summary, the numerical modeling of boiling flows has progressed tremendously within the last 10 to 20 years. Nevertheless, each of the above mentioned models has several shortcomings which restrict its use to a specific boiling configuration. In particular, the simulation of boiling in complex geometries is out of reach with any of these models. Such a complex geometry would lead to 3D simulations that definitely require adaptive mesh refinement at the liquid-vapor interface in order to keep the computational cost at a reasonable level. Furthermore, the use of unstructured meshes could be required depending on the complexity of the geometry. It is clear that none of the models that are summarized in Table 1.1 fulfills all of these criteria.

1.3 Goals

The first main goal of the work in the present thesis is the development of a boiling model that can be used to simulate different boiling phenomena which are relevant for research and application. The model should take into account the highly dynamic nature of the 2-phase flow, the transient and coupled heat transfer in fluid and solid and the microscale effects at the 3-phase contact line (see Table 1.1 for a detailed comparison to existing models). The focus of the thesis lies on the numerical simulation of nucleate boiling heat transfer at moderate heat flux. However, the model should also be applicable for other boiling regimes such as film boiling without any major modification.

The model is intended to be a research tool which can be used to gain a more detailed insight into the process and to enhance the understanding of the physics. For example, the above mentioned increase of the heat transfer coefficient and critical heat flux during boiling on structured surfaces are highly interesting for industrial applications. However, currently such structures are usually optimized by trial-and-error. The boiling model should be capable of handling such structured surface geometries in order to enhance the physical understanding and to use the obtained knowledge for optimization.

As the implementation of the boiling model in a *Computational Fluid Dynamics* (CFD) software requires a lot of interaction with existing parts of the software, the open-source CFD software *OpenFOAM* is chosen as the basic platform for the model. *OpenFOAM* comes with a large CFD library and very sophisticated mesh handling capabilities (e.g. general polyhedral meshes and adaptive mesh refinement). These features are highly valuable for any simulation in complex geometries. Among the different interface

tracking and capturing methods, the VOF method is the method that is most commonly used for the simulation of multiphase flows and is also implemented in the majority of the commercial CFD codes (e.g. Fluent, CFX, Star-CD). This is most probably due to its numerical stability and the rather straightforward implementation which does not rely on high-order schemes such as LS methods do. The VOF method is already implemented in *OpenFOAM*. For these reasons, the boiling model is developed within a VOF framework.

The second main goal of the present thesis is to validate the developed boiling model and to apply it to several boiling configurations. The validation is accomplished by comparison of simulation results to analytical test cases and to highly resolved experimental or numerical data of boiling phenomena which are available in literature. The simulations of different boiling configurations (pool boiling, bubble mergers, flow boiling in a near-wall shear flow, boiling in a structured microchannel and film boiling of droplets) are performed in order to validate the model and to evaluate its capabilities. Further, the simulation results are analyzed in detail with respect to the local and transient heat and mass transfer during boiling. This detailed analysis enables a very profound insight into the boiling process and helps to better understand the heat transfer mechanisms.

In summary, the goals of the present thesis are the development, implementation and validation of a boiling model that overcomes many of the limitations of existing models. Further, the model is used to simulate several boiling configurations with the aim to show and confirm the capabilities of the model. The obtained simulation results are analyzed in detail and provide detailed insight into and a better understanding of boiling heat transfer.

2 Governing equations

In this chapter, the underlying equations of the boiling model are described. The major assumptions which were applied for the sake of simplification and the corresponding justifications are discussed. In the first section of this chapter, the conservation equations for mass, momentum and energy transport are described. This set of equations needs to be solved numerically in order to simulate the heat and fluid flow in the liquid and the vapor phase. The additional equations that account for the 2-phase flow, the interface dynamics and the phase change at the interface are presented in the second section. In the last section the particular equations that are relevant for the microscale heat transfer at the 3-phase contact line are described.

2.1 Mass, momentum and energy transport

The basis of the model for the simulation of boiling phenomena are the continuity equation and the conservation equations for momentum and energy.

$$\frac{\partial \rho}{\partial t} + \nabla \cdot \left(\rho \vec{u}\right) = 0 \tag{2.1}$$

$$\frac{\partial \left(\rho \vec{u}\right)}{\partial t} + \nabla \cdot \left(\rho \vec{u}\vec{u}\right) = \nabla \cdot \boldsymbol{\tau} + \vec{f} \tag{2.2}$$

$$\frac{\partial \left(\rho e\right)}{\partial t} + \nabla \cdot \left(\rho e \vec{u}\right) = \nabla \cdot \left(\boldsymbol{\tau} \cdot \vec{u}\right) - \nabla \cdot \vec{q} + \vec{f} \cdot \vec{u} \tag{2.3}$$

The following assumptions are used in order simplify the set of equations (2.1) to (2.3).

- **The material properties are constant.**
  The material properties are taken at the saturation condition (i.e. the equilibrium between liquid and vapor phase) corresponding to the pressure level at which the simulation is performed. The actual temperature and also the pressure can locally be different from the values at saturation. However, this deviation is typically significantly smaller than 10 % of the absolute value of the temperature or the pressure. Therefore, all material properties are assumed to be independend of temperature and pressure.
- **The fluid is incompressible.**
  The liquid phase is obviously incompressible. As the maximum flow velocity within the vapor phase does usually not exceed some meters per second, the *Mach* number $\mathrm{Ma} = u/\sqrt{\kappa R_{\mathrm{gas}} T}$ is small enough to neglect compressibility effects. Therefore, both phases can be treated as incompressible and the velocity field is free of divergence.

$$\nabla \cdot \vec{u} = 0 \tag{2.4}$$

  Furthermore, the specific energy of an incompressible fluid with a constant heat capacity c is a linear function of temperature. For the sake of simplicity, the reference value for the specific

energy is defined as $e_0 = 0\,\mathrm{J/kg}$ at the reference temperature of $T_0 = 0\,\mathrm{K}$. The differences of potential and kinetic energy are very small in the cases that are discussed in the present thesis and are consequently neglected. Thus, the specific energy is only a function of the temperature.

$$e = e_0 + c\left(T - T_0\right) = cT \tag{2.5}$$

- **The fluid is Newtonian.**
  For the fluids which are used for the simulations in the present thesis the stress tensor $\boldsymbol{\tau}$ in Eq. (2.2) depends linearly on the pressure, the divergence of the velocity field and the deformation speed.

$$\boldsymbol{\tau} = -\left(p + \frac{2}{3}\mu\nabla\cdot\vec{u}\right)\mathbf{I} + \mu\left[\nabla\vec{u} + (\nabla\vec{u})^{\mathrm{T}}\right] \tag{2.6}$$

  For an incompressible fluid, this equation can be simplified because the velocity field is free of divergence.

$$\boldsymbol{\tau} = -p\mathbf{I} + \mu\left[\nabla\vec{u} + (\nabla\vec{u})^{\mathrm{T}}\right] \tag{2.7}$$

- ***Fourier's law* can be applied for the heat flux.**
  According to *Fourier's law* the heat flux vector $\vec{q}$ in Eq. (2.3) depends linearly on the temperature gradient and the thermal conductivity k of the fluid.

$$\vec{q} = -k\nabla T \tag{2.8}$$

- **Viscous dissipation and the power supply or release due to volumetric forces are negligible.**
  As discussed above, the speed of the flow and hereby also the shear stress is rather low. Therefore, the effect of viscous dissipation $\nabla\cdot(\boldsymbol{\tau}\cdot\vec{u})$ and the power supply or release due to volumetric forces $\vec{f}\cdot\vec{u}$ in Eq. (2.3) are negligible compared to the conductive and convective heat transport and the heat consumption or supply due to evaporation or condensation.

Applying the above mentioned assumptions, the general formulation of the mass, momentum and energy conservation equations can be simplified to the following set of equations:

$$\nabla\cdot\vec{u} = 0 \tag{2.9}$$

$$\frac{\partial\left(\rho\vec{u}\right)}{\partial t} + \nabla\cdot\left(\rho\vec{u}\vec{u}\right) - \nabla\cdot\left\{\mu\left[\nabla\vec{u} + (\nabla\vec{u})^{\mathrm{T}}\right]\right\} = -\nabla p + \vec{f} \tag{2.10}$$

$$\frac{\partial\left(\rho cT\right)}{\partial t} + \nabla\cdot\left(\rho cT\vec{u}\right) - \nabla\cdot(k\nabla T) = 0 \tag{2.11}$$

These conservation equations have to be solved in the liquid and the vapor phase to describe the mass, momentum and energy transport in the fluid. Additionally, the conservation equation for energy must also be solved in the solid phase if the transient conduction inside the heating wall is taken into account. In the solid phase the convective term is zero and the energy equation for the solid domain consists only of a transient and a diffusive term.

$$\frac{\partial\left(\rho cT\right)}{\partial t} - \nabla\cdot(k\nabla T) = 0 \tag{2.12}$$

Turbulence does not need to be modeled for the simulations performed in the present thesis. Taking into account the typical maximum values of the velocity magnitude ($u = 1\,\mathrm{m/s}$, which usually only appears in a very small region inside the vapor phase, see section 5.1), a typical bubble size ($D = 2\,\mathrm{mm}$) and a representative kinematic viscosity ($\nu = 0.3{\cdot}10^{-6}\,\mathrm{m^2/s}$), the *Reynolds* number $\mathrm{Re} = uL/\nu$ is below 5000. According to Hinze [35], the smallest turbulence scale is the *Kolmogorov* length.

$$L_\mathrm{K} = \left(\frac{\nu^3}{\epsilon}\right)^{1/4} = \left(\frac{\nu^3 L}{u^3}\right)^{1/4} \approx \frac{L}{\mathrm{Re}^{3/4}} \tag{2.13}$$

Herein, ϵ is the dissipation rate of turbulent kinetic energy which can be estimated as u^3/L. The *Kolmogorov* scale in the simulations that are presented and discussed in the present thesis is of the order of $2\,\mu\mathrm{m}$. The mesh size is typically slightly higher but still of the same order. Hence, according to Moin and Mahesh [75] no modeling of turbulence is required as the mesh is capable of resolving the smallest turbulence scales. In other words, the turbulent effects that might occur are captured by solving the set of equations (2.9) to (2.11) on a mesh that is fine enough to perform a *Direct Numerical Simulation* (DNS) of the flow. Strictly, a DNS of a turbulent flow cannot make use of any symmetries of the flow. Many of the simulations which are presented in the present thesis are performed on a 2D axisymmetric mesh or on a 3D mesh with one or two planes of symmetry. Therefore, the simulations are not DNS in the strict sense. However, the above estimation of the Reynolds number represents a worst case. The velocities are actually much smaller in most parts of the domain. Therefore, turbulence does certainly not play an important role in the cases which are simulated here.

2.2 2-phase flow and phase change

The multiphase flow that has to be described to simulate boiling phenomena is characterised by two immiscible phases. The main field of interest is nucleate boiling were the two phases are the liquid and vapor phase of a pure fluid. In the scale on which the phenomena are treated here, the interface that separates the bulk liquid and vapor phases is assumed to be infinitely thin and can be respresented by a surface. The equations presented in section 2.1 are valid in each of the bulk phases. Additional conditions for the mass, momentum and energy transport have to be defined at the liquid-vapor interface. Carey [6] describes the conditions for the interfacial transport in a very detailed manner.

One of the additional conditions that need to be defined at the liquid-vapor interface is the pressure difference between the two sides of the interface resulting from surface tension. This pressure difference can be derived from considerations on the free energy (see Carey [6]) leading to the so-called *Young-Laplace-Equation*.

$$\Delta p = p_\mathrm{v} - p_\mathrm{l} = \sigma\left(\frac{1}{r_1} + \frac{1}{r_2}\right) = \sigma\kappa \tag{2.14}$$

Herein, σ is the surface energy density of the liquid-vapor interface, r_1 and r_2 are the principal radii of curvature of the interface and κ is twice the mean curvature. The curvature is defined as positive if the the interface is convex with respect to the vapor phase, e.g. for a vapor bubble within a bulk liquid. The surface energy density σ (energy per unit surface area) can also be interpreted as a surface tension (force per unit length). Strictly, Eq. (2.14) is only valid for the case of an interfacial flow without phase change, i.e. if there is no mass flux across the interface. To derive the general equations for the conservation of mass, momentum and energy across the interface, the control volumes which are shown in Figure 2.1 are defined.

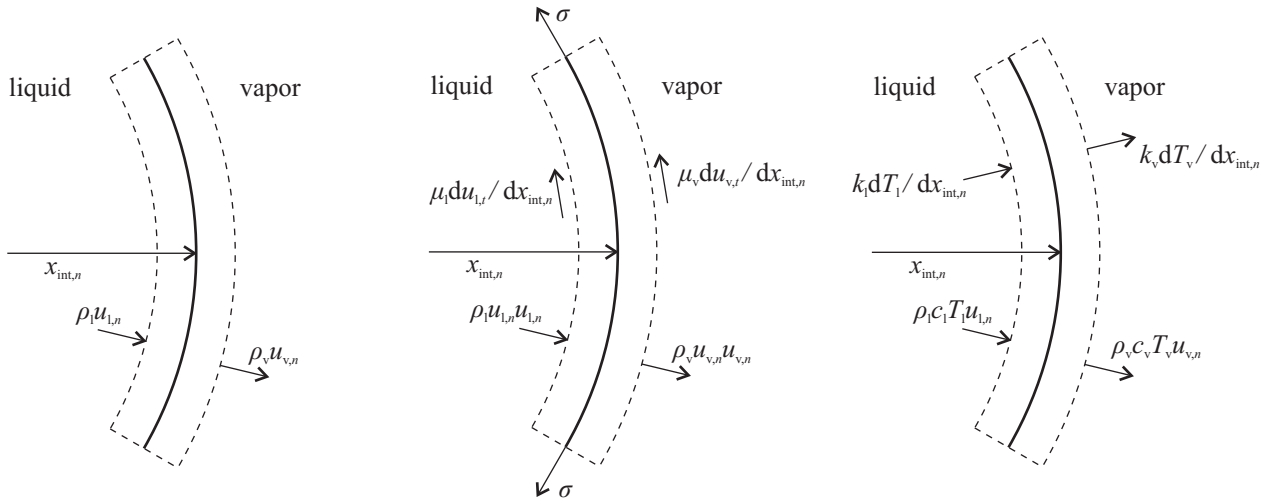

(a) Mass transport (b) Momentum transport (c) Energy transport

Figure 2.1: Control volumes for the calculation of mass, momentum and energy transport across the liquid-vapor interface as proposed by Carey [6].

As the interface is infinitely thin, it has no mass and therefore cannot store any mass, momentum or energy. Balancing the incoming and outgoing fluxes of each quantity in a reference frame moving with the speed of the interface $u_\mathrm{int} = \mathrm{d}x_{\mathrm{int},n}/\mathrm{d}t$ leads to the equations for the transport of mass, normal momentum, tangential momentum and energy across the liquid-vapor interface.

$$\rho_\mathrm{l} u_{\mathrm{l},n} - \rho_\mathrm{v} u_{\mathrm{v},n} = \left(\rho_\mathrm{l} - \rho_\mathrm{v}\right) u_\mathrm{int} \tag{2.15}$$

$$p_\mathrm{v} - p_\mathrm{l} = \sigma\kappa + \rho_\mathrm{l} u_{\mathrm{l},n}\left(u_{\mathrm{l},n} - u_\mathrm{int}\right) - \rho_\mathrm{v} u_{\mathrm{v},n}\left(u_{\mathrm{v},n} - u_\mathrm{int}\right) \tag{2.16}$$

$$\mu_\mathrm{l} \frac{\mathrm{d}u_{\mathrm{l},t}}{\mathrm{d}x_{\mathrm{int},n}} = \mu_\mathrm{v} \frac{\mathrm{d}u_{\mathrm{v},t}}{\mathrm{d}x_{\mathrm{int},n}} \tag{2.17}$$

$$\rho_\mathrm{l}\left(u_{\mathrm{l},n} - u_\mathrm{int}\right)\Delta h_\mathrm{V} = \rho_\mathrm{v}\left(u_{\mathrm{v},n} - u_\mathrm{int}\right)\Delta h_\mathrm{V} = -k_\mathrm{l}\frac{\mathrm{d}T_\mathrm{l}}{\mathrm{d}x_{\mathrm{int},n}} + k_\mathrm{v}\frac{\mathrm{d}T_\mathrm{v}}{\mathrm{d}x_{\mathrm{int},n}} \tag{2.18}$$

In all these equations and in Figure 2.1, the subscript n denotes the normal direction to the interface while the subscript t denotes the tangential direction. It can be seen that Eq. (2.16) is equivalent to the *Young-Laplace Equation* (2.14) if the terms describing the recoil pressure due to evaporation or condensation at the interface $\rho_{\mathrm{l/v}} u_{\mathrm{l/v},n}\left(u_{\mathrm{l/v},n} - u_\mathrm{int}\right)$ are negligible. Considering the typical material properties, curvature and vapor speed, the recoil pressure is at least one order of magnitude smaller than the pressure difference due to the curvature of the interface. It will be shown in section 4.1.2 that it is sufficient to impose the jump condition for the pressure according to Eq. (2.14) at the liquid-vapor interface as the recoil pressure directly results from the source term field which represents the phase change at the interface.

The region where the liquid-vapor interface is in contact to a solid wall is of special interest. In Figure 2.2 the contact between a liquid drop and a perfectly flat solid wall in a vapor atmosphere is shown. The liquid-vapor interface, the solid-liquid interface and the solid-vapor interface meet at the 3-phase contact line which degenerates to a point in 2D. The apparent contact angle is defined as the

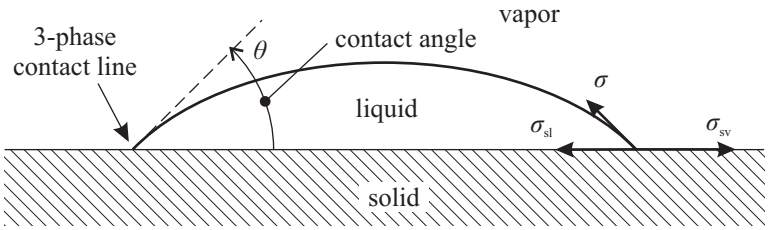

Figure 2.2: Definition of the contact angle and its dependence on the surface energies.

angle enclosed by the tangents to the liquid-vapor and the solid-liquid interface. If the surface energy density of each of the phase interfaces is known, the apparent contact angle can be calculated from the *Young Equation*.

$$\cos\theta = \frac{\sigma_{\mathrm{sv}} - \sigma_{\mathrm{sl}}}{\sigma} \tag{2.19}$$

Herein, σ is the surface energy density of the liquid-vapor interface and σ_{sv} and σ_{sl} are the surface energy densities of the solid-vapor and solid-liquid interfaces, respectively. The *Young Equation* (2.19) is obtained from a force balance between the components of the surface tensions which are parallel to the wall. Additionally, the force balance of the components which are normal to the wall can be used to calculate the attaching forces at the 3-phase contact line. The higher the surface tension and the contact angle, the higher the attaching forces at the 3-phase contact line are. The consequence of this relation is that a bubble detachment process is highly influenced by the contact angle. In practice, the surface energy densities are typically not known except for the liquid-vapor interface. Therefore, the contact angle is usually measured experimentally and then used for modeling purposes. Strictly, the *Young Equation* (2.19) is only valid for a non-moving 3-phase contact line on a perfectly flat and chemically homogeneous solid surface. In real conditions, the motion of the 3-phase contact line as well as the roughness and chemical heterogeneity of the solid surface can lead to significant deviations of the apparant contact angle from the static angle defined by the *Young Equation* (2.19). However, due to the high complexity and the small length scales, there is still no closed and completely physically based law or model for the dynamics of the contact angle. Therefore, the simulations in the present thesis are all performed with a constant apparent contact angle except for the simulation of flow boiling in a near-wall shear flow described in section 5.3.1. The value of the static contact angle and, if required, of the sub-model which describes the dynamics of the contact angle are given during the discussion of the results in chapter 5.

2.3 Microscale heat and fluid flow at the 3-phase contact line

The microscopic region at the 3-phase contact line where the liquid-vapor interface meets the solid wall is of tremendous importance for the heat transfer during boiling. Fundamental information on the microscale effects at the 3-phase contact line is given by Truong and Wayner [109] while a very comprehensive review has been published by Wayner [121]. It should be noted that several approaches exist to describe and solve the heat and fluid flow at the 3-phase contact line. Morris [77, 78, 79] formulates a free-boundary problem with an inner and outer solution and presents an asymptotic and numerical analysis. Plawsky and co-workers [86] formulate a boundary value problem which they solve numerically within the framework of a *Finite-Element-Method*. The model which is used here to describe the heat and fluid flow at the 3-phase contact line, has been developed and used by Stephan and Busse [108]. The equations are very similar to the equations which are derived and used by Plawsky and

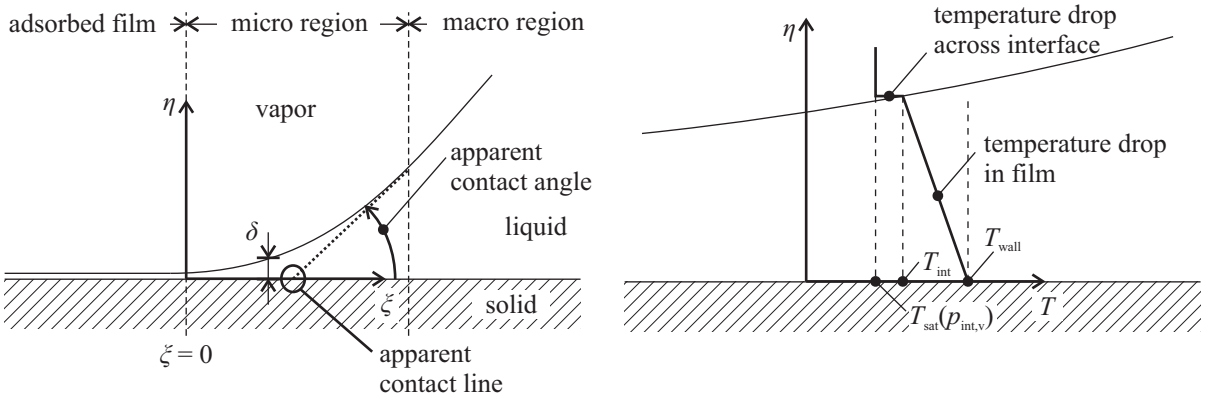

(a) Interface shape (b) Temperature profile

Figure 2.3: Explaining sketches for the heat and mass transfer in the microscopic region at the 3-phase contact line.

co-workers [86]. A very detailed describtion of the model is given by Stephan [104] and also by Fuchs [21]. Here, the main assumptions and equations of the model are briefly discussed.

A sketch of the microscopic region at the 3-phase contact line is shown in Figure 2.3(a). The micro region is defined as the region in which the adhesion forces between fluid molecules and wall molecules, and the effect of curvature on the local thermodynamic equilibrium are important. As illustrated in Figure 2.3(a), there is no contact line on the microscopic scale. For $\xi < 0$, there is an adsorbed layer of fluid molecules on the solid wall. No evaporation takes place in this region because of the strong attracting forces between fluid and wall molecules. The thickness of this so called *adsorbed film* is of the order of some nanometers. At $\xi = 0$, the curvature suddenly increases with rising ξ and the thickness of the liquid film starts to grow. As the distance between the liquid-vapor interface and the wall becomes larger, the adhesion forces decay rapidly and the meniscus shape is governed by macroscopic hydrodynamics.

There are three main aspects which distinguish the microscopic heat transfer at the 3-phase contact line from macroscropic heat transfer.

- **Intermolecular attraction forces between fluid and wall molecules are important.**
  In the vicinity of the wall, the fluid and wall molecules attract each other by *van der Waals* forces. This attraction is negligible on the macroscopic scale. However, is must be taken into account when very thin liquid films (thickness of some nanometers) are described. This is the case within the adsorbed film and also in the transition from the adsorbed film to the macroscopic shape of the interface.
- **Curvature and attraction forces cause a change of the local thermodynamic equilibrium.**
  The high values of curvature in the vicinity of the 3-phase contact line lead to a high pressure jump across the interface. As the saturation temperature is a function of pressure, the curvature changes the local thermodynamic equilibrium which means that the local saturation temperature is different from the saturation temperature that corresponds to the pressure in the macroscopic domain. Additionally, the pressure within the liquid film increases from the interface towards the wall due to the above mentioned attraction forces. This increased pressure within the liquid also leads to a change of the local thermodynamic equilibrium.
- **There is a temperature drop across the interface during evaporation**
  The liquid-vapor interface itself has a certain heat resistance which means that the temperature of

the interface must be slightly higher than the local saturation temperature in order to evaporate liquid. On a macroscopic scale, this so-called interfacial heat resistance is negligible compared to the heat resistance of a macroscopic liquid film. However, on the microscopic scale the liquid film is very thin and its heat resistance is of the same order as or even lower than the interfacial heat resistance. Therefore, the interfacial heat resistance has to be taken into account when describing the heat transfer in the microscopic region close to the 3-phase contact line.

In the following, the basic equations which are used to describe the heat and fluid flow in the micro region are explained briefly. As mentioned above, a detailed discussion of the modeling equations is given by Stephan [104]. It should be noted that this model for the heat and fluid flow in the micro region relies on a lot of assumptions which will be shown in the following. In principal, many of these assumptions can be viewed with skepticism. However, the results of the model have recently been compared to molecular dynamics simulations of the micro region by Akker [114] and Akker and co-workers [115]. The authors found a very satisfying agreement between the two approaches. Although the molecular dynamics simulations have only been performed for an Argon system, the good agreement allow the conclusion that the assumptions and simplifications which are required for the theoretical modeling approach are justified.

Pressure and velocity profile

The pressure difference between the bulk vapor and the liquid within the thin film consists of two contributions. First, according to Eq. (2.14) the local curvature of the interface leads to a pressure jump $\Delta p_{\text{Young-Laplace}}$ at the liquid-vapor interface. Second, the intermolecular attraction forces between fluid and wall molecules are described within a *disjoining pressure concept*. These forces do not lead to a pressure jump at the liquid-vapor interface but act as a volumetric force within the thin liquid film. Thus, the mean pressure in the liquid film is increased compared to the pressure directly at the liquid-vapor interface. The *disjoining pressure* $p_{\text{disjoining}}$ is proportional to the inverse cube of the film thickness δ^{-3}. Thus, the pressure difference between the liquid within the thin film and the bulk vapor can be calculated from the following equation.

$$\Delta p = p_{\text{v}} - p_{\text{l}} = \Delta p_{\text{Young-Laplace}} + p_{\text{disjoining}} = \sigma\kappa + \frac{A}{\delta^3} \tag{2.20}$$

As the pressure within the vapor phase is approximately constant, this pressure difference determines the pressure within the thin liquid film which drives the liquid flow and affects the local equilibrium saturation conditions. The effect of vapor recoil is not taken into account. As discussed above the typical vapor densities and evaporation rates in the present thesis lead to a vapor recoil pressure which is several orders of magnitude smaller than the pressure jump due to the curvature of the interface. This is also valid in the microscopic region at the 3-phase contact line. Although the evaporation rates and therefore the recoil pressure is higher than in the macroscopic domain, the effect is still negligible compared to the effect of the curvature which is also higher at the 3-phase contact line than in the macroscopic domain.

The curvature of a function $\delta = f(\xi)$ is given by the following expression.

$$\kappa = \frac{\dfrac{\mathrm{d}^2\delta}{\mathrm{d}\xi^2}}{\left[1 + \left(\dfrac{\mathrm{d}\delta}{\mathrm{d}\xi}\right)^2\right]^{3/2}} \tag{2.21}$$

In order to analytically determine the velocity profile as a function of the local film thickness and pressure gradient, the flow is assumed to be nearly parallel to the wall and can be completely described

by the profile of the velocity u in the ξ-direction. In other words, the thickness of the film is assumed to be much smaller than the characteristic length in the ξ-direction. Hence, the dimensional analysis of the momentum balance equation leads to the conclusion that the velocity component in η-direction can be neglected. Further, a rather slow flow at low Reynolds numbers is assumed. Thus, inertia effects can be neglected and the flow can be described with a lubrication approximation. The simplified momentum balance in ξ-direction leads to the following differential equation for the velocity field.

$$\mu_\mathrm{l}\frac{\mathrm{d}^2u}{\mathrm{d}\eta^2}=\frac{\mathrm{d}p_\mathrm{l}}{\mathrm{d}\xi}=-\frac{\mathrm{d}\left(\Delta p\right)}{\mathrm{d}\xi} \tag{2.22}$$

The only driving force is the pressure gradient. Surface tension is not considered to be temperature dependend in the present thesis. Therefore, there is no *Marangoni* effect (flow induced by gradients of the surface tension along the interface) and surface tension acts only perpendicular to the interface. In principal, it is straightforward to include the *Marangoni* effect into the equation for the heat and fluid flow at the 3-phase contact line as shown by Plawsky and co-workers [86] as well as Kern and Stephan [52]. The differential equation Eq. (2.22) can be integrated twice with respect to η. Using a no slip boundary condition at the wall and a slip condition (no shear rate, following from Eq. (2.17) and $\mu_\mathrm{v} \ll \mu_\mathrm{l}$) at the liquid-vapor interface, the velocity profile in the liquid can be expressed by the following equation.

$$u=-\frac{\delta^2}{\mu_\mathrm{l}}\frac{\mathrm{d}\left(\Delta p\right)}{\mathrm{d}\xi}\left[\frac{1}{2}\left(\frac{\eta}{\delta}\right)^2-\frac{\eta}{\delta}\right] \tag{2.23}$$

Heat transfer

The heat transfer is assumed to be one-dimensional and perpendicular to the wall. This assumption is valid if the convective heat transfer in the liquid film can be neglected and if the slope of the film is small. Generally, there are two contributions to the overall heat resistance of the liquid film (see Figure 2.3(b)). First, the heat is conducted through the liquid film. The heat flux can be calculated from the temperature drop in the film, the thermal conductivity of the liquid and the local film thickness.

$$q=\frac{k_\mathrm{l}}{\delta}\left(T_\mathrm{wall}-T_\mathrm{int}\right) \tag{2.24}$$

The second contribution to the overall heat resistance is the evaporation at the liquid-vapor interface itself. The heat transfer can be determined from considerations of the evaporation process on a molecular scale (see Schrage [92]).

$$q=\frac{2f}{2-f}\frac{\Delta h_\mathrm{V}}{\sqrt{2\pi R_\mathrm{gas}}}\left(\frac{p_\mathrm{int,v}}{\sqrt{T_\mathrm{int}}}-\frac{p_\mathrm{v}}{\sqrt{T_\mathrm{sat}\left(p_\mathrm{v}\right)}}\right) \tag{2.25}$$

Herein, p_v is the pressure of the bulk vapor and $p_\mathrm{int,v}$ is the pressure in the vapor phase immediately at the interface. The accomodation coefficient f takes into account molecular effects such as reflection of liquid molecules emitted from the interface during evaporation. Marek and Straub [69] point out that there is a lot of uncertainty regarding this coefficient. Typical values in literature scatter by more than two orders of magnitude. Here, a value of unity is used for all simulations which corresponds to an ideal system. Numerical experiments showed that a variation of the accomodation coefficient in a range between 0.5 and 1 does not much affect the results. In the next steps, Eq. (2.25) is simplified and

the pressures are expressed by known quantities. First, the difference between the interfacial temperature and the saturation temperature is small compared to the absolute values of the temperatures (i.e. $T_{\mathrm{sat}}/T_{\mathrm{int}} \approx 1$). Therefore, Eq. (2.25) can be simplified by elimination of T_{int}.

$$q = \frac{2f}{2-f} \frac{\Delta h_{\mathrm{V}}}{\sqrt{2\pi R_{\mathrm{gas}} T_{\mathrm{sat}}}} \left(p_{\mathrm{int,v}} - p_{\mathrm{v}} \right) \tag{2.26}$$

The pressure $p_{\mathrm{int,v}}$ on the vapor side of the interface can be determined from the *Thomson Equation* and depends on the pressure difference due to the curvature effect and the adhesion forces as well as the density ratio.

$$p_{\mathrm{int,v}} = p_{\mathrm{sat}}\left(T_{\mathrm{int}}\right) - \frac{\rho_{\mathrm{v}}}{\rho_{\mathrm{l}} - \rho_{\mathrm{v}}} \Delta p \approx p_{\mathrm{sat}}\left(T_{\mathrm{int}}\right) - \frac{\rho_{\mathrm{v}}}{\rho_{\mathrm{l}}} \Delta p \tag{2.27}$$

The saturation pressure at the temperature of the interface $p_{\mathrm{sat}}\left(T_{\mathrm{int}}\right)$ can be determined from the *Clausius-Clapeyron Equation* which can be linearized and simplified as $\rho_{\mathrm{v}} \ll \rho_{\mathrm{l}}$.

$$\frac{\mathrm{d}p}{\mathrm{d}T} = \frac{\Delta h_{\mathrm{V}} \rho_{\mathrm{l}} \rho_{\mathrm{v}}}{T_{\mathrm{sat}}\left(p_{\mathrm{v}}\right)\left(\rho_{\mathrm{l}} - \rho_{\mathrm{v}}\right)} \approx \frac{\Delta h_{\mathrm{V}} \rho_{\mathrm{v}}}{T_{\mathrm{sat}}\left(p_{\mathrm{v}}\right)} = \frac{p_{\mathrm{sat}}\left(T_{\mathrm{int}}\right) - p_{\mathrm{v}}}{T_{\mathrm{int}} - T_{\mathrm{sat}}\left(p_{\mathrm{v}}\right)} \tag{2.28}$$

The heat flux at the interface as a function of the temperature at the interface T_{int} and the saturation temperature T_{sat} corrected by the influence of the pressure jump can be obtained by combining equations (2.26) to (2.28).

$$q = \frac{2f}{2-f} \frac{\rho_{\mathrm{v}} \Delta h_{\mathrm{V}}^2}{T_{\mathrm{sat}}^{3/2} \sqrt{2\pi R_{\mathrm{gas}}}} \left[T_{\mathrm{int}} - T_{\mathrm{sat}} \left(1 + \frac{\Delta p}{\rho_{\mathrm{l}} \Delta h_{\mathrm{V}}} \right) \right] \tag{2.29}$$

Herein, the term in front of the brackets is the inverse of the heat resistance of the liquid-vapor interface which has already been mentioned above and which is called *interfacial heat resistance* R_{int} in the following.

$$R_{\mathrm{int}} = \frac{2-f}{2f} \frac{T_{\mathrm{sat}}^{3/2} \sqrt{2\pi R_{\mathrm{gas}}}}{\rho_{\mathrm{v}} \Delta h_{\mathrm{V}}^2} \tag{2.30}$$

The interfacial heat resistance R_{int} is a measure of how superior the interface temperature has to be compared to the corrected saturation temperature for a certain evaporation rate. By combining the equations (2.24), (2.29) and (2.30), the heat flux can be expressed as a function of the wall temperature and the bulk saturation temperature T_{sat}.

$$q = \frac{T_{\mathrm{wall}} - T_{\mathrm{sat}} \left(1 + \dfrac{\Delta p}{\rho_{\mathrm{l}} \Delta h_{\mathrm{V}}} \right)}{\dfrac{\delta}{k_{\mathrm{l}}} + R_{\mathrm{int}}} \tag{2.31}$$

In this equation one can immediately find two of the above mentioned aspects that distinguish the microscale heat transfer at the 3-phase contact line from macroscopic heat transfer. First, the interfacial heat resistance R_{int} is added to the heat resistance of the liquid film in the denominator. Second, the pressure difference Δp changes the local saturation temperature by the factor $\left(1 + \Delta p / \left(\rho_{\mathrm{l}} \Delta h_{\mathrm{V}}\right)\right)$ in the numerator.

Evaporation

The above considerations on the fluid flow and the heat transfer in the liquid film are coupled by the evaporation process. The heat flux q is removed by evaporation and the mass flux that evaporates locally is equal to the change of the mass flow in the liquid film along the ξ direction. The mean flow velocity u_{mean} in the liquid film and the mass flow per unit contact line length m^* (integrated between 0 and ξ) can be calculated from the velocity profile which is given by Eq. (2.23).

$$u_{\mathrm{mean}} = \frac{1}{\delta}\int_0^{\delta} u\,\mathrm{d}\eta = \frac{1}{3}\frac{\delta^2}{\mu_{\mathrm{l}}}\frac{\mathrm{d}\left(\Delta p\right)}{\mathrm{d}\xi} \tag{2.32}$$

$$m^* = -\rho_{\mathrm{l}}\delta u_{\mathrm{mean}} = -\frac{1}{3}\frac{\delta^3\rho_{\mathrm{l}}}{\mu_{\mathrm{l}}}\frac{\mathrm{d}\left(\Delta p\right)}{\mathrm{d}\xi} \tag{2.33}$$

Hence, the heat flux can be expressed by the change of the mass flow along the ξ direction and thereby as a function of the pressure gradient in the liquid film.

$$q = \frac{\mathrm{d}m^*}{\mathrm{d}\xi}\Delta h_{\mathrm{V}} = -\frac{1}{3}\frac{\rho_{\mathrm{l}}\Delta h_{\mathrm{V}}}{\mu_{\mathrm{l}}}\frac{\mathrm{d}}{\mathrm{d}\xi}\left(\delta^3\frac{\mathrm{d}\left(\Delta p\right)}{\mathrm{d}\xi}\right) \tag{2.34}$$

Complete equation for the heat and mass transfer

The complete equation for the heat and mass transfer in the microscopic region close to the 3-phase contact line is obtained by combining Eq. (2.31) and Eq. (2.34).

$$\frac{T_{\mathrm{wall}} - T_{\mathrm{sat}}\left(1+\dfrac{\Delta p}{\rho_{\mathrm{l}}\Delta h_{\mathrm{V}}}\right)}{\dfrac{\delta}{k_{\mathrm{l}}} + R_{\mathrm{int}}} = -\frac{1}{3}\frac{\rho_{\mathrm{l}}\Delta h_{\mathrm{V}}}{\mu_{\mathrm{l}}}\frac{\mathrm{d}}{\mathrm{d}\xi}\left(\delta^3\frac{\mathrm{d}\Delta p}{\mathrm{d}\xi}\right) \tag{2.35}$$

Further, Eq. (2.20) and Eq. (2.21) can be used to eliminate the pressure differene Δp from Eq. (2.35) and to obtain an equation in which the film thickness δ and its derivatives are the only unknowns.

$$\begin{aligned}\frac{1}{\dfrac{\delta}{k_{\mathrm{l}}} + R_{\mathrm{int}}}\left\{T_{\mathrm{wall}} - T_{\mathrm{sat}}\left[1+\frac{1}{\rho_{\mathrm{l}}\Delta h_{\mathrm{V}}}\left(\frac{\sigma\dfrac{\mathrm{d}^2\delta}{\mathrm{d}\xi^2}}{\left[1+\left(\dfrac{\mathrm{d}\delta}{\mathrm{d}\xi}\right)^2\right]^{3/2}} + \frac{A}{\delta^3}\right)\right]\right\} &= \ldots \\ \ldots = -\frac{1}{3}\frac{\rho_{\mathrm{l}}\Delta h_{\mathrm{V}}}{\mu_{\mathrm{l}}}\frac{\mathrm{d}}{\mathrm{d}\xi}&\left[\delta^3\frac{\mathrm{d}}{\mathrm{d}\xi}\left(\frac{\sigma\dfrac{\mathrm{d}^2\delta}{\mathrm{d}\xi^2}}{\left[1+\left(\dfrac{\mathrm{d}\delta}{\mathrm{d}\xi}\right)^2\right]^{3/2}} + \frac{A}{\delta^3}\right)\right]\end{aligned} \tag{2.36}$$

This mathematically complex equation is a 4th order *Ordinary Differential Equation* (ODE) which needs to be solved in order to describe the microscale heat and mass transfer at the 3-phase contact line. The method which is used to solve Eq. (2.36) and local results are described in section 4.2.1.

3 Numerical method

In this chapter, the numerical methods which are used to solve the conservation equations for the heat and fluid flow in the macroscopic scale (which are shown in chapter 2) are presented and discussed. First, the general numerical approach and the discretization method of the solver are presented. Then, the particular numerical method which is used to model the 2-phase flow is described in detail. Finally, the segregated approach which is used to solve the coupled partial differential equations is briefly explained.

3.1 Discretization method

3.1.1 Spatial and temporal discretization

The CFD software *OpenFOAM* which is the framework in which the boiling model is implemented uses the *Finite-Volume-Method* (FVM) to spatially discretize the computational domain and to transfer the partial differential equations into a linear algebraic system of equations.

$$\boldsymbol{A} \cdot \vec{x} = \vec{b} \tag{3.1}$$

The FVM is commonly used for the simulation of fluid dynamics problems. One of its main advantages is the conservative formulation of the discrete equations, i.e. the conservation of the field quantities is fulfilled up to the level of accuracy with which the algebraic system is solved. Here, the general background of the FVM is briefly shown. Detailed descriptions of the FVM in general can be found in text books on computational engineering (e.g. Schäfer [91]) while a more detailed description of the implementation of the FVM in *OpenFOAM* is given by Jasak [45], Ubbink [112] and Rusche [90]. Schäfer [91] divides the FVM into five steps.

- **Step 1:** Decomposition of the computational domain into control volumes (cells)
- **Step 2:** Formulation of integral balance equations for each control volume
- **Step 3:** Replacement of integrals by numerical approximations
- **Step 4:** Replacement of field values and derivatives by interpolation of cell values
- **Step 5:** Matrix assembly for a discrete algebraic system

The decomposition of the domain into discrete cells in step 1 is an important task during the setting up of a simulation. The cells as a whole build the numerical mesh for the simulation. The quality of this mesh, e.g. in terms of orthogonality, has a strong influence on the quality of the results. In the present thesis, the meshes are typically generated with *blockMesh*[1], *Gambit*[2] or *IcemCFD*[3]. The optimum mesh usually depends strongly on the particular simulation and its particular geometry. Therefore, this step is described for each individual case during the discussion of the results in chapter 5.

[1] Mesh generation utility of the *OpenFOAM* CFD package that can be used to generate meshes within simple geometries.
[2] Commercial mesh generator distributed by Fluent.
[3] Commercial mesh generator distributed by Ansys.

Once, the computational domain is discretized in space, the conservation equations have to be reformulated in order to express them by the variables stored in each cell. A typical conservation equation in fluid dynamics consists of a transient, a convective and a diffusive term as well as a source term.

$$\frac{\partial \Phi}{\partial t} + \nabla \cdot (\vec{u}\Phi) - \nabla \cdot (D \nabla \Phi) = \dot{\Phi} \tag{3.2}$$

In the FVM the transport of the variables is balanced for each cell. Therefore, Eq. (3.2) must be spatially integrated for an arbitrary control volume (step 2).

$$\iiint_V \frac{\partial \Phi}{\partial t} \mathrm{d}V + \iint_S \Phi \vec{u} \mathrm{d}\vec{S} - \iint_S D \nabla \Phi \mathrm{d}\vec{S} = \iiint_V \dot{\Phi} \mathrm{d}V \tag{3.3}$$

Herein, *Gauss' theorem* is already applied to transform the volume integral of the divergence terms into surface integrals. The volume and surface integrals in Eq. (3.3) are then replaced by numerical approximations (step 3).

$$\iiint_V \frac{\partial \Phi}{\partial t} \mathrm{d}V \approx \left(\frac{\partial \Phi}{\partial t} \right)_c V_c \tag{3.4}$$

$$\iint_S (\vec{u}\Phi) \, \mathrm{d}\vec{S} \approx \sum_f \Phi_f \vec{u}_f \vec{S}_f \tag{3.5}$$

$$\iint_S D \nabla \Phi \mathrm{d}\vec{S} \approx \sum_f D_f \left(\nabla \Phi \right)_f \vec{S}_f \tag{3.6}$$

$$\iiint_V \dot{\Phi} \mathrm{d}V \approx \dot{\Phi}_c V_c \tag{3.7}$$

Herein, the subscripts c and f are counters representing a certain cell or face of the computational mesh. Before the matrix of the algebraic system Eq. (3.1) can be build, the way by which the variables and their gradients at the cell faces (Φ_f and $(\nabla \Phi)_f$, respectively) are calculated from the variables stored in the cell centers must be determined (step 4). Further, the transient term in the conservation equation (3.3) must also be expressed by variables stored in the cell centers. Just like the decomposition of the space into discrete cells, the time is decomposed in discrete time steps. In general, the transient term can be expressed by a function of the time step size and the value of the variable at the current time step and at several passed time steps.

$$\frac{\partial \Phi}{\partial t} \approx f \left(\Delta t, \Phi^{(n)}, \Phi^{(n-1)}, \Phi^{(n-2)}, \ldots \right) \tag{3.8}$$

There are various spatial and temporal discretization schemes available and a large number of them is implemented in *OpenFOAM*. In the last step, the discretized conservation equation is generated in each cell. These equations as a whole are then used to determine the components of the matrix and the right hand side of the algebraic system Eq. (3.1) (step 5).

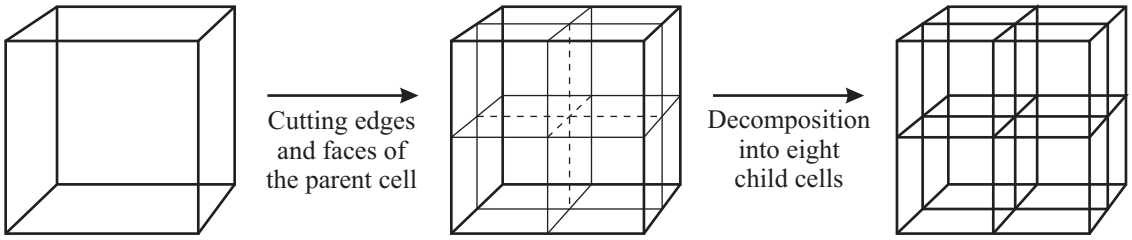

Figure 3.1: Illustration of the adaptive mesh refinement utility of *OpenFOAM*: A cell that is marked for refinement (parent cell) is decomposed into eight new cells (child cells).

The user of *OpenFOAM* needs to interact in the disretization process only in step 1 by providing the numerical mesh and in step 4 by choosing the spatial and temporal discretization schemes. The set of spatial and temporal discretization schemes which is used for the simulations in the present thesis is given in appendix D.

3.1.2 Time and space adaptivity

As mentioned above, the computational domain and also the temporal duration of the phenomenon which is to be simulated are decomposed into discrete elements. The resolution of this decomposition (i.e. the size of the cells and the time steps) must be fine enough to capture the relevant physical processes. Additionally, the time step size is limited by the propagation speed of information on the numerical mesh. The *Courant* number

$$\mathrm{Co} = \frac{u\Delta t}{\Delta x} \tag{3.9}$$

is a measure of how far a fluid particle travels during one time step compared to the size of a cell. 2-phase flows are particularly restricted by this criterion and the *Courant* number should not exceed unity in any case. *OpenFOAM* offers two ways for the temporal discretization. First, a constant time step size can be chosen. Second, a maximum value of the *Courant* number can be set. In this case the solver adapts the time step size such that the *Courant* number is always (i.e. at all times and everywhere in the computational domain) smaller than the maximum value that has been chosen. The second option was chosen for all the simulations in the present thesis.

In addition to the adaptivity of the time step size, *OpenFOAM* comes with the capability to locally refine the numerical mesh. This feature is highly valuable for 3D simulations of 2-phase flows. Typically, the relevant physical transport processes happen at or very close to the liquid-vapor interface. Therefore, a very fine mesh is required in this region while the mesh can be much coarser in the bulk phases far away from the interface. The local refinement can drastically reduce the total number of cells which can otherwise quickly become a limiting factor for 3D simulations. The adaptive mesh refinement utility of *OpenFOAM* allows the user to define arbitrary criteria for mesh refinement and unrefinement. The only shortcoming of the utility is the limitation to hexahedral meshes, i.e. the cells must be composed of six faces with four corner points each. It should be noted that this limitation to hexahedral meshes does not shorten the applicability of the adaptive mesh refinement algorithm to unstructured and highly non-orthogonal meshes.

The elementary process of the local mesh refinement is shown in Figure 3.1. Each cell that is marked for refinement is split into eight new cells. The splitting can be consecutively applied in several steps which means that the newly created cells can themselves be split. Moreover, the process is reversible and the split cells can be recombined into the original parent cell if they are marked for unrefinement. In the

present thesis, different criteria for refinement and unrefinement are used depending on the particular simulation. The information if adaptive mesh refinement is used and how the criteria are defined is given during the discussion of the results in chapter 5.

3.2 Interface capturing

3.2.1 Volume-of-Fluid method

As discussed in the introduction of the present thesis, several methods are available to simulate 2-phase flows. Here, the *Volume-of-Fluid* (VOF) method is applied which can capture a moving interface on a fixed mesh. It has been first developed in the 1970s and 1980s (e.g. Hirt and Nichols [37]) and has since been further developed continuously. The basic idea behind any VOF method is the definition of a volume fraction F_i which is the partial volume of the particular phase i in a control volume and to transport these quantities with the velocity field. As the sum of the volume fractions of all phases must equal unity, only $(N-1)$ volume fractions need to be defined to describe N different phases. In the present thesis, only two phases (liquid and vapor) are simulated in the fluid domain[4]. Hence, the volume fraction F is defined as the partial volume of the liquid phase in a particular cell.

$$F = \frac{V_\mathrm{l}}{V_\mathrm{cell}} \tag{3.10}$$

Consequently, F has a value of zero in the vapor phase and unity in the liquid phase. The liquid-vapor interface is located in the cells where the value of F jumps between the two constant values in the bulk phases. As this jump cannot be perfectly sharp on a discrete mesh, there is a thin band of cells in which F lies between zero and unity. A typical volume fraction field is shown in the top part of Figure 3.2. The material properties that occur in the conservation equations are calculated by weighting the individual material properties of the liquid and vapor phase with the volume fraction.

$$\psi = F\psi_\mathrm{l} + (F-1)\,\psi_\mathrm{v} \tag{3.11}$$

Herein, the variable ψ can be replaced by any of the material properties which are used in the conservation equations (i.e. density ρ, viscosity μ, specific heat capacity c and thermal conductivity k). Using Eq. (3.11), the material properties are weighted with the volume fraction of each phase. In principal, it is also possible to weight the material properties with the mass fraction of each phase. However, there is not much effect on the results as the interfacial region (where $0 < F < 1$) typically represents only a very small part of the whole computational domain. All potential weighting procedures which interpolate between the material properties of the two phases converge to the same solution as the mesh becomes finer.

The volume fraction field is transported only by the velocity field. Therefore, the transport equation for F contains only the transient and the convective term and there is no diffusion term.

$$\frac{\partial F}{\partial t} + \nabla \cdot (\vec{u}F) = 0 \tag{3.12}$$

The transport of volume fraction field according to Eq. (3.12) is difficult because of the step function characteristic of the field at the interface. Any algorithm for the transport of the volume fraction must

[4] The solid heater is simulated in its own domain with its own mesh (see 4.3).

fulfill two criteria. First, the volume fraction field must remain bounded between zero and unity and second, the jump of the volume fraction at the interface should remain as sharp as possible. Both criteria will typically cause problems if Eq. (3.12) is solved with standard differencing schemes in a FVM framework. Therefore, the volume fraction field is typically transported in an explicit manner. The most widely used approach is to geometrically reconstruct the interface and to use the geometric data for the calculation of the fluxes of the volume fraction across the faces of a cell (see Rider and Kothe [89] for an overview of reconstruction methods). This approach ensures the sharpness of the interface and the boundedness of the volume fraction field. *OpenFOAM* uses a different approach and adds a compression term to Eq. (3.12).

$$\frac{\partial F}{\partial t} + \nabla \cdot (\vec{u}F) + \nabla \cdot \left\{ c_F \left|\vec{u}\right| \vec{n} \left[F\left(F-1\right)\right] F \right\} = 0 \tag{3.13}$$

Herein, $\vec{n}$ is the normal vector of the interface. Its calculation is described below. The compression term acts only in the vicinity of the interface where the product $F\left(F-1\right)$ is non-zero. The compression factor c_F can be chosen by the user. The default value of $c_F = 1$ is used for all simulations presented in the present thesis. The compression term ensures the sharpness of the interface. To keep the volume fraction field bounded, Eq. (3.13) is solved using an explicit algorithm with flux limiting. The fluxes of the volume fraction are first predicted from the velocity field including the compression and then iteratively corrected. The correction of the fluxes is done by limiting them locally if they lead to a volume fraction of below zero or above unity in a particular cell.

As the correct transport of the volume fraction field is a crucial step in the simulation of 2-phase flows, *OpenFOAM* solves Eq. (3.13) in several subcycles within one time step. This means that the time step which is used for the transport of the volume fraction is smaller than the actual time step. The size of the time step for the volume fraction transport is $\Delta t_{\mathrm{VOF}} = \Delta t / N_{\mathrm{sub}}$ where N_{sub} is the number of subcycles. In all simulations discussed in the present thesis, three subcycles ($N_{\mathrm{sub}} = 3$) are used to transport the volume fraction field.

3.2.2 Sharp interface reconstruction

Using the VOF method one can distinguish between cells that contain pure liquid or vapor ($F = 1$ and $F = 0$, respectively) and cells that contain the liquid-vapor interface ($0 < F < 1$). A typical volume fraction field is shown in the top part of Figure 3.2. Thus, the location of the interface can be determined with an accuracy of around the size of a cell. The accurate calculation of the local rate of phase change requires very accurate information about the location of the interface as will be shown in section 4.1. Two approaches are possible to achieve sufficiently accurate information on the interface position. First, the mesh resolution and thereby the cell size can be chosen such that the accuracy is sufficient. The obvious disadvantage of this straightforward approach is that the high mesh resolution goes along with an extremely high number of cells. Therefore, this approach is usually limited by the computational resources. Second, the location of the interface within a cell can be determined by a local reconstruction of the interface. In addition to the information that the interface lies in a particular cell, the reconstruction provides more detailed data on where the interface is located within the cell. This augments the level of accuracy without changing the mesh resolution.

The VOF method that is implemented in *OpenFOAM* does not include any reconstruction of the interface. Therefore, this feature had to be developed and implemented within the framework of the present thesis. Typically, the reconstruction of the interface in VOF methods is done during the transport of the volume fraction field, i.e. for the calculation of the fluxes of the volume fraction through the faces of a cell. A commonly used approach is the *Piecewise Linear Interface Calculation* (PLIC). An overview of reconstruction methods is given by Rider and Kothe [89]. The reconstruction algorithm usually requires

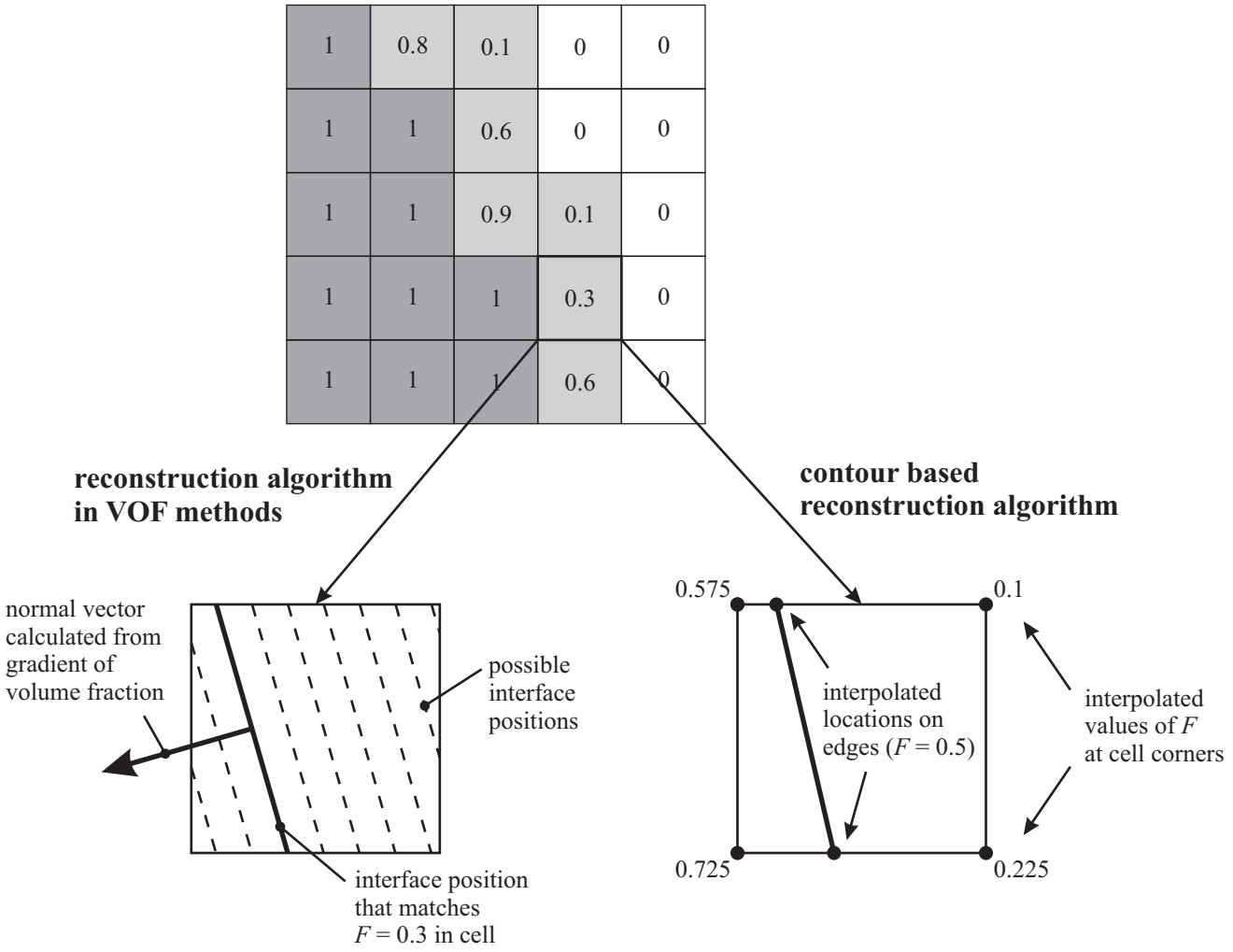

Figure 3.2: Comparison between classical reconstruction in VOF methods (left) and the reconstruction approach developed and used in the present thesis (right).

the interface normal vector $\vec{n}$ as an input parameter. It is typically calculated from the gradient of the volume fraction field.

$$\vec{n} = \frac{\nabla F}{|\nabla F|} \tag{3.14}$$

The interface normal vector describes the orientation the interface in each cell. However, the position of the interface within the cell is not yet known. Therefore, the interface is moved within the cell in order to match the volume fraction of the cell (see bottom left part of Figure 3.2). In the present thesis, the reconstruction of the interface is not used for the flux calculation but only for the calculation of phase change and curvature. Therefore, the reconstruction algorithm follows a different approach. Instead of matching the position of the interface to the volume fraction, the interface is reconstructed as the $F = 0.5$-contour (see bottom right part of Figure 3.2) similar to the work of Alke and Bothe [1] who model the enrichment of a surfactant at a fluidic interface. The computational effort for such a reconstruction of an iso-surface of the volume fraction is comparably smaller than a classical reconstruction algorithm like PLIC. The reconstruction of the iso-surface is called contour based reconstruction in the following.

The first step of the contour based reconstruction is the interpolation of the cell values of F to the corners of the cells. The intersection between the interface and a cell has the shape of a general polygon

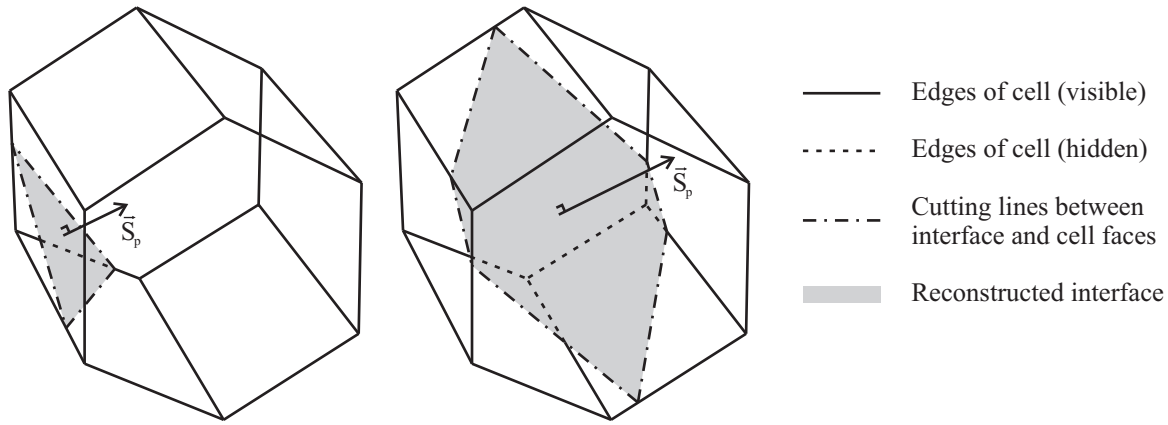

Figure 3.3: Illustration of the general polygon created by cutting a general polyhedral cell with the interface.

(see Figure 3.3). The corner points of this cutting polygon are located at the positions where the $F = 0.5$-contour cuts the edges of the cell. These positions are found by linearly interpolating the position where the volume fraction equals the contour value ($F = 0.5$) along an edge. The edge of the cell is defined by its end points $\vec{x}_1$ and $\vec{x}_2$ and by the interpolated volume fractions F_1 and F_2 at the end points. If the term $(F - 0.5)$ changes its sign between the two end points of an edge, a corner point of the cutting polygon exists on this edge. Its exact position is calculated from a linear interpolation.

$$\vec{x}_\mathrm{p} = \vec{x}_1 + \left(\vec{x}_2 - \vec{x}_1\right) \frac{0.5 - F_1}{F_2 - F_1} \tag{3.15}$$

Applying this equation to all edges of a cell gives the number and positions of the corner points of the cutting polygon. To properly define the cutting polygon, the corner points must be arranged in the right order, i.e. clock-wise with the face area vector pointing into the liquid phase. This is done by looping over the faces and edges of the cell in a particular way. Details on the procedure can be taken from López and Hernández [65] who describe the geometrical aspects of interface reconstruction on general polyhedral meshes in the framework of a classical reconstruction algorithm [34, 66], i.e. matching the volume fractions in each cell. Once the corner points are defined and sorted in the right order, the surface area vector of the cutting polygon can be calculated.

$$\vec{S}_\mathrm{p} = \sum_{i=1}^{N_\mathrm{p}} \frac{1}{2} \left(\vec{x}_{\mathrm{p},i} \times \vec{x}_{\mathrm{p},i+1}\right) \tag{3.16}$$

Herein, the counter $(i + 1)$ is set to $(i + 1) = 1$ if $i = N_\mathrm{p}$ in order to accomplish a closed loop over the corner points of the cutting polygon. The contour based reconstruction does not require the interface normal vector as an input parameter as classical reconstruction algorithms in VOF methods do. Here, the interface normal vector does not need to be calculated from Eq. (3.14) but is an output of the reconstruction and can be calculated from the surface area vector of the cutting polygon.

$$\vec{n} = \frac{\vec{S}_\mathrm{p}}{\left|\vec{S}_\mathrm{p}\right|} \tag{3.17}$$

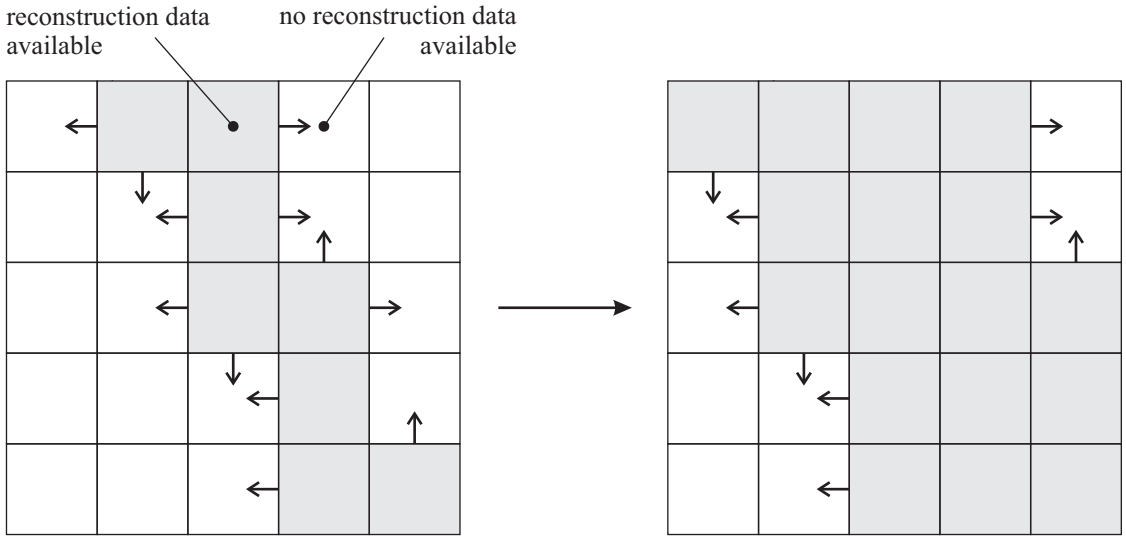

Figure 3.4: Passing of reconstruction data (normal vector $\vec{n}$ and offset λ) from cells containing reconstruction data to cells without reconstruction data. Averaging is applied in cells receiving data from more than one neighbor.

In addition to the normal vector and the surface area of the cutting polygon, the position of the cutting polygon and hereby of the interface is an important input parameter for the calculation of phase change (see section 4.1). The distance of an arbitrary point to the interface in a particular cell can be calculated from the equation describing the plane which represents the cutting polygon.

$$d_{\text{int}} = \vec{n} \cdot \vec{x} - \lambda \tag{3.18}$$

Herein, λ is the offset of the segment of the reconstructed interface in a particular cell to the origin of the coordinate system. It can be calculated as the average of the projected distance of each corner point to the origin of the coordinate system.

$$\lambda = \frac{1}{N_{\text{p}}} \sum_{i=1}^{N_{\text{p}}} \vec{n} \cdot \vec{x}_{\text{p},i} \tag{3.19}$$

As will be discussed in section 4.1 the reconstruction data should be available not only in cells that contain a part of the interface but in all cells that are close to the interface. However, the reconstruction data is at first only available in the cells that are actually cut by the interface. Therefore, the reconstruction data (normal vector $\vec{n}$ and offset λ) is passed consecutively from these interface cells to their neighboring cells. The process which is also illustrated in Figure 3.4 is run until the reconstruction data is availabe in all cells that lie within a band of five to ten cells around the interface. For each of these cells the distance to the interface can then be calculated according to Eq. (3.18).

The major drawback of this approach is the fact that the position of the interface does not necessarily represent the volume fractions of the phases correctly when it is used as an indicator for the phase distribution. In contrast to other interface reconstruction algorithms in VOF methods, it can therefore not be used for the flux calculation during the transport of the volume fraction field. For this purpose, the reconstruction must correctly reproduce the volume fraction in order to achieve a volume and mass conserving transport. However, in the present thesis the reconstruction is used mainly for the calculation of phase change which requires accurate data on the surface area of the interface rather than the

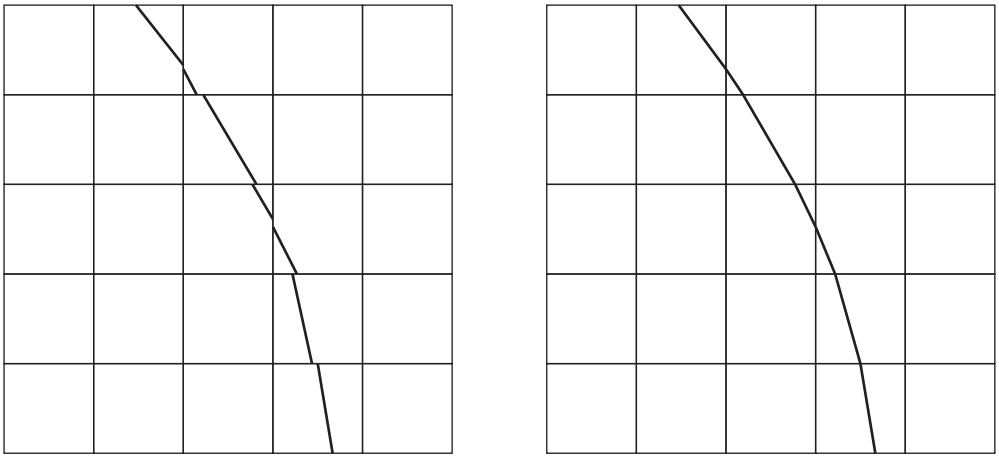

(a) Classical reconstruction (b) Contour based reconstruction

Figure 3.5: Comparison of reconstructed interface with discontinuities (classical reconstruction approach, e.g. PLIC) and without discontinuities (contour based approach).

volume of each phase. The contour based reconstruction algorithm which is used here reconstructs a surface without discontinuities. Therefore, the calculated surface area is more accurate (see Figure 3.5) compared to a reconstruction algorithm which allows discontinuities in the reconstructed interface.

The calculation of the interfacial area is also possible without reconstruction. As discussed by Hardt and Wondra [28], the volumetric density of the interface area can be calculated as the magnitude of the gradient of the volume fraction. Thus, the total interfacial area can be obtained by a volume integration of this quantity over the whole domain.

$$S_{\text{int}} = \iiint_V |\nabla F| \, \mathrm{d}V \tag{3.20}$$

Results of this approach and results obtained with the interface reconstruction which is presented above (by summing up the area of the cutting polygons obtained from Eq. (3.16)) are shown in Figure 3.6. The results are obtained for a 2D rod with a radius of 2.5 mm within a domain of $10 \times 10\,\text{mm}^2$ which is discretized in 25×25, 50×50, 100×100 and 200×200 cells. The interfacial area is calculated from Eq. (3.20) (without interface reconstruction) and from the interface reconstruction described above. The results are compared to the analytically calculated interface of a circular rod and the relative error is determined. It can clearly be seen that the interface reconstruction leads to a much better convergence while there is almost no convergence without interface reconstruction. Unfortunately, a comparison of the accuracy of the interface area between the contour based reconstruction method and a PLIC method was not possible as the latter is not implemented in *OpenFOAM*.

3.2.3 Surface tension calculation

The curvature and the resulting surface tension are calculated according to the *Continuum Surface Force* (CSF) approach which has been developed by Brackbill and co-workers [5]. Surface tension acts on a surface. However, as the FVM can only handle volumetric forces, surface tension has to be converted in a volumetric force (in N/m^3) which contributes to the source term $\vec{f}$ in Eq. (2.10). This is done by multiplying the pressure difference due to surface tension $\sigma\kappa$ (in N/m^2) with the gradient of the volume fraction which respresents a volumetric distribution of the interface as discussed above.

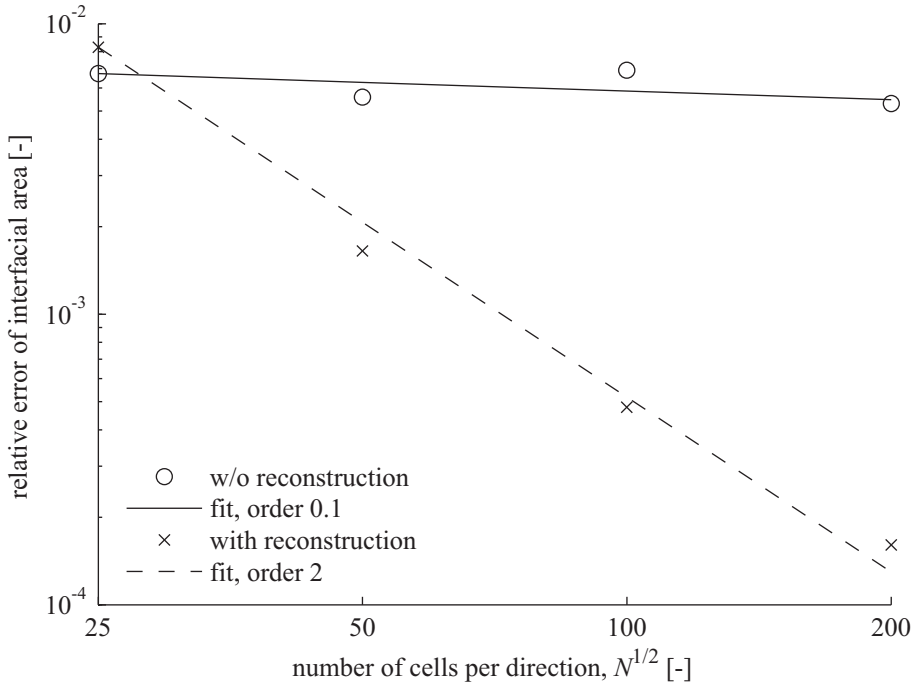

Figure 3.6: Convergence of interfacial area calculated without interface reconstruction (using Eq. (3.20)) and with contour based interface reconstruction.

$$\vec{f}_{\mathrm{ST}} = \sigma \kappa \nabla F \tag{3.21}$$

The curvature κ can be calculated as the divergence of the interface normal vector.

$$\kappa = -\nabla \cdot \vec{n} \tag{3.22}$$

In a classical VOF method, the interface normal vector is calculated from the gradient of the volume fraction field according to Eq. (3.14). Therefore, the curvature is calculated by two consecutive spatial derivations of the volume fraction field. The volume fraction field is not smooth but characterized by a sharp step at the interface. This unsteadiness of the volume fraction field causes large errors during the calculation of the second derivative. These errors lead to an inaccurate calculation of surface tension and can cause unphysical parasitic currents in the vicinity of the interface. Very often, these parasitic currents become a limiting factor during the simulation of surface tension dominated flows. In the contour based method which is used in the present thesis, the interface normal vector is obtained from the reconstruction algorithm which leads to more accuracy compared to applying Eq. (3.14). The magnitude of the parasitic currents can be significantly reduced.

3.2.4 Contact angle treatment

The surface energies of the interfaces between liquid and vapor, solid and liquid as well as solid and vapor determine the contact angle that is formed between the liquid-vapor interface and the wall (see section 2.2). The normal vector field that is obtained from the reconstruction algorithm and herewith the local orientation of the liquid-vapor interface does not necessarily fulfill this condition. In the following, the procedure which is applied to locally correct the interface normal vector in a face f on a wall boundary

is explained. The current normal vector of the interface at the wall obtained from the reconstruction algorithm is denoted $\vec{n}_{f,0}$. The current contact angle between the normal vector $\vec{n}_{f,0}$ and the normal vector to the wall $\vec{n}_{\text{wall}}$ is denoted θ_0 and can be calculated from the inner product of these vectors.

$$\vec{n}_{f,0} \cdot \vec{n}_{\text{wall}} = \cos\theta_0 \tag{3.23}$$

The interface normal vector at the wall must be corrected to the target normal vector which is denoted $\vec{n}_f$. The target normal vector must fulfill two critera. First, the angle between the target normal vector $\vec{n}_f$ and the normal vector of the wall $\vec{n}_{\text{wall}}$ must be equal to the target contact angle θ.

$$\vec{n}_f \cdot \vec{n}_{\text{wall}} = \cos\theta \tag{3.24}$$

Second, the target normal vector must lie in the plane that is spaned by the current normal vector $\vec{n}_{f,0}$ and the normal vector of the wall $\vec{n}_{\text{wall}}$.

$$\vec{n}_f = a\vec{n}_{f,0} + b\vec{n}_{\text{wall}} \tag{3.25}$$

By combining equations (3.23) to (3.25), the coefficients a and b can be obtained.

$$a = \frac{\cos\theta - \cos\theta_0 \cos\left(\theta_0 - \theta\right)}{1 - \cos^2\theta_0} \tag{3.26}$$

$$b = \frac{\cos\left(\theta_0 - \theta\right) - \cos\theta_0 \cos\theta}{1 - \cos^2\theta_0} \tag{3.27}$$

Once, the coefficients a and b are calculated at each face on the wall boundary, the target normal vector $\vec{n}_f$ is calculated and replaces the previously calculated normal vector $\vec{n}_{f,0}$. Hereafter, the curvature is calculated according to Eq. (3.22). This means that any difference between the current normal vector and the target normal vector leads to a local surface tension force. This local surface tension force adjusts the local interface shape until the target contact angle θ is matched.

3.3 Solution procedure

The conservation equations for mass, momentum and energy, equations (2.9) to (2.11), the transport equation for the volume fraction Eq. (3.13) and the particular boundary conditions at the liquid-vapor interface (2.15) to (2.18) are coupled one to another. However, the coupling is rather weak, e.g. compared to the strongly coupled equations in compressible flows at high *Mach* numbers. Therefore, the equations can be solved in a segregated manner, i.e. sequentially one after the other. In each time step, the following steps are accomplished.

- Transport of the volume fraction field with the velocity field from the last time step
- Calculation of source terms for the momentum equation (surface tension and gravity)
- Calculation of source terms due to phase change (see section 4.1)
- Solution of the energy equation (see section 4.3 for details) with velocity field from last time step
- Update of velocity and pressure fields by solution of continuity equation and momentum equation

A more detailed overview of the complete model is given in appendix B. The segregated solution of the equations has the advantage that the size of the matrix in Eq. (3.1) is equal to the number of cells as it is generated individually for each variable. In a coupled approach all variables are solved simultaneously. Therefore, the algebraic system is build for all variables at the same time, resulting in a matrix size that is equal to the number of cells times the number of variables. This leads to a much higher consumption of computational resources compared to the segregated approach.

Due to the incompressibility of the flow, the pressure appears only on the right hand side of the momentum equation (2.10) and is therefore only weakly coupled to the other variables. Therefore, the update of the velocity and pressure fields by solving the continuity equation and the momentum equation is performed using the *PISO*[5] algorithm [41, 42] which is implemented in *OpenFOAM*. The velocity is first predicted from the momentum equation using the pressure field from the last time step or iteration. Hereafter, the pressure and the velocity are iteratively corrected by solving the pressure correction equation. More details on the implementation can be found in [45, 90, 112].

[5] PISO is the abbreviation for *Pressure Implicit with Splitting of Operators*.

4 Model implementation and validation

In this chapter, the two most important ingredients of the boiling model are presented and discussed: The sub-model that treats the phase change at the liquid-vapor interface and the subgrid scale model for the evaporation at the 3-phase contact line. Both are of tremendous importance for the quality of the overall boiling model and are described in detail in the following. Furthermore, the implementation of the conjugate heat transfer between solid and fluid is discussed in detail as it is strongly related to the subgrid scale model for the evaporation at the 3-phase contact line. After the detailed describtion of these important parts of the boiling model, several validation cases are presented. These cases were simulated in order to check the accuracy and performance of the boiling model.

4.1 Phase change model

The task of the sub-model for phase change can be subdivided into the calculation of the local rate of evaporation or condensation and the calculation of corresponding source terms for the conservation equations.

- **Calculation of the local evaporation or condensation rate**
  In this step, the evaporating or condensating mass flux that is transferred locally at the liquid-vapor interface is calculated from the local temperature field. After this step, the evaporating mass is known in each cell that contains a part of the interface.
- **Calculation of the source terms for the conservation equations**
  Once the local mass flux through the liquid-vapor interface is calculated, it has to be incorporated into the conservation equations. This part of the sub-model for phase change can strongly affect the stability and convergence of the solution procedure.

In the following sections, these two aspects of the sub-model for phase change are presented and discussed separately. In principal, either of the two aspects can be changed or modified independently of the other.

4.1.1 Calculation of the local rate of phase change

In general, the appropriate modeling of phase change depends strongly on the length scale that is to be simulated. On the scale of the CFD simulations which are performed within the framework of the present thesis, saturation conditions can be assumed at the liquid-vapor interface. Furthermore, apart from the immediate region at the 3-phase contact line (see section 2.3) the influence of curvature on the local saturation conditions is negligible. Therefore, the temperature at the liquid-vapor interface can be assumed to be equal to the saturation temperature T_{sat} which corresponds to the global pressure level at which the simulation is performed. Together with the considerations on the interfacial transport of energy in section 2.2, this leads to a simple equation for the local evaporating mass flux j_{int} through the liquid-vapor interface.

$$j_{\mathrm{int}} = \frac{-k_{\mathrm{l}} \dfrac{\mathrm{d}T_{\mathrm{l}}}{\mathrm{d}x_{\mathrm{int},n}} + k_{\mathrm{v}} \dfrac{\mathrm{d}T_{\mathrm{v}}}{\mathrm{d}x_{\mathrm{int},n}}}{\Delta h_{\mathrm{V}}} \tag{4.1}$$

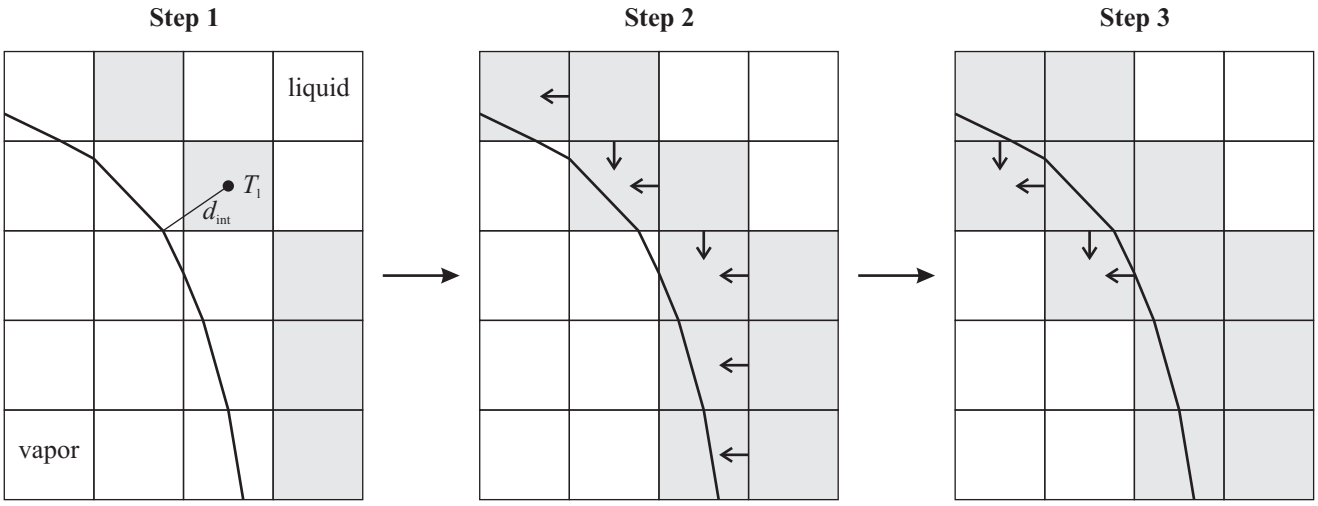

Figure 4.1: Passing of temperature gradient data from liquid cells to interface cells. Averaging is applied in cells receiving data from more than one neighbor. Gray cells contain temperature gradient data while blank cells do not contain temperature gradient data.

This equation is also valid for condensation which corresponds to a negative evaporating mass flux. In typical boiling configurations, the heat transfer within the vapor phase is negligible. Therefore, the term which describes the conductive heat flux on the vapor side of the interface in Eq. (4.1) can be neglected and only the heat supply from the liquid side of the interface is taken into account. The calculation of the liquid side temperature gradient at the liquid-vapor interface is not straightforward. Typical temperature profiles close to the liquid-vapor interface during a boiling process are shown during the discussion of the results of several validation simulations in section 4.4.1 and 4.4.2. The temperature profiles show a kink at the position of the liquid-vapor interface and have a very steep slope (high gradient) on the liquid side. Therefore, the temperature gradient normal to the liquid-vapor interface cannot be calculated using standard schemes for the gradient calculation, i.e. by a field calculation of $\nabla T \cdot \vec{n}$. This problem has lead to the implementation of the sharp interface reconstruction that is described in section 3.2.2. The interface reconstruction and subsequent distance calculation provides the geometric data that is needed to calculate the temperature gradient on the liquid side of the interface.

$$\frac{\mathrm{d}T_l}{\mathrm{d}x_{\mathrm{int},n}} = \frac{T_l - T_{\mathrm{sat}}}{d_{\mathrm{int}}} \tag{4.2}$$

The temperature gradient can also be calculated as a vector field by using the interface normal vector $\vec{n}$ which is also calculated during the interface reconstruction.

$$\nabla T_l = \frac{T_l - T_{\mathrm{sat}}}{d_{\mathrm{int}}} \vec{n} \tag{4.3}$$

The calculation of the temperature gradient is not performed directly in the cells that contain a part of the interface but in the neighboring cells that contain pure liquid. The reason is that the temperature in cells which contain a segment of the interface is not the liquid temperature but a mean temperature of the liquid and vapor phase within these cells and thus depends on the weighting procedure of the material properties (see section 3.2.1). Therefore, the calculation of a temperature gradient in these cells leads to erroneous results as the temperature of the pure liquid is required for Eq. (4.3). The calculation and passing of the gradient data into the interface cells is performed in several steps.

- **Step 1**
  The temperature gradient is calculated in the liquid cells which are close to the interface. The criterion for the closeness is that the cells must be a neighbor of at least one interface cell. The gradient is calculated as a vector by applying Eq. (4.3).
- **Step 2**
  The gradient data is passed from the liquid cells in step 1 to the neighboring interface cells. Only the magnitude of the vector is passed to the interface cells. The direction of the vector is recalculated with the interface normal vector $\vec{n}$ in the receiving cells.
- **Step 3**
  The gradient data is passed from the interface cells in step 2 to those interface cells that do not have a liquid neighbor. As in step 2, only the magnitude of the vector is passed and the direction is recalculated with the interface normal vector $\vec{n}$ in the receiving cells.

The whole procedure is illustrated in Figure 4.1. Once the gradient data is available in all interface cells the mass flux is calculated according to Eq. (4.1) in each of the interface cells.

The calculation of the local evaporating mass flux from the liquid side temperature gradient is a common approach. It is also used by other authors who use VOF or LS method for the calculation of boiling phenomena (e.g. Son and co-workers [102] and Welch and Wilson [126]). An alternative approach has been developed by Hardt and Wondra [28]. In their method, the evaporating mass flux is calculated from the interface temperature and the interfacial heat resistance (see section 2.3 for the definition).

$$j_{\mathrm{int}} = \frac{T_{\mathrm{int}} - T_{\mathrm{sat}}}{R_{\mathrm{int}}} \tag{4.4}$$

01

longkai guo

The concept of the interfacial heat resistance is based on considerations on a much smaller length scale than the length scale which can typically be resolved by a CFD simulation (see Schrage [92]). The superheat of the interface $T_{\mathrm{int}} - T_{\mathrm{sat}}$ is very small and can usually be neglected on the scale of a CFD simulation as discussed above. Nevertheless, the work of Hardt and Wondra [28] and of Kunkelmann and Stephan [58] prove that it can also be used in simulations where the mesh does not resolve the aforementioned small scales. The major advantage of using Eq. (4.4) instead of Eq. (4.1) is the more straightforward implementation. However, Kunkelmann and Stephan [59] could show that the calculation of the evaporating mass flux from the temperature gradient is much more accurate in boiling conditions. At the same level of accuracy, the mesh can be chosen four times coarser when using Eq. (4.1) together with interface reconstruction and distance calculation. In different conditions, e.g. film boiling where the temperature gradient at the interface are less localized and more continuous, Hardt and Wondra [28] obtained very satisfying results with their approach. The above mentioned procedure for the calculation of the temperature gradient does not take into account the vapor side temperature gradient. Thus, it is currently limited to the simulation of boiling conditions in which the latent heat is supplied from the liquid side of the interface (e.g. nucleate boiling). In future, it might be extended to the vapor side of the interface as well. Meanwhile, due to the high accuracy of the film boiling results of Hardt and Wondra [28], their straightforward approach for the calculation of the source terms (according to Eq. (4.4)) is also used here for the simulations on film boiling (see 5.3.3).

4.1.2 Representation of phase change by a continuous field of source terms

The evaporating or condensating mass flux which is transferred through the liquid-vapor interface is calculated according to Eq. (4.1) or Eq. (4.4) and must be incorporated into the conservation equations.

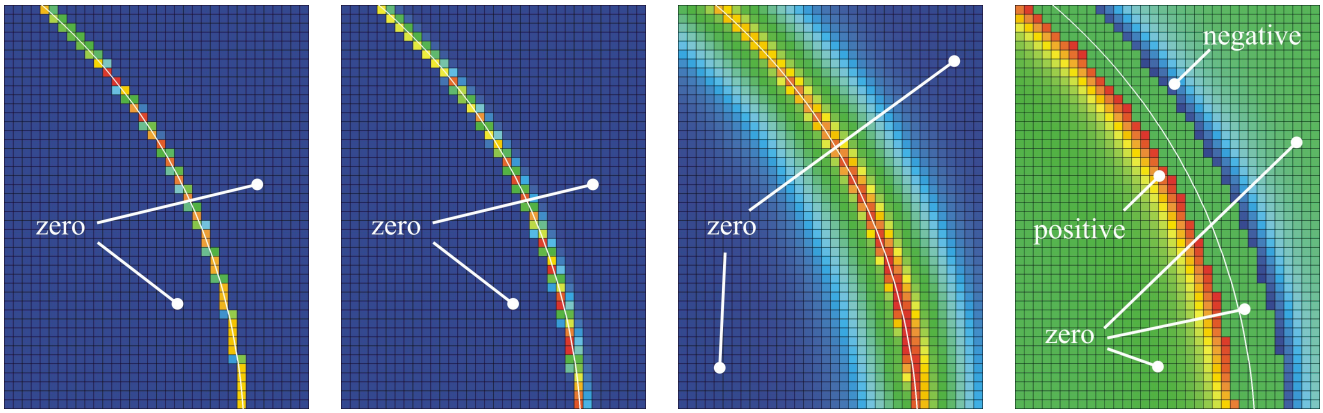

(a) $\left|\vec{S}_{\text{int}}\right| / V_{\text{cell}}$ (b) $\dot{\rho}_0$ (c) $\dot{\rho}_1$ (d) $\dot{\rho}$

Figure 4.2: Illustration of the smearing, cropping and scaling of the source term field. The interface ($F = 0.5$-contour) is represented by the white curves in the pictures.

This is done by the definition of volumetric source terms. The mass flux through the liquid-vapor interface can be transferred to a volumetric source term by using the interface density $\left|\vec{S}_{\text{int}}\right| / V_{\text{cell}}$ which represents the surface area of the interface in a cell relative to the volume of the cell.

$$\dot{\rho}_0 = j_{\text{int}} \frac{\left|\vec{S}_{\text{int}}\right|}{V_{\text{cell}}} \tag{4.5}$$

The stability and convergence of the solution procedure for the conservation equations can be very sensitive to source terms. The source term defined by Eq. (4.5) can have very large values at the liquid-vapor interface while it is zero elsewhere (see Figure 4.2(a)). Therefore, it is not used directly which is in contrast to the boiling models which were developed by Son and co-workers [102] and Shu [96]. In the present thesis the method of Hardt and Wondra [28] is used. They developed a method that smears the sharp source term distribution to a smooth distribution which is easier to handle numerically. Independent of the approach for calculating the evaporating or condensating mass flux (i.e. by using Eq. (4.1) or Eq. (4.4)), the method of Hardt and Wondra [28] for smearing the source term field is always used in the simulations of the present thesis. The basic idea behind this approach is to shift the source terms into cells which are close to the liquid-vapor interface but contain only pure liquid or pure vapor. In the case of evaporation a negative mass source is used on the liquid side of the interface and a positive mass source on the vapor side. The absolute values of the positive and negative source terms are chosen such that mass is globally conserved. In the following, the procedure is described in detail. The smooth source term field is obtained in four steps.

- **Step 1**
  The sharp source term field is calculated according to Eq. (4.5). An example for the resulting field is shown in Figure 4.2(b). Additionally, the sharp source term field is integrated over the whole computational domain in order to obtain the net mass flow through the entire liquid-vapor interface.

$$\dot{m}_{\text{int}} = \iiint_V \dot{\rho}_0 \mathrm{d}V \tag{4.6}$$

  This value is important for the global mass conservation (step 4), i.e. to ensure that the magnitudes of the mass sources in the liquid and vapor are equal and correspond to the net evaporation rate.

- **Step 2**
  The sharp source term field $\dot{\rho}_0$ is smeared. This is done by solving a diffusion equation for the smooth distribution of source terms $\dot{\rho}_1$.

$$\dot{\rho}_1 - \nabla \cdot \left[(D\Delta\tau) \nabla \dot{\rho}_1 \right] = \dot{\rho}_0 \tag{4.7}$$

  Herein, $\Delta\tau$ is an artificial time step. Neumann boundary conditions are imposed for the smooth source term field $\dot{\rho}_1$ on all boundaries of the domain. Thus, the integral values of the sharp source term field $\dot{\rho}_0$ and the smooth source term field $\dot{\rho}_1$ remain equal in spite of the smearing. An example for a resulting smooth source term field is shown in Figure 4.2(c). The width of the smeared source term field is proportional to the square root of the product of diffusion constant and artificial time step $(D\Delta\tau)^{1/2}$. The value of the diffusion constant must be adjusted to the mesh resolution. In general, it is chosen such that the source term field is smeared over several cells.

02

longkai guo

- **Step 3**
  The source terms in all cells that do not contain either pure liquid or pure vapor ($F < 1 - F_{\text{cut}}$ and $F > F_{\text{cut}}$, respectively[1]) are set to zero. This cropping step avoids that source terms appear in the smeared interface region of the VOF method. As discussed in section 3.2 the transport of the volume fraction field is not trivial. By applying the cropping step, the source terms are shifted into the pure vapor and liquid cells next to the interface. The interface itself is therefore not subjected to any source terms and is only transported by the velocity field. Thus, the transport algorithm for the volume fraction field and the associated interface compression can work efficiently and do not interfere with the source term field.

- **Step 4**
  The remaining source term field is scaled individually on the liquid and the vapor side in order to make sure that the mass is globally conserved and that the evaporating or condensating mass flow corresponds globally to the net mass flow through the interface $\dot{m}_{\text{int}}$ from Eq. (4.6). The scaling coefficients N_{l} and N_{v} for the source terms on the liquid and vapor side of the interface, respectively, are calculated by integrating the smooth source term field in each of the pure phases and comparing it to the net mass flow which is obtained by applying Eq. (4.6).

$$N_{\text{l}} = \dot{m}_{\text{int}} \left[\iiint_V H\left(F - 1 + F_{\text{cut}}\right) \dot{\rho}_1 \mathrm{d}V \right]^{-1} \tag{4.8}$$

$$N_{\text{v}} = \dot{m}_{\text{int}} \left[\iiint_V H\left(F_{\text{cut}} - F\right) \dot{\rho}_1 \mathrm{d}V \right]^{-1} \tag{4.9}$$

  Herein, H is the *Heaviside* function which cuts off the volume fraction field below $1 - F_{\text{cut}}$ and above F_{cut}, respectively. Using these scaling coefficients, the final source term distribution can be calculated.

$$\dot{\rho} = N_{\text{v}} H\left(F_{\text{cut}} - F\right) \dot{\rho}_1 - N_{\text{l}} H\left(F - 1 + F_{\text{cut}}\right) \dot{\rho}_1 \tag{4.10}$$

  An example for this final source term distribution $\dot{\rho}$ is shown in Figure 4.2(d).

[1] F_{cut} is chosen as 10^{-3}.

Taking into account phase change at the interface, several source terms are added to the right hand side of the system of conservation equations (2.9) to (2.11). The source term for the continuity equation accounts for the divergence of the velocity field in cells where mass is removed or added.

03 longkai guo

$$\nabla \cdot \vec{u} = \frac{\dot{\rho}}{\rho} \tag{4.11}$$

The source term in the energy equation consists of two contributions. First, the consumption or release of energy due to evaporation or condensation at the liquid-vapor interface must be taken into account. This part is calculated with the sharp source term field $\dot{\rho}_0$ and the enthalpy of vaporization Δh_V. As pointed out by Hardt and Wondra [28], the solution of the energy equation is not very sensitive to sharp source terms. Therefore, the energy consumption or release due to phase change can be directly imposed in the interface cells. Second, the removed or added mass in the pure liquid or vapor cells leads to a velocity field which is not free of divergence. This is associated to a certain amount of sensible heat cT which is added or removed due to the source terms. This effect is compensated by an additional source term in the energy equation which is calculated from the smooth source term field $\dot{\rho}$.

04 longkai guo

05 longkai guo

$$\frac{\partial \left(\rho c T\right)}{\partial t} + \nabla \cdot \left(\rho c T \vec{u}\right) - \nabla \cdot \left(k \nabla T\right) = \dot{\rho}_0 \Delta h_\mathrm{V} + \dot{\rho} c T \tag{4.12}$$

Due to the fact that the velocity field is not free of divergence in cells which contain source terms, an additional source term must also be added to the transport equation for the volume fraction Eq. (3.13).

$$\frac{\mathrm{d}F}{\mathrm{d}t} + \nabla \cdot \left(\vec{u}F\right) + \nabla \cdot \left\{c_F \left|\vec{u}\right| \vec{n} \left[F\left(F-1\right)\right] F\right\} = \frac{\dot{\rho}}{\rho} F \tag{4.13}$$

Without the source term on the right hand side of the transport equation for the volume fraction, the divergence of the velocity field can lead to volume fractions smaller than zero or larger than unity. This is due to the convective flux of F across the faces of the cells which is calculated from the velocity field. Without any mass source terms, the flux of the volume fraction into a cell is exactly equal to the flux of the volume fraction leaving a cell. However, if the velocity field is divergent (due to positive source terms) there might be a net transport of F directed out of the cell over its faces. Depending on the time step size, this could quickly lead to a negative value of the volume fraction F in this cell. This is avoided by the source term on the right hand side of Eq. (4.13).

No source term is required for the momentum equation. The recoil pressure is the only manifestation of the phase change in the momentum balance. It is a direct result of the source terms in the continuity equation and does not need to be modeled. If the velocity field (liquid velocity, vapor velocity and interface velocity) in the vicinity of the interface is correct, the recoil pressure is implicitly captured by the momentum equation. In order to demonstrate this, a simple 1D example of an evaporation process is discussed. The configuration is shown in Figure 4.3(a). The corresponding volume fraction field, source term distribution and the resulting velocity field are shown in figures 4.3(b), 4.3(c) and 4.3(d), respectively. The velocity field can be obtained by integration of the source term with respect to the length x.

$$u\left(x\right) = u_\mathrm{I} + \int_0^x \frac{\dot{\rho}\left(\tilde{x}\right)}{\rho\left(\tilde{x}\right)} \mathrm{d}\tilde{x} \tag{4.14}$$

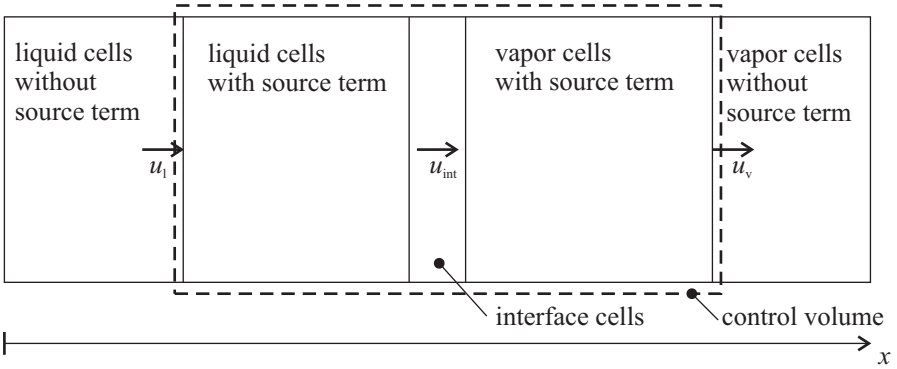

(a) Sketch of the 1D control volume

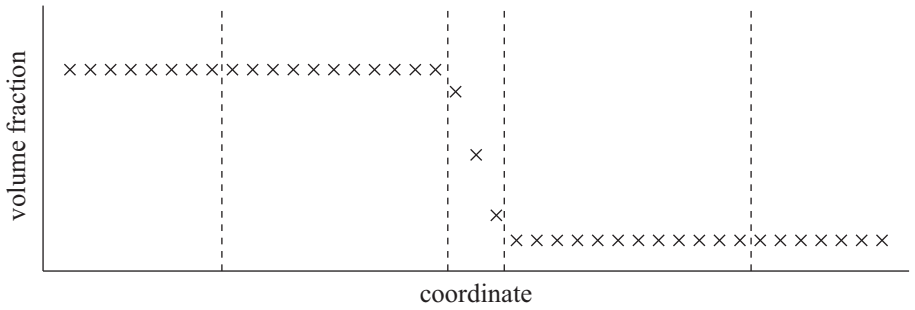

(b) Volume fraction field (between 0 and 1)

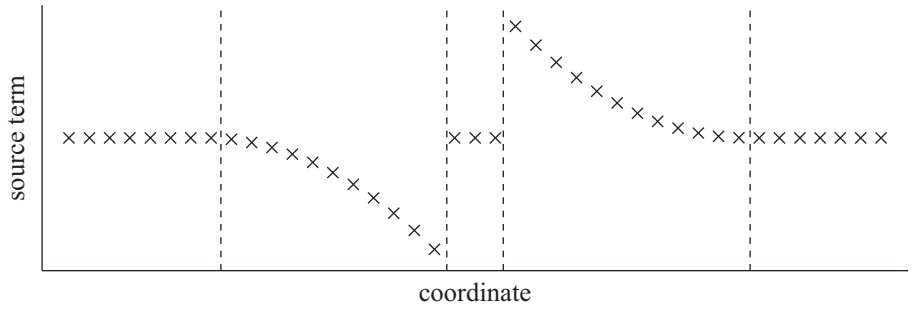

(c) Source term distribution

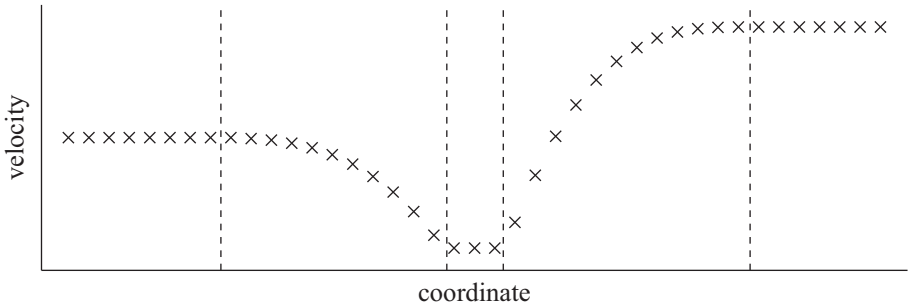

(d) Velocity field resulting from source term distribution

Figure 4.3: Illustration of a 1D example which is used to show that no source term is required in the momentum equation.

06 longkai guo

Using the integral formulations of the mass conservation equation for the non-moving control volume (consisting of several cells), the correct prediction of the liquid and vapor velocities and the interface velocity can be shown. In the following set of equations the integral balancing of the FVM (see section 3.1.1) is applied to Eq. (4.11).

$$\iint_S \vec{u} \mathrm{d}\vec{S} = \iiint_V \frac{\dot{\rho}}{\rho} \mathrm{d}V \tag{4.15}$$

$$-u_\mathrm{l} S + u_\mathrm{v} S = \frac{S}{\rho_\mathrm{l}} \int_0^{x_\mathrm{l}} \dot{\rho} \mathrm{d}x + \frac{S}{\rho_\mathrm{v}} \int_{x_\mathrm{l}}^{x_\mathrm{v}} \dot{\rho} \mathrm{d}x \tag{4.16}$$

$$u_\mathrm{v} - u_\mathrm{l} = j_\mathrm{int} \left(\frac{1}{\rho_\mathrm{v}} - \frac{1}{\rho_\mathrm{l}} \right) \tag{4.17}$$

Hence, the FVM correctly predicts the velocities u_l and u_v on the left and right boundary of the domain shown in Figure 4.3(a). Using the fact that the mass flux through the interface j_int is equal to $\rho_\mathrm{l} \left(u_\mathrm{l} - u_\mathrm{int} \right)$ and $\rho_\mathrm{v} \left(u_\mathrm{v} - u_\mathrm{int} \right)$, respectively, Eq. (4.17) can simply be transformed to Eq. (2.15) which was obtained from analytical considerations on the interfacial transport. Hence, the velocities on the liquid and vapor side of the interface are correctly predicted if the source term field is used as discussed above. Note that this is valid only outside the region where the source terms are active, i.e. at the distance of several cells to the interface (where a constant velocity can be observed in Figure 4.3(d)).

07 longkai guo

Additionally, the momentum conservation equation can also be applied to the 1D problem in Figure 4.3(a). Again, the integral balancing of the FVM is mimicked. For the sake of lucidity, there are no viscous or volumetric forces. In the following set of equations the integral balancing of the FVM (see section 3.1.1) is applied to the momentum equation.

$$\iiint_V \frac{\partial \left(\rho \vec{u} \right)}{\partial t} \mathrm{d}V + \iint_S \rho \vec{u} \vec{u} \mathrm{d}\vec{S} = - \iiint_V \nabla p \mathrm{d}V \tag{4.18}$$

$$\frac{\Delta \left(\rho u \right)}{\Delta t} V - \rho_\mathrm{l} u_\mathrm{l} u_\mathrm{l} S + \rho_\mathrm{v} u_\mathrm{v} u_\mathrm{v} S = - \frac{p_\mathrm{v} - p_\mathrm{l}}{\Delta x} V \tag{4.19}$$

The change of the system's momentum with time can be expressed by the momentum of the liquid and vapor volumes in the control volume. These volumes change with time due to the interface velocity and thus, the total momentum of the mass within the control volume changes, too.

$$\frac{\Delta \left(\rho u \right)}{\Delta t} = \frac{1}{\Delta t} \left(\rho_\mathrm{l} u_\mathrm{l} \frac{x_\mathrm{l} + u_\mathrm{int} \Delta t}{\Delta x} + \rho_\mathrm{v} u_\mathrm{v} \frac{x_\mathrm{v} - x_\mathrm{l} - u_\mathrm{int} \Delta t}{\Delta x} - \rho_\mathrm{l} u_\mathrm{l} \frac{x_\mathrm{l}}{\Delta x} - \rho_\mathrm{v} u_\mathrm{v} \frac{x_\mathrm{v} - x_\mathrm{l}}{\Delta x} \right) \tag{4.20}$$

$$= \rho_\mathrm{l} u_\mathrm{l} \frac{u_\mathrm{int}}{\Delta x} - \rho_\mathrm{v} u_\mathrm{v} \frac{u_\mathrm{int}}{\Delta x} \tag{4.21}$$

The combination of the equations (4.19) and (4.21) leads to the final result of the momentum balance for the non-moving control volume in Figure 4.3(a).

$$p_\mathrm{l} - p_\mathrm{v} = -\rho_\mathrm{l} u_\mathrm{l} \left(u_\mathrm{l} - u_\mathrm{int}\right) + \rho_\mathrm{v} u_\mathrm{v} \left(u_\mathrm{v} - u_\mathrm{int}\right) \tag{4.22}$$

This equation corresponds exactly to Eq. (2.16) which has been analytically derived for the normal momentum balance at a moving interface with phase change. Only the pressure difference due to the surface tension forces is not reproduced as the interface of the example is not curved. Hence, it could be shown that there is no additional source term needed for the momentum equation to account for phase change. The recoil pressure is exactly reproduced by balancing the momentum for a control volume containing the liquid-vapor interface and the regions with the source terms. It should be noted that the above integration of the mass and momentum conservation equations is performed in a region around the liquid-vapor interface and not directly at the interface itself. Hence, the recoil pressure is correctly predicted in some distance (several cells) to the interface. Certainly, it is not correctly predicted directly at the liquid-vapor interface.

08

longkai guo

4.2 Heat and fluid flow at the 3-phase contact line

4.2.1 Solution and parameterization of the microscale model

In order to transform the 4th order *Ordinary Differential Equation* (ODE) Eq. (2.36) that is derived in section 2.3 into a formulation which can more easily be solved numerically, the integrated heat flux Q is introduced.

$$Q = \int_0^\xi q \mathrm{d}\xi \tag{4.23}$$

The integrated heat flux Q represents the amount of heat per unit contact line length that is transferred in the contact line region. Using the definition (4.23) and the equations presented in section 2.3, the 4th order ODE can be transformed into a system of coupled 1st order ODEs for the film thickness δ, the slope δ', the pressure difference Δp and the integrated heat flux Q.

$$\frac{\mathrm{d}\delta}{\mathrm{d}\xi} = \delta' \tag{4.24}$$

$$\frac{\mathrm{d}\delta'}{\mathrm{d}\xi} = \frac{\left(1+\delta'^2\right)^{3/2}}{\sigma}\left(\Delta p - \frac{A}{\delta^3}\right) \tag{4.25}$$

$$\frac{\mathrm{d}\left(\Delta p\right)}{\mathrm{d}\xi} = -\frac{3\mu_\mathrm{l} Q}{\rho_\mathrm{l} \Delta h_\mathrm{V} \delta^3} \tag{4.26}$$

$$\frac{\mathrm{d}Q}{\mathrm{d}\xi} = \frac{T_\mathrm{wall} - T_\mathrm{sat}\left(1 + \dfrac{\Delta p}{\rho_\mathrm{l} \Delta h_\mathrm{V}}\right)}{\dfrac{\delta}{k_\mathrm{l}} + R_\mathrm{int}} \tag{4.27}$$

This system of 1st order ODEs is solved with a shooting method. The initial conditions at $\xi = 0$ are obtained from the conditions within the adsorbed film. As there is no evaporation from the adsorbed film

its thickness can be obtained by setting Eq. (4.27) to zero and by taking into account that the curvature of the adsorbed film is zero. The initial conditions for the remaining variables can then be obtained, too.

$$\delta_{\mathrm{ad}} = \left(\frac{A}{\rho_{\mathrm{l}} \Delta h_{\mathrm{V}} \left(\frac{T_{\mathrm{wall}}}{T_{\mathrm{sat}}} - 1 \right)} \right)^{1/3} \tag{4.28}$$

$$\delta'_{\mathrm{ad}} = 0 \tag{4.29}$$

$$\Delta p_{\mathrm{ad}} = \frac{A}{\delta_{\mathrm{ad}}^3} \tag{4.30}$$

$$Q_{\mathrm{ad}} = 0 \tag{4.31}$$

This system of equations is solved using the software *Matlab*[2]. A 4th order *Runge-Kutta* method[3] with error estimation and step size adaption is used for the integration. As the conditions within the adsorbed film are the trivial solution of the system of ODEs (4.24) to (4.27), they cannot be directly used for the numerical integration. Instead, the film thickness δ and the integrated heat flux Q are slightly perturbed[4]. The perturbation on the integrated heat flux Q is used as parameter within the shooting method in order to achieve the target value for a macroscopic curvature at the end of the micro region. A detailed description of the solution procedure is given by Stephan [104].

The system of ODEs (4.24) to (4.27) is integrated from the adsorbed film at $\xi = 0$ to a chosen value $\xi = \xi_{\mathrm{mic}}$. In principal, the choice of ξ_{mic} is arbitrary. However, two aspects must be taken into account. First, the film thickness at ξ_{mic} must be large enough such that the microscale effects (i.e. disjoining pressure and change of thermodynamic equilibrium by extremely high curvature) have decayed. This criterion provides a lower limit for the choice of ξ_{mic}. Second, the film thickness and its slope at ξ_{mic} must be small enough such that the assumptions which are made during the derivation of the equations for the contact line heat transfer in section 2.3 are still valid. In particular, the film must still be thin and flat enough to justify the assumptions of 1D heat conduction and of a flow which is nearly parallel to the wall. In the calculations performed for the present thesis, a value of $\xi_{\mathrm{mic}} = 0.5\,\mu$m was chosen.

A typical result of the contact line evaporation model is shown in Figure 4.4. The film thickness and slope are shown in Figure 4.4(a). Starting at the very small value of δ_{ad} which is not visible in the plot, the film thickness starts to grow rapidly at around $\xi = 0.1\,\mu$m. This goes along with a step-like increase of the slope δ' and thereby of the angle $\theta = \arctan \delta'$ which approaches the apparent contact angle. The sharp rise in contact angle is a result of the rapidly decaying intermolecular forces which are taken into account by the disjoining pressure concept. The corresponding pressures are shown in Figure 4.4(b). The total pressure difference between liquid and vapor is the sum of disjoining pressure A/δ^3 and capillary pressure $\sigma\kappa$. Although recoil pressure is not taken into account in the modeling equations, it is calculated from the local heat flux ($q^2/\Delta h_{\mathrm{V}}^2 \left(1/\rho_{\mathrm{v}} - 1/\rho_{\mathrm{l}}\right)$, this equation is valid for a non-moving interface) and also plotted in Figure 4.4(b). It can clearly be seen that the disjoining pressure is highly dominant within the adsorbed film. When the film thickness starts to grow, the disjoining pressure decreases rapidely and is replaced by the capillary pressure. In the presented case, the recoil pressure is very low compared to disjoining and capillary pressure. It was checked that this is also valid for higher wall superheats and different material properties. Thus, under the conditions which are subject of the

[2] Technical computing software distributed by *The MathWorks*.

[3] The *ode45* function of the *Matlab* software package is used.

[4] The magnitude of the perturbation of the film thickness is chosen as $\Delta\delta = \delta_{\mathrm{ad}}/1000$.

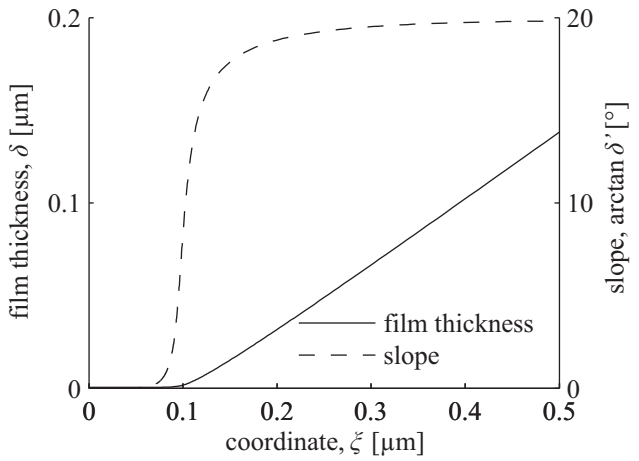

(a) Film thickness δ and slope $\arctan\delta'$

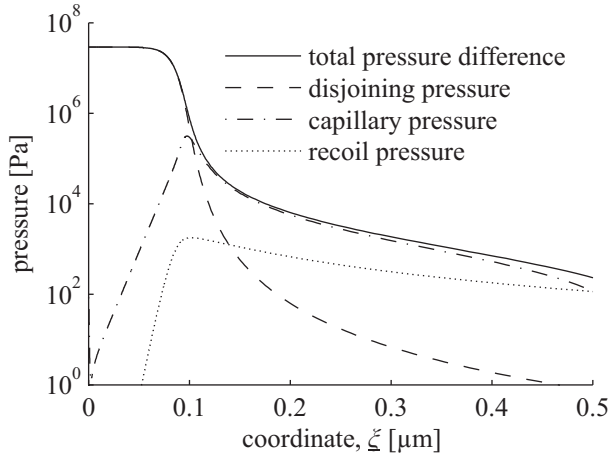

(b) Pressure comparison (logarithmic scale)

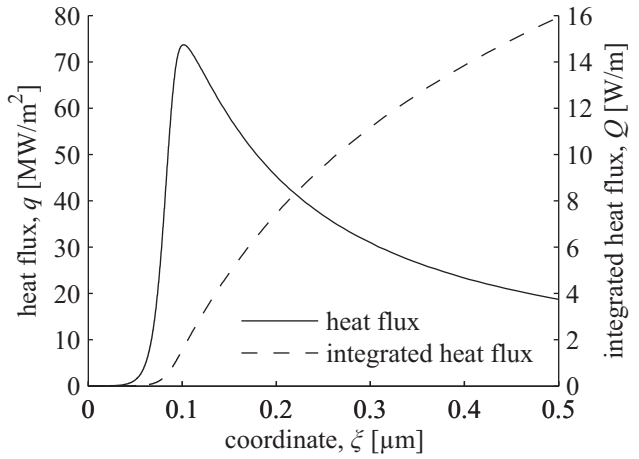

(c) Heat flux q and integrated heat flux Q

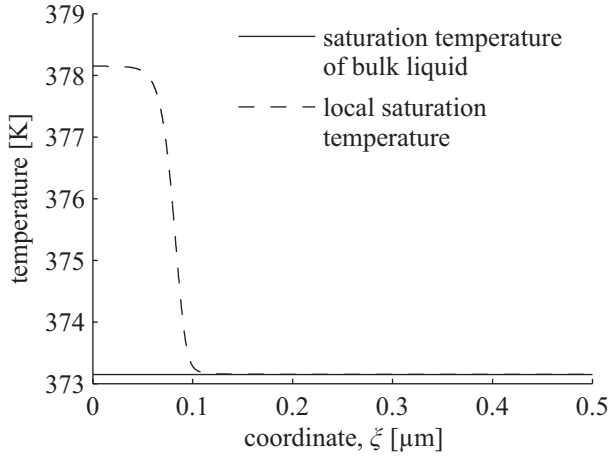

(d) Saturation temperature

Figure 4.4: Example of the results obtained from the microscale model for the evaporation at the 3-phase contact line. The fluid is saturated water ($p = 1013\,\mathrm{mbar}$) at a wall superheat of $\Delta T_{\mathrm{wall}} = 5\,\mathrm{K}$.

present thesis, the effect of the recoil pressure can be neglected in the microscopic region at the 3-phase contact line. However, this statement is not necessarily valid in cases with much higher wall superheat, e.g. in a situation close to the critical heat flux. The heat transfer at the contact line is shown in Figure 4.4(c). There is no evaporation from the adsorbed film and therefore the heat flux is zero in this region. At the point where the film thickness starts to grow, the heat flux increases and quickly reaches a maximum value. The position of the maximum heat flux represents the point where the film thickness is still very small (which enhances heat transfer) while the intermolecular forces (which reduce heat transfer) have already become very small. After the maximum, the heat flux continuously decreases due to the growing thickness of the film. The effect of the intermolecular forces can be better understood when looking at Figure 4.4(d) in which the bulk saturation temperature and the local saturation temperature are compared. The bulk saturation temperature of water at $p = 1013\,\mathrm{mbar}$ is $T_{\mathrm{sat}} = 373.15\,\mathrm{K}$ (100 °C). However, the intermolecular forces and the strong capillary pressure lead to a change of the local thermodynamic equilibrium in the vicinity of the wall. The local saturation temperature is the minimum temperature at the interface which is required for the evaporation of liquid. Its value is equal to the wall temperature within the adsorbed film. Thus, the intermolecular forces preemt evaporation at the adsorbed film. As the film thickness grows, the local saturation temperature drops down to the bulk saturation temperature due to the decay of the microscale effects.

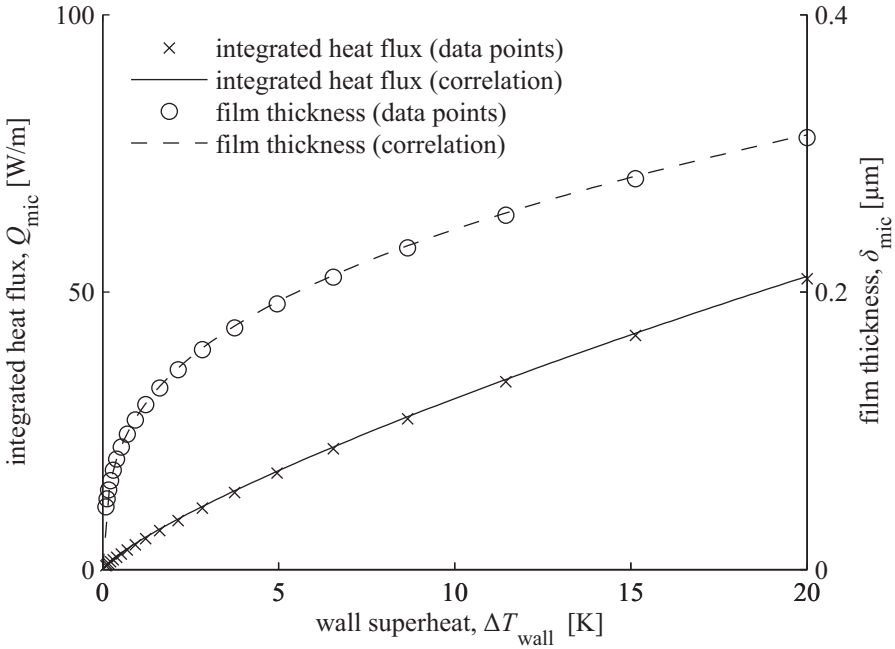

Figure 4.5: Integrated heat flux and film thickness at the end of the integration domain of the contact line evaporation model for different wall superheats. Results obtained from contact line evaporation model (data points) and correlations (according to Eq. (4.32) and Eq. (4.33)). The fluid is saturated water ($p = 1013\,\mathrm{mbar}$).

From the results shown in Figure 4.4(a) to Figure 4.4(d) one can see that the choice of $\xi_{mic} = 0.5\,\mu m$ is appropriate in this case. At the end of the integration of the system of ODEs (4.24) to (4.27) the microscale effects have decayed completely while the thickness and slope of the liquid film are still small enough to justify the assumptions of the model.

The solution algorithm for the integration of the system of ODEs is too time consuming to be used directly in the CFD simulation. The calculation of one solution for a particular fluid and a particular wall superheat only takes several seconds[5]. However, it would have to be performed at each segment of the contact line during one time step of the CFD simulation (see section 4.2.2 for details) leading to a large number of solutions which must be calculated for the contact line evaporation model. Therefore, the results of the contact line evaporation model are parameterized prior to the CFD simulation. For a given set of material properties, the results of the contact line evaporation model depend mainly on the wall superheat. There is also some influence of the target curvature that is achieved at the end of the integration domain of the shooting method. However, the influence is far inferior to the influence of the wall superheat. Hence, the contact line evaporation model is solved for different wall superheats and a correlation is determined. The results which are required for the coupling to the CFD simulation are the integrated heat flux, the film thickness and prospectively the contact angle at the end of the integration domain (see section 4.2.2 for details). These results are correlated to the wall superheat. A series of root functions was found to fit the data best.

[5] These computations were performed on a single core of an Intel Core 2 Duo with 3 GHz using *Matlab* 7.6.0.324 (R2008a).

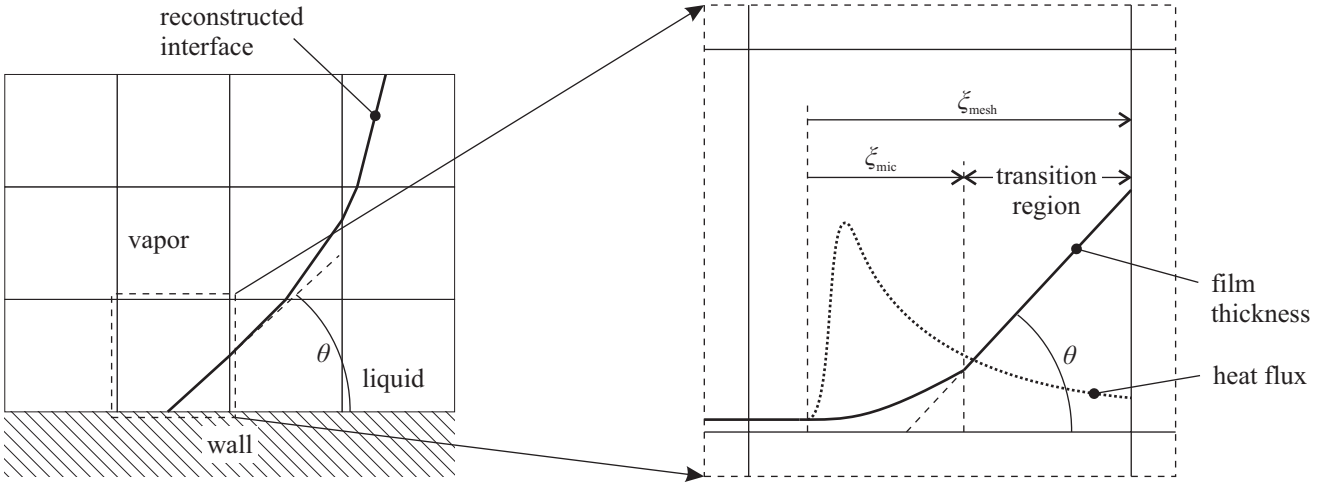

Figure 4.6: Illustration of the coupling between the subgrid scale model for the contact line evaporation and the CFD simulation. A transition region is defined between the different length scales of the subgrid scale model and the CFD simulation.

$$Q_{\mathrm{mic}} = Q\left(\xi_{\mathrm{mic}}\right) = \sum_{i=1}^{N_i} a_{Q,i} \Delta T_{\mathrm{wall}}^{1/i} \tag{4.32}$$

$$\delta_{\mathrm{mic}} = \delta\left(\xi_{\mathrm{mic}}\right) = \sum_{i=1}^{N_i} a_{\delta,i} \Delta T_{\mathrm{wall}}^{1/i} \tag{4.33}$$

$$\theta_{\mathrm{mic}} = \arctan \delta'\left(\xi_{\mathrm{mic}}\right) = \sum_{i=1}^{N_i} a_{\theta,i} \Delta T_{\mathrm{wall}}^{1/i} \tag{4.34}$$

Typical results of the parameterization procedure are shown in Figure 4.5. It can easily be seen that the correlation fits the data points very accurately. The coefficients $a_{Q,i}$, $a_{\delta,i}$ and $a_{\theta,i}$ are calculated for different fluids. The values of the coefficients are given in appendix C.

4.2.2 Coupling of the microscale model to the CFD simulation

The contact line evaporation model or - more precisely - the above mentioned correlations are embedded as a subgrid scale model within the CFD simulation. In the work of Stephan [104] and Stephan and Busse [108] the contact line evaporation model is coupled to a steady-state CFD simulation with an interface fitted mesh. In this context, it was possible to match the mesh locally to the geometrical data (film thickness and slope) obtained at the end of the integration domain of the contact line evaporation model. Here, the interface and hereby also the position of the 3-phase contact line is changing with time and moving on a fixed grid. Therefore, the coupling between the contact line evaporation model and the CFD simulation is less straightforward. The length of the integration domain ξ_{mic} is chosen independent of the CFD mesh during the parameterization procedure. This means that there is usually a gap between the end of the calculation of the subgrid scale model ($\xi_{\mathrm{mic}} = 0.5\,\mu$m) and the smallest length scale that is still resolved by the CFD mesh (ξ_{mesh} which has typically a size of several micrometers in the simultions performed within the framework of the present thesis). The problem is illustrated in Figure 4.6. It can be overcome by defining a transition region which closes the gap between ξ_{mic} and

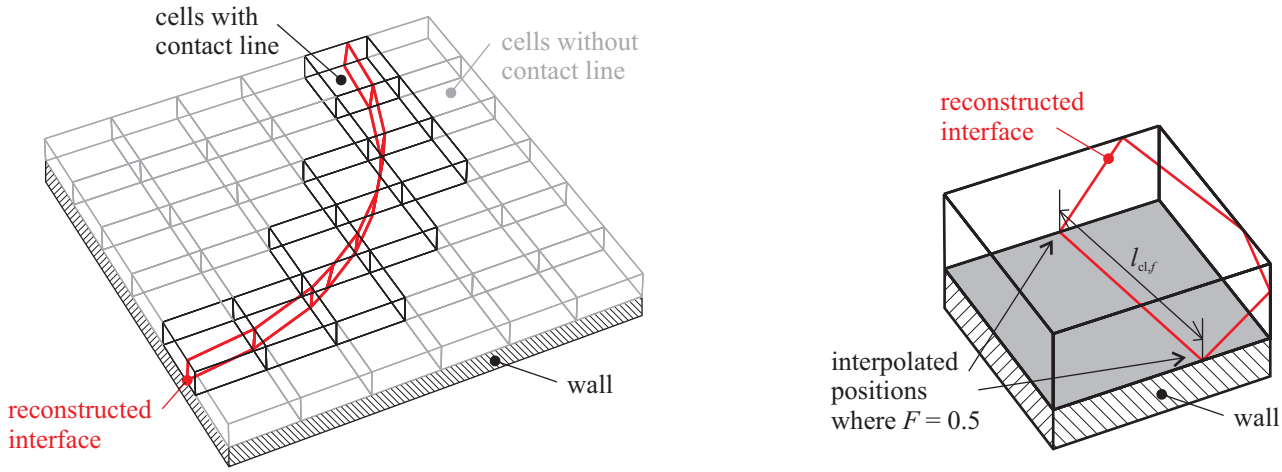

(a) Layer of cells adjacent to a wall

(b) Single cell with contact line

Figure 4.7: Illustration of the reconstructed interface in the cells adjacent to a wall and of a segment of the 3-phase contact line on a particular face at the wall.

ξ_{mesh}. In this region, the heat transfer can still be assumed to be 1D while the microscale effects have already decayed. Furthermore, the radius of curvature is very large compared to the distance between ξ_{mic} and ξ_{mesh}. Therefore, the slope of the film can be assumed as constant and Eq. (4.27) can be integrated analytically between ξ_{mic} and ξ_{mesh}.

$$Q_{\text{trans}} = Q\left(\xi_{\text{mesh}}\right) - Q_{\text{mic}} = \frac{k_{\text{l}}\left(T_{\text{wall}} - T_{\text{sat}}\right)}{\tan\theta} \ln\left(1 + \frac{\left(\xi_{\text{mesh}} - \xi_{\text{mic}}\right)\tan\theta}{\delta_{\text{mic}} + k_{\text{l}} R_{\text{int}}}\right) \tag{4.35}$$

Herein, the contact angle which is used as boundary condition for the CFD simulation (see section 3.2.4) is used for the value of θ. The reason to use this value rather than the contact angle obtained from the contact line evaporation model θ_{mic} is that the transition region should close the gap between the contact line evaporation model and the CFD simulation. The shape of the film at the end of the transition region should be similar to the shape of the film predicted by the CFD simulation. The latter depends on the contact angle which is used as a boundary condition in the simulation. The contact angle θ_{mic} predicted by the contact line evaporation model and the contact angle θ which is used in the CFD simulation are not necessarily equal. Hence, this approach can lead to an unphysical kink in the profile of the film thickness (see Figure 4.6) at the position where the contact line model and the CFD simulation are coupled. However, the film thickness remains continuous while the use of θ_{mic} in Eq. (4.35) would lead to a discontinuity in the film thickness. Therefore, the use of the contact angle which is used as a boundary condition in the CFD simulation is justified. The alternative could be to use θ_{mic} in Eq. (4.35) and also as boundary condition in the CFD simulation which would neither lead to a kink nor to a discontinuity in the film thickness. This modification should be further investigated and potentially be implemented during a future optimization of the boiling model. Note that the above mentioned kink or discontinuity appears neither in the CFD simulation nor in the subgrid scale model but only virtually during the coupling of the two as shown in Figure 4.6. It has no effect on the integral heat transfer through the face at the solid-fluid interface containing a segment of the 3-phase contact line.

The integrated heat flux obtained from the contact line evaporation model Q_{mic} and the heat flux in the transition region Q_{trans} must be calculated in each face on a wall boundary which contains a part of the 3-phase contact line. These faces are found during the interface reconstruction algorithm. The length of the segment of the contact line that lies within a particular face $l_{\text{cl},f}$ is also calculated during

the interface reconstruction (see Figure 4.7). The length scale ξ_{mesh} that is resolved by the CFD mesh is calculated from the area of the face f and the length of the segment of the contact line.

$$\xi_{\text{mesh}} = \frac{\left|\vec{S}_f\right|}{l_{\text{cl},f}} \tag{4.36}$$

This value is used for the calculation of the heat transfer in the transition region according to Eq. (4.35). The amount of heat that is transferred from the heating wall to the fluid in a particular face f containing a segment of the contact line can then be calculated from the integrated heat fluxes in the microscopic and the transition region as well as the length of the segment.

$$Q_{\text{cl},f} = \left(Q_{\text{mic}} + Q_{\text{trans}}\right) l_{\text{cl},f} \tag{4.37}$$

Some of the heat transfer is already captured by the CFD simulation and the thermal coupling between wall and fluid which is described in the following section. Therefore, the subgrid scale model does not impose the heat transfer from Eq. (4.37) as a whole but only corrects the heat transfer locally. The heat flow $Q_{\text{cl},f}^{(\text{CFD})}$ denotes the heat transfer that is predicted by the CFD simulation in a particular face f at the heating wall. The subgrid scale model must compare this value to the heat flow obtained from the contact line evaporation model and from the transition region and only impose the difference as an additional heat flow.

$$\Delta Q_{\text{cl},f} = Q_{\text{cl},f} - Q_{\text{cl},f}^{(\text{CFD})} \tag{4.38}$$

This heat flow corrects the local heat transfer such that it corresponds to the heat transfer predicted by the contact line evaporation model and the transition region. The magnitude of the correction relative to the heat flow resolved by the CFD simulation depends on the mesh resolution. In the simulations which are presented within the present thesis, the correction is typically of the same order as the heat flow which is resolved by the CFD simulation. The ratio between the resolved heat transfer and the correction is a measure of a proper mesh resolution at the 3-phase contact line. If the heat transfer correction strongly exceeds the resolved heat transfer, a finer mesh should be chosen.

4.3 Conjugate heat transfer between solid and fluid

In contrast to the liquid-vapor interface, the solid heating wall and consequently the solid-fluid interface is not moving or being deformed during the simulation. Furthermore, only the heat conduction equation (2.12) needs to be solved in the solid domain. For these two reasons it is convenient to use a separate mesh for the solid domain. The energy equation in the fluid domain and the energy equation in the solid domain are solved separately on their individual meshes and coupled by the common boundary at the solid-fluid interface (see Figure 4.8). In the following the subscripts F and S are used to denote quantities on the fluid and solid side of the solid-fluid interface, respectively. The classical conjugate heat transfer problem between two domains is solved by applying the thermal equilibrium, i.e. continuity of temperature and heat flux. For any face f on the solid-fluid interface, the following equations are applied.

$$T_{\text{F},f} = T_{\text{S},f} \tag{4.39}$$

$$q_{\text{F},f} = q_{\text{S},f} \tag{4.40}$$

	Solid	Fluid
Temperature	calculated	boundary condition
Heat flux	boundary condition	calculated

Table 4.1: The temperature field and heat flux field at the solid-fluid interface are imposed as boundary conditions or calculated depending on the domain (solid or fluid).

The following boundary conditions are chosen: For the solid domain, a fixed value for the normal temperature gradient (corresponding to a particular heat flux at the face f) is imposed on the solid-fluid interface while a fixed value for the temperature is used as boundary condition for the fluid domain (see Table 4.1). In the numerical model, the classical coupling of the energy equations is implemented in the following iterative procedure.

- **Step 1**
  The temperature field at the solid-fluid interface of the solid domain (calculated in the last time step or iteration loop) is imposed as a boundary condition on the solid-fluid interface of the fluid domain.
- **Step 2**
  The heat flux field at the solid-fluid interface of the fluid domain (calculated in the last time step or iteration loop) is imposed as a boundary condition on the solid-fluid interface of the solid domain.
- **Step 3**
  The energy equation is solved in the fluid domain taking into account the boundary condition that is imposed on the solid-fluid interface during step 1. Hereby, the fluid side heat flux at the solid-fluid interface is calculated.
- **Step 4**
  The energy equation is solved in the solid domain taking into account the boundary condition that is imposed on the solid-fluid interface during step 2. Hereby, the solid side temperature field at the solid-fluid interface is calculated.
- **Step 5**
  The newly calculated temperature field on the solid side of the solid-fluid interface is compared to the temperature field on the fluid side. If the maximum of the magnitude of the difference between the two fields is larger than a certain value[6], another correction loop is performed beginning with step 1. Otherwise, the solution is converged and the temperature fields are kept.

In *OpenFOAM* it is also possible to directly couple the energy equations in the two domains by combining the two matrices which result from the FVM treatment of the energy equations into a single matrix. The explicit, iterative coupling which is applied here has the major drawback of a limited time step size. However, the time step is typically much more limited by the transport of the volume fraction field than by the solution of the energy equation. Therefore the temperature fields are typically converged after less than five iterations and do not change much from one time step to another. The advantage of the explicit, iterative coupling is the straightforward implementation and the possibility to directly manipulate the conjugate heat transfer. The latter is used for coupling the subgrid scale model for the contact line evaporation to the CFD simulation. After the reconstruction of the liquid-vapor interface, the faces which are adjacent to the solid-fluid interface are subdivided into three groups.

- **Group 1:** Faces on the liquid side of the liquid-vapor interface without 3-phase contact line
- **Group 2:** Faces on the vapor side of the liquid-vapor interface without 3-phase contact line

[6] In the present thesis, an absolute temperature difference of 10^{-4} K is used as convergence criterion.

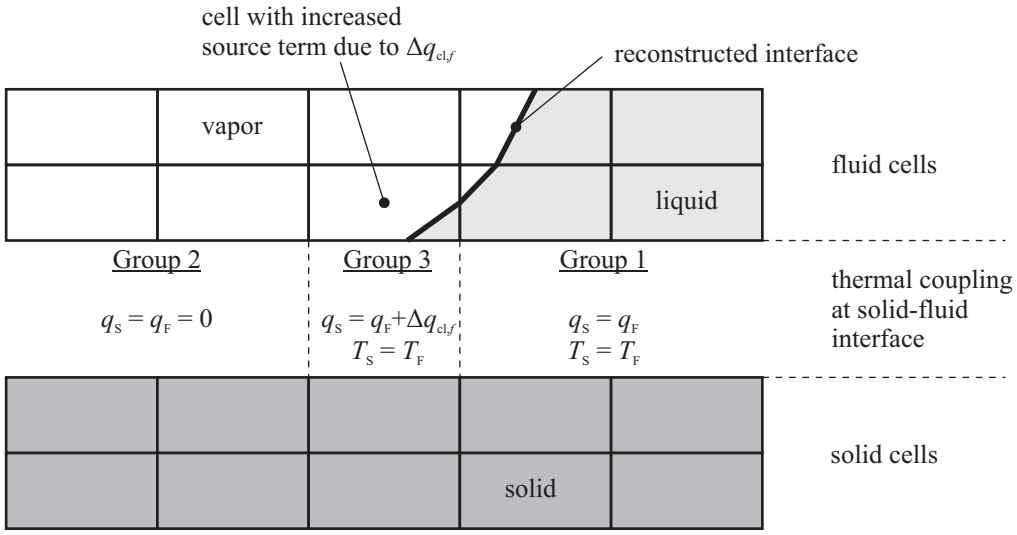

Figure 4.8: Illustration of the solid and fluid domains and the thermal coupling across the solid-fluid interface.

- **Group 3:** Faces containing a segment of the 3-phase contact line

These groups and the corresponding coupling conditions are shown in Figure 4.8. For group 1 and group 2, the classical thermal coupling as described above can be applied. However, in nucleate boiling conditions the heat transfer from the wall into the vapor is usually negligible compared to the heat transfer into the liquid. Therefore, the above mentioned coupling is only applied for those parts of the solid-fluid interface which are in contact to liquid (group 1). The heat transfer at those parts of the solid-fluid interface which are in contact to vapor (group 2) is assumed to be zero. Even though the use of the VOF method enables the solution of the energy equation in both phases, the temperature of the vapor is assumed to be constant and equal to the bulk saturation temperature. The consequence is that the heat transfer in the vapor phase is decoupled from the heat transfer in the solid. The faces which contain a segment of the 3-phase contact line (group 3) are treated in a particular way, i.e. the classical coupling which is described above is modified. While Eq. (4.39) is directly used to ensure continuity of the temperature field, the heat flux at a particular face f of group 3 on the solid side of the solid-fluid interface is modified by the heat transfer correction from the contact line evaporation model (according to Eq. (4.38)) .

$$q_{S,f} = q_{F,f} + \frac{\Delta Q_{cl,f}}{\left|\vec{S}_f\right|} = q_{F,f} + \Delta q_{cl,f} \tag{4.41}$$

Hence, the heat flux is discontinous over the faces on the solid-fluid interface which contain a segment of the 3-phase contact line. The heat flux which is transported out of the solid domain $q_{S,f}$ is higher than the heat flux which is transported into the fluid domain $q_{F,f}$. Nevertheless, the energy is conserved as the difference between the two heat fluxes directly intensifies the local rate of evaporation. The difference is equal to the heat transfer correction of the subgrid scale model for contact line evaporation. Due to the very small local film thickness, the heat that is transferred at the 3-phase contact line does not contribute to the heating up of the liquid but is almost immediatly consumed by the evaporation. Therefore, the heat flux correction according to Eq. (4.38) directly enhances evaporation locally by contributing to the sharp source term field described in section 4.1.1. The sharp source term field $\dot{\rho}_0$ is increased by the term $\Delta Q_{cl,f} / \left(\Delta h_V V_{cell}\right)$ in a cell c if it has a face f on which a segment of the 3-phase contact line has been reconstructed. This local increase of the sharp source term field is performed prior to the smearing, cropping and scaling of the source term field that is described in section 4.1.2.

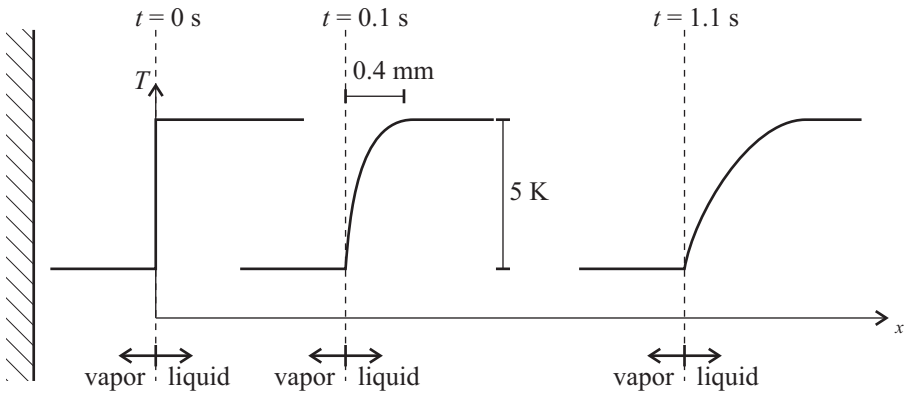

Figure 4.9: Sucking interface problem: Sketch of the problem setup with interface positions (dashed lines) and temperature profiles (solid curves) at different instances. The fluid is water at $p = 1013\,\text{mbar}$, the wall superheat is 5 K.

4.4 Validation simulations

In this section, several validation simulations that were performed with the boiling model are presented and their results are discussed. As already discussed by Fuchs [21], the validation of the complete boiling model is difficult. This is mainly due to the high complexity of boiling phenomena which limits the use of analytical approaches. Highly resolved experiments are available. However, the boundary conditions are usually not completely known with exactitude. Moreover, rather high measurement uncertainties make a validation of the model by pure comparison to experimental data difficult. Therefore, several simplified validation cases with phase change but without evaporation at a 3-phase contact line were simulated. For these validation cases analytical solutions exist and can be used for comparison. Furthermore, a test case with phase change and evaporation at the 3-phase contact line is simulated. In this case, no analytical solution exists and the results are therefore compared to data from a highly resolved numerical analysis which is available in literature.

4.4.1 1D test case (sucking interface problem)

The sucking interface problem is a 1D test case with phase change that is described by Welch and Wilson [126]. The existence of an analytical solution provides the possiblity to validate the implementation of the phase change model. The setup of the problem is shown in Figure 4.9. A layer of vapor separates superheated liquid from a wall. The superheat in the liquid leads to evaporation at the liquid-vapor interface. Due to the density difference between the vapor and the liquid, the liquid-vapor interface is pushed away from the wall. As the evaporation process takes place, the initial sharp temperature step at the liquid-vapor interface becomes more and more smooth which is due to thermal diffusion. The smoothing of the temperature profile is illustrated in Figure 4.9. The analytical solution to this problem provides information about the temperature profile in the liquid and the instantaneous evaporation rate at arbitrary times. This data can be integrated over time and thus the development of the interface position with time can be obtained.

As the initial sharp temperature step at the interface cannot be resolved on a discrete mesh, the initial condition for the simulation is the temperature profile and interface position at $t = 0.1\,\text{s}$ (see Figure 4.9). The temperature profile at this time is taken from the analytical solution and has a width of around 0.4 mm. Saturated water at a pressure of $p = 1\,\text{bar}$ with a liquid superheat of 5 K is used as fluid in the simulations (see appendix A for material properties). Simulations were performed on four

09
01/10/2018
longkai guo

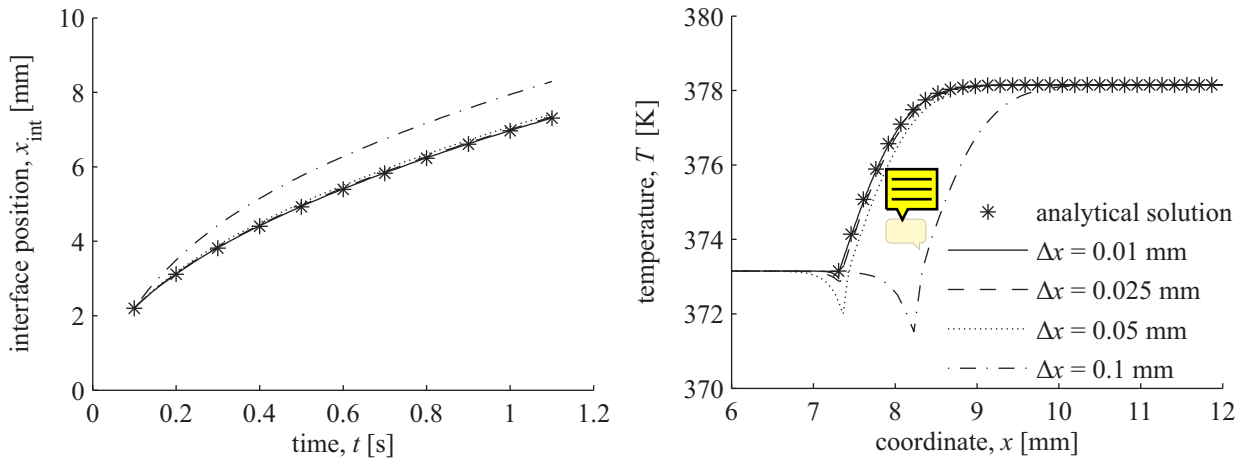

(a) Interface position (b) Temperature profile after $t = 1.1$ s

Figure 4.10: Sucking interface problem: Simulation results compared to the analytical solution. The fluid is water at $p = 1013$ mbar, the wall superheat is 5 K.

	interface position [mm]	**absolute error [mm]**
analytical solution	7.307	-
simulation 1 ($\Delta x = 0.01$ mm)	7.314	0.007
simulation 2 ($\Delta x = 0.025$ mm)	7.342	0.035
simulation 3 ($\Delta x = 0.05$ mm)	7.417	0.110
simulation 4 ($\Delta x = 0.1$ mm)	8.293	0.986

Table 4.2: Sucking interface problem: Interface position and its absolute error at $t = 1.1$ s. The fluid is water at $p = 1013$ mbar, the wall superheat is 5 K.

different meshes with different levels of resolution to check the convergence of the phase change model. The cell size Δx ranges between 0.1 mm and 0.01 mm.

The development of the interface position with time is shown in Figure 4.10(a). The results of the simulation are in very good agreement to the analytical solution except for the simulation on the coarsest mesh ($\Delta x = 0.1$ mm) where rather large differences are observed. The interface position and its absolute error at $t = 1.1$ s are given in Table 4.2. It is interesting to note that a coarser mesh leads to an overestimation of the evaporation rate and therefore of the interface speed. This seems to be in contradiction to the fact that the temperature gradient is usually underestimated on a coarser mesh and therefore leads to an underestimation of the evaporation rate. The overestimation can probably be explained by an undershot of the temperature on the vapor side of the interface which can be seen in Figure 4.10(b). An undershot like this is typical when a steplike variable is convected on a discrete mesh using linear interpolation. The undershot could probably be avoided by using an upwind or higher-order differencing scheme. In spite of the undershot of the vapor temperature close to the interface, the liquid side temperature profile is in excellent agreement to the analytical solution.

The correctness of the phase change model and its implementation is confirmed by this first test case. The results converge towards the analytical solution on finer meshes and the required mesh size for an accuracy of 1.5 % (simulation 3 with $\Delta x = 0.05$ mm) is equal to the mesh size used by Welch and Wilson [126].

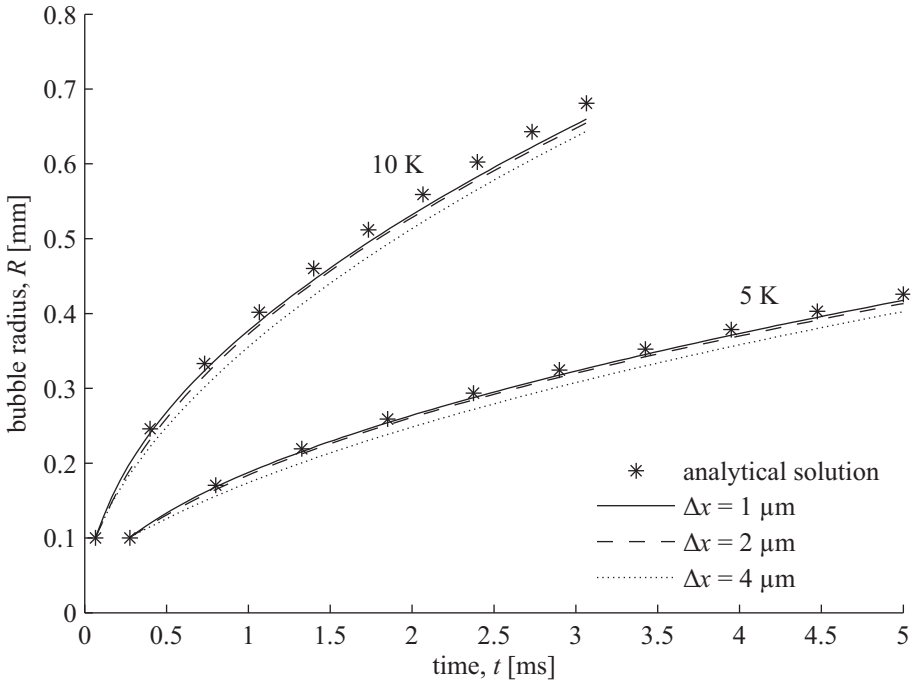

Figure 4.11: Spherical bubble growth: Bubble radius over time, simulation results and analytical solution. The fluid is HFE-7100 at $p = 500\,\mathrm{mbar}$, the wall superheat is 5 K and 10 K.

4.4.2 2D test case without 3-phase contact line (spherical bubble growth)

The second test case is the growth of a spherical vapor bubble in an infinitely extended superheated liquid. The phenomenon and the different stages of growth are well described by Plesset and Zwick [87]. After an initial stage during which the bubble growth is controlled by surface tension and inertia effects, the growth is controlled only by the rate at which heat can be transferred from the superheated liquid to the liquid-vapor interface. During this second stage, which is the subject of this validation case, it can be assumed that the bulk vapor and the liquid-vapor interface are at saturation temperature. Scriven [95] derived an analytical solution for this situation by applying a similarity approach. The analytical solution is used to predict the growth rate of a vapor bubble in a superheated liquid. Similar to the sucking interface problem, the analytical solution permits to calculate the initial conditions for the simulations and to validate the numerical results.

The curvature of the liquid-vapor interface leads to several additional challenges compared to the aforementioned 1D test case. First, the calculation of the interface normal vector and the temperature gradient becomes more difficult as their direction is generally not aligned with the mesh. Second, surface tension and curvature lead to a pressure jump at the liquid-vapor interface. The calculation of the surface tension forces can lead to parasitic currents as discussed in section 3.2.3. These currents can locally disturb the temperature field and consequently lead to an erroneous calculation of the local evaporation rate. The heat transport very close to the liquid-vapor interface is governed by diffusive heat transfer. The parasitic currents lead to an unphysical convective heat transfer and thus increase the local evaporation rate at the liquid-vapor interface. It is important to check that the magnitude of the parasitic currents is small enough and does not lead to an additional, unphysical convective heat transfer.

The simulations are performed on a 2D, axisymmetric mesh with a size of 0.8 mm × 0.8 mm. Only a quarter of the bubble is simulated. Three orthogonal, equally distanced meshes with different mesh resolutions are used. The cell size of the different meshes is 1, 2 and 4 μm. The fluid is refrigerant HFE-7100 (see appendix A for material properties) and two different liquid superheats (5 K and 10 K)

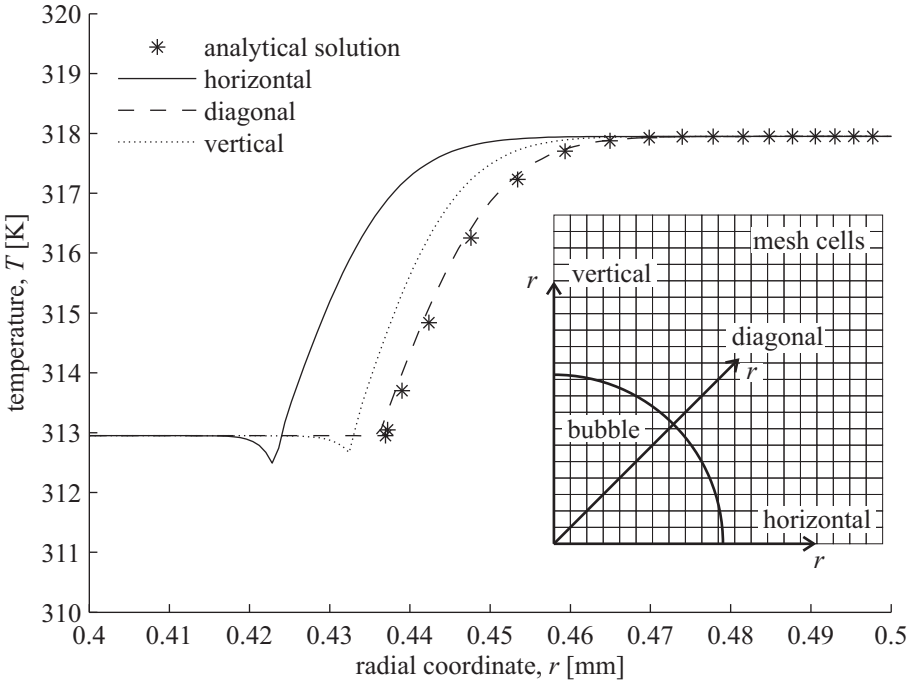

Figure 4.12: Spherical bubble growth: Temperature profile at the end of the simulation (case with 5 K superheat and cell size of 1 μm), simulation results and analytical solution. The fluid is HFE-7100 at $p = 500$ mbar, the wall superheat is 5 K and 10 K.

were applied. The starting point of the simulations is the instance at which the vapor bubble has a radius of $R = 0.1$ mm. The temperature profile at this instance is taken from the analytical solution. The temperature drop at the interface looks qualitatively like the temperature drop in the 1D test case which is discussed above (see Figure 4.9). However, due to the fast growth of the bubbles, the thickness of the thermal layer is much smaller. The temperature drops on a length of only 6.8 μm and 3.3 μm from the superheated level in the liquid to the saturation temperature at the liquid-vapor interface for 5 K and 10 K superheat, respectively.

The growth of the bubble radius is shown in Figure 4.11. The radius of the bubbles is determined as the equivalent radius corresponding to the instantaneous volume of the bubble. Its development with time is very nicely predicted by the numerical model. The results converge towards the analytical solution as the mesh becomes finer. The bubble radius and its absolute error at the end of the simulation is given in Table 4.3. Even with the coarsest mesh the numerical results match the analytical solution within an error of less than 6 % for both superheats. The temperature profiles from the simulation with 5 K superheat and a cell size of 1 μm are plotted in Figure 4.12. The profiles are sampled along three lines (horizontal, diagonal and vertical to the mesh orientation). Although all profiles have the same shape as the analytical solution, they are slighty shifted one to another. This means that the bubble is not perfectly spherical in the simulation, i.e. the radius of the bubble is not the same at all positions along the liquid-vapor interface. However, the shift measures only about 3 % of the equivalent bubble radius. As already observed in the 1D test case, there is a small undershot of temperature at the liquid-vapor interface in the temperature profiles sampled along the horizontal and vertical direction. However, no undershot can be observed in diagonal direction. In contrast to the 1D test case, the undershot does not lead to a global overestimation of the evaporation rate. As expected, a coarser mesh leads to a underprediction of the temperature gradient and consequently to a slower bubble growth.

The main outcome of this second test case is the confirmation that the phase change model predicts the evaporation rate correctly even if the liquid-vapor interface is not aligned with the mesh. There is only a very small difference between the local temperature profiles in the vicinity of the liquid-vapor

	bubble radius [mm]	absolute error [mm]
5 K superheat		
analytical solution	0.437	-
simulation 1 ($\Delta x = 1\,\mu$m)	0.429	0.008
simulation 2 ($\Delta x = 2\,\mu$m)	0.425	0.012
simulation 3 ($\Delta x = 4\,\mu$m)	0.413	0.024
10 K superheat		
analytical solution	0.681	-
simulation 1 ($\Delta x = 1\,\mu$m)	0.660	0.021
simulation 2 ($\Delta x = 2\,\mu$m)	0.655	0.026
simulation 3 ($\Delta x = 4\,\mu$m)	0.644	0.037

Table 4.3: Spherical bubble growth: Bubble radius and its absolute error at the end of the simulation. The fluid is HFE-7100 at $p = 500\,$mbar, the wall superheat is 5 K and 10 K.

interface. Thus, the same local evaporation rate is calculated independent of the alignment of the liquid-vapor interface with the mesh. A secondary outcome is that parasitic currents are small enough and do not disturb the solution at typical bubble growth speeds.

4.4.3 2D test case with 3-phase contact line (meniscus evaporation)

As discussed during the introduction of the present thesis the microscale heat and fluid flow at the 3-phase contact line can have a tremendous influence on the overall heat and mass transfer in boiling. Therefore, one of the main goals of the present thesis is the implementation of a subgrid scale model into the VOF framework of *OpenFOAM*. To the authors knowledge there is, unfortunately, no test case with a 3-phase contact line that comes with an analytical solution. However, highly resolved numerical simulations with a mesh resolution of below $1\,\mu$m at the 3-phase contact line have been performed by Stephan and Busse [108] for the evaporation of steady menisci in heat pipe grooves. The authors developed the model for the evaporation at the 3-phase contact line which is also used for this thesis and coupled it to a macroscopic *Finite-Element* solver which solves the stationary heat conduction in the liquid and in the solid. Due to the rather small evaporation rates convective heat transfer is negligible and the position of the meniscus can be assumed to be steady.

The reference simulation of Stephan and Busse [108] was performed for ammonia in triangular aluminum grooves (see Figure 4.13(a) for the geometry and appendix A for material properties of fluid and solid). A constant wall temperature of 301.31 K is imposed at the bottom of the solid structure which corresponds to a superheat of 1.31 K above the saturation temperature of ammonia at 11 bar. The resulting heat transfer coefficient of $23\,\mathrm{kW/(m^2\,K)}$ corresponds to a heat flux of $30.13\,\mathrm{kW/m^2}$. The apparent contact angle is $19.7\,^\circ$. The very same geometry and boundary conditions are used for the test simulation which is described here. However, due to the nature of the model, the simulations are performed fully transient and take into account the fluid flow in the liquid and the vapor phase. The initial volume of the liquid in the groove is chosen according to the results of Stephan and Busse [108]. Initially, the liquid and vapor phase are at saturation temperature and the interface is flat (see Figure 4.13(b)). The temperature in the solid is initially set to a constant value of 301.31 K. As the simulation runs, the liquid-vapor interface becomes curved due to the contact angle which is imposed as a boundary condition at the solid-fluid interface. Moreover, the temperature profiles in solid and liquid develop with time until they reach a quasi-steady state. Due to the transient nature of the model, the evaporation lead to a decrease of the liquid volume. However, this decrease happens rather slowly and the temperature field

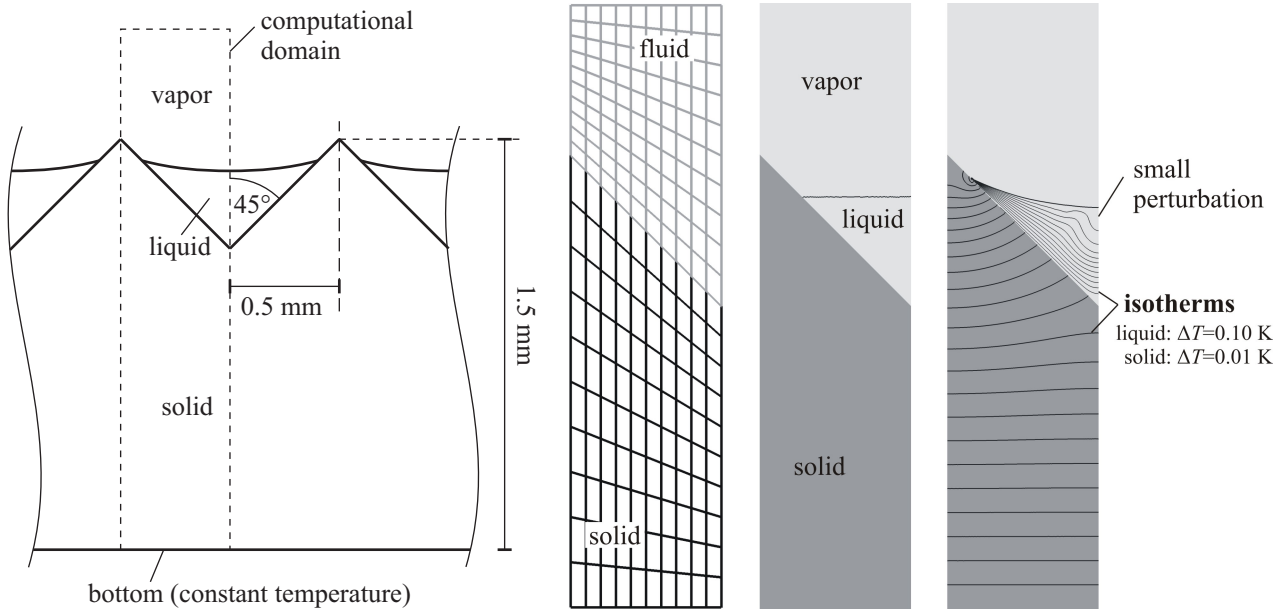

(a) Sketch of the problem (b) Mesh, initial solution and steady state solution

Figure 4.13: Meniscus evaporation: Problem definition, mesh (only every fifth grid line of the coarsest mesh is shown), initial conditions and steady-state results (obtained on finest mesh with contact line evaporation model). The fluid is ammonia at $p = 1\,\mathrm{bar}$, the solid is aluminum with a wall superheat of 1.31 K at the bottom.

and evaporation rate is quasi-steady. The converged temperature profile in solid and liquid is shown in Figure 4.13(b). There is a small perturbation of the temperature field close to the symmetry plane. This is due to small convective energy transport which is caused by parasitic currents. However, in spite of this small perturbation, the temperature field agrees very well to the results obtained by Stephan and Busse [108].

The simulations are performed on three different meshes with different resolutions in the vicinity of the 3-phase contact line (2.5, 5 and 10 μm, see Figure 4.13(b)). On each mesh, the simulation is performed with and without the subgrid scale model for the evaporation at the 3-phase contact line. The development of the mean heat flux at the bottom of the solid structure with time is shown in Figure 4.14. The simulations with the contact line evaporation model predict the heat flux very accurately while it is significantly underestimated by the simulations without the contact line evaporation model. Moreover, the simulations with contact line evaporation model do not show any mesh dependency while those without show an increasing heat flux for higher mesh resolution. Hence, if the heat transfer at the 3-phase contact line is not modeled properly, the overall model is not converging. The use of finer meshes leads to an ever increasing heat transfer.

This test case confirms the correctness and accuracy of the subgrid scale model for the heat and fluid flow at the 3-phase contact line, its coupling to the macroscopic CFD simulation and the implementation of the conjugate heat transfer between the solid and fluid domain. The heat flux transferred in a triangular heat pipe groove with an evaporating meniscus is calculated and shows a deviation of below 7 % compared to the highly resolved simulation which was performed by Stephan and Busse [108]. Further, the results of this test case show that the correct modeling of the heat and fluid flow at the 3-phase contact line is of tremendous importance for the accuracy and convergence of the overall model as an important amount of heat can be transferred in this small region.

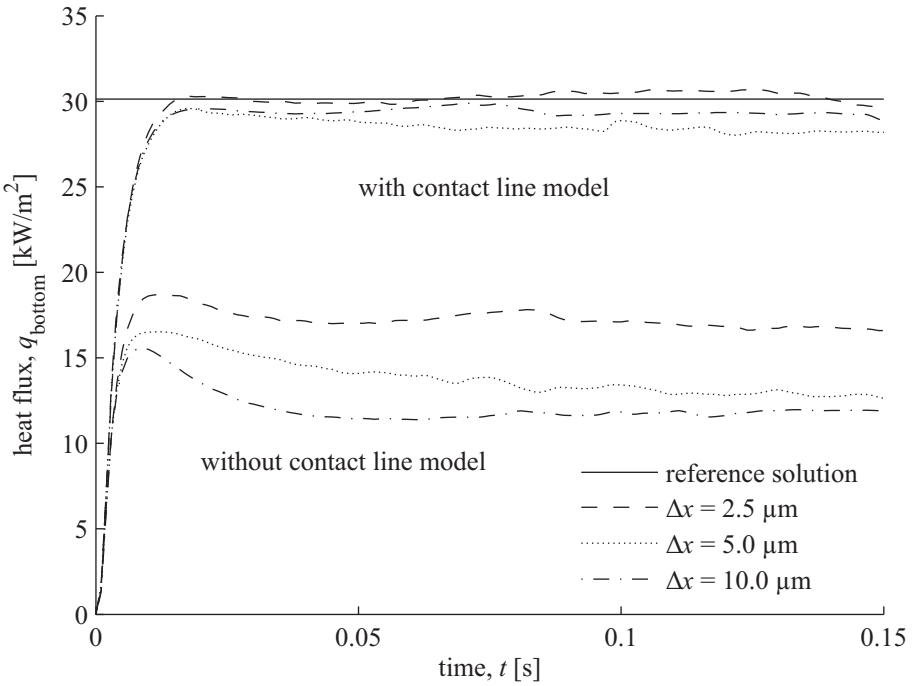

Figure 4.14: Meniscus evaporation: Development of simulated mean heat flux at the bottom of the solid structure with time in comparison to the reference data of Stephan and Busse [108]. The fluid is ammonia at $p = 1\,\mathrm{bar}$, the solid is aluminum with a wall superheat of 1.31 K at the bottom.

5 Results and discussion

In this chapter, the simulations that were performed with the boiling model are presented and their results are discussed. The focus of the present thesis is on the simulation of nucleate pool boiling. In the first two sections of this chapter, the simulation results on pool boiling at a single nucleation site and on lateral bubble mergers are presented, analyzed and discussed. A detailed comparison to highly resolved experimental data is accomplished. The third section of this chapter is dedicated to additional simulations on boiling configurations which are different from nucleate pool boiling. These simulations were performed to prove the capabilities of the boiling model and to check its applicability to a wide range of applications. The emphasis of these simulations is on the feasability and on qualitative agreement rather than detailed quantitative comparison to experiments.

5.1 Single bubble pool boiling

Wagner and co-workers [120] investigated boiling of HFE-7100 at 500 mbar on a steel heating foil with a thickness of 50 μm (see appendix A for material properties of fluid and solid). An artificial nucleation site on the heating foil enables the generation of single bubbles at a prescribed position. The steel foil is heated by an electric current resulting in a surface heat flux of 5400 W/m^2. The authors state that the heat transfer to the surrounding air at the back side of the foil can be neglected compared to the heat transfer to the boiling fluid. The bubble shape was observed with a high-speed camera from the side, while the temperature of the steel heating foil was measured with a high-speed infrared camera from below. The authors observed periodic bubble events with a bubble growth time of 13 ms and a departure diameter of 1.9 mm. The mean superheat of the heating foil is around 15 K while the temperature of the bulk liquid is close to saturated conditions. The temporal and spatial resolution of the experimental apparatus enables the observation of the high local heat flux at the 3-phase contact line and the resulting strong local cooling of the heater surface. At the 3-phase contact line the authors measured a temperature decrease of around 1.5 K and a local heat flux peak of around 150 kW/m^2. Due to the perdiodicity of the bubble cycles and the high temporal and spatial resolution, this experiment is an excellent validation case for the boiling model. However, the simulations which are presented here are not only used for model validation but also to gain detailed insights into the boiling process. In the following, the setup of the simulation is explained and its results are presented and compared to the experimental data. Some of the simulation results on the same case but with an earlier version of the model were published by Kunkelmann and Stephan [59, 60].

5.1.1 Simulation setup, input parameters and post-processing

The geometric setup of the simulation and the most relevant boundary conditions are shown in Figure 5.1. The computational domain is axisymmetric and subdivided into different regions corresponding to different levels of mesh resolution. The simulation results that are presented in the next section are all obtained on the fine mesh with a mesh resolution of 4 μm in the region close to the bubble (region 4 according to the naming used in Figure 5.1). The electric heating of the foil which is used in the experiment is implemented via a constant volumetric energy source term in the solid domain. The initial temperature profile in the liquid layer close to the heating wall is assumed to be linear with a thickness of 0.18 mm while the heating wall is assumed to have an initial constant superheat of 15 K. The

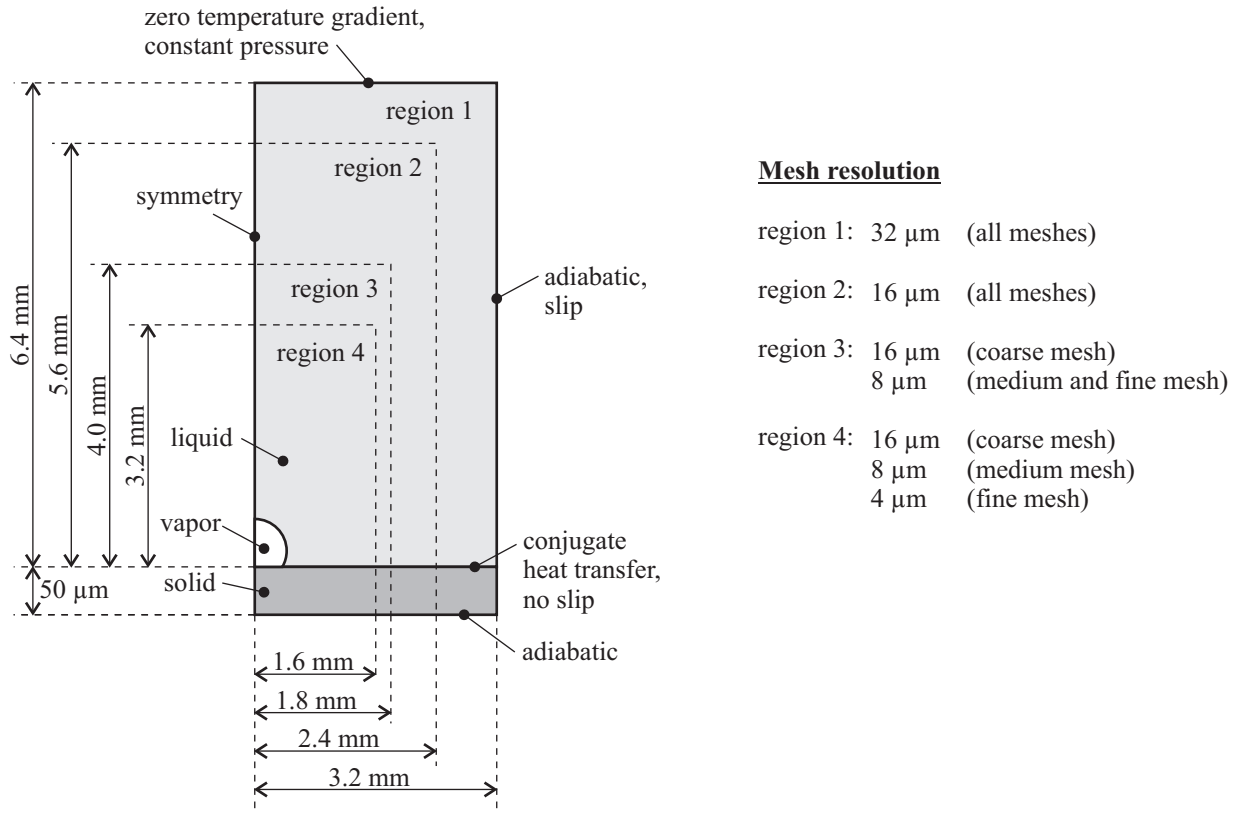

Figure 5.1: Geometry of the problem and mesh resolution in the different regions of the mesh (thickness of heating foil is scaled up for better visibility).

temperature of the bulk liquid is set to the saturation temperature. These choices are arbitrary, but the simulation of several consecutive bubble cycles permits to reach a periodic regime which is independent of these initial conditions. The developments of the departure diameter D_{dep} and the bubble frequency f_{bubble} during the simulation are shown in Figure 5.2(a). It can be seen that the values change very much from one cycle to another in the beginning of the simulation. Towards the end of the simulation, the values become almost constant and the difference between two cycles becomes very small. The temporal development of the mean wall temperature[1] and the heat transfer at the heater surface are plotted in Figure 5.2(b). The periodic fluctuations of the mean wall temperature and of the heat transfer corresponds to the periodic nucleation, growth, detachment and rise of the bubbles. Again, it can be seen that an almost completely periodic regime is reached after several bubble cycles.

At the current state of development, the boiling model does not include any sub-model for the nucleation process. Therefore, the waiting time Δt_{wait} between the departure of a bubble and the nucleation of the succeeding bubble is taken from the experiment in which an almost constant value of 25 ms was measured. The detachment of the bubble is detected in the simulation and leads to the start of a count-down of 25 ms. When the count-down is finished, a small bubble ($R = 0.1$ mm) is put on the heater by local manipulation of the volume fraction field. The volume of this initial bubble is smaller than the volume of a departing bubble by a factor of around 1000. This ratio must be chosen very large to avoid that the results (e.g. bubble shape) are anticipated by the initialization of the bubbles.

The postprocessing is focused on the periodic transient heat transfer during a single bubble cycle. Following the explanations of Schweizer [93], different heat transfer mechanisms are quantified and the corresponding heat flows are calculated. The heat transfer paths are shown in Figure 5.3. Here, the

[1] The mean wall temperature is obtained by spatially averaging the instantaneous wall temperature in a circular area with a radius of 1 mm around the nucleation site.

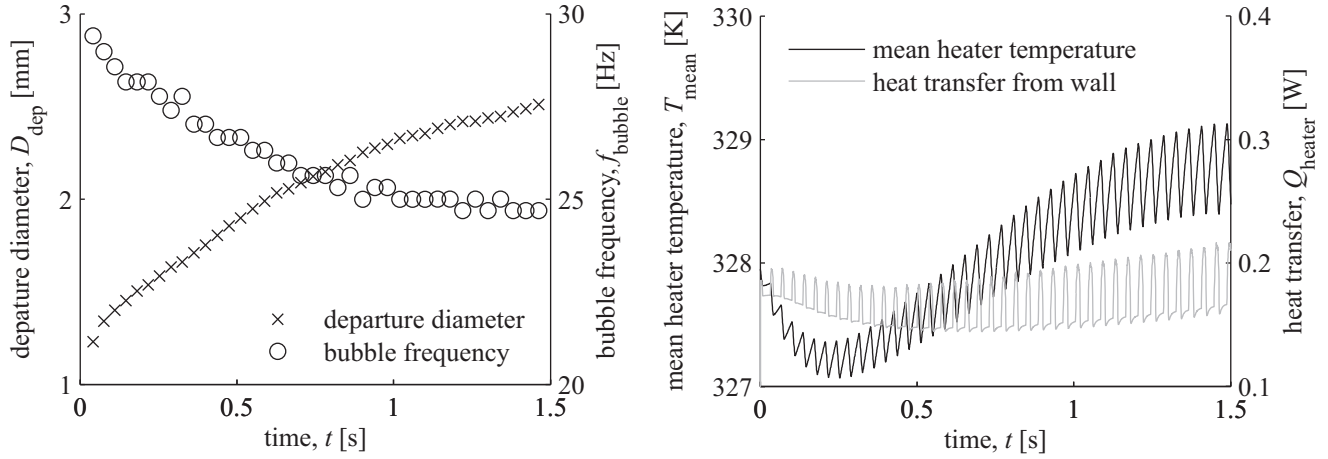

(a) Departure diameter and bubble frequency (b) Temperature and heat transfer at heater surface

Figure 5.2: Convergence of the simulation results after several bubble cycles.

input heat flow Q_{in} can be calculated from the electrical heating and is constant over time. The total heat flow at the heater surface Q_{heater} is the sum of all heat that is transferred into the fluid.

$$Q_{heater} = \iint_{S_{heater}} q \mathrm{d}S = Q_{liquid} + Q_{cl} + Q_{vapor} \tag{5.1}$$

The heat flow Q_{heater} is not constant over time. The instantaneous difference between the heat flows Q_{in} and Q_{heater} represents the heat storage or release in the heating foil. The total heat transfer at the heater surface Q_{heater} is subdivided in the heat flow to the liquid Q_{liquid} and the heat flow at the 3-phase contact line Q_{cl}. The latter directly intensifies the local evaporation rate and does not increase the thermal energy of the liquid. It is assumed that there is no heat flow into the vapor, thus the heat flow Q_{vapor} is assumed to be zero. This assumption is based on the small thermal conductivity of the vapor compared to the liquid and experimental observations (in particular Wagner [120] and Schweizer [93, 94]). It is difficult to define the heat flow at the 3-phase contact line in the simulation because it is a result of the coupling between the subgrid scale model for contact line evaporation and the CFD simulation (see sections 4.2.2 and 4.3). This coupling is adjusted to the mesh resolution, i.e. the heat flow which is resolved by the CFD simulation and the correction via the subgrid scale model do individually depend on the mesh resolution while their sum is independend of the mesh. In order to obtain a measure of the contact line heat transfer which is also independent of the mesh, the heat flow Q_{cl} is obtained by integrating the heat flux in the region close to the 3-phase contact line where the heat flux is larger than a threshold value[2]. The heat flux field is extracted at the solid-fluid interface of the solid domain and thus includes the correction of the subgrid scale model.

$$Q_{cl} = \iint_{S_{heater}} H\left(q - q_{threshold}\right) q \mathrm{d}S \tag{5.2}$$

Herein, H is the *Heaviside* function which cuts of the heat flux field below a value of $q_{threshold}$. A similar approach is also used by Schweizer [93] for the reduction of the experimental data. The heat flow to

[2] The mean heat flux Q_{heater}/S_{heater} is used as threshold value.

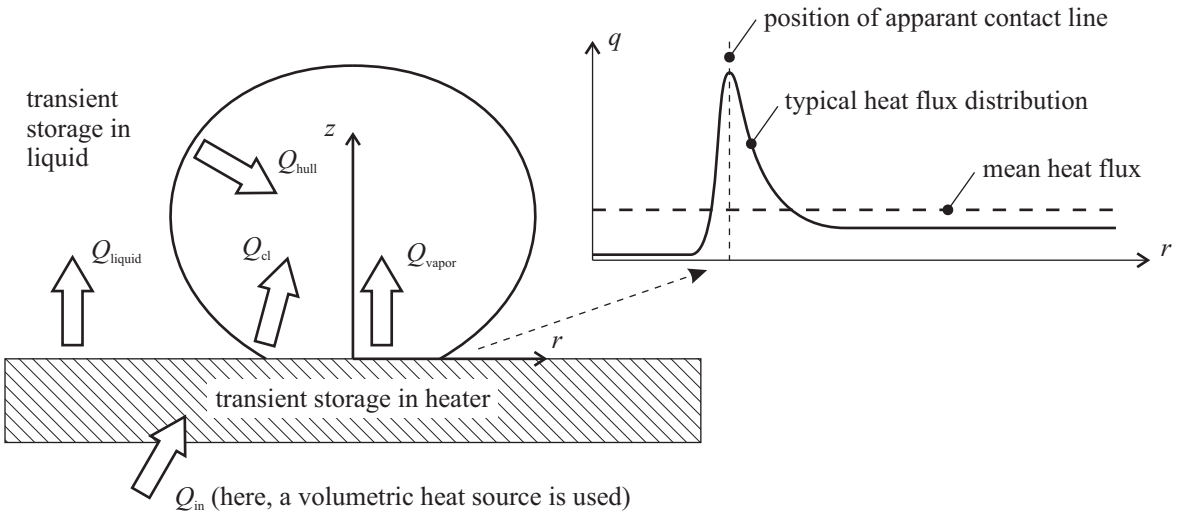

Figure 5.3: Illustration of the heat paths and the transient heat storage in heater and liquid.

the liquid Q_{liquid} increases the thermal energy of the liquid. The energy that is stored in the liquid can lead to evaporation at the bubble hull. The total latent heat flow Q_{latent} is the sum of the heat flow at the 3-phase contact line and the evaporation at the bubble hull. It is calculated from the volume increase of the bubble.

$$Q_{\text{latent}} = \rho_{\text{v}} \frac{\mathrm{d}V_{\text{bubble}}}{\mathrm{d}t} \Delta h_{\text{V}} = Q_{\text{cl}} + Q_{\text{hull}} \tag{5.3}$$

In addition to the total heat transfer on the heater surface, the local heat flux distribution on the heater is of particular interest for the investigation of boiling phenomena. However, the heat flux that is obtained from the simulation cannot be directly compared to the experimental results. The heat flux is calculated from the temperature field on the adiabatic back-side of the heating foil in the experiment. A pixel-wise energy balance, including heat input, storage and conduction, is applied to the data recorded by the high-speed infrared camera. The temperature field is assumed to be constant over the thickness of the foil. Hence, the local heat flux q that is tranferred from the heater to the fluid can be calculated by solving a 2D, transient heat conduction equation.

$$q = q_{\text{in}} - \delta_{\text{foil}} \left[\rho_{\text{S}} c_{\text{S}} \frac{\partial T}{\partial t} - \nabla \cdot \left(k_{\text{S}} \nabla T \right) \right] \tag{5.4}$$

The equation is solved using a *Finite-Difference-Method*. The transient term is approximated using a first order Euler scheme and the heat conduction term is approximated using second order central differencing scheme. Due to the noise on the measurement signal of the high-speed infrared camera, the temperature field is smoothed slightly before the second derivatives are calculated. It should be noted that the temperature which is used in Eq. (5.4) is measured on the back side of the heating foil assuming that the temperature is constant over the thickness of the heating foil. However, this assumption is a strong simplification of the heat conduction within the heating foil. Due to the conduction inside the heater the temperature field on the back side of the heater is much smoother than the temperature field at the solid-fluid interface. Therefore, the heat flux distribution which is calculated from the temperature field on the back side is also more smooth than the real heat flux distribution at the solid-fluid interface. Hence, the numerically obtained heat flux field at the solid-fluid interface is not comparable to the measurement data. In order to enable quantitative comparison of simulation and experiment, the

experimental post-processing of the temperature field is mimicked. The temperature field on the back side of the heater is extracted from the simulation results, a slight smoothing is performed and Eq. (5.4) is applied to obtain a heat flux profile which can directly be compared to the experimental results.

5.1.2 Major findings

Bubble dynamics and flow field

A complete bubble cycle in the periodic regime is shown in Figure 5.4. It can be subdivided into three phases: Bubble growth (0 to 8 ms), bubble detachment (8 to 15 ms) and waiting time (15 to 40 ms). After the nucleation (numerical initialization of the bubble at 0 ms) the bubble grows very rapidly. During this bubble growth phase, the bubble is completely surrounded by superheated liquid and consumes much of the energy that is stored in the liquid. At around 8 ms the bubble foot diameter has reached its maximum value and starts to decrease. The bubble detaches from the heater surface. The detachment phase is completed at around 15 ms when the bubble lifts off from the heater surface. During its rise, the bubble sucks some of the superheated liquid in its wake. Thus, the slim streak of superheated liquid around the axis of symmetry is formed which is already visible at the moment of nucleation. The bubble is still growing in volume during the detachment phase, but much slower compared to the growth phase. The waiting time of 25 ms is elapsed at around 40 ms and the process begins once more. Unfortunately, the temperature field in the fluid was not measured in the experiment (only a punctual measurement was performed by using a micro-thermocouple) and therefore cannot be compared. Probably, the slim streak of superheated liquid around the axis of symmetry would not be observed in experiment because the bubbles do not grow perfectly axisymmetric and because the trajectories of consecutive bubbles are always slightly different.

The velocity fields within and around a growing and a detaching bubble are shown in Figure 5.5. It can clearly be seen that the highest velocities are reached within the vapor phase and are still significantly below 1 m/s, resulting in maximum values for the *Reynolds* number of approximately $\mathrm{Re} = 650$ in the liquid phase and $\mathrm{Re} = 350$ in the vapor phase. Hence, the assumption of an incompressible flow without any unresolved turbulence scales (see section 2.1) is justified. An interesting aspect of the flow field is the strong evaporation from the 3-phase contact line region which leads to a ring shaped jet flow from the 3-phase contact line region towards the middle of the bubble. The consequence is a region of high flow velocities in the middle of the bubble. No perturbation of the flow field in vicinity of the liquid-vapor interface can be observed. Hence, parasitic currents apparently do not influence the simulation results. At the upper part of the bubble hull, the fluid is accelerated across the liquid-vapor interface, i.e. the velocity of the liquid is higher than in the vapor. At first glance, this seems to be odd, but can be explained by the mass transfer through the liquid-vapor interface. as discussed in section 2.2 (see section 2.2). Eq. (2.15) which is obtained from a straightforward mass balance at the liquid-vapor interface can be transformed into the following equation.

$$u_\mathrm{l} = u_\mathrm{v} - j_\mathrm{int}\left(\frac{1}{\rho_\mathrm{v}} - \frac{1}{\rho_\mathrm{l}}\right) \tag{5.5}$$

Herein, the velocity of the vapor u_v is negative in the coordinate system which is used in section 2.2. Thus, the evaporating mass flux across the liquid-vapor interface j_int leads to a larger magnitude of the velocity of the liquid compared to the velocity of the vapor, similar to the sucking interface problem described in section 4.4.1 in which the vapor is quiescent and the liquid is pushed away from the vapor due to the evaporation.

The developments of the equivalent bubble diameter (calculated from the bubble volume, assuming a spherical shape) and of the bubble foot diameter are shown in Figure 5.6. As mentioned above, the

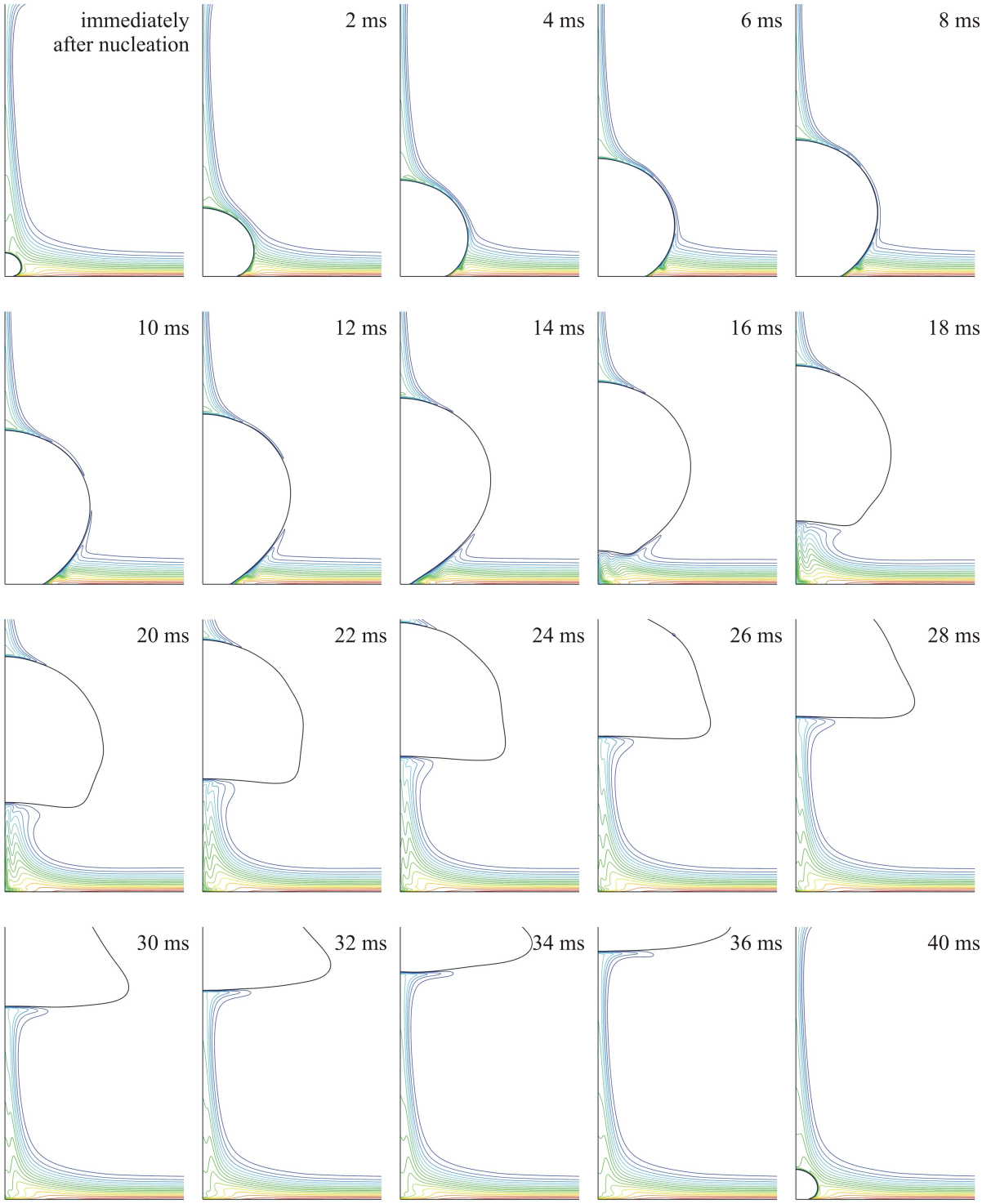

Figure 5.4: Bubble contour and isotherms (distance: 1 K) during a complete bubble cycle.

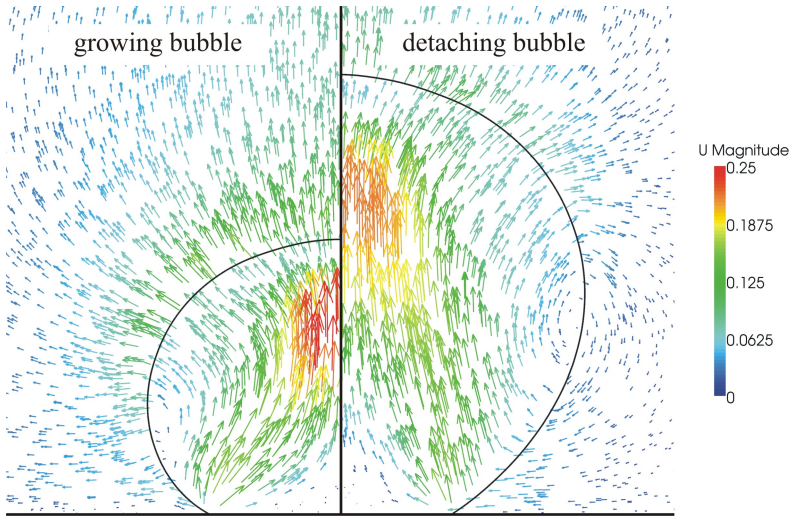

Figure 5.5: Velocity field (in m/s) within and around a growing (4 ms after nucleation) and a detaching (10 ms after nucleation) vapor bubble.

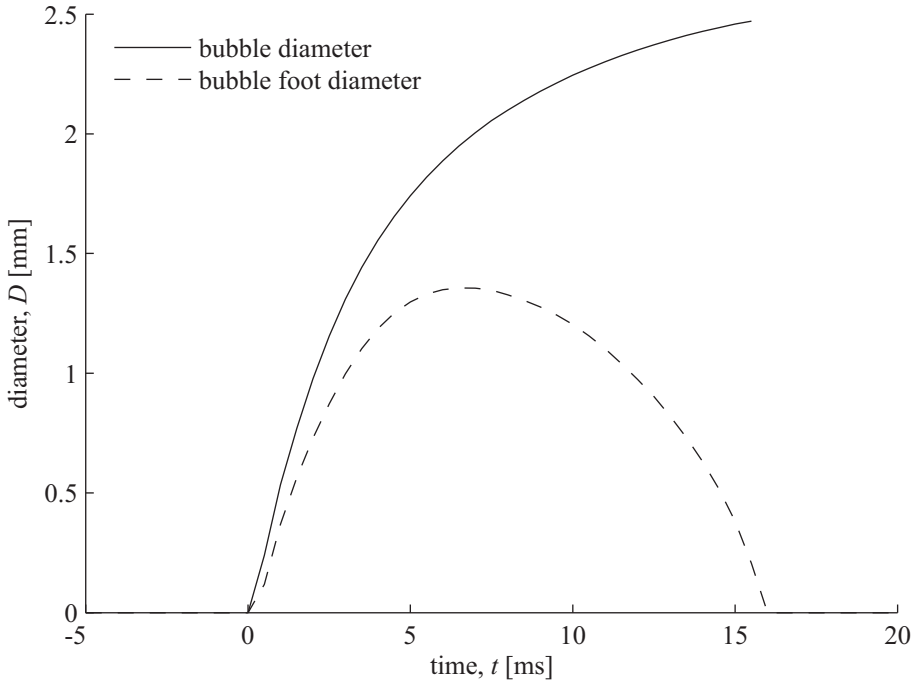

Figure 5.6: Equivalent bubble diameter and bubble foot diameter over time.

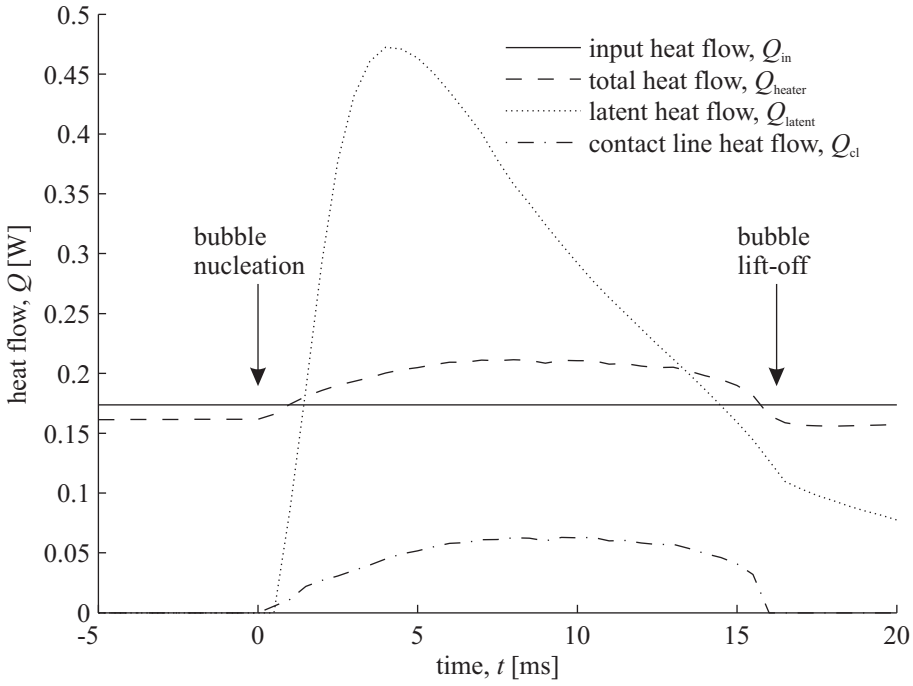

Figure 5.7: Input heat flow and total heat flow at heater surface (both are obtained by integrating the heat flux on the entire heater surface within the computational domain), latent heat flow and contact line heat flow over time.

initial growth rate of the bubble volume is much higher than during the detachment phase which can be concluded from the steep slope of the curve describing the bubble diamter shortly after nucleation. The curve for the bubble foot diameter has a slight asymmetric shape, i.e. the foot diameter grows very fast while it decreases more slowly during the detachment phase. This asymmetric shape has also been observed experimentally by Wagner and co-workers [120]. The time between nucleation and lift-off is around 15 ms which is only around 15 % above the value observed experimentally. The diameter of the bubble at lift-off is around 2.5 mm and lies around 30 % above the value observed in the experiment. This agreement is satisfying enough for such a complex process as nucleate boiling. Most probably the deviations result from the incomplete knowledge of the exact boundary conditions of the experiment. More detailed and comprehensive explanations of the possible sources of error are given at the end of this section.

Heat transfer mechanisms

The input heat flow Q_{in}, the total heat flow at the heater surface Q_{heater}, the latent heat flow Q_{latent} and the contact line heat flow Q_{cl} are plotted over time in Figure 5.7. The total heat flow from the heater surface Q_{heater} is almost constant over time when there is no bubble attached to the heater. The value is slightly smaller than the input heat flow Q_{in}, thus energy is stored in the heating foil in this phase. When the bubble growth starts, the total heat transfer from the heater surface Q_{heater} is increasing significantly above the input heat flow Q_{in}. Hence, more heat is removed from the heater than is supplied by the electric heating and the heater globally cools down. This periodic storage and release of energy can also be seen in the fluctuations of the heater temperature in Figure 5.2(b). The latent heat flow Q_{latent} is the sum of evaporation at the 3-phase contact line and at the bubble hull. During the bubble growth phase, Q_{latent} quickly rises to a maximum value. When comparing the development of the heat flows Q_{latent} and Q_{cl} it can easily be seen that the latent heat is mainly supplied by the superheated liquid which controls the evaporation at the bubble hull. The heat flow at the 3-phase contact line Q_{cl} represents only a rather

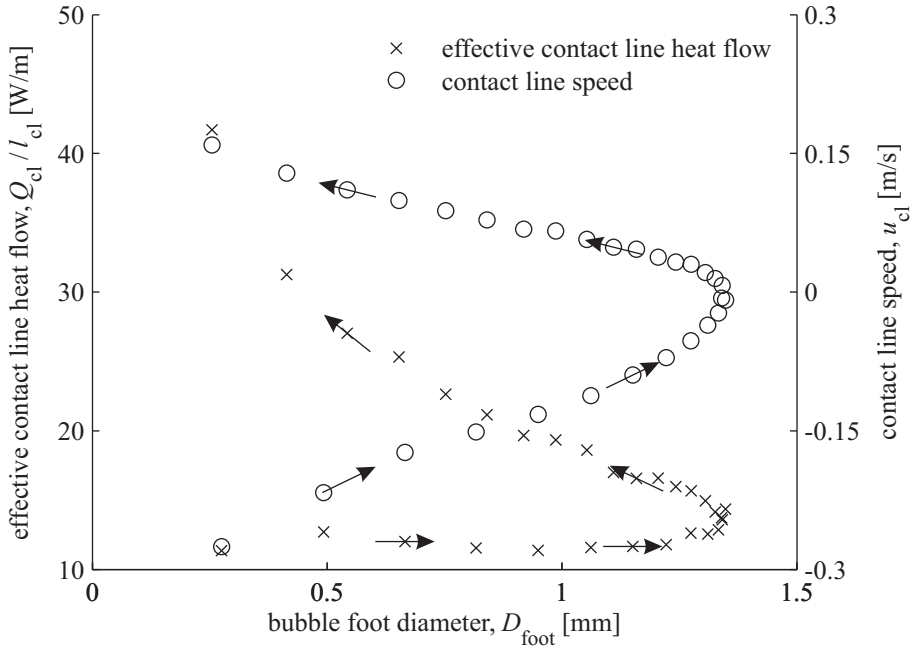

Figure 5.8: Effective contact line heat flow and contact line velocity over bubble foot diameter. The arrows indicate the temporal development during the growth and detachment of the bubble.

small part of the latent heat flow Q_{latent}. The maximum value of the latent heat flow is around 0.47 W which is in excellent agreement to the experimental observations by Wagner and co-workers [120] who measured a value of around 0.4 W. After reaching its maximum value the latent heat flow decreases slowly. At the moment of lift-off and during the bubble rise there is still evaporation at the bubble hull as the bubble is still in contact to superheated liquid. As mentioned above, the bulk liquid is assumed to be at saturation temperature. In the case of a subcooled bulk liquid, the latent heat flow would decrease more rapidely after the maximum and could even become negative due to the condensation at the bubble hull. In principal, the heat transfer at the contact line Q_{cl} follows the development of the bubble foot diameter (see Figure 5.6) as it depends on the length of the 3-phase contact line. However, as shown and discussed by Schweizer [93], the heat transfer at the 3-phase contact line becomes more intense during bubble detachment compared to bubble growth. The heat flow per unit contact line length $Q_{\text{cl}}/l_{\text{cl}}$, called effective contact line heat flow in the following, and the contact line velocity are plotted in Figure 5.8. The values are sampled at particular times and plotted over the instantaneous bubble foot diameter at these times. The effective contact line heat transfer has an almost constant value during the bubble growth (negative contact line speed, receding contact line) while the value is rapidly growing during bubble detachment (positive contact line speed, advancing contact line). This effect is due to the transient conduction, i.e. the transient re-establishment of the superheated liquid layer. The phenomenon is related to the motion direction and speed of the contact line. It has been experimentally observed by Demiray and Kim [10], Myers and co-workers [82], Delgoshaei and Kim [9], Schweizer [93] and others. It should be noted that the increase of the effective contact line heat flow is not due to a change of the local wall superheat at the 3-phase contact line between the growing and the detaching situation but only due to transient conduction. It will be shown below that the changes of the local wall superheat at the 3-phase contact line are too small to cause such an increase of the local heat transfer. The numerical simulation of nucleate boiling allows to investigate the effect of transient conduction in detail which is done in the following.

The temperature and flow field in the vicinity of the 3-phase contact line are shown in Figure 5.9. The streamlines that respresent the local flow field are calculated from a relative velocity which is obtained by adding the contact line speed to the radial component of the velocity vector.

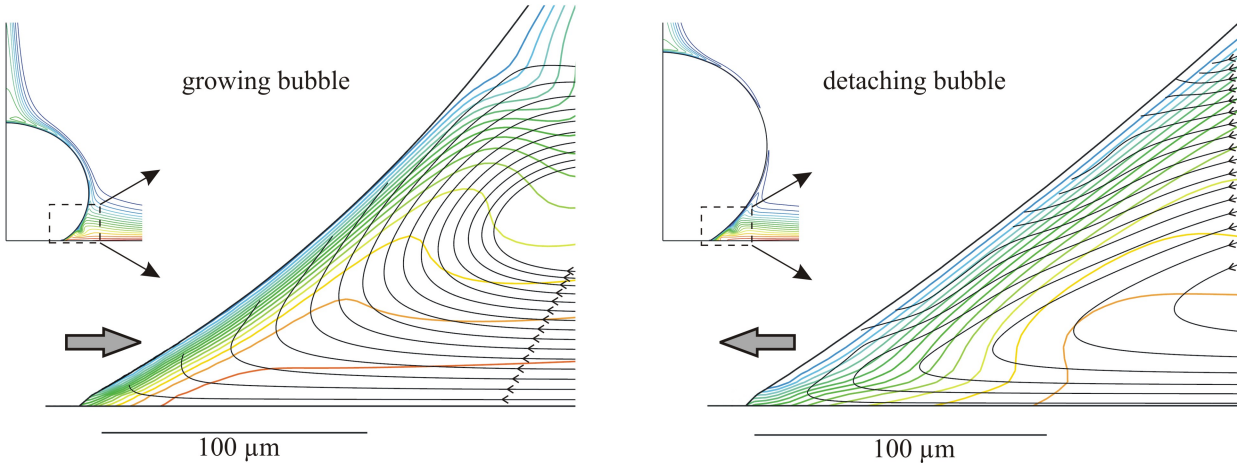

Figure 5.9: Temperature field (colored curves, distance: 1 K) and streamlines of relative velocity (black curves) in close vicinity of the 3-phase contact line during bubble growth (4 ms after nucleation) and detachment (10 ms after nucleation).

$$\vec{u}_{\mathrm{rel}} = \begin{pmatrix} u_{\mathrm{rel},r} \\ u_{\mathrm{rel},\phi} \\ u_{\mathrm{rel},z} \end{pmatrix} = \vec{u} + \begin{pmatrix} u_{\mathrm{cl}} \\ 0 \\ 0 \end{pmatrix} \tag{5.6}$$

The contact line speed is defined as the advancing speed of the 3-phase contact line. Hence, it has a positive value for an advancing contact line (detaching bubble) and a negative value for a receding contact line (growing bubble). The streamlines of the relative velocity in Figure 5.9 show that the motion of the 3-phase contact line and the no-slip condition at the heating wall lead to a vortex right next to the 3-phase contact line. The vortex is rotating clockwise in the case of a growing bubble and counterclockwise in the case of a detaching bubble. The fact that some of the streamlines end at or very close to the liquid-vapor interface is due to the evaporation which causes a liquid flow towards the interface.

The effect of the transient conduction is a result of two causes. First, the liquid-vapor interface moves away from the superheated liquid in the detaching case. This leads to a more streched temperature field compared to the case of a growing bubble. The isotherms have a much larger distance in the detaching case while they are very close one to another and close to the liquid-vapor interface in the growing case. Second, the above mentioned vortex leads to a further deformation of the local temperature field during detachment in such a way that colder liquid is carried down along the liquid-vapor interface towards the heater surface. Hence, there is an accumulation of liquid with less superheat close to the heater which intensifies the local heat transfer from the heater to the liquid. Although this increased heat transfer is not related to the microscale heat transfer at the 3-phase contact line (described in section 2.3), it is a consequence of the presence and motion of the 3-phase contact line. Therefore, the contact line heat transfer Q_{cl} which is discussed here and plotted in Figure 5.7 and Figure 5.8 is the sum of two heat transfer mechanisms which act at (microscale heat transfer) or in close vicinity of (transient conduction) the 3-phase contact line.

Local heat flux and heater temperature

In the preceding section, the heat flows corresponding to different heat tranfer mechanisms were analyzed and discussed. One of the main aims of the highly resolved experimental observations and also of the simulations within the present thesis is the determination of local temperature and heat flux fields at the heater. These results can easily be extracted from the simulation while the measurement is rather

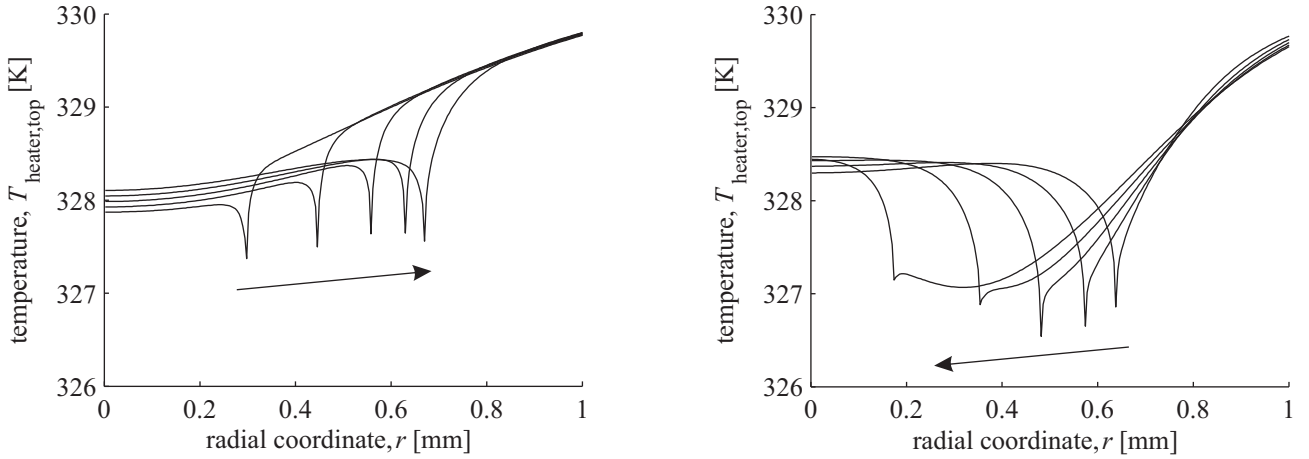

(a) Bubble growth (b) Bubble detachment

Figure 5.10: Temperature profiles at the solid-fluid interface during bubble growth and detachment. The time step between the different curves is 1 ms in the growing phase and 1.5 ms in the detachment phase. The arrows indicate the motion direction of the 3-phase contact line.

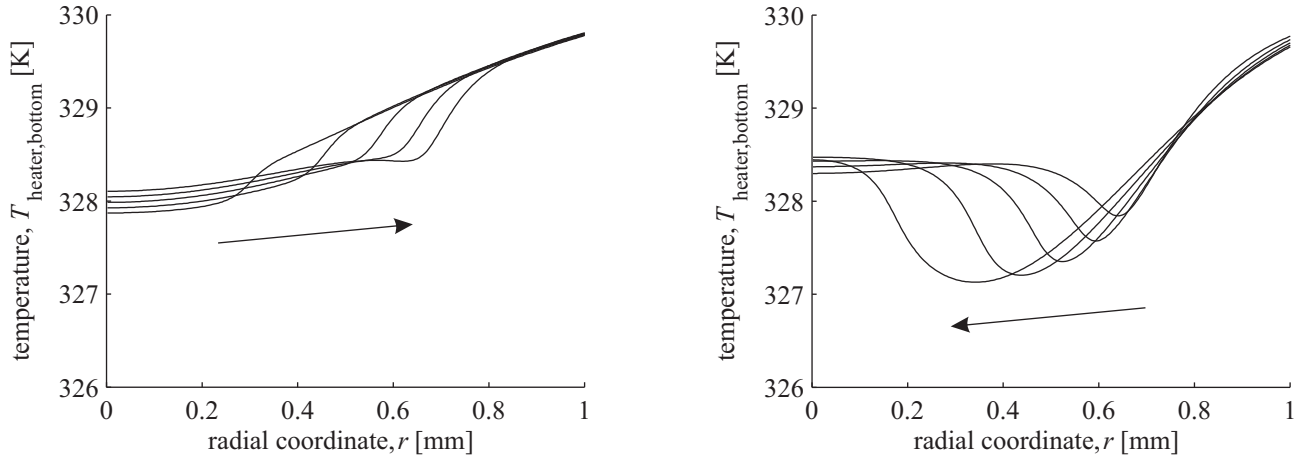

(a) Bubble growth (b) Bubble detachment

Figure 5.11: Temperature profiles at the back side of the heater during bubble growth and detachment. The time step between the different curves is 1 ms in the growing phase and 1.5 ms in the detachment phase. The arrows indicate the motion direction of the 3-phase contact line.

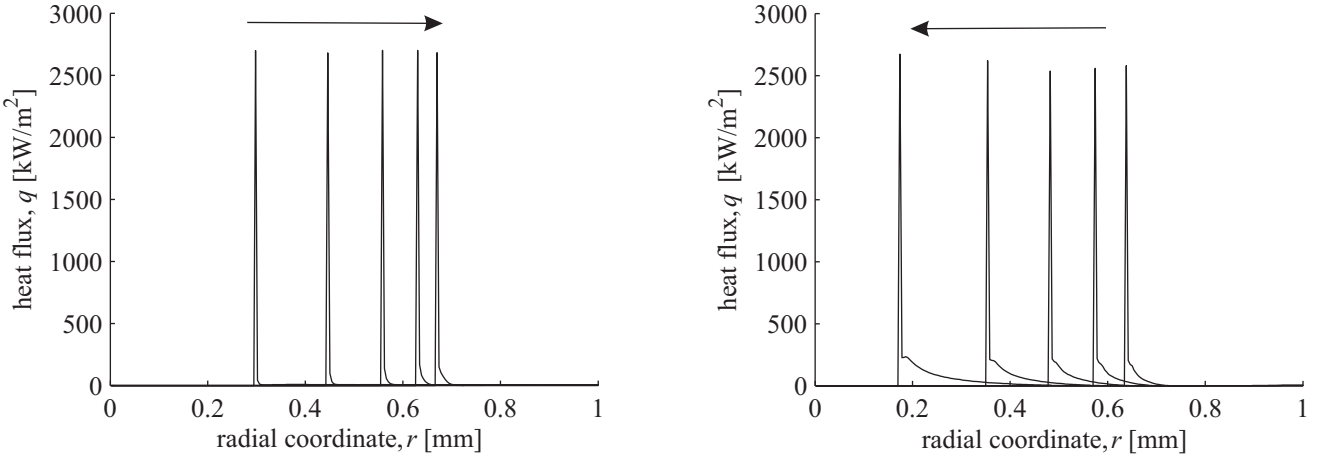

(a) Bubble growth (b) Bubble detachment

Figure 5.12: Heat flux profiles at the solid-fluid interface during bubble growth and detachment. The time step between the different curves is 1 ms in the growing phase and 1.5 ms in the detachment phase. The arrows indicate the motion direction of the 3-phase contact line.

complex. The radial temperature profile at the solid-fluid interface during bubble growth and detachment is shown in Figure 5.10(a) and Figure 5.10(b), respectively. An obvious temperature minimum can be observed at the position of the 3-phase contact line. The temperature drop at the 3-phase contact line measures around 1.5 K over a radial distance of only around 100 μm. The strong local cooling is a result of the high heat transfer rate at the 3-phase contact line. Another interesting feature of the temperature profile is the width of the temperature minimum. It can clearly be seen that the minimum is very sharp and narrow during bubble growth while it becomes much wider during bubble detachment. This effect is due to the above mentioned transient conduction[3], i.e. the local flow field close to the 3-phase contact line which transports liquid with less superheat towards the heater.

The radial temperature profile at the back side of the heating foil during growth and detachment is shown in Figure 5.11(a) and Figure 5.11(b), respectively. The sharp profile which is observed directly at the solid-fluid interface is not visible anymore. The profile is much smoother and the temperature minimum is not visible during bubble growth but can only be observed during bubble detachment. Due to the transient conduction, the temperature minimum at the solid-fluid interface is much wider during detachment than during bubble growth as shown above (see Figure 5.10). Therefore, the temperature minimum can also be captured on the back side of the heating foil during bubble detachment. The difference between the temperature at the 3-phase contact line and the temperature at some distance from the 3-phase contact line (on the liquid side) has a maximum value of around 1.5 K which is in excellent agreement to the experimental observations of Wagner and co-workers [120].

The radial heat flux profile directly at the solid-fluid interface is extracted from the simulation results and shown in Figure 5.12(a) and Figure 5.12(b). The sharp heat flux peak at the position of the contact line can clearly be seen. The heat flux reaches values of more than 2500 kW/m^2 at these positions which is far more than any maximum heat flux that has been measured experimentally. It should be noted that the actual maximum heat flux at the 3-phase contact line is even higher. However, it is not visible in the CFD simulation as the heat transfer at the 3-phase contact line predicted by the subgrid scale model is imposed as a uniform heat flux in the faces at the wall which contain a segment of the 3-phase contact line (see section 4.2.2). Therefore, the maximum heat flux that is observed in the CFD simulation is mesh dependend. However, the coupling between the subgrid scale model and the CFD simulation is

[3] The term *transient conduction* is established in the scientific community. However, the results which are presented here show that the phenomenon is governed by convection rather than conduction

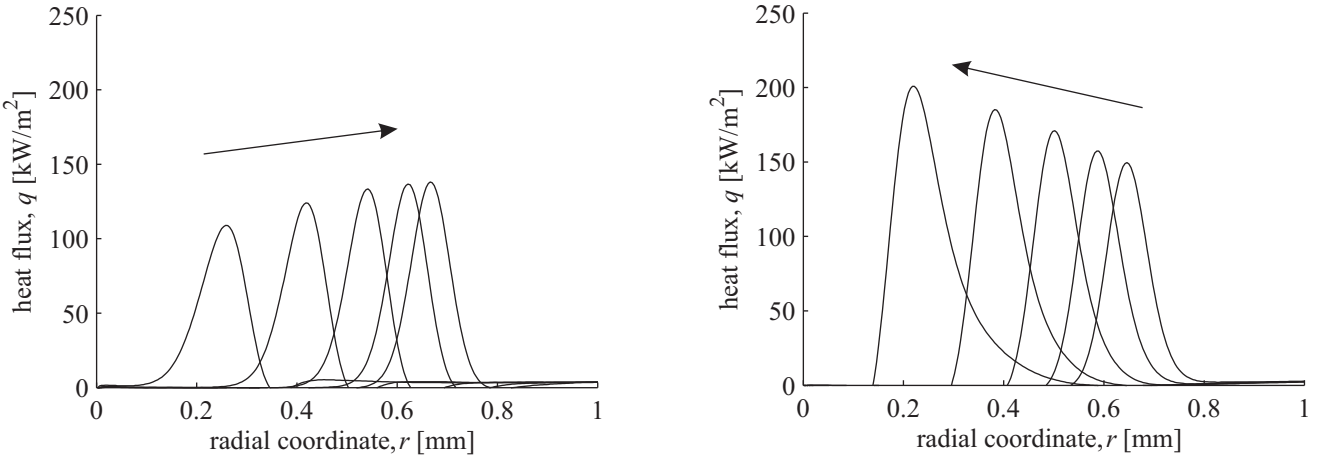

(a) Bubble growth (b) Bubble detachment

Figure 5.13: Heat flux profiles obtained by applying the experimental post-processing procedure according to Eq. (5.4) during bubble growth and detachment. The time step between the different curves is 1 ms in the growing phase and 1.5 ms in the detachment phase. The arrows indicate the motion direction of the 3-phase contact line.

done in such a way that the integral heat flows are conserved. The local correction of the heat flux by the subgrid scale model is also the reason why the heat flux profiles in Figure 5.12(a) and Figure 5.12(b) are not smooth but have a single maximum value at one point which is much larger than the heat flux at any other point. As mentioned above, the calculation procedure of the heat flux in the experiment incorporates the damping of the peak due to the heat conduction within the heating foil. Inspite of the fact that the heat flux at the solid-fluid interface cannot be directly compared to experimental data, the heat flux profiles in Figure 5.12(a) and Figure 5.12(b) reveal two interesting aspects. First, the maximum value of the heat flux peak is almost constant during bubble growth and detachment. This can be expected as the maximum value of the heat flux is a result of the coupling between the subgrid scale model for the contact line evaporation and the CFD simulation. On the scale of the subgrid scale model for the contact line evaporation, contact line motion is not taken into account and the micro scale heat transfer at the 3-phase contact line only depends on the wall superheat. The latter changes during bubble growth and detachment, but only by around 1 to 1.5 K which is less than 10 % of the wall superheat (approximately 15 K). Therefore, there is not much impact on the maximum heat flux in the CFD simulation. The second interesting aspect is revealed by comparing the heat flux profiles during bubble growth and detachment in Figure 5.12(a) and Figure 5.12(b), respectively. Although the maximum values are almost the same, an important qualitative and quantitative difference can be observed on the right side of the peak at the 3-phase contact line. During bubble detachment, there is a region with a length of around 100 μm at the liquid side of the contact line where a rather large heat flux of around 100 to 200 kW/m^2 can be observed. This local increase of the heat transfer from the heater into the liquid results from the above mentioned transient conduction phenomenon which acts only during bubble detachment and not during bubble growth.

In order to obtain heat flux profiles that can be compared to the measurement data, the experimental data reduction procedure (calculation of the heat flux field from infrared thermography measurements) is mimicked. Hence, the temperature field on the back side of the heating foil is extracted from the simulation and used to calculate the heat flux profile. The results during bubble growth and detachment are shown in Figure 5.13(a) and Figure 5.13(b), respectively. The calculated heat flux profiles are much smoother compared to the heat flux extracted directly at the solid-fluid interface. The heat flux profile at the maximum bubble foot diameter has a peak value of around 140 kW/m^2 which is in good agreement

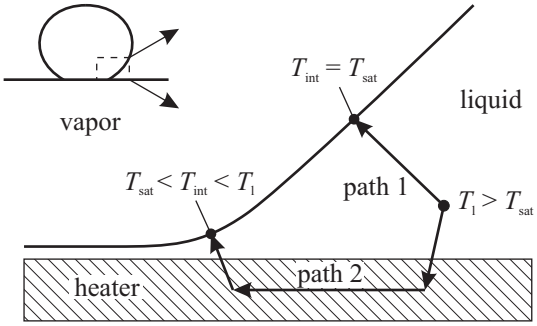

Figure 5.14: Sketch of the near contact line region explaining the phenomenon of heat flux reversal.

to the value of around 150 kW/m^2 that is reported by Wagner and co-workers [120]. However, the heat flux peak in the experiment of Wagner and co-workers [120] is only visible during bubble growth and decays rapidely when the bubble foot diameter reaches its maximum value and during detachment. The simulation results show a different behavior. The heat flux peak grows slightly during bubble growth from around 120 to 140 kW/m^2. During bubble detachment, the heat flux peak grows significantly from 140 up to 200 kW/m^2. Again, this effect can be explained by the transient conduction phenomenon that acts very close to the 3-phase contact line within the liquid phase. The growing heat flux peak during bubble detachment which is observed in the simulation is the only qualitative difference between the simulation results and the experimental data of Wagner and co-workers [120]. Possible explanations for this deviation are given below. However, it should already be noted that the increase of the heat transfer during bubble detachment predicted by the simulation is in excellent agreement to other experimental works (e.g. Schweizer and Stephan [94], Demiray and Kim [10], Myers and co-workers [82] and Delgoshaei and Kim [9]) and also to another work of Wagner and Stephan [119] in which the authors used a heating foil with a thickness of only 20 μm instead of 50 μm. Further, the intensification of the heat transfer during the advancing motion of a 3-phase contact line (wetting) is also observed in experimental investigations of meniscus evaporation [38, 39] and it is the topic in a recent publication of Kunkelmann and co-workers [57].

The highly efficient heat transfer at the 3-phase contact line can under certain circumstances lead to the phenomenon of heat flux reversal, i.e. a local heat flux from the fluid back into the heater. The phenomenon has already been observed experimentally in 1982 by Ilyin and co-workers [40]. An excellent explanation for the heat flux reversal is given by Mitrovic [71, 72] and the effect could be numerically predicted by aus der Wiesche [3]. In principal, the heat flux reversal is the result of the high local heat transfer coefficient at the 3-phase contact line and the ratio of the thermal transport properties of the liquid and the solid. Under certain circumstances which are described in detail by Mitrovic [71, 72], the heat transfer from the liquid into the wall, along the wall towards the 3-phase contact line, back into the liquid and through the thin film to the liquid-vapor interface (path 2 in Figure 5.14) is associated with a smaller heat resistance than directly through the liquid to the liquid-vapor interface (path 1 in Figure 5.14). As the heat is transferred mostly along the path with the lowest heat resistance, there can be a local heat flow from the liquid back into the heater. The magnitude of the radial heat flux profile at different instances during bubble growth and detachment in a logarithmic scale is shown in Figure 5.15. The results are taken from the same bubble cycle for which the heat flux profiles are shown in Figure 5.12(a) and Figure 5.12(b). The maximum value of the heat flux at the 3-phase contact line can clearly be seen. The curves seem to start at this maximum value because the heat flux at the solid-vapor interface on the left side of the 3-phase contact line is zero and is therefore not visible in this logarithmic plot. At the solid-liquid interface to the right of the 3-phase contact line, there is a very obvious minimum of the heat flux which can even be at negative values. During bubble growth, only a minimum of the heat flux can be observed while the value of the heat flux is still positive. Hence, no heat is transferred from the liquid into the heater. However, the heat transfer from a position within the

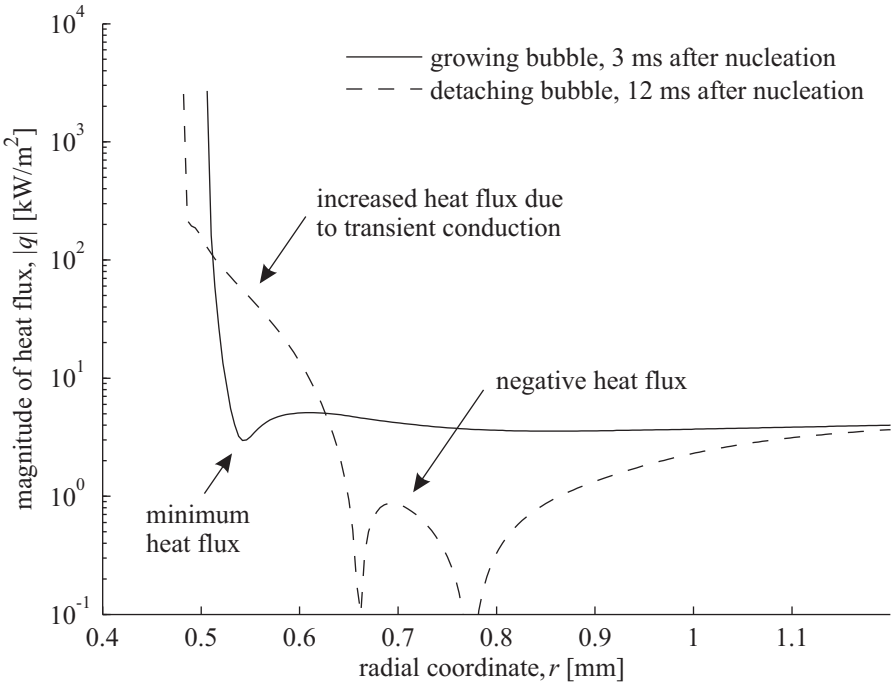

Figure 5.15: Magnitude of the local heat flux during bubble growth and detachment on a logarithmic scale.

solid along the heater towards the 3-phase contact line is preferred to the heat transfer into the liquid. This causes a local minimum of the heat flux into the liquid. During bubble detachment, negative values of the heat flux can be observed. Hence, the above described minimum becomes more pronounced and develops into a negative heat flux. In this situation, the heat transfer from a position within the liquid back into the heater and then through the heater to the 3-phase contact line is preferred to the heat transfer to the liquid-vapor interface (see Figure 5.14). The phenomenon of heat flux reversal is not very pronounced in the simulation presented here. The reason for this is the fact that the heater is made of steel which has a poor thermal conductivity compared to copper or aluminum. The higher the thermal conductivity of the heater material compared to the heat conductivity of the liquid, the easier heat can travel into and through the heater towards the 3-phase contact line rather than travel directly through the liquid towards the liquid-vapor interface. For such investigations, it is of course required to solve the heat transfer not only in the fluid domain but also in the solid domain. The assumption of a constant temperature at the solid-fluid interface (e.g. used by Son and co-workers [100]) implicitly avoids the occurance of a heat flux reversal or even of a minimum heat flux next to the 3-phase contact line.

In addition to the heat flux reversal, the curves in Figure 5.15 also show the increased heat flux next to the 3-phase contact line due to transient conduction during bubble detachment. When comparing the decay of the heat flux next to the maximum value at the 3-phase contact line, it can clearly be seen that the decay is less rapid during bubble detachment than during bubble growth. During bubble growth, the heat flux drops immediately down to the minimum while there is an approximately 100 μm wide region where the heat flux reaches values of around 100-200 kW/m^2 in the detaching situation.

5.1.3 Influence of mesh resolution, natural convection and contact angle

In order to check that the results are not dependend on the mesh resolution, simulations were performed on three different meshes. The mesh in region 1 (at the position where the bubble grows, see Figure 5.1) has a mesh resolution of 4 μm on the fine mesh, 8 μm on the medium mesh and 16 μm on the coarse

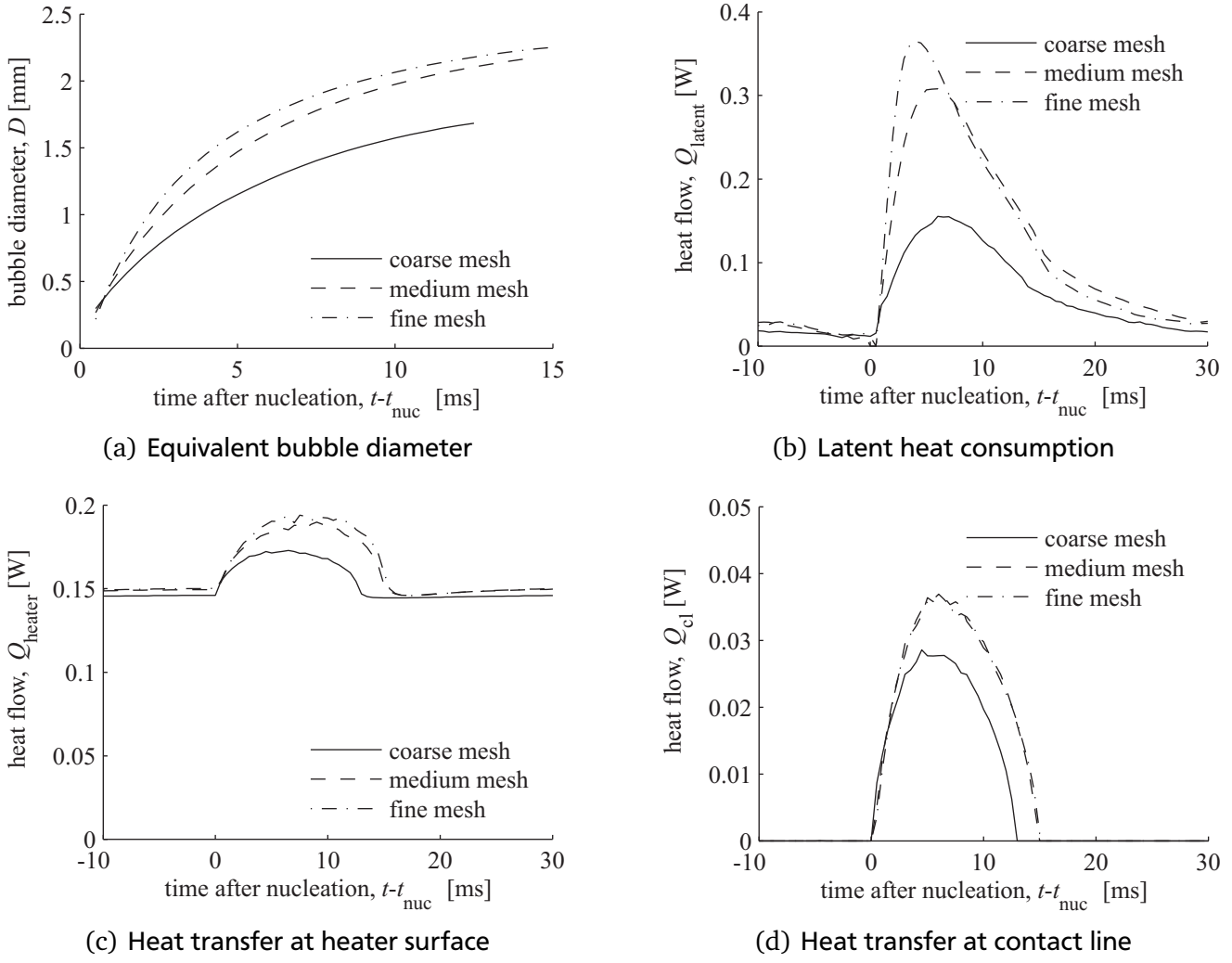

(a) Equivalent bubble diameter

(b) Latent heat consumption

(c) Heat transfer at heater surface

(d) Heat transfer at contact line

Figure 5.16: Simulation results on bubble growth and heat transfer obtained on a coarse ($\Delta x = 16\,\mu$m), medium ($\Delta x = 8\,\mu$m) and fine ($\Delta x = 4\,\mu$m) mesh. The contact angle is $\theta = 30°$ in all cases.

mesh. The results for a particular bubble nucleating around 1 s after the initialization of the simulation (i.e. almost periodic regime, see Figure 5.2) are shown in Figure 5.16. The development of the bubble diameter with time (see Figure 5.16(a)) reveals that the mesh resolution of 16 μm seems to be too coarse for an accurate prediction of the rate of phase change. In particular, the very fast growth in the beginning (0 to 5 ms) is not simulated accurately. There is also a difference between the medium and the fine mesh but it is much smaller than the difference between the coarse and the medium mesh. The underprediction of the first period of bubble growth is confirmed by the temporal development of the latent heat flow. As discussed above, the curves show a sharp rise to a maximum value and a slow decay after the maximum. The results obtained on the 2D test case in section 4.4.2 show that a fine mesh is required to correctly capture the thermal boundary layer in the vicinity of the liquid-vapor interface. This is confirmed by the rather inaccurate results that are obtained here on the coarse mesh. The total heat transfer from the heater surface Q_{heater} in Figure 5.16(c) and the heat transfer at the 3-phase contact line in Figure 5.16(d) also show an underprediction for the simulation on the coarse mesh. As for the development of the bubble diameter, the difference between the medium and the fine mesh is rather small compared to the difference between the coarse and the medium mesh.

The major outcome of the comparative simulations on different meshes is that the results converge with increasing mesh resolution. The results also show that an additional mesh refinement on the finest

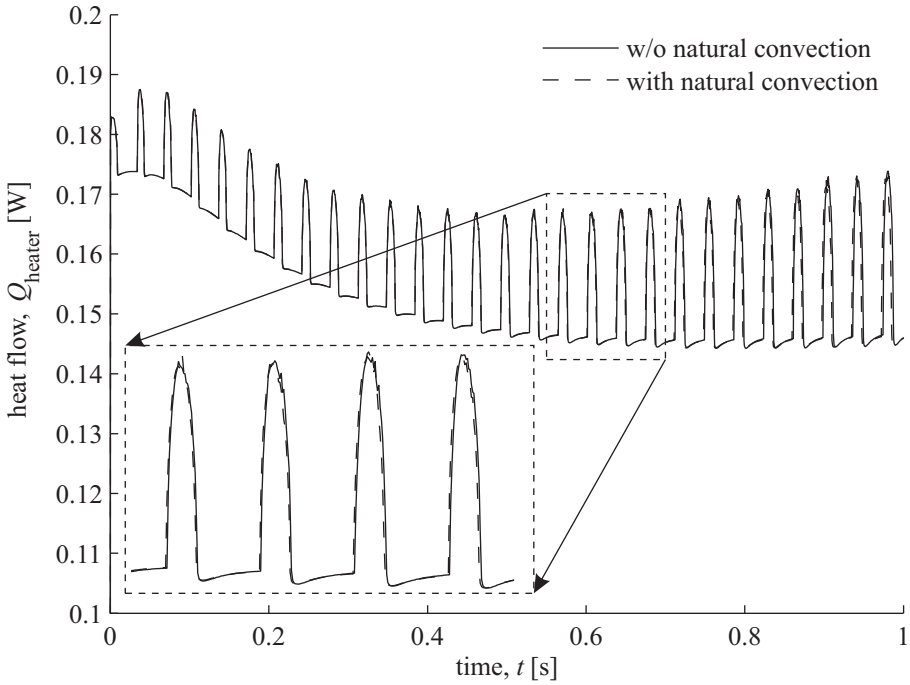

Figure 5.17: Comparison of the heat transfer at the heater surface obtained from simulations with and without natural convection. Case with a contact angle of $\theta = 30°$ and a mesh resolution of $\Delta x = 16\,\mu$m.

mesh which is used here would probably still lead to a quantitative change in some of the results. No further refinement was performed however, as the computational effort would be too high. The simulation of a single bubble cycle would be possible on an even finer mesh but the difficulty lies in the simulation of many bubble cycles which lead to very long computation times. In spite of the fact that some of the results are still mesh dependent, the differences are already very small. The difference in total heat transfer from the heater integrated over a whole bubble cycle is only around 2 % between the medium and the fine mesh while it is around 9 % between the coarse and the medium mesh. Applying a *Richardson extrapolation* (see Schäfer [91]), it can be shown that the difference between the integrated heat flow obtained on the finest mesh used here and the mesh independend solution obtained on an infinitely refined mesh is around 0.6 %. Hence, the heat transfer can be predicted with sufficient accuracy on the finest mesh which is used here.

As discussed in section 2.1 all material properties are assumed to be constant. Consequently, the density does not depend on the temperature and natural convection is not taken into account. However, the liquid in the vicinity of the heating wall can be significantly superheated as it is shown in Figure 5.4. In order to check the influence of natural convection on the overall heat transfer, a comparative simulation is performed on the coarse mesh with a contact angle of $\theta = 30°$. It is shown above that the coarse mesh is not capable of producing very accurate results. Nevertheless, the qualitative bubble dynamics and heat transfer is correctly predicted. Thus, the coarse mesh should not be used for a detailed analysis but it can well be used for a comparative simulation. In this particular simulation, the *Boussinesq approximation* (see Turner [111]) is used to include the buoyancy effect of density differences within the fluid. As the density differences are small, the continuity equation (2.9) remains unchanged while a source term is added to the right hand side of the momentum equation (2.10). The outcome of the comparison between the simulations with and without natural convection is that the influence of natural convection is negligible. The total heat flow at the heater surface in both cases is shown in Figure 5.17. It can clearly be seen that there is almost no difference between the curves obtained from the simulations with and without natural convection. This finding is in agreement to the expectations as the tempera-

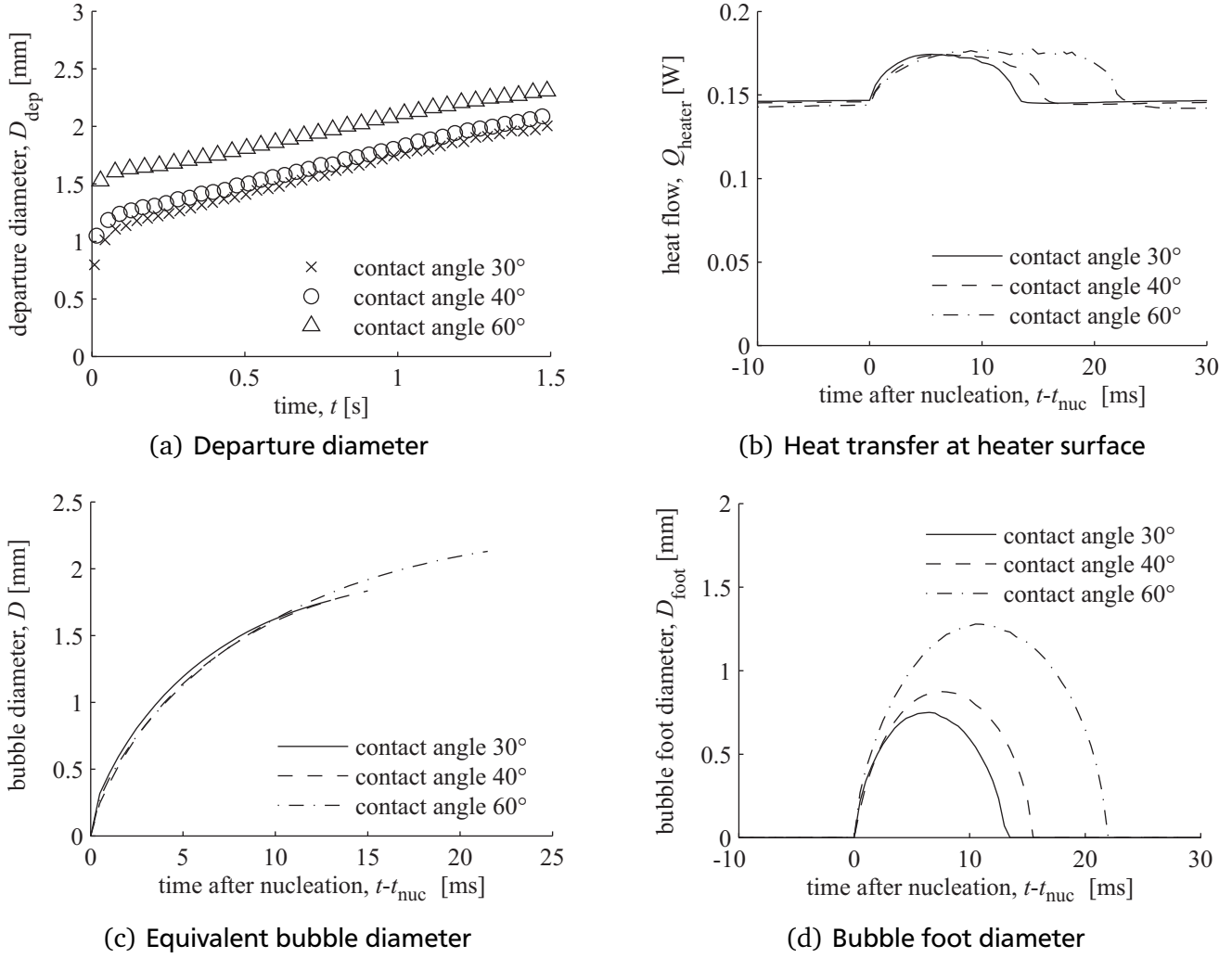

(a) Departure diameter

(b) Heat transfer at heater surface

(c) Equivalent bubble diameter

(d) Bubble foot diameter

Figure 5.18: Simulation results on bubble growth and heat transfer obtained for contact angles of $\theta = 30°$, $\theta = 40°$ and $\theta = 60°$. The coarsest mesh with a resolution of 16 μm is used in all cases.

ture dependence of the densities is much smaller than the density difference between liquid and vapor phase. Hence, the buoyancy force that acts on the vapor bubble is much larger than any buoyancy force within either of the pure phases. The dynamic growth and detachment of the bubbles causes a forced convection that is much stronger than the natural convection.

The contact angle is one of the input parameters for the simulations. The results that are discussed in detail during the preceding section were obtained with a contact angle of $\theta = 30°$. In principal, HFE-7100 is perfectly wetting with a very small contact angle of far below 10°. However, this is only valid under isothermal conditions without evaporation. If the wall is heated above saturation temperature, the resulting evaporation preempts complete wetting and can lead to a comparably large contact angle. This effect has been studied by Elbaum and co-workers [16] and is subject of ongoing experimental and theoretical research. In addition, the contact angle can also strongly depend on the motion direction and speed of the 3-phase contact line. Unfortunately, the complex interactions between wetting characteristics, hydrodynamics and heat transfer are not yet completely understood. Therefore, the contact angle must be prescribed in the simulation. For the sake of simplicity, a constant value is chosen. The choice of $\theta = 30°$ is based on the microscale model for the heat transfer at the 3-phase contact line[4] which is described in section 2.3. In order to check the influence of the contact angle on the simulation

[4] The microscale model predicts a contact angle of 37° for HFE-7100 at 500 mbar at a wall superheat of 15 K.

results, simulations with different contact angles (30, 40 and 60°) are performed. As mentioned above, a high mesh resolution is required to obtain accurate results. However, the high level of mesh resolution in combination with the fact that a large number of bubble cycles must be simulated leads to very long computation times. Therefore, the comparative studies for the investigation of the influence of the contact angle are performed on the coarse mesh with a mesh resolution of 16 μm. The simulations are not accurate enough for a detailed analysis of the heat transfer mechanisms, but are sufficient to check the influence of the contact angle on the simulation results. The development of the departure diameter during several bubble cycles is shown in Figure 5.18(a). It can clearly be seen that a larger contact angle leads to an increased bubble departure diameter. This tendency is expected as the attaching forces at the 3-phase contact line are stronger for larger contact angles and a larger buoyancy force, i.e. a larger bubble volume, is required to detach the bubbles from the heater surface. Already in 1935, Fritz [20] has incorporated this tendency into his well known correlation for the departure volume of vapor bubbles. The equivalent departure diameter which can be derived from his correlation is proprotional to the contact angle ($D_{\mathrm{dep}} \propto \theta$). Thus, the correlation predicts that the departure diameter is doubled if the the contact angle is increased from 30° to 60°. However, the simulation predicts an increase of only around 16 % between these two cases. Most probably, the equilibrium force balance which is applied by Fritz [20] is not sufficient to completely describe the bubble detachment process.

The total heat flow at the heater surface during the complete cycle of a particular bubble nucleating around 1 s after the initialization of the simulation (i.e. almost in the periodic regime, see Figure 5.2) is shown in Figure 5.18(b). As expected, the constant value of the heat transfer when no bubble is attached to the heater is independend of the contact angle. Furthermore, the maximum value of the heat flow when the bubble grows on the heater depends only little on the contact angle. The only major difference between the curves is the growth time of the bubble. The curves for larger contact angles drop back to the constant value much later. In other words, the bubbles are attached to the heater for a longer period of time. A comparison of the growth of the bubble diameter of the particular bubble is shown in Figure 5.18(c). Again, it can be seen that the departure diameter increases with increasing contact angle which is due to the stronger attaching forces and the larger bubble volume that is required to detach the bubble from the heater surface. The curves are very similar one to another, in particular during the first growth phase. Thus, the bubble with a larger contact angle does not grow faster than a bubble with a smaller contact angle but only departs later. More time is needed to reach the bubble volume which is required to detach the bubble from the heater surface. As expected, the contact angle has a large influence on the bubble foot diameter. Its development is shown in Figure 5.18(d). The maximum value of the bubble foot diameter is much larger for the contact angle of 60° compared to the contact angle of 30°. Furthermore, the longer growth time during which the bubble is attached to the heater is also visible in this plot.

It is difficult to summarize the outcome of this investigation regarding the influence of the contact angle. On the one hand, it has become obvious that the contact angle has a strong influence on the simulation results. Therefore, the value of the contact angle which is an input parameter of the simulation must be chosen with care and should be based on experimental data or physical considerations. On the other hand, it is also obvious that the qualitative outcome of the simulation depends only little on the contact angle. The principal qualitative features of the bubble dynamics and of the heat transfer are captured independent of the contact angle. This is valid in a range between 30° and 60° which covers the contact angles that can be expected for HFE-7100 under evaporating conditions.

5.1.4 Discussion of simulation and measurement uncertainties

The level of agreement that could be achieved between simulation and experiment is very satisfying. Almost all qualitative findings observed experimentally by Wagner and co-workers [120] are reproduced by the simulation and there is also a lot of quantitative agreement. Nevertheless, some differences

between the simulation and the experiments are also found. In the following, several simulation and measurement uncertainties are discussed as possible sources of the differences between simulation and experiment. Regarding the simulation, the most dominant uncertainty is the modeling of the contact angle. Here, a single constant value is used while the contact angle might in reality be a function of contact line motion and of the local wall superheat. Further, there is no reliable measurement data on the wetting characteristics of HFE-7100 under evaporating conditions. In the results presented above, it is shown that the value of the contact angle influences mainly the departure diameter and the growth time of the bubbles. However, the fact that the departure diameter is overpredicted by the simulation does not necessarily mean that the choice of the contact angle is wrong. We will see in the following that there are several uncertainties about the boundary conditions of the experiment which most probably have an even larger influence than the contact angle.

Wagner and co-workers [120] state that the temperature of the bulk liquid above the heater is very close to saturation conditions. The uncertainty of the temperature measurement in the bulk liquid is given as 1.2 K. The assumption that the bulk liquid is at saturation temperature is incorporated into the boundary conditions of the simulation. However, already a subcooling of the order of the measurement uncertainty (1.2 K) could have an effect on the results and would decrease the departure diameter (see Wu and Dhir [130]). Further, the electrodes which supply the electric current into the heating foil are cooled to avoid parasitic boiling at any place other than the artificial nucleation site. The cooling of the electrodes could lower the mean heater temperature and hereby also change the thermal layer in the liquid close to the heater. As discussed above, the heat supply to the bubble during the first phase of the growth is contributed mainly from the superheated liquid layer. Therefore, the cooling of the electrodes can also lead to a smaller departure diameter. The measurement error on the bulk liquid temperature and the cooling of the electrodes are possible explanations for the too high departure diameter predicted by the simulation. Furthermore, the cooling of the electrodes could induce a natural convection vortex above the heating foil, i.e. the liquid might rise above the artificial nucleation site and flow back towards the heating foil at the position of the electrodes. Such a liquid flow would also lead to an earlier departure of the bubbles and therefore to a smaller departure diameter compared to a situation without any cooling of the heating foil.

The only qualitative difference between the simulation and the experiment of Wagner and co-workers [120] is the development of the heat flux peak during bubble detachment. The simulation predicts a growing peak during bubble detachment while the peak vanishes during detachment in the experiment. However, the simulation results are confirmed by a number of other experimental observations [9, 10, 82, 93, 94]. The different development of the heat flux peak during detachment of a bubble is most probably due to the measurement technique applied in the experiment of Wagner and co-workers [120]. The exposure time of the infrared camera used in the experiment is 1 ms (frame rate of 1000 Hz). During this time, the 3-phase contact line can move by 100 to 300 μm, depending on the contact line speed. Hence, independend of the spatial resolution of the camera, the infrared images are smeared due to the limited temporal resolution. Together with the signal damping in the heating foil due to lateral heat conduction this could lead to a non-detection of the heat flux peak during detachment. The peak might still be visible in the experiment during bubble growth as the transient cooling of the heating foil is detected in this phase while the detachment phase could be dominated by heat conduction rather than transient cooling. On the same setup, Wagner and Stephan [119] used heating foils with a thickness of 20 μm (less temperature difference between top and bottom side of the heating foil) and detected a significant heat flux peak during detachment. The simulation results are not averaged within the exposure time, but provide instantaneous temperature fields. This could possibly explain why the peak is captured in the simulation but not in the experiment. The above mentioned experiments in which a growing heat flux peak during detachment could also be observed are either based on a different measurement technique for the wall heat flux [9, 10, 82] or performed using thinner heating foils in reduced gravity conditions [93, 94] during parabolic flights. Possibly, the slower bubble growth in reduced gravity and the resulting

enhancement of the temporal and spatial measurement resolution enable the measurement of the heat flux peak during detachment while it could be totally or partially masked in earth gravity experiments.

5.2 Bubble merger

The interaction between bubbles growing at neighboring nucleation sites depends on the active nucleation site density. At moderate heat fluxes, bubbles grow at isolated nucleation sites and do not interact with each other. In the preceding section, it could be shown that the boiling model is capable of predicting the bubble dynamics and heat transfer associated with a single bubble at a very satisfying level of accuracy. As the heat flux increases, more and more nucleation sites become active. When two bubbles grow at nucleation sites which are located at a distance of not more than the bubble departure diameter, the phenomenon of bubble merger can occur. There are several modes of bubble merger. Depending on the time shift between the nucleation of the bubbles and eventually their different growth rates, one of the bubbles might already be detached while the second bubble is still attached to the surface leading to a diagonal bubble merger. If the bubbles grow almost identically, a lateral merger can occur. The third mode is a vertical bubble merger when two bubbles growing one after the other at the same nucleation site merge. This can happen if the waiting time between two consecutive bubbles becomes very short. Here, a lateral bubble merger is simulated in order to investigate some of the phenomena that are observed experimentally by Wagner [117] as well as Schweizer and Stephan [94]. Wagner [117] performed experiments on ground, while Schweizer and Stephan [94] observed boiling in micro gravity. In both experiments, lateral bubble mergers could be observed and the local heat flux distribution could be calculated from infrared thermography measurements on the backside of the thin foil heaters. The procedure for the calculation of the heat flux is the same which is used for the single bubble experiment by Wagner and co-workers [120] and which is described in the preceding section. A very interesting finding of the experimental investigations is the formation of a small droplet inside the merged bubble. The droplet could be detected due to the high evaporation rates at its 3-phase contact line. The calculated heat flux fields show a large ring of high heat flux corresponding to the 3-phase contact line of the bubble and a second ring of high heat flux within the large ring. The second ring of high heat flux can only be explained by the existence of a droplet inside the merged bubble. Unfortunately, the shape and formation of the droplet itself cannot be seen and investigated experimentally but only the high heat flux which is caused by its existence. Numerical simulations of a lateral bubble merger are performed for two reasons. First, the simulations shall show if the boiling model correctly predicts the bubble dynamics and the formation of the droplet. Second, if the bubble dynamics and the formation of the droplet are correctly predicted, the simulation results can be further examined in order to understand the formation process of the droplet.

5.2.1 Simulation setup and input parameters

Wagner [117] used a thin steel heating foil (thickness 50 μm) with two artificial nucleation sites for the investigation of lateral bubble mergers. The distance between the nucleation sites is 1 mm. The working fluid is HFE-7100 at different pressures. The probability and thereby the frequency of bubble mergers is strongly dependend on the departure size of the bubbles which itself depends on the pressure. For the simulations presented here, the material properties of HFE-7100 at 500 mbar are used (see appedix A for material properties of fluid and solid). As the bubbles grow almost identically in the case of a lateral merger, the simulation was performed only for one half of a bubble using two planes of symmetry (see Figure 5.19). In contrast to the single bubble simulations presented in section 5.1, the simulation does not run for several bubble cycles but only for one merger event. Initially, a small vapor bubble with a radius of $R = 0.1$ mm is placed on the surface of the heater at a distance of 0.5 mm to the right symmetry plane in Figure 5.19 which corresponds to the distance between the nucleation site in the experiment.

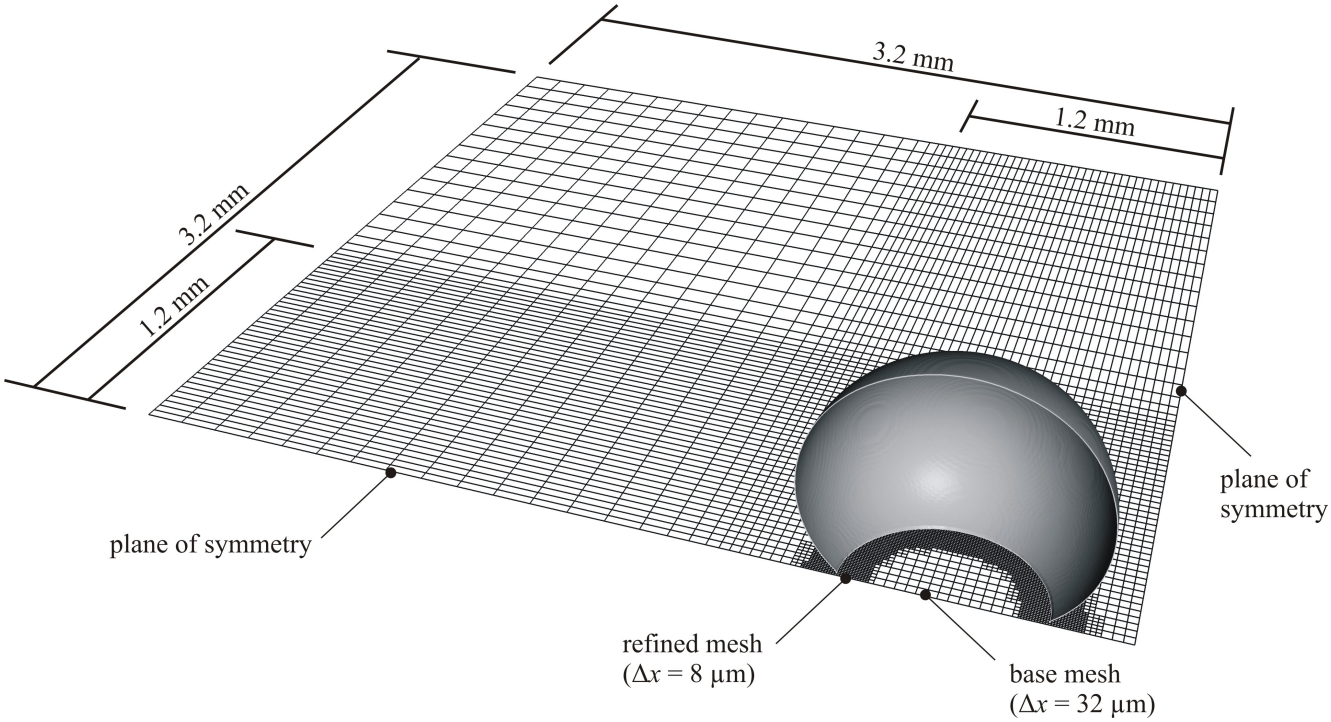

Figure 5.19: Computational domain for the simulation of a lateral bubble merger. The wireframe shows the cell faces at the solid-fluid interface. Adaptive mesh refinement is used around the liquid-vapor interface to enhance the local mesh resolution.

The heating wall is initialized with a constant superheat of 15 K and the initial thermal boundary layer is assumed to be linear with a thickness of 0.5 mm. As it was also the case for the single bubble simulations, the choice of the initial conditions is arbitrary. In the case of the single bubble simulation, the results are not dependent on the initial conditions after several periodic bubble cycles and therefore the problem of the arbitrary initial conditions could be overcome. In the case of the bubble merger, the experimental data is not periodic. The mergers occur randomly with a certain probablity in a chaotic process. Thus, the initial conditions for the simulation are not known and the simulation results depend on the choice of the initial wall and liquid temperature field. Nevertheless, the choice of the initial conditions will certainly not influence the qualitative results. Further, the bubble dynamics during the merger event are much more influenced by the topological change of the liquid-vapor interface than by the growth rate due to evaporation. The bubble shape during the merger and the formation of the droplet inside the merged bubble can be compared in detail to the experimental data. However, in contrast to the single bubble simulations, a precise quantitative comparison of the bubble departure diameter, its growth time as well as local temperature and heat flux profiles is not possible due to the arbitrarity of the initial conditions.

The simulations are performed on a 3D mesh. Adaptive mesh refinement is used in a band of ten cells around the liquid-vapor interface. The mesh and the local refinement are illustrated in Figure 5.19. The base mesh without any refinement has a minimum cell size of 32 μm within a core around the nucleation site. At a horizontal distance of 1.2 mm to the planes of symmetry, a growing cell size is used to reduce the number of cells. A similar growth of the cell size is also applied in vertical direction, beginning at a distance of 1.6 mm from the heater. Two levels of mesh refinement are applied, leading to a local minimum mesh resolution at the liquid-vapor interface of 8 μm. The high mesh resolution is mainly required very close to the heater where the liquid is highly superheated and strong temperature gradients can be expected. Therefore two levels of refinement are only applied where the liquid-vapor interface is not more than 1 mm away from the heater surface. If the liquid-vapor interface has a distance

of more than 1 mm to the heater surface, only one level of refinement is applied. Due to the local mesh refinement at the liquid-vapor interface, the total number of cells is a function of the bubble size. Initially, the mesh has around 400,000 cells. As the bubble grows, the total number of cells approaches 1 million. As for the single bubble simulations presented in the preceding section, the contact angle is one of the input parameters which can be expected to have a strong influence on the simulation results. Here, a parameter study is performed to check the influence of the contact angle on the bubble dynamics during the merger and on the formation of the droplet inside the merged bubble. Contact angles of $\theta = 20°$, $\theta = 40°$ and $\theta = 60°$ are used.

It should be noted, that the simulation of bubble merger or breakup with a *Volume-of-Fluid* (VOF) method can be mesh dependend. When two liquid-vapor interfaces approach each other, they will suddenly merge as soon as they have come as close as the size of a cell. In reality, a stable thin liquid film can be created between the bubbles and strong, short-range intermolecular forces can preempt the merger. The occurance of this situation depends mainly on the size of the bubbles and their inertia as well as the surface tension as discussed in detail by Wagner [117]. Such a behaviour cannot be captured within a standard VOF formulation. An approach to implement the short-range forces into a VOF framework is presented by Hardt [27]. Here, such an approach was not implemented as the emphasis of the simulation is on the bubble dynamics after the merger and not on the question whether or not a merger will occcur.

5.2.2 Major findings

The bubble shape during the growth of the bubbles, the merger event and the departure of the merged bubble is shown in Figure 5.20 for a contact angle of $\theta = 40°$. Both bubbles are shown although only one of them is actually simulated as mentioned above. From the moment of nucleation to around 5.7 ms the bubbles grow without having any visible influence on each other. However, if the results are analyzed in detail, one can see that there is a small influence. Rather than growing directly above the nucleation site, the bubble centers move slightly away from each other. At 5.7 ms the bubbles have grown big enough to touch each other and they immediately merge by generating a small circular vapor bridge from one bubble to the other. Due to the very high curvature of the liquid-vapor interface at the perimeter of the vapor bridge, the circular opening between the bubbles grows rapidely (see Figure 5.21). In a very short time of less than 0.5 ms the vapor bridge grows to a considerable size reaching almost down to the heater surface. In the following images of the sequence, capillary waves can be seen which travel along the liquid-vapor interface. These waves originate from the position where the liquid-vapor interfaces merge and cause a large excitation of the interface motion. Once the waves have run all the way along the liquid-vapor interface, they are reflected at the outer part of the bubble and move back inwards. The barrel-like shape and the lemon-like shape that can be seen at 7.9 ms and 10.2 ms, respectively, are typical for bubble or droplet mergers. Siedel and co-workers [97] observed very similar bubble shapes and capillary wave motion during experimental investigations of lateral bubble mergers. Ata [2] investigated the dynamics of merging air bubbles with and without particles deposited on the liquid-gas interface and also observed very similar bubble shapes and capillary wave motion. As mentioned above, the vapor bridge between the bubbles does not reach all the way down to the heater surface. A small amount of liquid is trapped underneath the vapor bridge. At 10.2 ms one can see that the shape of this trapped liquid volume corresponds almost to a truncated cylinder. Although the bubbles have already merged, their vapor patches on the heater surface are still separated from each other by the trapped liquid. In principal, the trapped liquid is pushed sideways into the bulk liquid by surface tension forces (see Figure 5.22). However, this process does not seem to be fast enough. The trapped liquid volume becomes unstable and pinches of the bulk liquid. At the moment when the vapor patches merge (between 11.2 and 11.7 ms) a considerable amount of trapped liquid remains within the merged vapor patches. Thus, the generation of the liquid droplet sitting inside the merged bubble which was observed

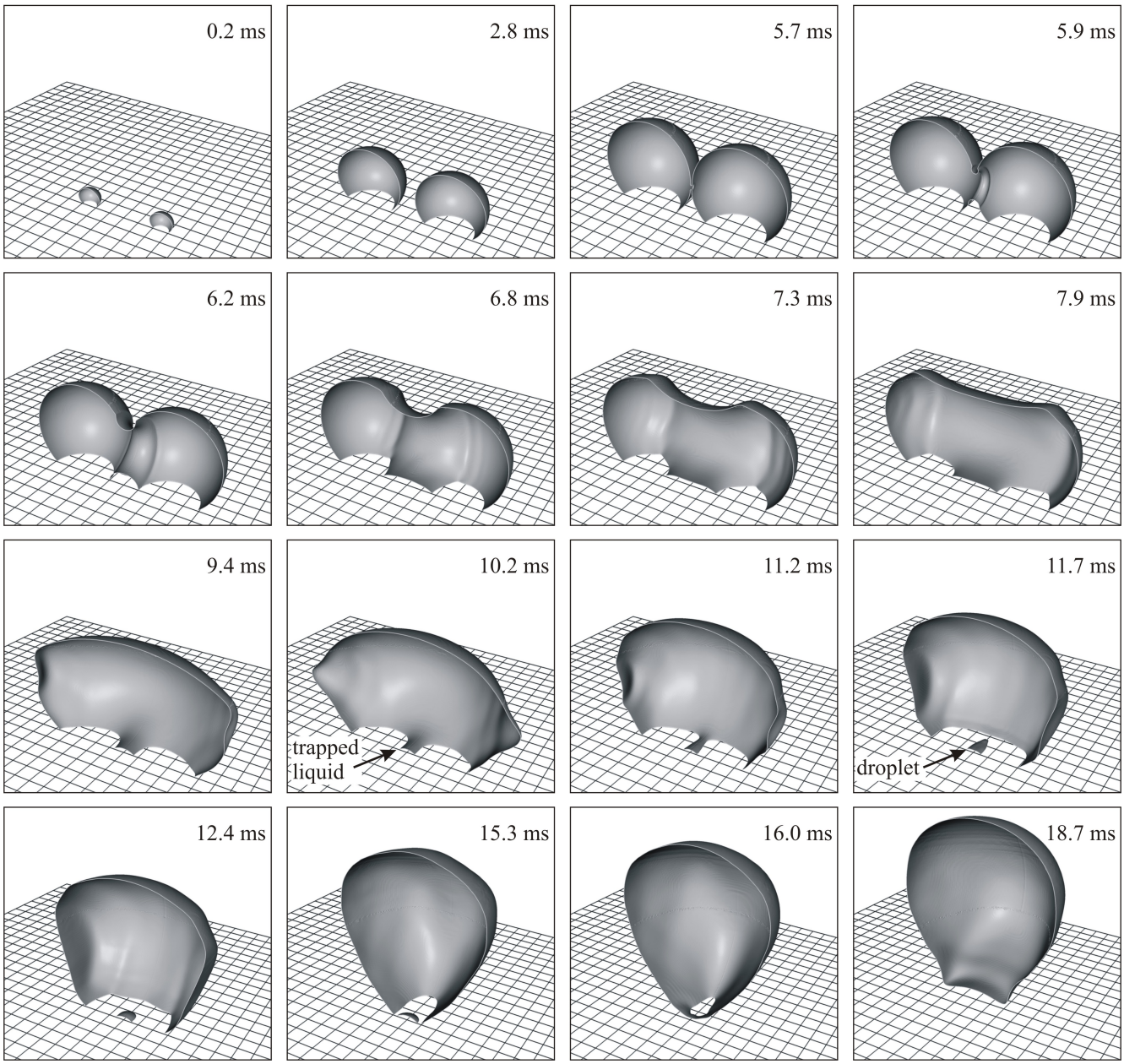

Figure 5.20: Bubble dynamics during a lateral bubble merger. Contact angle is $\theta = 40°$.

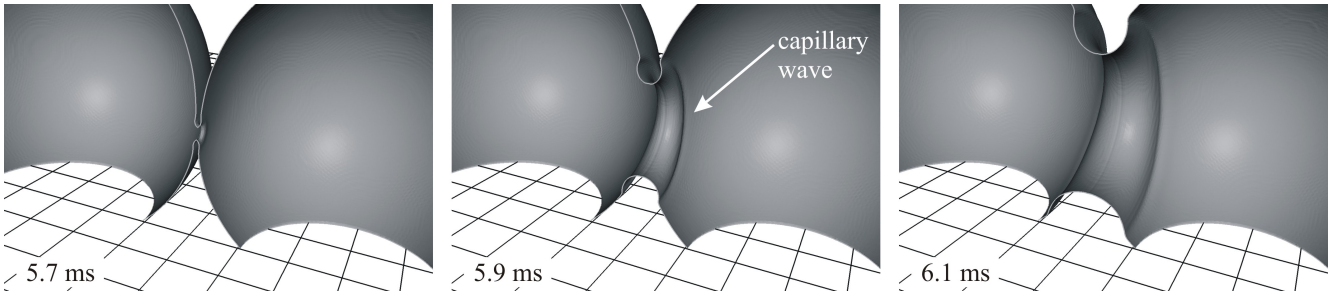

Figure 5.21: Detailed view of the merging process and the growth of the vapor bridge between the bubbles. Contact angle is $\theta = 40°$.

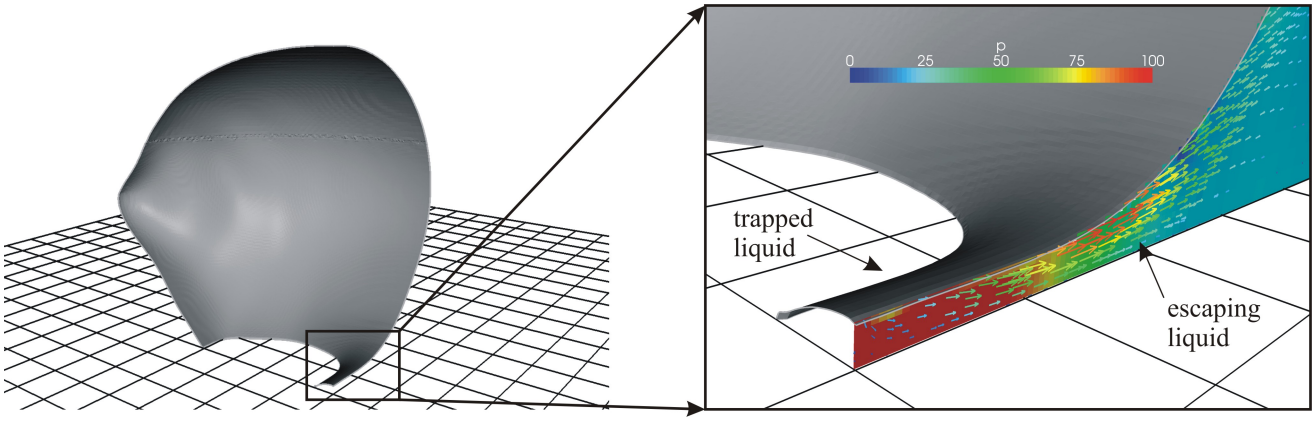

Figure 5.22: Detailed view of the trapped liquid, the elevated pressure (in Pa) within the trapped liquid and the resulting flow into the bulk liquid at 10.2 ms. Contact angle is $\theta = 40°$.

experimentally, is nicely predicted by the simulation. After the formation of the droplet, the merged bubble starts to detach from the heater surface due to buoyancy. The droplet has only little effect on the detachment of the merged bubble. At 16 ms one can see that the droplet only causes a separation of the dry vapor patch on the heater surface into two vapor patches just before the bubble lifts off.

The formation of the droplet inside the merged bubble is a result of the hydrodynamics and the wetting behavior. In principal, there are two competing effects that govern the process. The first effect results from surface tension and leads to an elevated pressure inside the trapped liquid which pushes the liquid sideways into the bulk liquid. This elevated pressure inside the trapped liquid and the resulting flow are shown in Figure 5.22. The magnitude of the pressure elevation depends on the surface tension coefficient and the curvature of the liquid-vapor interface of the trapped liquid. As mentioned above, the volume of the trapped liquid corresponds to a truncated cylinder. The curvature of the truncated cylinder depends on its size, but also on the contact angle. The second effect is the inertia of the trapped liquid which limits the transport of the liquid from the trapped position into the bulk. If the overall merging process is slow enough or if the surface tension forces are strong enough, the trapped liquid might be able to flow completely into the bulk liquid. However, if the merging process is very fast, the trapped liquid does not have enough time to escape. Consequently, the trapped liquid pinches of the bulk liquid and forms a droplet. These considerations are supported by the fact that Mukherjee and Dhir [80] did not observe the formation of a droplet when they simulated lateral mergers of two bubbles. Their simulations were performed with water at a pressure of 1 bar which has a significantly higher surface tension coefficient and a smaller liquid density than HFE-7100. Under these circumstances the pressure within the trapped liquid is higher while the inertia of the liquid is smaller. Thus, the trapped liquid can more quickly escape to the bulk liquid and no droplet formation can be observed.

It is obvious that the bubble dynamics during a bubble merger strongly depend on the contact angle. In order to learn more about the bubble dynamics and the droplet formation, a small parameter study for the contact angle was accomplished. The contact angle is assumed to be independent of the local evaporation rate and of the speed of the 3-phase contact line. In addition to the simulation with a contact angle of $\theta = 40°$ which has been discussed above, simulations with larger and smaller contact angles are performed. The results of the simulation with a contact angle of $\theta = 60°$ are shown in Figure 5.23. There is not much qualitative difference compared to the simulation with a contact angle of $\theta = 40°$. The growth time until the bubbles are grown big enough to first touch each other is almost identical. After the bubbles merge, the vapor bridge between the bubbles grows rapidely and causes some capillary waves that run along the liquid-vapor interface. The volume which is occupied by the trapped liquid is rather slim compared to the case with a contact angle of $\theta = 40°$, which results in an earlier formation of the droplet (around 8.4 ms compared to 11.5 ms). The fact that the trapped liquid volume is rather

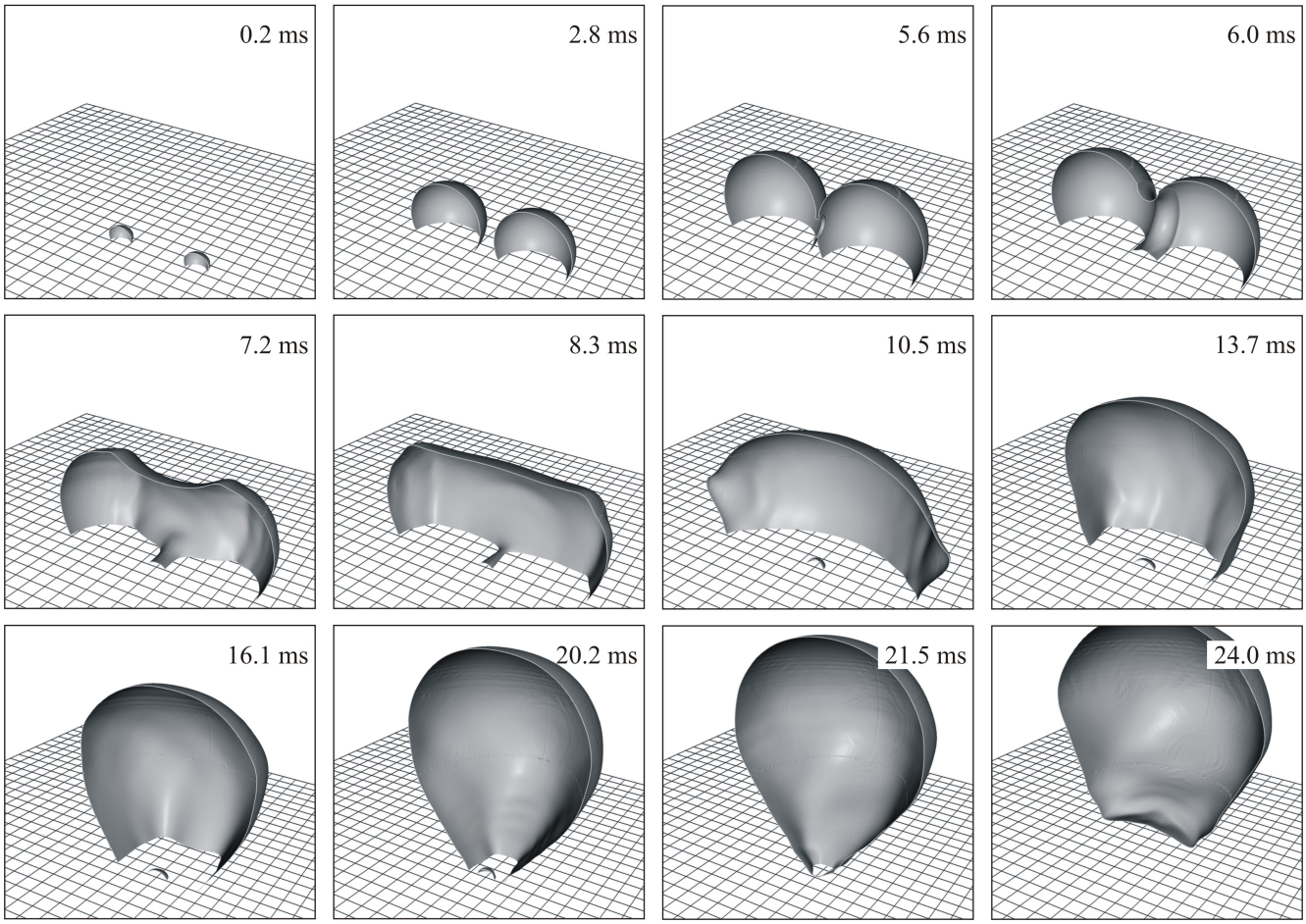

Figure 5.23: Bubble dynamics during a lateral bubble merger. Contact angle is $\theta = 60°$.

slim is due to the shape of a truncated cylinder. If the volume of the trapped liquid is the same, a higher contact angle leads to a slimer cylinder shape. While the droplet formation happens earlier, the bubble detachment process takes longer compared to the case with a contact angle of $\theta = 40°$. The merged bubble lifts off from the heater surface at around 22 ms compared to 16.5 ms. The longer contact to the heater surface is expected as the attaching forces at the 3-phase contact line are higher in the case of a higher contact angle. The effect has also been mentioned during the discussion of the simulation results for the single bubble configuration (see section 5.1).

The results of the simulation with a contact angle of $\theta = 20°$ are shown in Figure 5.24. While an increase of the contact angle compared to $\theta = 40°$ did not change the results qualitatively, the small contact angle of $\theta = 20°$ leads to significantly different bubble dynamics. As in the simulations discussed before, the bubbles grow without much interaction until around 5.8 ms. However, here the formation of the vapor bridge between the bubbles leads to a complete lift-off of the merged bubble from the heater surface. As discussed above, the vapor bridge forms and grows rapidely. The liquid underneath the vapor bridge is pushed down towards the heater. It can either escape to the side into the bulk liquid or flow towards the contact line region and push the 3-phase contact line of the trapped liquid outwards. The situation is shown in Figure 5.25 for the simulation with a contact angle of $\theta = 40°$. The downward motion of the liquid-vapor interface pushes the liquid towards the stagnation point underneath the vapor bridge. The resulting outward motion of the 3-phase contact line of the trapped liquid can clearly be seen. This leads to a decreasing size of the vapor patches and in the case of a contact angle of $\theta = 20°$ to a bubble lift-off at around 8.9 ms. Interestingly, the dynamics of the upper part of the bubble does not seem to be much affected by the lift-off. Again, a barrel-like shape and a lemon-like shape can be

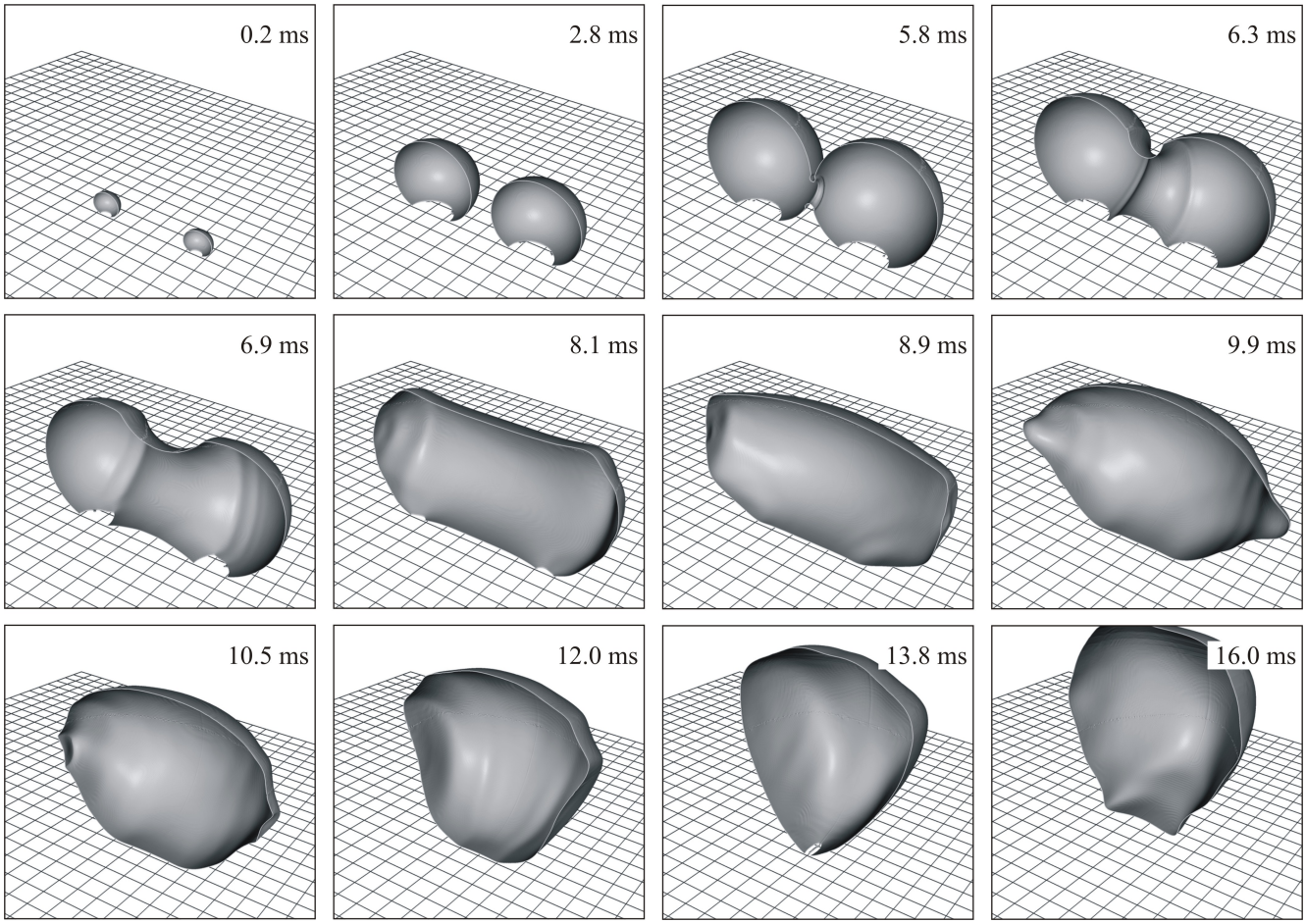

Figure 5.24: Bubble dynamics during a lateral bubble merger. Contact angle is $\theta = 20°$.

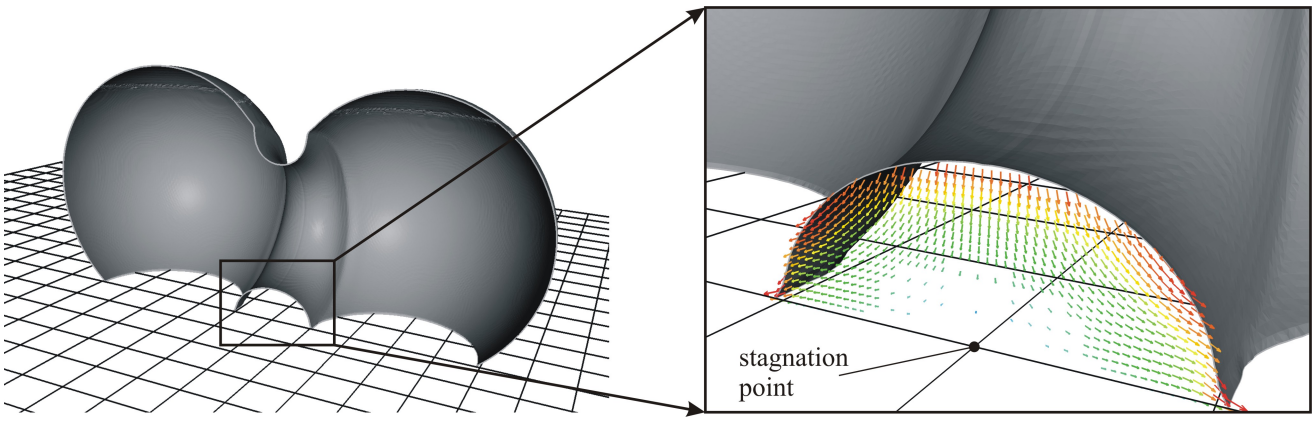

Figure 5.25: Detailed view of the flow underneath the liquid bridge at 6.2 ms. The flow towards the stagnation point and the outward motion of the 3-phase contact line of the trapped liquid can clearly be seen. Contact angle is $\theta = 40°$.

observed at 8.1 ms and 9.9 ms, respectively. After the lift-off, the bubble remains oscillating in a very short distance to the heater and starts to rise only slowly. The slow rise and the oscillations lead to a re-attachment of the bubble at around 13.8 ms. However, the re-attachment lasts only for a very short time as the bubble is now rising with a higher velocity and lifts off completely from the heater surface.

5.2.3 Brief review and relevance of the results

The results which are discussed above show an excellent agreement to experimental observations of Wagner [117]. In spite of the difficulty to match the boundary and initial conditions between simulation and experiment, the results meet all expectations with repect to the bubble dynamics and the formation of a droplet inside the merged bubble. It is shown that the contact angle has a large influence on the bubble dynamics and the formation of the droplet. For very small contact angles, the merger can even lead to an immediate lift-off of the merged bubble from the heater surface without the formation of a droplet. Of course, the contact angle is not the only parameter with a potentially large influence. The distance between the nucleation sites, the time delay between the nucleation of the bubbles and the material properties certainly have a strong influence on the results as well. From this point of view, the simulations which are discussed above can only be understood as a first step towards more comprehensive numerical studies. The important outcome of this first step is that the model is capable of accurately predicting very complex boiling flows. In other words, the simulations show that the model can well be used as a research tool in order to obtain a better understanding of complex boiling flows. Thanks to the adaptive mesh refinement algorithm of *OpenFOAM*, the number of cells can be kept rather low and the computation of a bubble merger can be performed within a day[5] which enables parametric studies of the process.

5.3 Test simulations for further boiling phenomena

In addition to the simulations of pool boiling with a single bubble and with a system of two bubbles that are described above, further simulations in different boiling configurations were performed to test the applicability of the boiling model which was developed within the present thesis. The simulation results for three different boiling configurations are presented in this section. These are flow boiling in a near-wall shear flow, boiling in a structured microchannel and film boiling of droplets, i.e. droplets which hover above a surface which is heated above the Leidenfrost temperature. The focus of these simulations lies rather on the proof of the general capability of the boiling model to predict the 2-phase flow dynamics and heat transfer in such conditions than on the quantitative analysis of the results or the detailed comparison to experimental data.

5.3.1 Flow boiling in a near-wall shear flow

Flow boiling heat transfer is used in many technical applications. In contrast to the cases of single bubble pool boiling and bubble merger which are presented in section 5.1 and 5.2, the vapor bubbles do not grow in a quiescent bulk liquid during flow boiling but in a near-wall shear flow. The shear flow strongly influences the bubble dynamics by imposing drag and lift forces on the bubble. Thus, the bubble can slide along the heater surface due to the drag force. The lift force is the result of the higher liquid flow velocity at the top part of the bubble hull compared to the bottom part which is closer to the heater surface. In the case of a horizontal heater surface, the lift force supports the buoyancy force and leads to an earlier bubble detachment compared to the bubble growth in a quiescent liquid. Here, the influence of the flow

[5] The simulations which are presented here were performed on 8 cores with 3.16 GHz each (2 Intel Xeon Quadcore CPUs).

field is examined numerically by simulation of the growth and detachment of a single bubble in a liquid flow. Due to its high technological relevance, flow boiling has intensively been studied experimentally. In particular, the work of Klausner and co-workers [55, 56, 133] and of Duhar and co-workers [13, 14, 15] is focussed on the dynamics of single bubbles in a near-wall shear flow. Unfortunately, the work of Klausner and co-workers [55, 56, 133] does not provide very detailed information about the liquid flow field. Thus, the boundary conditions for the numerical simulation cannot be chosen accurately. Duhar and co-workers [13, 14, 15] measured the flow field with *Laser-Doppler-Anemometry*, thus providing the boundary conditions for the liquid flow. However, only the wall temperature and not the temperature profile in the liquid is known. As a growing bubble obtaines a large amount of the heat required for its growth from the superheated liquid layer, the results are sensitive to the thermal layer within the liquid.

As the transfer of the boundary conditions from existing experimental data is not straightforward or the boundary conditions are not even available, the simulations of flow boiling which are presented in this section are based on a numerical study of flow boiling by Li and Dhir [63]. Again, the data which is given in the publication is not comprehensive. In particular, the exact thicknesses of the velocity boundary layer and of the thermal boundary layer are not given explicitely. Further, the authors implement a model for the contact angle dynamics but do not provide the exact equation. Therefore, only a qualitative study of the influence of the liquid flow is accomplished here. Li and Dhir [63] studied the growth of single vapor bubbles on a wall with a constant superheat of 5.3 K. The authors do not take into account the transient heat conduction within the heater but assume the heater surface to be isothermal. Hence, a constant wall temperature is also assumed for the simulations which are presented here. The fluid is water at a pressure of 1 bar and the velocity of the bulk liquid is 0.076, 0.135 or 0.23 m/s. One important outcome of the study is the decrease of the bubble departure diameter at higher liquid bulk velocities which has also been observed experimentally.

The simulations which are presented here are performed on a 3D mesh using one plane of symmetry. The mesh has a length of 9 mm in flow direction, a height of 6 mm above the heater and a width of 3 mm and is discretized into cubic cells with a size of 62.5 μm. Adaptive mesh refinement is used with two levels of refinement in cells that are close to the liquid-vapor interface and are located at a distance of less than 1 mm to the heater. Only one refinement step is applied for all other cells which are close to the liquid-vapor interface (within a band of 10 cells around the interface). Initially, a small vapor bubble with a radius of 0.1 mm is placed at a location which lies 3 mm downstream of the velocity inlet. As proposed by Li and Dhir [63], the temperature profile in the thermal boundary layer and the flow field in the velocity boundary layer at the inlet are functions of the coordinate y which counts normal to the wall.

$$T(y) = T_{\text{sat}} + (T_{\text{wall}} - T_{\text{sat}}) \left[1 - \left(\frac{y}{\delta_T} \right)^{1/7} \right] \tag{5.7}$$

$$u(y) = U_{\text{bulk}} \left(\frac{y}{\delta} \right)^{1/7} \tag{5.8}$$

These profiles are also used as initial conditions in the whole liquid volume within the computational domain. Outside of the boundary layers, the liquid is assumed to be at saturation temperature and flows with the bulk liquid velocity. Unfortunately, Li and Dhir [63] do not provide exact information about how the thickness of the thermal boundary layer δ_T is obtained. They only state that the thickness of the velocity boundary layer is calculated form the expression $\delta = 1.026 \text{Pr}^{1/3} \delta_T$ where the *Prandtl* number is defined as $\text{Pr} = c\mu/k$. In default of more exact values, the following values for the thickness of the thermal boundary layer and of the velocity boundary layer are used for all simulations presented here.

$$\delta_T = 0.797\,\text{mm} \tag{5.9}$$

$$\delta = 0.743\,\text{mm} \tag{5.10}$$

These values are estimated from the heat transfer data which is given by Li and Dhir [63]. It should be noted that the values depend on the bulk liquid velocity and that a higher bulk liquid velocity leads to thinner boundary layers. However, the decrease of these values for higher bulk velocities is not taken into account. As mentioned above, the departure diameter of the bubbles becomes smaller for higher liquid bulk velocities. This is caused by two effects. First, the lift force which acts on the bubble in the near-wall shear flow increases. Second, the thermal boundary layer becomes thinner and therefore the mean superheat of the liquid is decreased. As it is shown by Son and co-workers [102], the decrease of the wall superheat and herewith also of the mean superheat in the liquid leads to a smaller departure diameter of the bubbles. The second effect is not taken into account here as the thicknesses of the thermal boundary layer and of the velocity boundary layer are kept constant for different liquid bulk velocities. Hence, the focus of the simulations which are presented here is on the correct prediction of the hydrodynamic lift force on the bubble which leads to an earlier bubble lift-off at higher liquid bulk velocities.

It could be shown in section 5.1 that the contact angle has an important influence on the bubble dynamics during nucleate pool boiling. In flow boiling conditions, the effect of the contact angle and of its dynamic behavior can be even more important. The liquid flow imposes a drag force on the bubble which can lead to a sliding of the bubble along the heater. In such a case, the upstream part of the 3-phase contact line at the bubble foot is advancing while the downstream part is receding. Depending on the fluid and on the surface characteristics (e.g. roughness), the contact angle can be influenced strongly by the motion direction (contact angle hysteresis) and the speed (contact angle dynamics) of the 3-phase contact line. The variation of the contact angle along the 3-phase contact line of a bubble leads to a resultant horizontal component of the attaching forces (see section 2.2) which counteracts the drag force due to the liquid flow. Unfortunately, Li and Dhir [63] do not provide detailed information about their sub-model for the contact angle dynamics. Here, the following equation is applied to calculate the contact angle as a function of the speed of the 3-phase contact line.

$$\theta = \theta_\text{R} + 0.5\left(\theta_\text{A} - \theta_\text{R}\right)\sin\left(\frac{\pi}{2}\frac{u_\text{cl}}{\text{B}}\right) \tag{5.11}$$

This equation describes the hysteresis between an advancing contact angle θ_A and a receding contact angle θ_R. The speed of the 3-phase contact line u_cl can be obtained from the reconstruction data of the liquid-vapor interface and by comparing the position of the 3-phase contact line at successive time steps. The constant B and the sine function are used to obtain a smooth transition between the advancing contact angle for $u_\text{cl} > \text{B}$ and the receding contact angle for $u_\text{cl} < -\text{B}$. In principal, it is also possible to implement a sharp step of the contact angle between $u_\text{cl} < 0$ and $u_\text{cl} > 0$. However, this could possibly lead to numerical instabilities which are avoided by the implementation of the smooth transition. The constant B is chosen small compared to the expected speed of the 3-phase contact line[6].

The results of several numerical simulations of flow boiling are presented and discussed in the following. First, the influence of the liquid bulk velocity on the bubble dynamics is investigated. The bubble shapes for different liquid flow velocities are shown at various times in Figure 5.26. In all cases which are shown in this figure, the same combination of advancing and receding contact angle is used ($\theta_\text{A} = 50°$, $\theta_\text{R} = 10°$). The most obvious influence of the liquid bulk velocity is the horizontal sliding of the bubbles

[6] A value of $\text{B} = 0.001\,\text{m/s}$ is chosen for the simulations presented here.

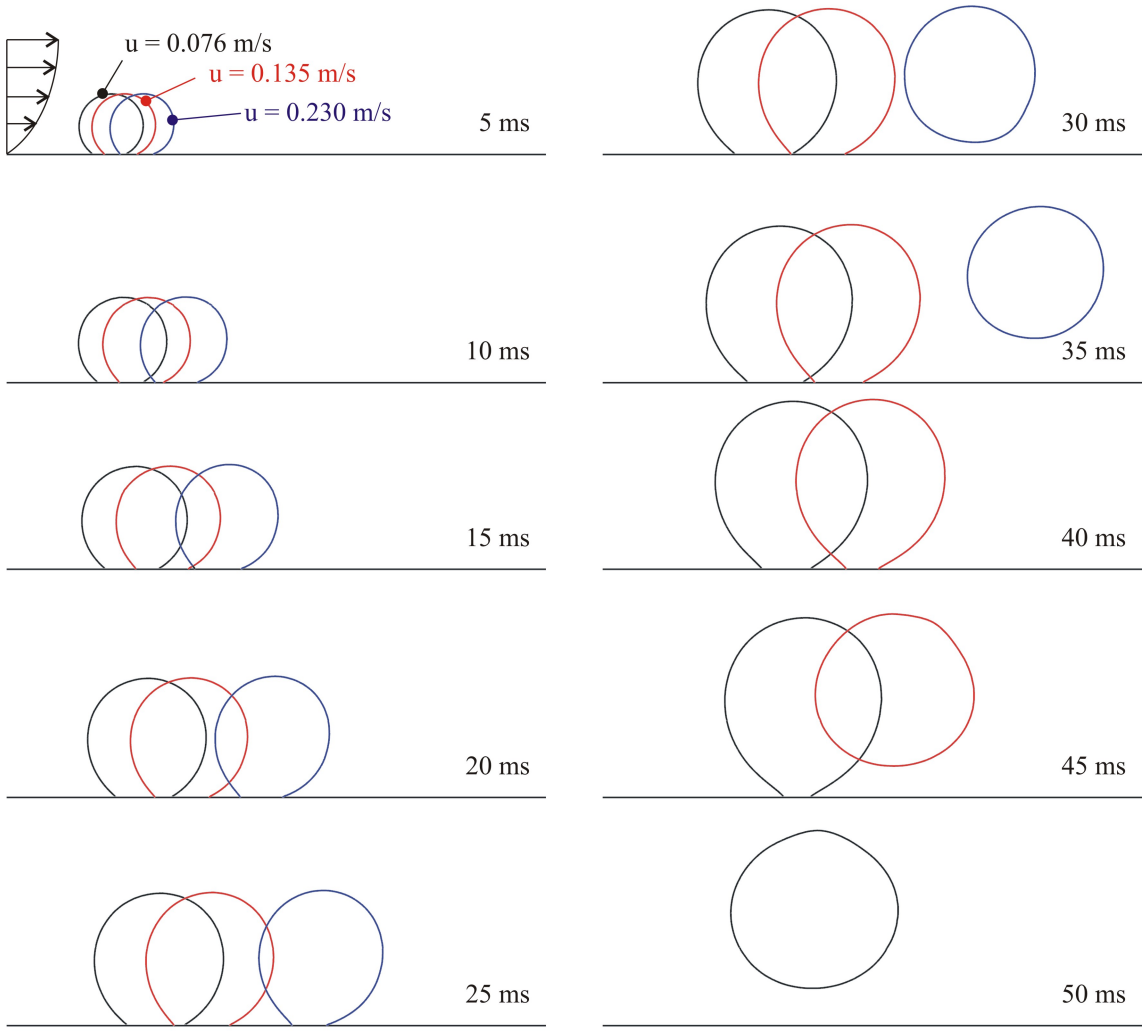

Figure 5.26: Bubble shape during growth and detachment for different bulk liquid velocities. Advancing contact angle is $\theta_A = 50°$, receding contact angle is $\theta_R = 10°$.

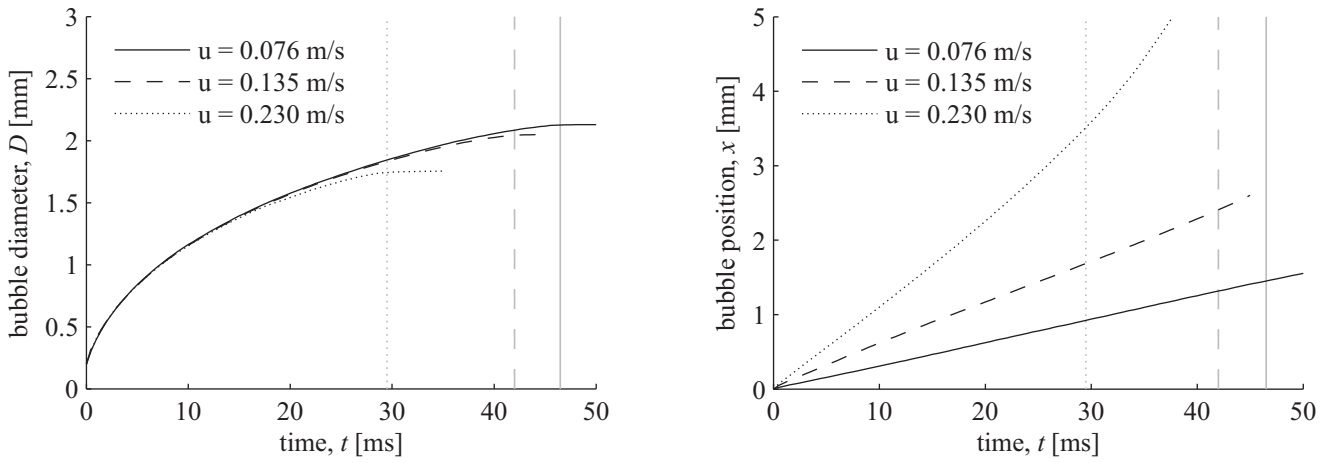

(a) Bubble diameter

(b) Bubble position (center of gravity)

Figure 5.27: Development of bubble diameter and bubble position (center of gravity in downstream direction) for different liquid bulk velocities. Advancing contact angle is $\theta_A = 50°$, receding contact angle is $\theta_R = 10°$. Vertical gray lines represent the moment when the bubbles lift-off.

along the heater. While the bubble stays almost at the same horizontal position as the nucleation site for a liquid bulk velocity of 0.076 m/s, the bubble slides along the heater for almost 4 mm before the lift-off from the heater surface for the highest liquid bulk velocity of 0.23 m/s. As mentioned above, the different contact angles at the upstream and downstream part of the bubble foot lead to a resultant horizontal component of the attaching force. In all three simulations that are shown in Figure 5.26 the same advancing and receding contact angle is used. Hence, the resultant horizontal component of the attaching force is approximately the same in all three simulations. The drag force which is due to the liquid flow is partly compensated by this horizontal component of the attaching force. The inequality between the two competing forces changes with the liquid bulk velocity, i.e. the drag force becomes more dominant when the liquid bulk velocity increases. Thus, the bubble slides along the heater surface. Furthermore, a higher liquid bulk velocity leads to a decrease of the bubble departure diameter which is in excellent agreement to the results of Li and Dhir [63] and the above mentioned experimental investigations. The difference of the departure diameter is uniquely due to the earlier bubble lift-off at higher liquid bulk velocities. Interestingely, the liquid bulk velocity does not seem to influence the growth rate of the bubbles. The diameters of the of bubbles which are shown at different times in Figure 5.26 are very similar. This can also be seen more precisely in Figure 5.27(a). In this figure, the equivalent bubble diameter (calculated from the bubble volume, assuming a spherical shape) is plotted over time. No difference can be seen between the curves during the first 30 ms of the bubble growth although the horizontal position of the bubbles differs significantly (see Figure 5.27(b)). Only after the departure of the bubbles from the heater surface, the curves show a different behavior as the departed bubbles almost completely stop to grow. The moment of bubble lift-off is also shown in Figure 5.27(a) and Figure 5.27(b). While the bubble remains attached to the heater surface for more than 45 ms in the case of the slowest liquid bulk velocity of 0.076 m/s, it detaches already after less than 30 ms in the case of the highest liquid bulk velocity of 0.23 m/s. As the growth rate is almost the same, the earlier lift-off leads to a smaller departure diameter of 1.75 mm for the highest velocity compared to 2.13 mm for the slowest velocity.

The results are in very good qualitative agreement to the results obtained by Li and Dhir [63]. The absolute values of the bubble growth time (nucleation to departure) and of the bubble departure diameter are predicted higher than the data reported by Li and Dhir [63]. However, the thickness of the thermal layer and of the velocity boundary layer as well as the equation for the contact angle dynamics are not provided precisely by Li and Dhir [63]. All three parameters can be expected to have a strong impact on the results. In particular, the thickness of the thermal layer strongly influences the growth rate and the departure size of the bubbles. Therefore, a direct and quantitative comparison of the results is not available.

In order to investigate the influence of the sub-model for the contact angle dynamics, the simulation with the slowest liquid bulk velocity of 0.076 m/s was repeated for different combinations of advancing and receding contact angle. The development of the bubble diameter and of the position of the bubble's center of gravity in downstream direction are plotted over time in Figure 5.28(a) and Figure 5.28(b), respectively. It can be seen that there is some influence of the contact angle dynamics on the bubble growth rate. The simulation with equal values for advancing and receding contact angle ($\theta_A = \theta_R = 30°$) predics a slower growth compared to the other two cases. This is most probably due to the different length of the 3-phase contact line at the bubble foot. A higher contact angle leads to a larger bubble foot diameter, herewith to a longer 3-phase contact line and eventually to an increased heat transfer. Further, a difference between the advancing and the receding contact angle leads to a deviation from a circular shape of the bubble foot which can also increase the length of the 3-phase contact line. Although the growth of the bubble diameter depends on the contact angles, the influence is rather small compared to the influence on the sliding of the bubbles and the growth time. It can clearly be seen in Figure 5.28(b) that the sliding of the bubbles directly depends on the difference between the advancing and the receding contact angle. The larger the difference between the two angles, the higher the horizontal component of the attaching force becomes and the less the attached bubble is transported with the liquid flow. The

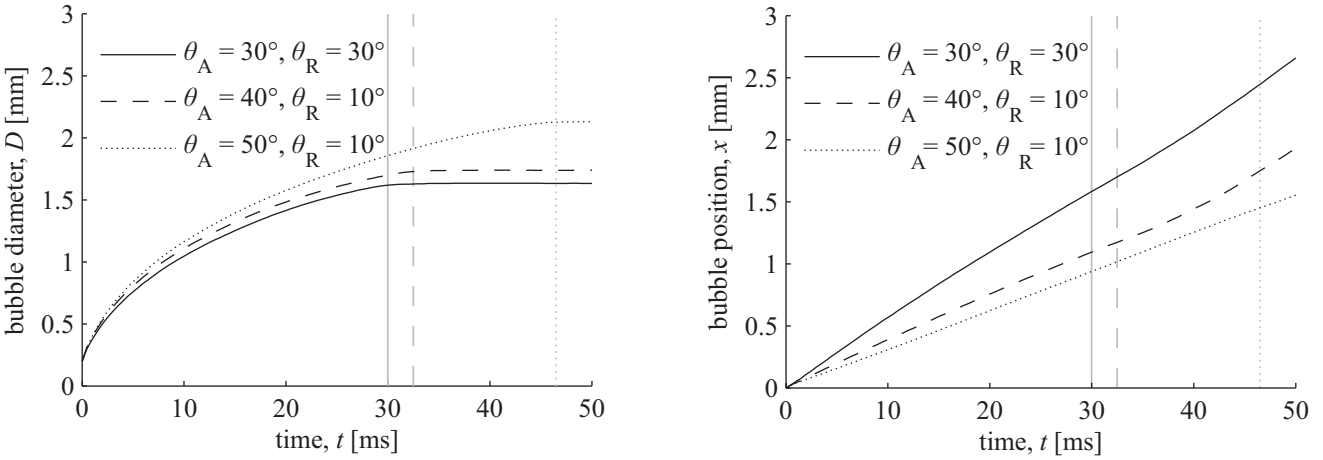

(a) Bubble diameter

(b) Bubble position (center of gravity)

Figure 5.28: Development of bubble diameter and bubble position (center of gravity in downstream direction) for different combinations of advancing and receding contact angle. Vertical gray lines represent the moment when the bubbles lift-off.

highest impact of the choice of the contact angles can be observed on the growth time. The increase of the advancing contact angle leads to a stronger attaching force in normal direction to the wall. Thus, the bubble must grow to a larger volume until the detaching buoyancy forces overcome the attaching forces at the 3-phase contact line. In particular, the change of the advancing contact angle from 40° to 50° has a significant influence on the growth time which increases from around 32 ms to 46 ms. Additionally, the longer growth time leads to an increase of the departure diameter from 1.73 mm to 2.13 mm. These results show that the influence of the contact angle and its dynamics in flow boiling conditions is even higher than in pool boiling conditions (see section 5.1). The contact angle has a strong influence on many aspects of the boiling process, such as the bubble shape and herewith the length of the 3-phase contact line as well as the attaching forces normal and parallel to the wall. Rather small changes of the contact angle can lead to large changes in the results.

The results which are presented in this section show that the effect of the near-wall shear flow on the bubble dynamics during flow boiling can be predicted by the boiling model. Further, the results clearly show that contact angle dynamics must be taken into account if the aim is to quantitatively compare or predict bubble growth times, departure diameters or sliding distances. The equation which describes the dependence of the contact angle on the speed of the 3-phase contact line (here, Eq. (5.11) is used) must be chosen with care and should be based on either physically based models or experimental observations.

5.3.2 Boiling in a structured microchannel

In the past five to ten years, boiling in channels with a very small hydraulic diameter compared to the capillary length $L_c = \sqrt{\sigma / \left[g \left(\rho_l - \rho_v \right) \right]}$ of the fluid has been studied intensively and has proven to enable high heat transfer coefficients. Comprehensive articles about the fundamental issues and the heat transfer mechanism during boiling in microchannels were published by Kandlikar [47, 48]. Another potential improvement of the heat transfer coefficient can be achieved by using a micro-structured heater surface. This principal has proven to significantly increase the heat transfer on heater surfaces with a plane macroscopic shape [62, 122] and on tube evaporators [107, 128, 129]. When combining the two approaches, i.e. using micro-structured channels with a small hydraulic diameter, high heat transfer coefficients can be expected. Further, the structuring of the channel walls might also be used to

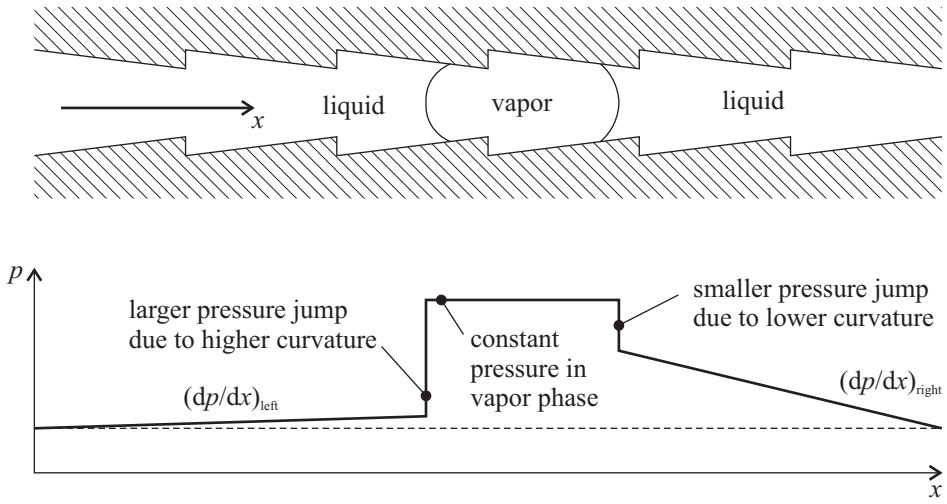

Figure 5.29: Principal idea: Vapor bubble moves to the right as the meniscus curvature on the left side is higher than on the right side which leads to a higher magnitude of the pressure gradient in the liquid on the right side of the bubble.

incorporate additional features into a boiling device. One idea of such an additional feature is the use of an asymmetric sawtooth structure to achieve a preferred direction of growth of the vapor bubbles that nucleate and grow within the small channel. The principal is shown in Figure 5.29. Due to the slope of the sawteeth, the menisci which border the bubble on either side have different curvatures. The meniscus with the higher curvature (left in Figure 5.29) creates a larger pressure jump between the vapor and the liquid which influences the pressure profiles in the liquid on the left and right side of the bubble. A generic pressure profile is shown in the bottom part of Figure 5.29. The pressure within the vapor phase is approximately constant as the friction is negligible compared to the friction within the liquid phase. The different magnitudes of the pressure jumps at the menisci on the left and right side of the bubble result in different pressure gradients in the liquid phase. The generic pressure profile in Figure 5.29 corresponds to a situation when the bubble grows in both directions as the pressure drops from the bubble towards the left and right boundary. However, the magnitude of the pressure gradient on the right side is higher and thus, the growth to the right is faster than the growth to the left. In general, the following conditions for the pressure gradients on the left and right side of the bubble govern the preferred growth direction of the fluid.

$$\left(\frac{\mathrm{d}p}{\mathrm{d}x}\right)_{\mathrm{left}} + \left(\frac{\mathrm{d}p}{\mathrm{d}x}\right)_{\mathrm{right}} \begin{cases} < 0\,, & \text{preferred growth to the right} \\ = 0\,, & \text{no preferred growth direction} \\ > 0\,, & \text{preferred growth to the left} \end{cases} \tag{5.12}$$

The idea which is decribed above is the basis of a so-called seed fund project within the Center of Smart Interfaces at Technische Universität Darmstadt. The aim of the seed fund project is to show analytically and experimentally[7] that a sawtooth structure can lead to a preferred growth direction of the bubbles. Another goal is to prepare more detailed studies within a larger follow-up project aiming at the design of self-pumping boiling heat transfer systems.

The simulations which are shown here were performed prior to the setup of the experiment. Their aim was to check the general feasibility and to get an idea of the bubble growth and bubble dynamics within the structured microchannel. Due to the preliminary nature of the simulations, they were only performed

[7] The theoretical and experimental work within the seed fund project is performed by Dr. Shadi Majhoob.

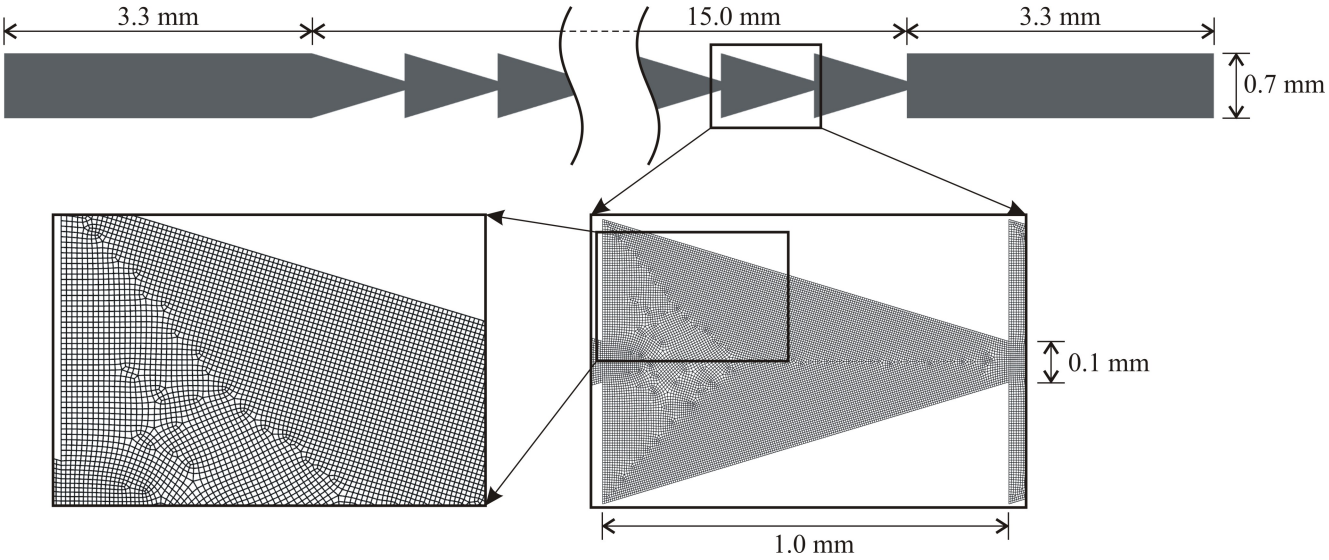

Figure 5.30: Geometry of the computational domain for the simulation of boiling in the structured microchannel. The unstructured mesh which is used is shown in the blow-ups.

in 2D, i.e. the computational domain represents a channel of infinite length in the third dimension and without any variation of the flow field and phase distribution in the third direction. The geometry of the computational domain and the mesh are shown in Figure 5.30. The channel consists of two parts at the left and right boundary with smooth channel walls and 15 sawteeth with a total length of 15 mm on each side. The largest width of the channel is 0.7 mm and the smallest width at the bottleneck between two peaks of opposing sawteeth is 0.1 mm. An unstructured hexahedral mesh with a cell size of around 5 μm is used for the simulations. In several large patches of the computational domain the mesh is quasi-structured and only becomes unstructured and non-orthogonal at the interfaces between these patches (see blow-up in Figure 5.30). In the experiment the channel is mounted horizontally, i.e. the gravity vector points into the drawing plane of Figure 5.30. Therefore, the simulations are performed without taking into account the effect of gravity which is anyhow inferior to surface tension effects in such a small channel. In the simulation, equal pressures are imposed on the left and the right boundary of the domain while a no-slip boundary condition and a contact angle are prescribed at the channel walls. The walls are assumed to be at a constant temperature at all times and the liquid is initially at saturation temperature. The fluid is water at a pressure of 1 bar (see appendix A for material properties).

The growth of a single bubble is simulated with different parameters. This single bubble is assumed to nucleate in one of the corners of the surface structure on the lower wall in the middle of the channel (see first image of Figure 5.31 and Figure 5.32). One of the most important parameters is the wall superheat. Numerical experiments quickly showed that the wall superheat must be chosen rather small. At a superheat of 5 K the bubble grows very fast and almost the whole channel is filled with vapor after only a few milliseconds. The extremely fast bubble growth compared to pool boiling conditions is a result of the confinement of the bubble by the heated walls of the channel. Further, as the bubble front moves from one sawtooth to the next, a liquid meniscus remains in the corners of the structure (e.g. in Figure 5.31). Thus, the total length of the contact line in the whole domain becomes very large, leading to a very rapid growth of the bubble. In these conditions, no preferred growth direction of the bubble could be observed as the flow was dominated by intertia rather than surface tension. Therefore, a very small superheat of only 0.1 K is chosen for the simulations which are presented here. In addition to the wall superheat, the contact angle can also be expected to have a strong influence on the results. Therefore, the simulations are performed with two different contact angles of $\theta = 30°$ and $\theta = 60°$.

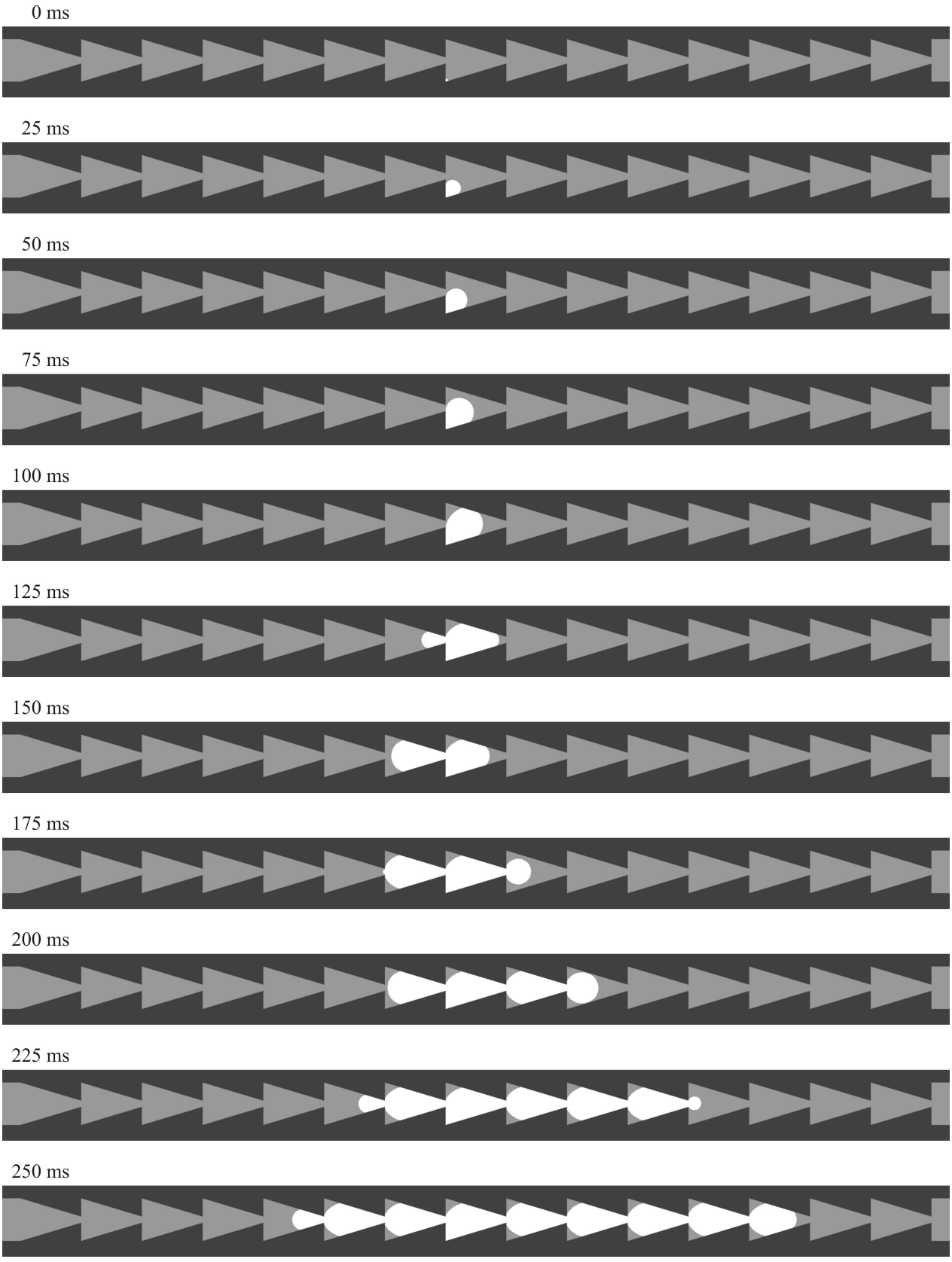

Figure 5.31: Bubble growth in a structured microchannel (white: vapor, light gray: liquid, dark gray: solid). The contact angle is $\theta = 30°$ and the wall superheat is 0.1 K. The pinning of the 3-phase contact line at the peaks of the sawteeth and a preferred motion of the bubble to the right can be seen.

The bubble growth dynamics within the channel which is obtained in the simulation with a contact angle of $\theta = 30°$ is shown in Figure 5.31. At the start of the simulation (0 ms) the bubble is very small (the initial radius is $R = 50\,\mu$m) and located in the corner of the structure. Due to the small wall superheat, the bubble grows rather slowly and it takes around 50 ms until the bubble reaches a peak of a sawtooth. Between 50 and 100 ms, the 3-phase contact line of the bubble remains pinned at this peak and continues to grow to the right. As the meniscus which borders the bubble on the right side moves further to the right, its curvature increases. This can clearly be seen when comparing the bubble shape at 100 and 125 ms. The higher curvature results in a higher pressure jump across the liquid-vapor interface which then leads to a preferred motion to the left according to Eq. (5.12). The meniscus which borders the bubble on the left side is pushed through the bottleneck between the opposing sawtheeth and enters the next segment of the channel (see images at 125 and 150 ms). At 175 ms the left meniscus reaches the next bottleneck. Again, the 3-phase contact line of the left meniscus remains pinned at the peaks of the opposing sawteeth and the right meniscus is pushed into the next segment of the channel. The alternating growth of the bubble to the left and to the right continues in the following. However, a preferred direction of growth to the right can be observed.

The described behavior agrees nicely to the basic idea of the research project which is illustrated in Figure 5.29. The sawtooth structure leads to a situation in which the meniscus which borders the bubble on the left side has a higher curvature than the meniscus on the right side. The higher curvature leads to a higher pressure jump on the left side of the bubble. According to Eq. (5.12), this causes a preferred direction of growth to the right. Thus, the general idea of the seed fund project is confirmed by this simulation. However, the simulations also revealed that the pinning of the 3-phase contact line at the peaks of the sawteeth is an additional effect that was not considered before. It is obvious that the behavior of the bubble within the channel is strongly dominated by the wetting characteristic, i.e. by the contact angle. Therefore, the simulation was repeated with a larger contact angle of $\theta = 60°$ instead of $\theta = 30°$. The growth of the bubble in this case is shown in Figure 5.32. The initial growth phase between 0 and 75 ms is very similar to the case with the smaller contact angle which is shown in Figure 5.31. In the following, the bubble grows first into the segment on the right side (see image at 150 and 175 ms). Then, the 3-phase contact line of the meniscus which borders the bubble on the right side remains pinned at the peaks of two opposing sawteeth and the bubble grows only to the left (see images between 200 and 250 ms). This behavior does not agree to the basic idea which is illustrated in Figure 5.29. In principal, the meniscus which borders the bubble on the left side has a higher curvature (at the same channel width) due to the inclination of the walls. However, the bubble grows to the left and not to the right because the meniscus on the right side is pinned at a bottleneck of the structure. The pinning seems to be very stable. The meniscus on the left side might have a higher curvature at some times but this cannot reverse the growth direction of the bubble anymore due to inertia forces. The inertia of the moving liquid and the fact that the meniscus on the right side remains always at the bottleneck and can therefore assume a highly curved shape keep the liquid on the left side of the bubble flowing towards the left boundary. Hence, the system is not governed by the effect which is described in the basic idea (see Figure 5.29) but is dominated by the pinning of the 3-phase contact line.

Instantaneous pressure profiles along the channel extracted from the two simulations with different contact angles are plotted in Figure 5.33. In principal, the profiles agree nicely to the generic profile which is shown in Figure 5.29. The pressure within the vapor phase is almost constant and there is a pressure drop in the liquid phase from the position of the bubble towards the left and right boundary. The oscillations of the pressure in the liquid phase are due to the sawtooth structure which leads to comparably higher friction pressure losses at the position of the bottlenecks between two opposing sawteeth. When comparing the pressure jumps, it can be seen that the pressure jump at the left side of the bubble is higher in the case of the smaller contact angle while the inverse situation is found for the larger contact angle. The pressure profiles correspond to the preferred growth directions which can be seen in Figure 5.31 and Figure 5.32. The different pressure jumps on the left and right side of the bubble lead

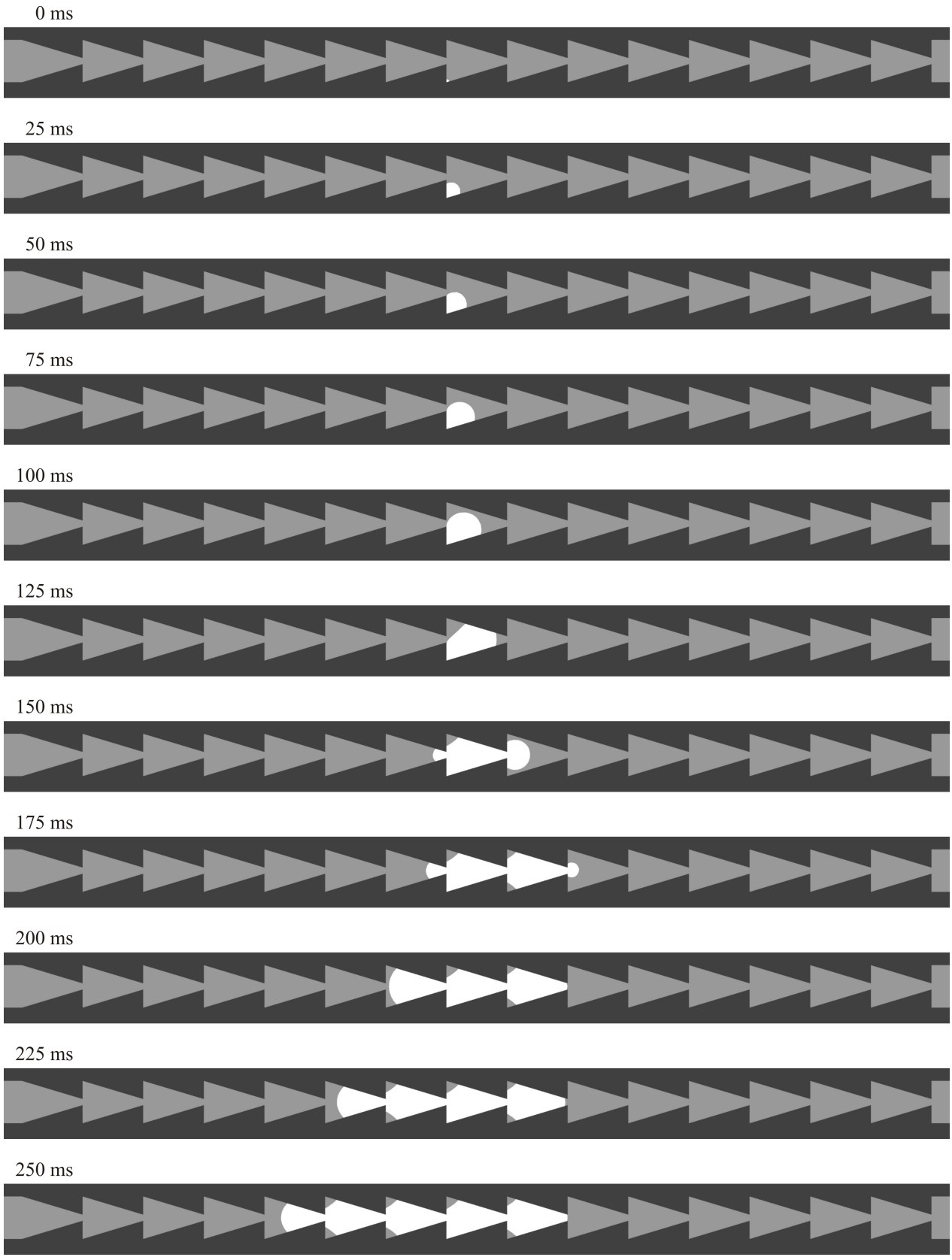

Figure 5.32: Bubble growth in a structured microchannel (white: vapor, light gray: liquid, dark gray: solid). The contact angle is $\theta = 60^\circ$ and the wall superheat is 0.1 K. The pinning of the 3-phase contact line at the peaks of the sawteeth and a preferred motion of the bubble to the left can be seen.

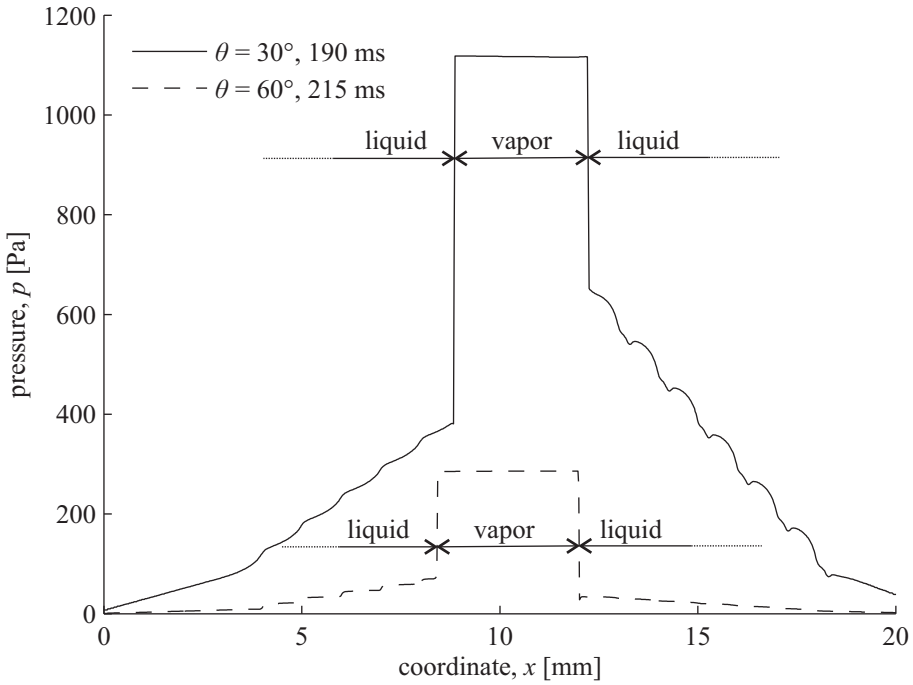

Figure 5.33: Pressure profile in the direction along the structured microchannel for contact angles of $\theta = 30°$ and $\theta = 60°$.

to different pressure gradients in the liquid phase and cause a preferred direction of growth. The inverse behavior compared to the idea which is illustrated in Figure 5.29 in the case of a larger contact angle is due to the pinning effect which is described above.

In summary, there are several conclusions that can be drawn from these preliminary simulations. First, the principal idea of the seed fund project has been confirmed. It could be shown that the wall superheat or alternatively the heat input, must be chosen rather small in the experiment in order to put into practice a system which is not dominated by inertia effects but only by surface tension. The simulations enabled an estimation of how sensitive such a system can be with respect to the contact angle. Further, it could be shown that the pinning of the 3-phase contact line at the peak of the sawteeth might also strongly influence the bubble dynamics. In spite of the very preliminary and simplified nature of the simulations, the application of the boiling model enabled a better understanding of the heat and mass transfer in a structured microchannel. In future, the boiling model can be used for a more comprehensive parameter study including also different geometries. The results of such a parameter study can then be used to chose promising geometries for a well-directed experimental investigation.

5.3.3 Leidenfrost phenomenon

If the surface of a heater in a boiling device or the surface of an element which has to be cooled is highly superheated above the saturation temperature, the mode of heat transfer changes from nucleate to film boiling, i.e. a stable vapor layer exists between the solid wall and the liquid phase. The temperature above which the wetting of the heater by the liquid is preempted is called the Leidenfrost temperature. Although film boiling heat transfer is used much less than nucleate pool boiling or flow boiling heat transfer, it is highly interesting for a number of applications such as spray cooling or quenching. The classical film boiling problem which has often been studied numerically (e.g. [46, 99, 100, 101, 126]) can be described as bulk liquid separated from the heater surface by a vapor layer. Due to the evaporation at the liquid-vapor interface, vapor bubbles are periodically released from the vapor layer. Here, a

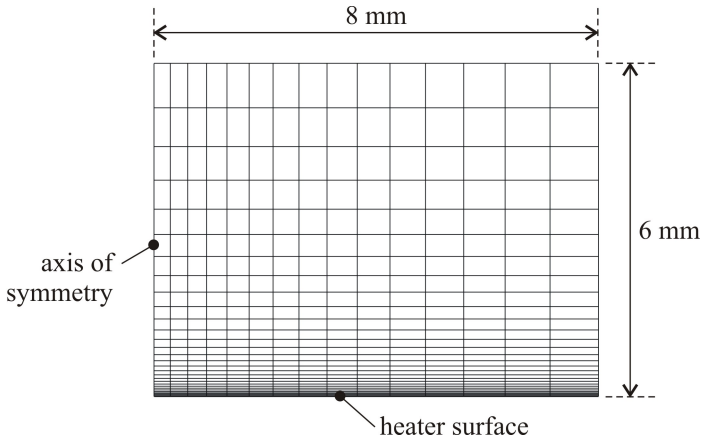

Figure 5.34: The mesh which is used for the simulation of a Leidenfrost droplet hovering over a highly superheated, smooth surface (only every tenth grid line is shown).

different configuration is discussed. Instead of a bulk liquid over the heater surface, a single droplet impacting on the heater surface is investigated. As the droplet approaches the wall, the evaporation rate at the liquid-vapor interface increases rapidely due to the low thermal resistance of the thin vapor layer. The large amount of vapor that is produced must escape from the narrow space between the droplet and the wall, thus generating an increased pressure underneath the droplet. If the wall is superheated above the Leidenfrost temperature, the pressure underneath the droplet becomes large enough to compensate the gravitational acceleration and the inertia of the impacting droplet. Hence, the droplet hovers on a steady vapor layer without wetting the surface. Kistemaker [54] as well as Gottfried and Bell [24] published experimental results on the Leidenfrost phenomenon in the 1960s. In the last decade, there has been a number of publications on the numerical simulation of the phenomenon. While the interface of the droplet is often captured with a *Volume-of-Fluid* (VOF) or *Level-Set* (LS) method, the vapor layer is typically not included in the computational domain but handled by a subgrid-scale model which is based on a lubrication approximation (e.g. [23, 30, 31, 132]). Such an approach is highly efficient, but limited to rather smooth heater surfaces. Here, the boiling model which is developed within the present thesis is used for the simulation of hovering droplets. The vapor flow is part of the computational domain and solved on the numerical mesh. As already mentioned in section 4.1, the original phase change model of Hardt and Wondra [28] for the calculation of the local evaporation rate is used here, while a modified approach is used for all the aforementioned simulations on boiling flows. This is due to the fact that the modified approach requires the calculation of the temperature gradient at the liquid-vapor interface which is only available for the liquid side in the current version. The extension to the vapor side is straightforward but not yet accomplished. Hence, the modified approach cannot be used if the heat is transferred through the vapor phase. Two different configurations of film boiling are discussed in this section. First, a droplet hovering over a highly superheated, smooth wall and second, a droplet hovering over a highly superheated, structured surface.

Smooth wall

The simulation of a droplet hovering over a highly superheated, smooth surface shall show the capability of the boiling model to predict the Leidenfrost phenomenon and to quantitatively validate its accuracy. The setup of the simulation is based on the experimental work of Biance and co-workers [4] who measured the thickness of the vapor layer underneath droplets of different size. The thickness of the vapor layer is measured by analyzing the diffraction pattern of a laser beam which is send through the vapor layer. Droplets of water at a pressure of $p = 1$ bar are deposited on a wall which is superheated 300 K above the saturation temperature. A syringe and a needle are used to feed water into the droplet

and to control the steady state size of the droplets. The experiments were not performed in a pure vapor atmosphere while the simulation treats the gaseous phase as pure vapor. However, the governing processes act in the very thin gas layer underneath the droplet where the vapor generation rate is very high and quickly washes out the air. Therefore, the assumption of a gaseous phase consisting of pure vapor is justified. Due to the high temperature difference between the wall and the liquid-vapor interface, radiative heat transfer might also play an important role although it is not implemented in the boiling model. The radiative heat transfer between two parallel black bodies at 573.14 K (heater surface) and 373.15 K (saturation temperature) is around 5 kW/m^2. The actual radiative heat transfer between the wall and the liquid-vapor interface is even lower due to the absorption within the vapor layer and the fact that neither the heater surface nor the liquid-vapor interface are ideal black bodies. In contrast, the conductive heat transfer through the vapor layer can be estimated to be around 75 kW/m^2 for a vapor layer thickness of 100 μm. This estimation is based on the measured thickness of the vapor layer which is reported by Biance and co-workers [4]. Therefore, the evaporation process is governed by conductive heat transfer rather than radiative heat transfer and neglecting the latter is justified.

The axisymmetric mesh which is used for the simulation is shown in Figure 5.34. A very high mesh resolution is required in vertical direction directly at the heater surface in order to capture correctly the very thin vapor layer. The mesh consists of a single block with growing cell sizes in horizontal and vertical direction. The smallest cell in the lower left corner has a width of around 30 μm and a height of around 1.4 μm. The high aspect ratio of the cells is necessary to achieve the required mesh resolution across the vapor layer while keeping the total number of cells low. Due to the improved surface tension calculation procedure (see section 3.2.2), the high aspect ratio of the cells is not problematic for the calculation of the 2-phase flow dynamics.

Instead of performing multiple simulations with droplets of different size, only one simulation is performed during which the droplet grows from a radius of below 1 mm up to a radius of above 4 mm. An artificial volumetric mass source is imposed within the liquid, i.e. even though the liquid is evaporating the size of the droplet increases artificially during the simulation. This approach is chosen in order to reduce the computation time in comparison to performing multiple simulations with different droplet radii. In accordance to the approach of Biance and co-workers [4], the radius is defined as the distance between the center axis of the droplet and its perimeter (see Figure 5.35). The artificial volumetric mass source within the liquid is chosen such that the radius of the droplet reaches a value of 4 mm after around 0.08 s. As the growth of the droplet might potentially lead to results which are different from the results of a droplet with a steady radius, the simulation is repeated with a slower growth rate (radius of 4 mm reached after around 0.14 s). No difference is observed between the two simulations. Hence, the growth of the droplet is slow enough and the simulation is quasi-steady at all times.

The shape of the droplet at different times during the simulation is shown in Figure 5.35. As stated by Biance and co-workers [4], the shape of the droplet is almost spherical if the radius of the droplet is much smaller than the capillary length ($L_c = \sqrt{\sigma / \left[g \left(\rho_l - \rho_v \right) \right]} \approx 2.5$ mm for saturated water at 1 bar) while it becomes very flat for higher radii. It can also be seen that the thickness of the vapor layer increases with the droplet radius. The thickness of the vapor layer is not constant but a function of the radial coordinate. In particular for the larger droplet radii, there is a maximum thickness underneath the center of the droplet and a minimum close to its perimeter. The flow and the pressure within the vapor layer are shown in the blow-up of Figure 5.35. The vapor which is generated by the evaporation escapes to the side and creates a pressure drop due to its viscosity. The speed of the vapor flow can locally become as high as 3 m/s. As the thickness of the vapor layer is only in the range of 10 to 100 μm, the friction pressure drop is high and the pressure underneath the droplet compensates the gravitational acceleration of the droplet. The maximum thickness of the vapor layer underneath the center of the doplet is due to the high local pressure in the vapor phase at this location.

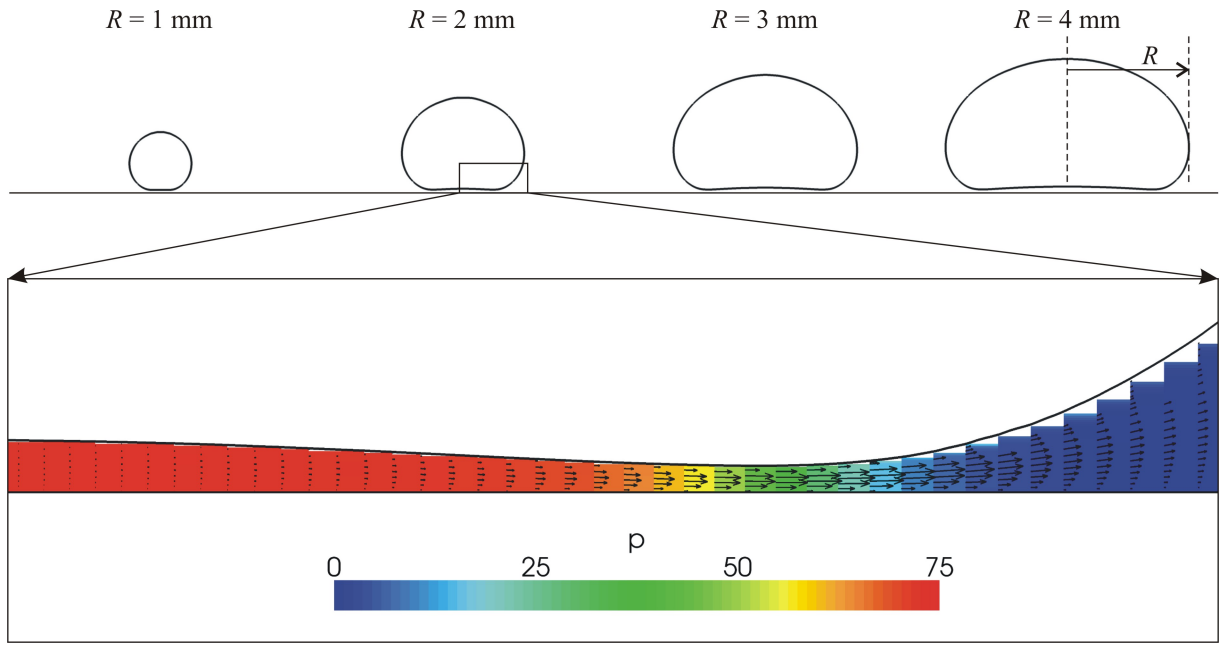

Figure 5.35: Droplet shape for different droplet radii and flow and pressure field (in Pa) within the vapor layer.

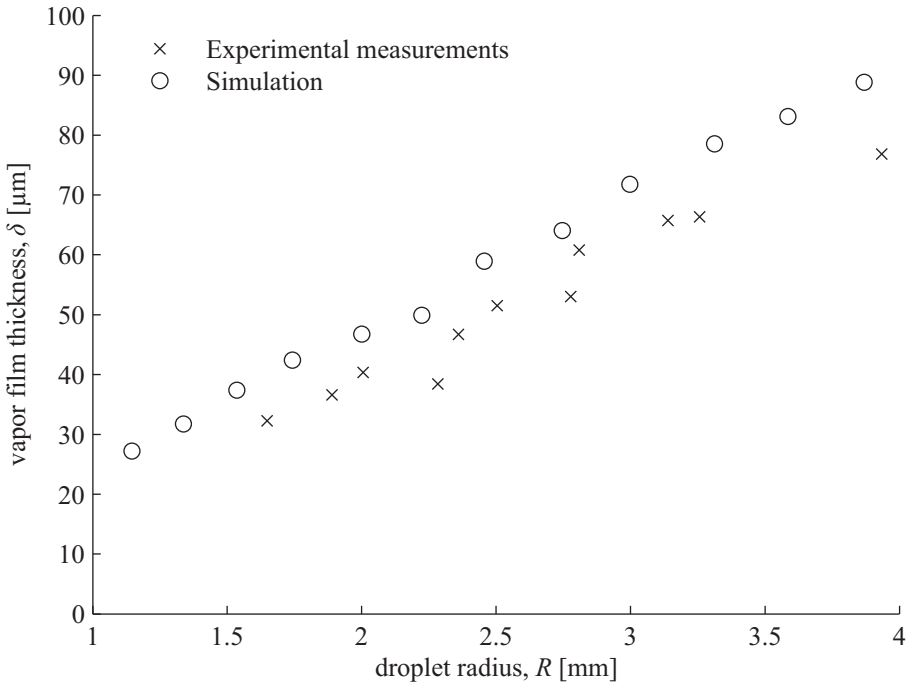

Figure 5.36: Thickness of the vapor layer as a function of the droplet size. Comparison between numerical simulation and experimental data of Biance and co-workers [4].

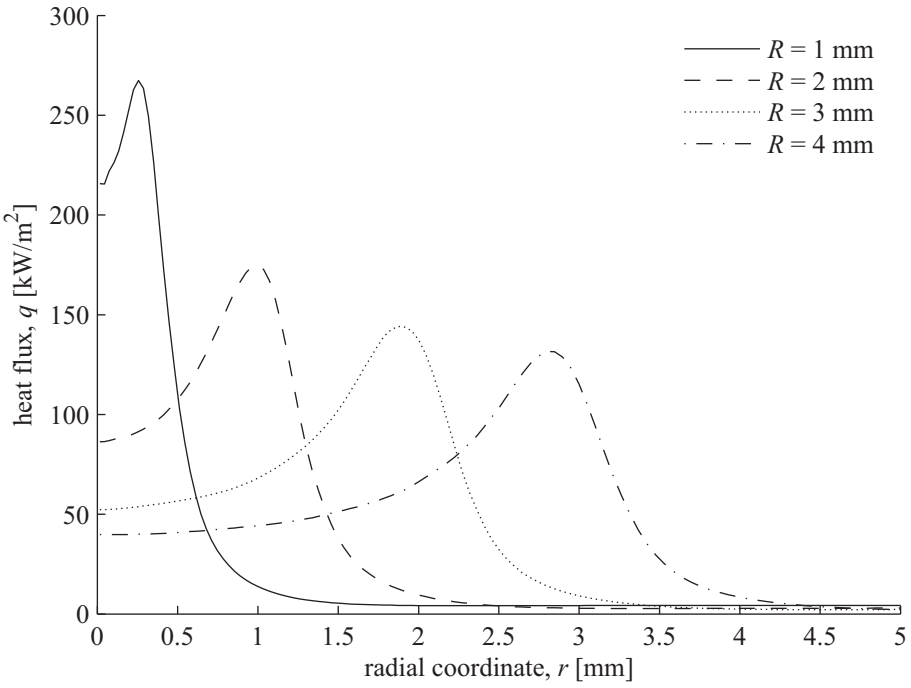

Figure 5.37: Heat flux profile at the heater surface underneath hovering Leidenfrost droplets of different size.

The thickness of the vapor layer as a function of the droplet radius is plotted in Figure 5.36. The simulation data which is shown here represents a mean thickness obtained by averaging the maximum and minimum thickness under the droplet center and its perimeter, respectively. The maximum and minimum thickness of the vapor layer are obtained from the simulation results by extracting the lowest y-coordinate of the cells containing pure liquid at the axis of symmetry (maximum thickness) and in the whole field (minimum thickness). Therefore, the thickness is only determined with an accuracy of approximately the height of the cells. This explains why the simulation data in Figure 5.36 shows significant fluctuations. Nevertheless, it can be seen that the thickness of the vapor layer strongly depends on and continuously increases with the droplet radius. The value of the vapor layer thickness and its growth with the droplet radius agrees nicely to the experimental data obtained by Biance and co-workers [4] who, unfortunately, do not give much information about the measurement uncertainties of the applied diffraction method.

The heat flux profile at the heater surface is shown in Figure 5.37. As expected, it is basically a function of the thickness of the vapor layer. There is a peak of the heat flux at the position of the minimum thickness of the vapor layer and a minimum of the heat flux underneath the center of the droplet where the thickness of the vapor layer has a maximum. The peak of the heat flux decreases with increasing droplet size which is a direct consequence of the increased thickness and hereby larger heat resistance of the vapor layer. The minimum of the heat flux underneath the center of the droplet becomes more pronounced as the size of the droplet increases. For a small radius ($R = 1\,\text{mm}$), the droplet is almost spherical and the thickness of the vapor layer under the center of the droplet is almost as small as the minimum thickness. Therefore, the minimum of the heat flux under the center of the droplet is not very pronounced. For large radii ($R = 4\,\text{mm}$), the thickness of the vapor layer under the center of the droplet is much larger than the minimum thickness. Therefore, the heat resistance of the vapor layer becomes large under the center of the droplet and the minimum of the heat flux at this position is much more pronounced compared to the case of a small droplet. The heat flux profiles also confirm the above rough estimation that the conductive heat flux is dominant over the radiative and convective heat transfer. The simulation does only take into account the conductive and convective heat

transfer. However, from the flow field in the lower part of Figure 5.35 one can easily see that there is no flow in vertical direction and therefore no convective heat transfer in vertical direction through the vapor layer. Hence, the heat flux profiles in Figure 5.37 represent pure conductive heat transfer. The mean heat flux averaged over the surface area underneath the droplet is around 60 to 80 $\mathrm{kW/m^2}$ depending on the droplet size. As mentioned above, the radiative heat transfer between two parallel black bodies at the temperatures which are used here can be estimated as 5 $\mathrm{kW/m^2}$ and is therefore at least one order of magnitude smaller than the heat transfer by conduction.

In summary, the simulation of the Leidenfrost droplet hovering over a highly superheated, smooth surface shows that the model correctly predicts the droplet shape and the thickness of the vapor layer. The boiling model does neither take into account the air in the gaseous phase nor the radiative heat transfer. However, these assumptions are justified as discussed above and as it is also confirmed by the nice agreement between the simulation results and the experimental data of Biance and co-workers [4]. Hence, the boiling model can be used with high accuracy not only for the simulation of nucleate boiling in various conditions but also for very high wall superheats when film boiling occurs.

Structured wall

The results for a droplet on a smooth wall which are discussed above could in principal also be obtained with a simulation that applies a subgrid scale model for the vapor layer. This is a common and very efficient modeling approach in this context as discussed above. However, in cases with a structured wall, such a model is not applicable as the vapor layer cannot be described by a thin, flat film. Linke and co-workers [64] have accomplished intensive experimental studies on droplets impacting on and hovering above highly superheated, structured walls. In most of their experiments, a wall with a sawtooth structure is used. Interestingly, they found that the droplets were accelerated in a preferred direction. This could be observed independently of the size of the droplets and of the exact geometry of the sawtooth structures. Linke and co-workers [64] explained this effect by a preferred escape direction of the vapor which is generated between the droplet and the wall. However, they could only suppose an explanation as the measurement techniques and resolution did not provide enough detailed insight into the process. Other effects which can *a priori* be responsible for the motion of the droplet are its deformation which could lead to a gradient of the capillary pressure or its bouncing motion which could be transferred into a horizontal motion due to the asymmetric shape of the surface structure.

Here, the dynamics of a droplet on a sawtooth structure is simulated to check the capability of the boiling model to predict the acceleration of the droplet. In the case of a successful prediction, the simulation results can be used to clarify what causes this acceleration of the droplet. According to one of the experiments performed by Linke and co-workers [64], a droplet with a diameter of 3 mm on a sawtooth structure with a width of 1.5 mm and a depth of 0.3 mm is simulated (see Figure 5.38). R134a at a pressure of 1 bar is used as fluid (see appendix A for material properties) and the wall temperature lies 96 K above the saturation temperature of -26.4° C. The simulation is performed in a 3D domain using only one plane of symmetry. First numerical tests showed that the thickness of the vapor layer can locally become very small. This is particularly valid at the peaks of the sawtooth structure. As the peaks are not infinitely sharp edges in the experiment, and in order to slightly simplify the numerical simulation, the peaks are assumed to be round with a radius of curvature of 20 μm. Preliminary results showed that, in spite of the roundness of the peaks, the distance between the liquid-vapor interface and the wall can still become as small as 2.5 μm at these peaks. Therefore, a very fine mesh must be used in the vicinity of the wall. To keep the total number of cells at a reasonable level, the mesh is chosen much coarser far away from the wall. This is achieved by using a base mesh which has already large differences in cell size and additionally applying adaptive mesh refinement at the liquid-vapor interface if it is very close to the wall.

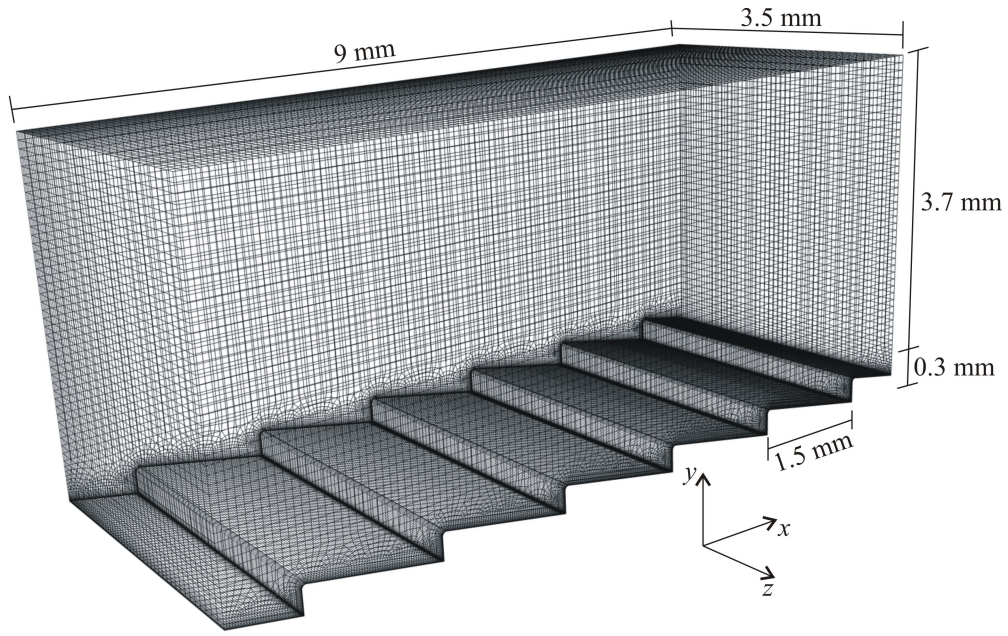

(a) Dimensions of the computational domain

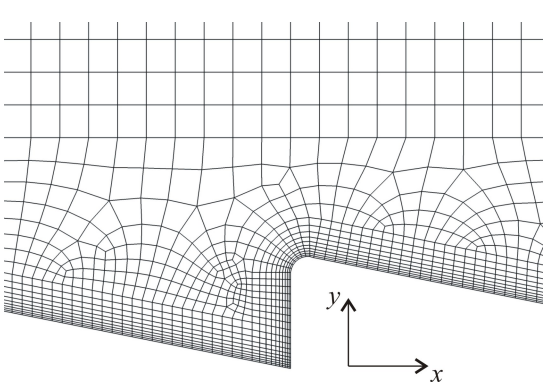

(b) x, y-view of the mesh (blow-up)

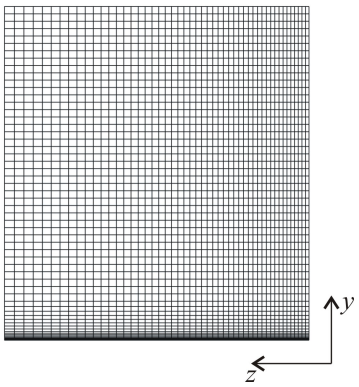

(c) y, z-view of the mesh

Figure 5.38: Computational domain and mesh which is used for the simulation of a Leidenfrost droplet on a structured wall.

The computational domain and its dimensions are shown in Figure 5.38(a). The mesh is first generated in the x, y-plane and then extruded into the z-direction. A blow-up of the mesh on the x, y-plane is shown in Figure 5.38(b). It consists of a highly resolved structured part very close to the wall, an intermediate unstructured part and a rather coarse structured part far away from the wall. The cells directly at the wall have a width of $10\,\mu$m (parallel to the wall) and a heigth of $4\,\mu$m (normal to the wall) while the cells in the structured part far away from the wall have a width and height of $75\,\mu$m. As mentioned above, the mesh is extruded in the third direction. The length of the cells in the third direction is $40\,\mu$m at the plane of symmetry (x, y-plane) and grow up to a maximum size of $100\,\mu$m at the side of the domain opposing the plane of symmetry. The y, z-view of the mesh is shown in Figure 5.38(c). The computational domain has a length of 9 mm (six sawtooth structures in x-direction), a heigth of 3.7 mm above the peaks of the structure (in y-direction) and a depth of 3.5 mm (in z-direction). The above mentioned adaptive mesh refinement is applied in a band of five cells around the liquid-vapor interface. The number of refinement steps depends on the distance of the liquid-vapor interface to the wall. If the distance is larger than $50\,\mu$m, no refinement is applied. One refinement is applied, if the distance is between $10\,\mu$m and $50\,\mu$m. Two refinements are applied if the distance is between $5\,\mu$m and

10 μm and three refinements are applied if the distance is below 5 μm. The adaptive mesh refinement leads to a minimum cell height of 0.5 μm (normal to the wall) in the cells which are directly at the wall. Thus, the mesh is locally fine enough to resolve the above mentioned minimum thickness of the vapor layer of approximately 2.5 μm. Only six sawtooth structures with a total length of 9 mm lie within the computational domain. This length is actually too short and the droplet would leave the domain before reaching its final speed. Increasing the length of the domain would lead to a higher number of cells. To avoid this, the length of 9 mm is kept and the mesh is moved relative to the droplet in steps of 3 mm once the droplet has come close to the end of the domain. The mesh is moved three times during the whole simulation. Thus, the droplet can move by a total length of around 13 mm.

The shape of the droplet during the impact on the surface is shown in Figure 5.39(a). The volume fraction field is represented by a grayscale coloring of the cell values with no interpolation between the cells. Thus, the grainy appearance in the top part of the droplet is an immediate result of the coarse mesh resolution in this region. In contrast, the interface appears much sharper in the vicinity of the wall which is explained by the fine mesh resolution at the wall. The simulation starts with a spherical droplet located directly above one of the peaks of the sawtooth structure. Initially, the droplet is at rest and is accelerated towards the wall only by gravitation. The impact of the rather large droplet (compared to the capillary length of $L_c = \sqrt{\sigma / \left[g \left(\rho_l - \rho_v \right) \right]} \approx 1.1$ mm for R134a at a pressure of 1 bar) on the peak of the structure leads to a large deformation of the droplet and a breakup into a ring (see image at 30 ms). However, this breakup lasts only for a very short time and the ring merges into a droplet again. In the following, the droplet dynamics is governed by the bouncing motion of the droplet. However, it can also be seen in Figure 5.39(a) that the droplet starts to move after some time (e.g., see image at 120 ms compared to image at 20 ms). The mean acceleration of the droplet is between 0.1 and 0.2 m/s^2 which is in excellent agreement to the measurements of Linke and co-workers [64] who report values between 0.15 and 0.2 m/s^2. While the droplet moves over the sawtooth structures, the vertical oscillations decay and the dynamics becomes more and more governed by the motion of the droplet over the sawteeth. The shape of the droplet in this regime is shown in Figure 5.39(b). At this time the droplet has almost reached its terminal speed and the dynamics become periodic. The sequence of the pictures in Figure 5.39(b) show that the motion of the front of the droplet slows down slightly when the peak of a sawtooth is reached at a time of 400 ms. The front of the droplet remains close to the peak for some time and then overcomes the peak at a time of around 416 ms. Once the front of the droplet has overcome the peak, it moves quickly to the next peak where it arrives at a time of around 440 ms.

The position of the center of gravity of the droplet in x-direction and its height in y-direction and width in z-direction are shown in Figure 5.40. It can clearly be seen that the droplet is strongly accelerated at the beginning of the simulation. After some time, the droplet speed reaches an almost constant value resulting in an almost constant slope of the curve for the x-position of the center of gravity. The simulation was run for a physical time of 0.48 s. At this time, the speed of the droplet oscillates around a value of approximately 43 mm/s but does not change globally any more. The predicted speed of the droplet is higher than the values observed in the experiment of Linke and co-workers [64] who measured a final velocity of around 37 mm/s. The deviation is most probably due to the assumption of a pure vapor atmosphere around the droplet. The dynamic viscosity of pure R134a vapor is much smaller than the dynamic viscosity of pure air which can possibly lead to a higher final velocity in the simulation. The width of the droplet is obtained by measuring the extend of the droplet in z-direction while the height is obtained by measuring the highest point of the droplet above the peaks of the wall. The height and the width of the droplet oscillate strongly at the beginning of the simulation which is due to the initial impact on the wall. The magnitude of these oscillations decays with time and is very small at the end of the simulation. It can thus be concluded that the dynamics of the droplet at the end of the simulation is not much affected by the initial impact anymore but only by the motion of the droplet across the sawteeth.

As mentioned above, the vapor flow and the shear stress which the vapor flow imposes on the droplet are suggested to cause its acceleration. In order to check this suggestion, the flow field in the vapor

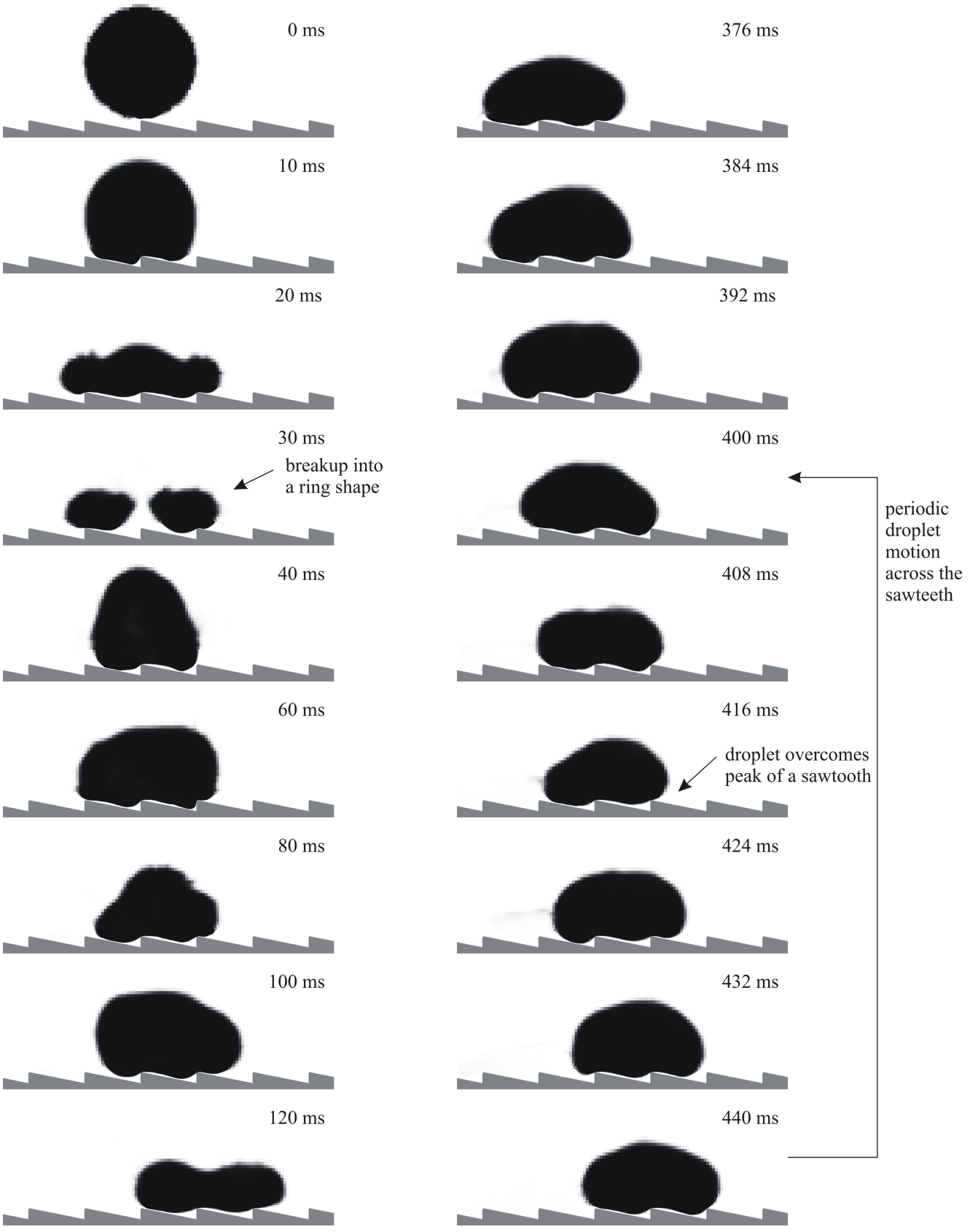

Figure 5.39: Droplet shape (on the plane of symmetry) during the initial impact on the wall (0 to 120 ms, left column) and during the motion over a sawtooth (376 to 440 ms, right column).

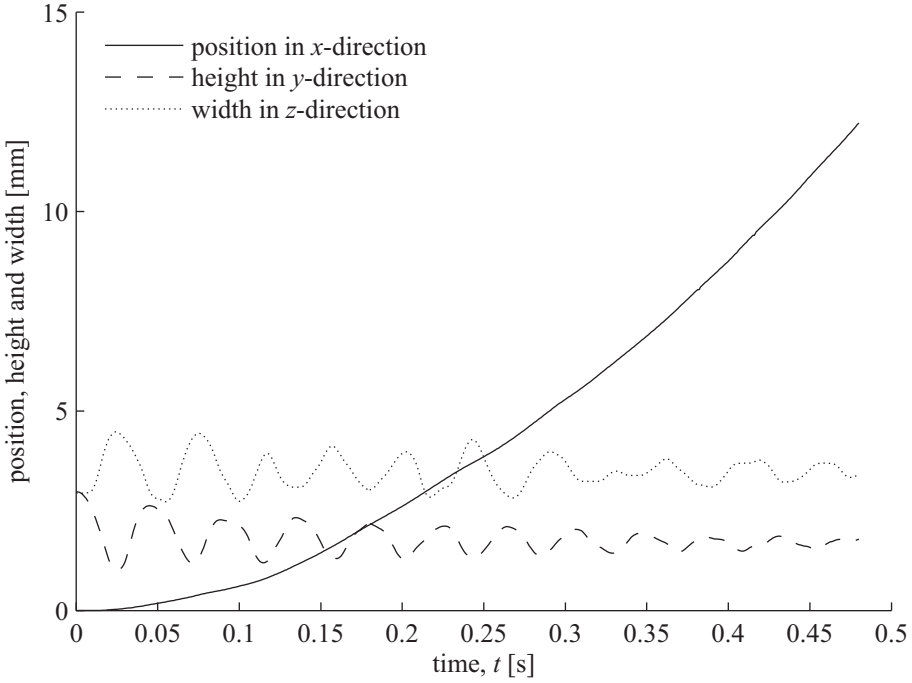

Figure 5.40: Position of the center of gravity of the droplet in x-direction and of its height and width in y-direction and z-direction, respectively.

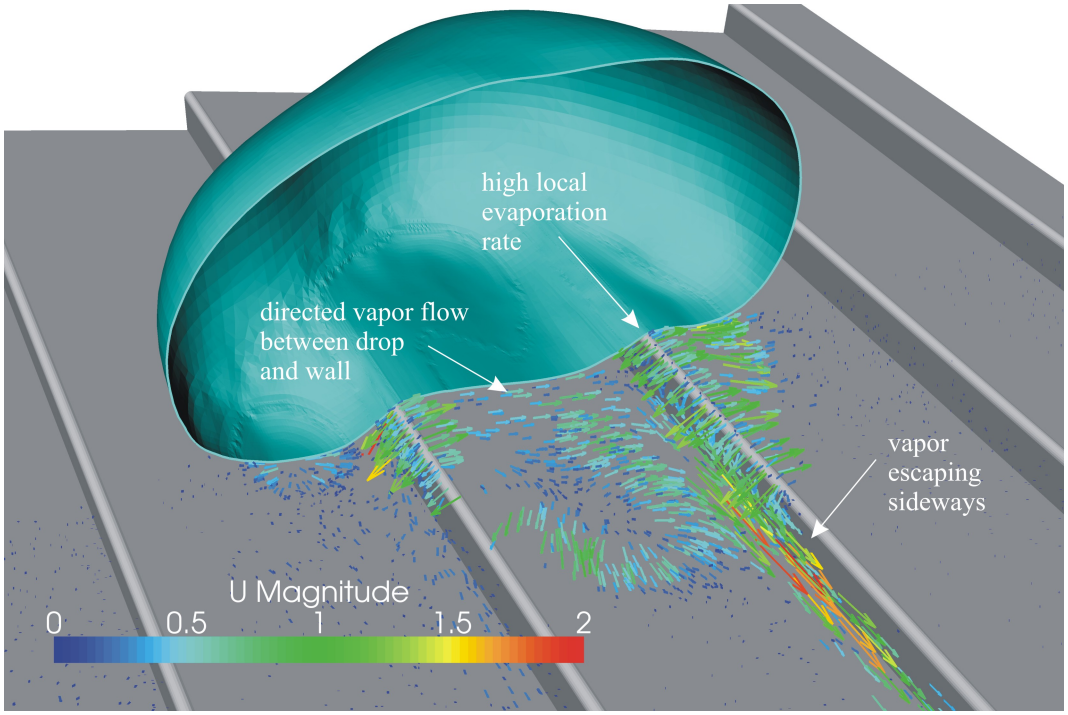

Figure 5.41: Visualization of the droplet and the vapor flow between the droplet and the wall at 424 ms (velocity is given in m/s).

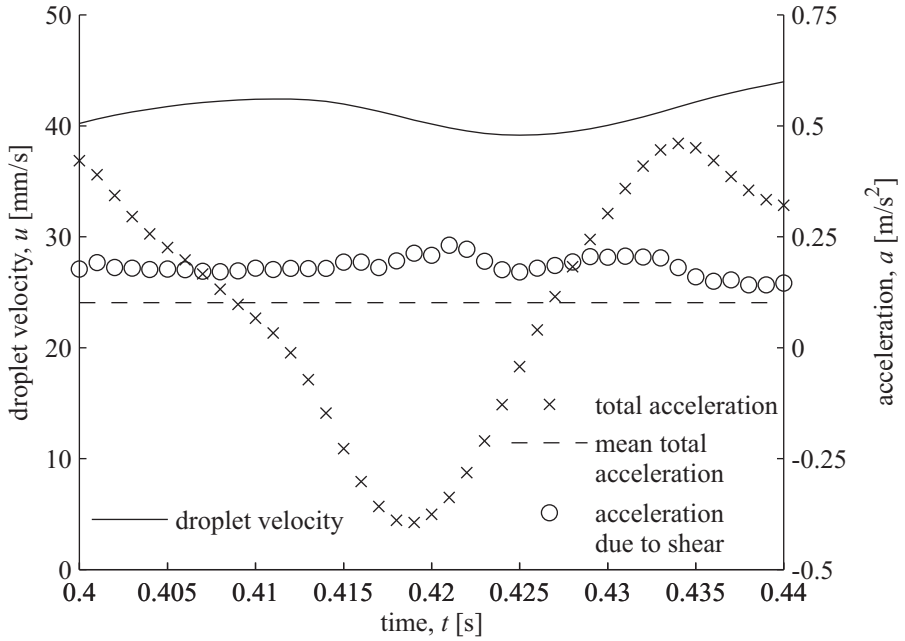

Figure 5.42: Oscillation of the droplet speed, the total acceleration required for the change of the speed and the acceleration which is due to the shear rate at the liquid-vapor interface between 400 and 440 ms (see also Figure 5.39(b)).

predicted by the simulation is analyzed and shown in Figure 5.41. It can clearly be seen that most of the vapor is generated above the peaks of the sawtooth structure where the thickness of the vapor layer is very small. The vapor which is generated locally at these positions can either flow directly down into the valley of the structure which is on the left side of the peak or flow between the liquid-vapor interface and the wall down into the valley of the structure which is on the right side of the peak. Both possible ways of the vapor flow are visible in Figure 5.41. The vapor which flows into the valley which is on the left side of the peak can directly escape to the side (in z-direction) without imposing any shear stress on the droplet. In contrast, the vapor which flows into the other direction must flow between the liquid-vapor interface and the wall for a rather long distance before it reaches the valley of the structure and escapes to the side. Hence, only the vapor which flows to the right imposes a shear stress on the droplet. This causes an acceleration of the droplet to the right. The velocity of the droplet between 400 and 440 ms is plotted in Figure 5.42. It can be seen that the velocity of the droplet oscillates as the droplet moves across the sawteeth. The total acceleration of the droplet results from the sum of all forces that act on the droplet. It can be calculated from the time derivative of the velocity $a = \mathrm{d}u/\mathrm{d}t$ and is also plotted in Figure 5.42. The value of the total acceleration of the droplet oscillates between positive values up to $0.5\,\mathrm{m/s^2}$ and negative values down to $-0.37\,\mathrm{m/s^2}$. The negative acceleration results from the short stagnation of the front of the droplet when it arrives at a peak of a sawtooth which is mentioned above. The pressure which is generated locally due to the vapor generation between the liquid-vapor interface and the peak of the sawtooth pushes against the droplet in opposite direction of its motion direction. The forces acting on the droplet can be subdivided into the pressure (including capillary pressure) which acts in normal direction of the liquid-vapor interface and the shear rate which acts in tangential direction of the liquid-vapor interface. The acceleration which results from the shear rate is also plotted in Figure 5.42. It can be seen that the shear force which the vapor flow imposes on the droplet generates an almost constant acceleration of the droplet in its direction of motion while the pressure which acts normal to the liquid-vapor interface generates positive and negative accelerations. The sum of the two influences results in the total acceleration of the droplet which also oscillates between positive and negative values.

The mean total acceleration is positive and of the same size as the acceleration due to the shear stress. This leads to the conclusion that the shear stress is the driving mechanism for the motion of the droplet. Thus, the results of the simulation confirm the suggestion of Linke and co-workers [64] and observations which are reported in a very recent publication of Lagubeau and co-workers [61]. These authors showed that the self-propelling effect can also be observed for solid disks of dry ice which are deposited on a similar sawtooth structure. As these solid disks have a constant shape, all potential causes of the droplet motion which are related to its deformation can be excluded. Hence, the droplet motion seems to be primarily caused by the vapor flow. However, Lagubeau and co-workers [61] suggest an inversed vapor flow (jet thrust) compared to the suggestion of Linke and co-workers [64] and to the simulation results presented above. This contradiction shows how valuable the simuations are for a detailed analysis and a better understanding of the physics.

The excellent qualitative and very satisfying quantitative agreement between the simulation and the experimental results of Linke and co-workers [64] proves the capability of the boiling model to accurately predict highly complex flows with phase change. The strongly coupled interaction between the capillary forces that govern the shape of the droplet, the evaporation due to the heat conduction through the vapor layer and the vapor flow which generates an increased pressure, keeps the droplet hovering over the wall and accelerates it into a preferred direction of motion.

6 Summary and outlook

The work that has been accomplished within the present thesis can be subdivided into two parts which will be summarized in the following: First, the development, implementation and validation of the boiling model and second, the numerical simulation and analysis of different boiling phenomena.

6.1 Model development, implementation and validation

The boiling model which has been developed meets all the requirements and goals that are formulated in the introduction of the present thesis. It resolves all length and time scales that are relevant for boiling phenomena, in particular close to the 3-phase contact line, takes into account the transient heat conduction in the solid, enables the simulation of 2-phase flows with high interface distortion and can be used for 3D simulations in complex geometries. The boiling model consists of a whole set of sub-models. Some of these sub-models were entirely developed within the present thesis while others are established models which were only implemented in either *OpenFOAM* or *Matlab*. Hence, the boiling model is a conjuction of new ideas and of a recombination of established models. The basis of the boiling model is the *Volume-of-Fluid* solver of *OpenFOAM* which can be used for the simulation of 2-phase flows without phase change. In the following, the major modifications and extensions which were applied upon this basis are summarized. The distinction between new ideas and established models is accentuated in order to clarify which parts of the work can be attributed to the present thesis.

- **Phase change at the liquid-vapor interface**
  In a first step, the phase change model which was developed by Hardt and Wondra [28] was implemented and used without any modification. This model consists of the calculation of the local rate of phase change and of a procedure which transforms the local rate of phase change into a continuum-field representation of source terms. In the present thesis, an interface reconstruction algorithm was developed and implemented in order to calculate the local rate of phase change more accurately, and only the procedure for the transformation of the source terms was kept from the original approach of Hardt and Wondra [28]. By this modification, the required mesh resolution could be reduced by a factor of 4 while conserving the level of accuracy in boiling conditions. An additional benefit of the reconstruction algorithm is the amelioration of the curvature calculation which leads to a significant reduction of parasitic currents in surface tension dominated flows.
- **Microscale heat and mass transfer at the 3-phase contact line**
  The contact line evaporation model of Stephan and Busse [108] is used to describe the microscale heat and mass transfer at the 3-phase contact line which is of utmost importance for the correct modeling of boiling phenomena. This model was implemented in *Matlab* without any modifications. In the present thesis, a strategy was developed for the coupling between the contact line evaporation model and the CFD simulation of boiling processes. In order to save computational resources, the results of the contact line evaporation model are parameterized prior to the CFD simulation by use of a correlation. The parameterized results are then used to locally correct the heat transfer predicted by the CFD simulation. A transition region was defined in order to match the length scale at which the contact line model and the CFD simulation are coupled. Thus, the very same set of parameterized results can be used for CFD simulations with different mesh resolution.
- **Conjugate heat transfer between solid and fluid**
  The transient heat conduction within the solid heater wall can be important for the boiling process

and should thus be taken into account by the boiling model. A straightforward approach with separate meshes for the solid and fluid domain and a coupling of the domains by iterative exchange of boundary conditions at the solid-fluid interface was implemented. The simplicity of this approach provides a large flexibility with respect to a local manipulation of the conjugate heat transfer. Such a manipulation is required for the local correction of the heat transfer during the coupling of the contact line evaporation model to the CFD simulation.

All the aforementioned sub-models were implemented in *OpenFOAM* (except the model of Stephan and Busse [108] which is implemented in *Matlab*) and several validation simulations were performed to check the correctness and performance of the boiling model. In particular, the simulation of a one-dimensional phase change problem and the simulation of vapor bubbles growing in an infinetely extended superheated liquid show that the sub-model for phase change correctly predicts the evaporation at the liquid-vapor interface. The sub-model for the evaporation at the 3-phase contact line as well as the coupling of the heat transfer within solid and fluid were tested during the simulation of a liquid meniscus evaporating in a triangular heat pipe groove which also showed excellent results.

6.2 Numerical simulation and analysis of boiling phenomena

The focus of the simulations was on nucleate pool boiling. In this context, the boiling model was used for the simulation of nucleate boiling at artificial nucleation sites. The material properties and the boundary conditions were chosen according to a highly resolved experiment of Wagner and co-workers [120]. Good agreement between the simulation results and the experiment could be found. In particular, the local heat transfer in the vicinity of the 3-phase contact line and the resulting local cooling of the heater are predicted very accurately by the boiling model. The high temporal and spatial resolution of the simulation enables a very detailed analysis of the heat transfer mechanism and extends the understanding that could be achieved with the highly resolved experiment. Thus, it was possible to identify the different heat transfer paths which were also reported by Schweizer [93] who performed pool boiling experiments in a reduced gravity environment, thus expanding the temporal and spatial resolution. In his experiment, evidence was found that the local heat transfer in the vicinity of the 3-phase contact line during bubble detachment is a superposition of microscale heat transfer at the 3-phase contact line and transient conduction close to the 3-phase contact line. The simulation allows a detailed analysis of the local temperature and velocity fields. This analysis clearly shows that the advancing motion of the 3-phase contact line during bubble detachment leads to an accumulation of rather cold liquid at the wall next to the 3-phase contact line. This micro-convection enhances the local heat transfer from the heater into the liquid and is the origin of the transient conduction phenomenon. Thus, two main conclusions can be drawn from the simulation of nucleate pool boiling. First, the correctness and accuracy of the boiling model is confirmed once more and the results support the excellent level of agreement that was found for the validation cases. Second, it was shown that the simulation of nucleate pool boiling enables a very detailed insight into the process and leads to a more comprehensive understanding of the complex transient heat and mass transfer.

In addition to the aforementioned simulation of pool boiling at an artificial nucleation site, the lateral merger of two bubbles growing at neighboring nucleation sites was simulated. Such bubble mergers were experimentally investigated by Wagner [117] as well as Schweizer and Stephan [94]. In both works, the calculated heat flux field at the heater surface showed an interesting feature: Two concentric rings of high heat flux were observed shortly after the merger. A ring of high heat flux indicates the existance of a 3-phase contact line and thus, it was concluded that a droplet exists within the merged bubble. The simulation results fully confirm this conclusion and correctly predict the formation of a droplet within the merged bubble. The simulation results are analyzed with respect to the bubble dynamics during the merger. Thus, the formation of the droplet can be visualized and understood while the experimental investigation could only show the existence of the droplet. A detailed experimental investigation of

the droplet formation would not have been possible. Again, two conclusions can be drawn from the simulation results. First, the capability of the boiling model to predict highly complex and dynamic boiling flows was confirmed. The second and even more important conclusion is that the simulation results enable a detailed insight into the process far beyond the experimental measurement resolution. Thus, the simulation could significantly increase the level of understanding which was already achieved by the experimental investigation.

In order to show the capabilities of the boiling model and its wide range of potential applications, additional simulations were performed on flow boiling in a near-wall shear flow, boiling in a structured microchannel and on droplets in the film boiling regime (Leidenfrost phenomenon). Again, excellent qualitative and quantitative agreement to experimental and numerical data available in literature was found. Further, the analysis of the simulation results was used to gain a better understanding of the heat transfer mechanisms and the fluid dynamics. The simulation of a self-propelled droplet on a highly superheated, structured wall in the film boiling regime is an excellent example for such a gain of understanding. The simulation results show the same effect of self-propulsion as it was observed experimentally by Linke and co-workers [64], thus confirming the correctness of the boiling model and providing detailed insight into the phenomenon. In contrast to the experiment, the flow dynamics and the heat transfer can be observed with a very high spatial and temporal resolution at any point within the computational domain. In the particular case of the self-propelled droplet, the simulation results could be used to clarify the cause of the droplet motion while only suggestive conclusions could be drawn from the experiment.

In summary, the simulations confirmed that the boiling model is a highly valuable tool which can be used for fundamental as well as for application oriented research. A large amount of the work that was accomplished within the framework of the present thesis was related to the development and implementation of the boiling model. The simulation results that were obtained are highly interesting, they match experimental observations and they lead to a more comprehensive understanding of boiling heat transfer. Nevertheless, they should be seen as a first step towards a more intensive numerical investigation of various boiling flows. In contrast to the present thesis, future work can focus more directly on the simulations and their physical analysis rather than model development and implementation.

6.3 Outlook on ongoing work and potential future projects

In the present thesis, the boiling model was developed, implemented, validated and tested. The boiling model is now ready to be applied in a number of ongoing and future research activities. As mentioned above, the focus of the future work with the boiling model will be on the simulations and on the physical analysis of the results. Nevertheless, in many cases the model will have to be slightly adapted, modified or extended. The required changes will, of course, depend strongly on the specific problem. However, there are several potential improvements of the model that can already be derived from the simulations that have been performed within the present thesis.

First, it was found that the contact angle and its dynamics can strongly influence the simulation results, e.g. in flow boiling conditions. In the current version, the user must choose a value for the static contact angle and, if required, an equation for the dependence of the contact angle on the displacement speed of the 3-phase contact line. The model can thus reproduce contact angle dynamics and even contact angle hysteresis. However, in its current version, the modeling approach is not founded on a physical basis. Future work should be aimed at the development of a more physically based modeling approach for the contact angle. A promising approach is to use the contact angle which is predicted by the subgrid scale model for the heat and fluid flow at the 3-phase contact line. A lot of this work

will surely be accomplished within the research project *SFB-TRR 75*[1] in which the Institute of Technical Thermodynamics of Technische Universität Darmstadt is involved. Within this research project, the subgrid scale model was already extended to moving contact lines and will be further adapted to also take into account chemically heterogeneous and nanostructured surfaces.

A second potential improvement of the boiling model is to incorporate the effects of an inert gas in the gaseous phase. For nucleate boiling conditions, the gaseous phase consists of almost pure vapor. However, in many other configurations of evaporating 2-phase flows (e.g. evaporating droplets), the gaseous phase is a mixture of an inert gas (typically air) and vapor. The inert gas leads to a decrease of the partial pressure of the vapor and hereby to a decrease of the saturation temperature. Further, the bulk material properties of the gaseous phase can significantly differ from the material properties of the pure vapor. In spite of the assumption of a pure vapor atmosphere, good results could be obtained for the simulations on droplets in the film boiling regime. Nevertheless, the consideration of the inert gas would certainly increase the accuracy of the results. As the above mentioned research project *SFB-TRR 75* is focussed on droplet dynamics, the extension of the boiling model to a mixture of an inert gas and vapor will certainly be accomplished within its framework.

The detailed and physically correct modeling of the nucleation process represents a third possible improvement of the boiling model. However, compared to the other two improvements, this work package is not yet scheduled to be incorporated within a particular research project. Within the present thesis, a constant waiting time between two consecutive bubbles was prescribed in default of a physically based sub-model for the nucleation process. There is some theoretical research on the nucleation process (see Carey [6]). However, the criteria for the activation of a particular nucleation site and their dependence on the geometry of the nucleation site are still not understood and therefore, the implementation of a physically based sub-model for the nucleation process into the boiling model is not straightforward. Nevertheless, it should be checked if the established models which are available in literature can be implemented into the boiling model.

In addition to the above mentioned *SFB-TRR 75* research project, the boiling model is currently used for an analysis of the Leidenfrost phenomenon which is more detailed than the simulations presented here. In particular, the dynamics of Leidenfrost droplets on smooth surfaces will be analyzed more quantitatively in order to further check and validate the capabilities of the boiling model. Additionally, the analysis of self-propelled Leidenfrost droplets on structured surfaces is ongoing. Here, the focus is on the reduction of the computational effort with the aim to enable parametric studies of the phenomenon. Another potential future field of application for the boiling model can be the further investigation of boiling in complex geometries. Such complex geometries could be porous media, micro-structured tube evaporators (e.g. with sub-surface channels as experimentally investigated by Stephan and Wondra [107]) or the structured microchannel for which preliminary simulations were already performed within the framework of the present thesis. The detailed analysis of boiling in complex geometries requires 3D simulations and a high flexibility regarding the mesh. The boiling model has proven to be applicable on unstructured and non-orthogonal meshes, is compatible to the adaptive mesh refinement algorithm of *OpenFOAM* and can be used for parallel computations. Thus, the boiling model fulfills all the above mentioned requirements and is ready to be used for the detailed analysis of boiling in complex geometries.

[1] *SFB-TRR 75* is an abbreviation for *Sonderforschungsbereich Transregio 75* which focusses on droplet dynamics under extreme ambient conditions. In particular, M.Sc. Stefan Herbert works on this topic on behalf of the Institute of Technical Thermodynamics.

A Material properties

		density [kg/m^3]	**specific heat capacity** [J/(kg K)]	**thermal conductivity** [W/(m K]	**kinematic viscosity** [m^2/s]	**surface tension** [N/m]	**enthalpy of vaporization** [J/kg]
Water	*liquid*	958.35	4217	0.6791	$0.294 \cdot 10^{-6}$	0.0589	$2256.5 \cdot 10^3$
(1.013 bar, 100 °C)	*vapor*	0.59814	2077	0.0251	$20.51 \cdot 10^{-6}$		
HFE-7100[a]	*liquid*	1447.99	1212.6	0.0659	0.3246	0.0136	$118.06 \cdot 10^3$
(0.5 bar, 39.8 °C)	*vapor*	4.975	870	0.01[b]	$1.4 \cdot 10^{-6}$		
R134a	*liquid*	1377.6	1280	0.105	0.267	0.01548	$217.16 \cdot 10^3$
(1.013 bar, -26.37 °C)	*vapor*	5.19	793	0.00949	$1.91 \cdot 10^{-6}$		
Ammonia	*liquid*	600	4809.5	0.477	0.217	0.0202	$1155.95 \cdot 10^3$
(11 bar, 26.85 °C)	*vapor*	8.547	3195	0.0267	$1.16 \cdot 10^{-6}$		
Aluminum	*solid*	2700	856.7	235.7			
Steel[c]	*solid*	7840	460	15			

Table A.1: Physical properties of the fluid and solid materials that are used in the simulations. If not marked otherwise, the material properties are taken from [70]. Liquid and vapor properties are taken at saturation conditions.

[a] Material properties are taken from 3M datasheets.

[b] This property is estimated because no reliable data is available and its influence on the simulation results is negligible.

[c] These properties depend on the composition of the steel. The values that are used here represent average values.

B Overview of the boiling model

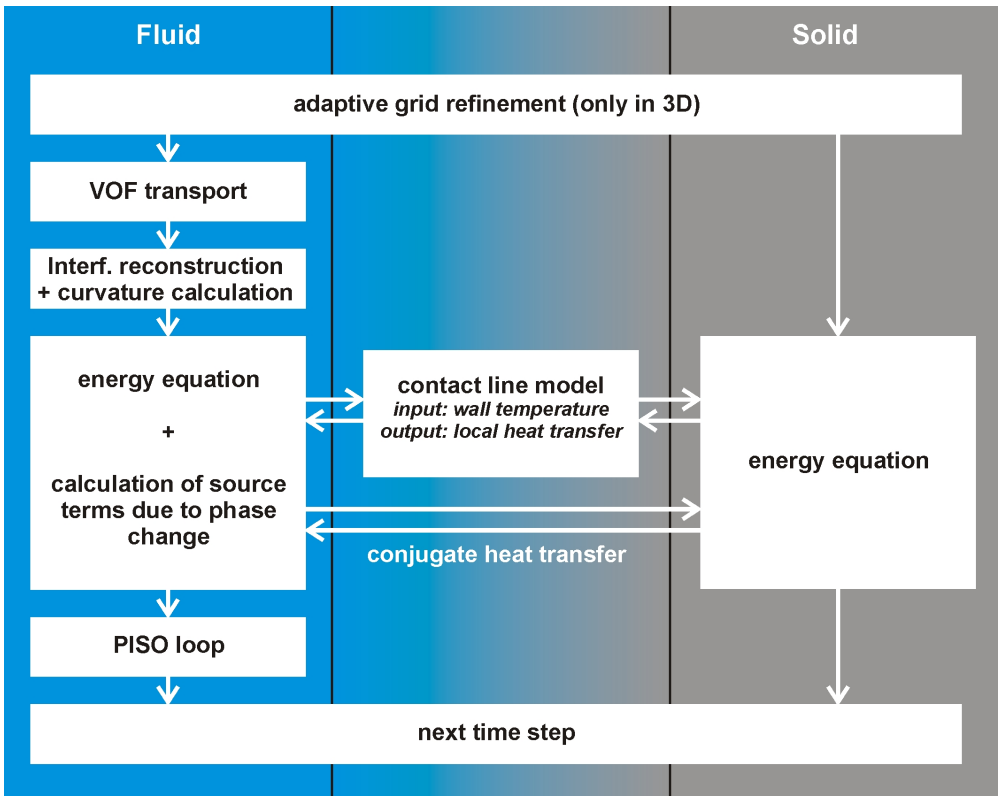

Figure B.1: Overview of the boiling model: Sub-steps which are performed within one time step and coupling of heat transfer in solid and fluid by conjugate heat transfer and subgrid scale model for the evaporation at the 3-phase contact line.

C Correlation coefficients for contact line evaporation model

i	$a_{Q,i}$	$a_{\theta,i}$	$a_{\delta,i}$
1	-1.052097·10^{+0}	1.216592·10^{-1}	1.510259·10^{-9}
2	6.120384·10^{+2}	-1.188287·10^{+2}	1.488864·10^{-7}
3	-1.762533·10^{+4}	4.949978·10^{+3}	-1.103309·10^{-5}
4	1.548371·10^{+5}	-5.138412·10^{+4}	1.376620·10^{-4}
5	-5.707494·10^{+5}	2.093512·10^{+5}	-6.077290·10^{-4}
6	1.000734·10^{+6}	-3.925187·10^{+5}	1.190254·10^{-3}
7	-8.287453·10^{+5}	3.411686·10^{+5}	-1.061506·10^{-3}
8	2.609429·10^{+5}	-1.114348·10^{+5}	3.523133·10^{-4}

Table C.1: Correlation coefficients for water at 1 bar ($\xi_{\mathrm{mic}} = 0.5\,\mu\mathrm{m}$, $\Delta T = T_{\mathrm{wall}} - T_{\mathrm{sat}} = 0.1 \ldots 20\,\mathrm{K}$)

i	$a_{Q,i}$	$a_{\theta,i}$	$a_{\delta,i}$
1	-1.986240·10^{-1}	1.100199·10^{-1}	7.932350·10^{-11}
2	1.021029e·10^{+2}	-1.355099·10^{+2}	1.469089·10^{-6}
3	-2.891267·10^{+3}	6.065227·10^{+3}	-6.532326·10^{-5}
4	2.527213·10^{+4}	-6.563762·10^{+4}	6.965052·10^{-4}
5	-9.292321·10^{+4}	2.743023·10^{+5}	-2.865719·10^{-3}
6	1.626841·10^{+5}	-5.231156·10^{+5}	5.394978·10^{-3}
7	-1.345908·10^{+5}	4.602403·10^{+5}	-4.694837·10^{-3}
8	4.234802·10^{+5}	-1.517037·10^{+5}	1.533051·10^{-3}

Table C.2: Correlation coefficients for HFE-7100 at 0.5 bar ($\xi_{\mathrm{mic}} = 0.5\,\mu\mathrm{m}$, $\Delta T = T_{\mathrm{wall}} - T_{\mathrm{sat}} = 0.1 \ldots 20\,\mathrm{K}$)

i	$a_{Q,i}$	$a_{\theta,i}$	$a_{\delta,i}$
1	-1.002965·10^{+0}	8.699869·10^{-3}	-2.636927·10^{-9}
2	3.217080·10^{+2}	-4.586789·10^{+0}	3.672211·10^{-6}
3	-7.002331·10^{+3}	1.574134·10^{+2}	-1.250036·10^{-4}
4	5.390965·10^{+4}	-1.480183·10^{+3}	1.164062·10^{-3}
5	-1.836652·10^{+5}	5.670714·10^{+3}	-4.410402·10^{-3}
6	3.055467·10^{+5}	-1.019403·10^{+4}	7.855184·10^{-3}
7	-2.436986·10^{+5}	8.592831·10^{+3}	-6.568381·10^{-9}
8	7.459548·10^{+4}	-2.741850·10^{+3}	2.081188·10^{-3}

Table C.3: Correlation coefficients for ammonia at 11 bar ($\xi_{\mathrm{mic}} = 0.5\,\mu\mathrm{m}$, $\Delta T = T_{\mathrm{wall}} - T_{\mathrm{sat}} = 0.1 \ldots 20\,\mathrm{K}$)

D Numerical schemes

Operator	Variable	Scheme[ab]
Time derivative, $\mathrm{d}\Phi/\mathrm{d}t$	default	Euler implicit
Gradient, $\nabla\Phi$	default	Gauss linear
Divergence, $\nabla\cdot\Phi$	default $\rho\vec{u}\vec{u}$ $\vec{u}F$ $c_F\,\lvert\vec{u}\rvert\,\vec{n}\,[F\,(F-1)]\,F$	Gauss linear Gauss upwind Gauss vanLeer Gauss interfaceCompression
Laplacian, $\nabla\cdot\nabla\Phi$	default	Gauss linear corrected
Surface normal gradient, $\nabla\Phi\vec{n}_f$	default	corrected

Table D.1: Numerical discretizeation schemes which are used within the present thesis.

[a] The name of the schemes which are given here correspond to the names of the schemes in *OpenFOAM*. Detailed information about the schemes can be found in the documentation and the source code of *OpenFOAM* (see http://www.openfoam.com).

[b] Numerical experiments showed that the results could in principal be ameliorated by adjusting the schemes in some cases. The set of schemes which is shown here has proven to be appropriate for all cases which were simulated within the framework of the present thesis, although it might not necessarily represent the optimum choice.

Bibliography

[1] A. Alke and D. Bothe. 3D numerical modelling of soluble surfactant at fluidic interfaces based on the Volume-of-Fluid method. *Fluid Dynamics & Materials Processing*, 5:345–372, 2009.

[2] S. Ata. Coalescence of bubbles covered by particles. *Langmuir*, 24:6085–6091, 2008.

[3] S. aus der Wiesche. Bubble growth and departure during nucleate boiling: The occurrence of heat flux reversal. In *Proceedings of the 4th International Conference on Computational Heat and Mass Transfer*, 2005.

[4] A.-L. Biance, C. Clanet, and D. Quéré. Leidenfrost drops. *Physics of Fluids*, 15:1632–1637, 2003.

[5] J. U. Brackbill, D. B. Koethe, and C. Zemach. A continuum method for modeling surface tension. *Journal of Computational Physics*, 100:335–354, 1992.

[6] V. P. Carey. *Liquid-Vapor Phase-Change Phenomena*. McGraw-Hill, 1992.

[7] R. Cole. Bubble frequencies and departure volumes at subatmospheric pressures. *AIChE Journal*, 13:779–783, 1967.

[8] M. G. Cooper and A. J. P. Lloyd. The microlayer in nucleate pool boiling. *International Journal of Heat and Mass Transfer*, 12:895–913, 1969.

[9] P. Delgoshaei and J. Kim. Microscale heat transfer measurements during subcooled pool boiling of pentane: Effect of bubble dynamics. In *Proceedings of the 14th International Heat Transfer Conference IHTC14*, 2010.

[10] F. Demiray and J. Kim. Microscale heat transfer measurements during pool boiling of FC-72: Effect of subcooling. *International Journal of Heat and Mass Transfer*, 47:3257–3268, 2004.

[11] V. K. Dhir. Boiling heat transfer. *Annual Review of Fluid Mechanics*, 30:365–401, 1998.

[12] V. K. Dhir. Numerical simulations of pool-boiling heat transfer. *AIChE Journal*, 47:813–834, 2001.

[13] G. Duhar. *Croissance et détachement de bulles en paroi d'un écoulement cisaillé: Etude expérimentale de l'injection et de l'éullition nucléée*. PhD thesis, Institute National Polytechnique de Toulouse, 2003.

[14] G. Duhar and C. Colin. Dynamics of bubble growth and detachment in a viscous shear flow. *Physics of Fluids*, 18:1–13, 2006.

[15] G. Duhar, G. Riboux, and C. Colin. Vapour bubble growth and detachment at the wall of shear flow. *Heat and Mass Transfer*, 45:847–855, 2009.

[16] M. Elbaum, S. G. Lipson, and J. S. Wettlaufer. Evaporation preempts complete wetting. *Europhysics Letters*, 29:457–462, 1995.

[17] A. Esmaeeli and G. Tryggvason. Computations of film boiling. Part I: Numerical method. *International Journal of Heat and Mass Transfer*, 47:5451–5461, 2004.

[18] A. Esmaeeli and G. Tryggvason. Computations of film boiling. Part II: Multi-mode film boiling. *International Journal of Heat and Mass Transfer*, 47:5463–5476, 2004.

[19] A. Esmaeeli and G. Tryggvason. A front tracking method for computations of boiling in complex geometries. *International Journal of Multiphase Flow*, 30:1037–1050, 2004.

[20] W. Fritz. Berechnung des Maximalvolumens von Dampfblasen. *Physikalische Zeitschrift*, 36:379–384, 1935.

[21] T. Fuchs. *Numerische Analyse transienter Wärmetransport- und Wärmespeicherungsmechanismen in Heizwand und Fluid beim Blasensieden eines binären Gemisches*. PhD thesis, Technische Universität Darmstadt, 2008.

[22] T. Fuchs, J. Kern, and P. Stephan. A transient nucleate boiling model including microscale effects and wall heat transfer. *Journal of Heat Transfer*, 128:1257–1265, 2006.

[23] Y. Ge and L.-S. Fan. Three-dimensional simulation of impingement of a liquid droplet on a flat surface in the Leidenfrost regime. *Physics of Fluids*, 17:027104 (20 pages), 2005.

[24] B. S. Gottfried and K. J. Bell. Film boiling of spheroidal droplets. *Industrial & Engineering Chemistry Fundamentals*, 5:561–568, 1966.

[25] C.-Y. Han and P. Griffith. The mechanism of heat transfer in nucleate pool boiling - Part I: Bubble initiation, growth and departure. *International Journal of Heat and Mass Transfer*, 8:887–904, 1965.

[26] C.-Y. Han and P. Griffith. The mechanism of heat transfer in nucleate pool boiling - Part II: The heat flux-temperature difference relation. *International Journal of Heat and Mass Transfer*, 8:905–914, 1965.

[27] S. Hardt. An extended volume-of-fluid method for micro flows with short-range interactions between fluid interfaces. *Physics of Fluids*, 17:100601 (9 pages), 2005.

[28] S. Hardt and F. Wondra. Evaporation model for interfacial flows based on a continuum-field representation of the source terms. *Journal of Computational Physics*, 227:5871–5895, 2008.

[29] F. H. Harlow and J. E. Welch. Numerical calculation of time-dependent viscous incompressible flow of fluid with free surface. *Physics of Fluids*, 8:2182–2189, 1965.

[30] D. J. E. Harvie and D. F. Fletcher. A hydrodynamic and thermodynamic simulation of droplet impacts on hot surfaces, Part I: Theoretical model. *International Journal of Heat and Mass Transfer*, 44:2633–2642, 2001.

[31] D. J. E. Harvie and D. F. Fletcher. A hydrodynamic and thermodynamic simulation of droplet impacts on hot surfaces, Part II: Validation and applications. *International Journal of Heat and Mass Transfer*, 44:2643–2659, 2001.

[32] G. Hazi and A. Markus. On the bubble departure diameter and release frequency based on numerical simulation results. *International Journal of Heat and Mass Transfer*, 52:1472–1480, 2009.

[33] C. D. Henry and J. Kim. A study of the effects of heater size, subcooling, and gravity level on pool boiling heat transfer. *International Journal of Heat and Fluid Flow*, 25:262–273, 2004.

[34] J. Hernández, J. López, P. Gómez, C. Zanzi, and F. Faura. A new volume of fluid method in three dimensions - Part I: Multidimensional advection method with face-matched flux polyhedra. *International Journal for Numerical Methods in Fluids*, 58:897–921, 2008.

[35] J. O. Hinze. *Turbulence*. McGraw-Hill, 2nd edition, 1975.

[36] C. W. Hirt, A. A. Amsden, and J. L. Cook. An arbitrary lagrangian-eulerian computing method for all speeds. *Journal of Computational Physics*, 14:227–253, 1974.

[37] C. W. Hirt and B. D. Nichols. Volume of fluid (VOF) method for the dynamics of free boundaries. *Journal of Computational Physics*, 39:201–225, 1981.

[38] K. Ibrahem, M. F. Abd Rabbo, T. Gambaryan-Roisman, and P. Stephan. Experimental investigation of evaporative heat transfer characteristics at the 3-phase contact line. *Experimental Thermal and Fluid Science*, 34:1036–1041, 2010.

[39] K. Ibrahem, M. F. Abd Rabbo, T. Gambaryan-Roisman, and P. Stephan. Experimental investigation of micro-scale heat transfer at an evaporating moving 3-phase contact line. In *Proceedings of the 14th International Heat Transfer Conference IHTC14*, 2010.

[40] I. N. Ilyin, V. P. Grivtsov, and S. R. Yaundalders. Holographic interferometry studies of temperature profiles in thermal boundary layer in free convection and bubble boiling. In *Proceedings of the 7th International Heat Transfer Conference*, volume 4, pages 55–59, 1982.

[41] R. I. Issa. Solution of the implicitly discretised fluid flow equations by operator-splitting. *Journal of Computational Physics*, 62:40–65, 1985.

[42] R. I. Issa, A. D. Gossman, and A. P. Watkins. The computation of compressible and incompressible recirculating flows by a non-iterative implicit scheme. *Journal of Computational Physics*, 62:66–82, 1986.

[43] M. Jakob and W. Fritz. Versuche über den Verdampfungsvorgang. *Forschung auf dem Gebiet der Ingenieurwissenschaften*, 2:435–447, 1931.

[44] D. Jamet, O. Lebaigue, N. Coutris, and J. M. Delhaye. The second gradient method for the direct numerical simulation of liquid-vapor flows with phase change. *Journal of Computational Physics*, 169:624–651, 2001.

[45] H. Jasak. *Error analysis and estimation for finite volume method with applications to fluid flow*. PhD thesis, Imperial College of Science, Technology and Medicine, London, 1996.

[46] D. Juric and G. Tryggvason. Computations of boiling flows. *International Journal of Multiphase Flow*, 24:387–410, 1998.

[47] S. G. Kandlikar. Fundamental issues related to flow boiling in minichannels and microchannels. *Experimental Thermal and Fluid Science*, 26:389–407, 2002.

[48] S. G. Kandlikar. Heat transfer mechanisms during flow boiling in microchannels. *Journal of Heat Transfer*, 126:8–16, 2004.

[49] D. B. R. Kenning, T. Kono, and M. Wienecke. Investigation of boiling heat transfer by liquid crystal thermography. *Experimental Thermal and Fluid Science*, 25:219–229, 2001.

[50] D. B. R. Kenning and Y. Yan. Pool boiling heat transfer on a thin plate: Features revealed by liquid crystal thermography. *International Journal of Heat and Mass Transfer*, 39:3117–3137, 1996.

[51] J. Kern and P. Stephan. Investigation of decisive mixture effects in nucleate boling of binary mixtures using a theoretical model. *Journal of Heat Transfer*, 125:1116–1122, 2003.

[52] J. Kern and P. Stephan. Theoretical model for nucleate boiling heat and mass transfer of binary mixtures. *Journal of Heat Transfer*, 125:1106–1115, 2003.

[53] J. Kim. Review of nucleate pool boiling bubble heat transfer mechanisms. *International Journal of Multiphase Flow*, 35:1067–1076, 2009.

[54] J. Kistemaker. The spheroidal state of a waterdrop - The Leidenfrost phenomenon. *Physica*, 29:96–104, 1963.

[55] J. F. Klausner, R. Mei, D. M. Bernhard, and L. Z. Zeng. Vapor bubble departure in forced convective boiling. *International Journal of Heat and Mass Transfer*, 36:651–662, 1993.

[56] J. F. Klausner, R. Mei, and L. Z. Zeng. Predicting stochastic features of vapor bubble detachment in flow boiling. *International Journal of Heat and Mass Transfer*, 40:3547–3552, 1997.

[57] C. Kunkelmann, K. Ibrahem, N. Schweizer, and P. Stephan. The effect of three-phase contact line speed on local evaporative heat transfer: Experimental and numerical investigations. *Submitted to International Journal of Heat and Mass Transfer*, expected to be published in 2011.

[58] C. Kunkelmann and P. Stephan. CFD simulation of boiling flows using the volume-of-fluid method within OpenFOAM. *Numerical Heat Transfer, Part A*, 56:631–646, 2009.

[59] C. Kunkelmann and P. Stephan. Modification and extension of a standard volume-of-fluid solver for simulating boiling heat transfer. In *Proceedings of the V European Conference on Computational Fluid Dynamics (ECCOMAS CFD2010)*, 2010.

[60] C. Kunkelmann and P. Stephan. Numerical simulation of the transient heat transfer during nucleate boiling of refrigerant HFE-7100. *International Journal of Refrigeration*, 33:1221–1228, 2010.

[61] G. Lagubeau, M. Le Merrer, C. Clanet, and D. Quéré. Leidenfrost on a ratchet. *Nature Physics*, published online, 2011.

[62] C. Li and G. P. Peterson. Parametric study of pool boiling on horizontal highly conductive microporous coated surfaces. *Journal of Heat Transfer*, 129:1465–1475, 2007.

[63] D. Li and V. K. Dhir. Numerical study of single bubble dynamics during flow boiling. *Journal of Heat Transfer*, 129:864–876, 2007.

[64] H. Linke, B. J. Alemán, L. D. Melling, M. J. Taormina, M. J. Francis, C. C. Dow-Hygelund, V. Narayanan, R. P. Taylor, and A. Stout. Self-propelled Leidenfrost droplets. *Physical Review Letters*, 96:154502 (4 pages), 2006.

[65] J. López and J. Hernández. Analytical and geometrical tools for 3D volume of fluid methods in general grids. *Journal of Computational Physics*, 227:5939–5948, 2008.

[66] J. López, C. Zanzi, P. Gómez, F. Faura, and J. Hernández. A new volume of fluid method in three dimensions - Part II: Piecewise-planar interface reconstruction with cubic-bézier fit. *International Journal of Numerical Methods in Fluids*, 58:923 – 944, 2008.

[67] I. G. Malenkov. The frequency of vapor-bubble separation as a function of bubble size. *Fluid Mechanics - Soviet Research*, 1:36–42, 1972.

[68] R. M. Manglik. On the advancements in boiling, two-phase flow heat transfer, and interfacial phenomena. *Journal of Heat Transfer*, 128:1237–1241, 2006.

[69] R. Marek and J. Straub. Analysis of the evaporation coefficient and the condensation coefficient of water. *International Journal of Heat and Mass Transfer*, 44:39–53, 2001.

[70] H. Martin, V. Gnielinski, D. Mewes, D. Steiner, K. Stephan, K. Schaber, D. Vortmeyer, and S. Kabelac, editors. *VDI Wärmeatlas: Berechnungsblätter für den Wärmeübergang*, volume 9. Verein Deutscher Ingenieure, 2002.

[71] J. Mitrovic. Wärmetransport in der Umgebung einer wachsenden Dampfblase. *Wärme- und Stoffübertragung*, 19:47–52, 1985.

[72] J. Mitrovic. On the profile of the liquid wedge underneath a growing vapour bubble and the revearsal of the wall heat flux. *International Journal of Heat and Mass Transfer*, 45:409–415, 2002.

[73] S. Moghaddam and K. Kiger. Physical mechanisms of heat transfer during single bubble nucleate boiling of FC-72 under saturation conditions-I. Experimental investigation. *International Journal of Heat and Mass Transfer*, 52:1284–1294, 2009.

[74] S. Moghaddam and K. Kiger. Physical mechanisms of heat transfer during single bubble nucleate boiling of FC-72 under saturation conditions-II. Theoretical analysis. *International Journal of Heat and Mass Transfer*, 52:1295–1303, 2009.

[75] P. Moin and K. Mahesh. Direct numerical simulation: A tool in turbulence research. *Annual Review of Fluid Mechanics*, 30:539–578, 1998.

[76] G. E. Moore. Cramming more components onto integrated circuits. *Eletronics*, 38:114–117, 1965.

[77] S. J. S. Morris. A phenomenological model for the contact region of an evaporating meniscus on a superheated slab. *Journal of Fluid Mechanics*, 411:59–89, 2000.

[78] S. J. S. Morris. Contact angles for evaporating liquids predicted and compared with existing experiments. *Journal of Fluid Mechanics*, 432:1–30, 2001.

[79] S. J. S. Morris. The evaporating meniscus in a channel. *Journal of Fluid Mechanics*, 494:297–317, 2003.

[80] A. Mukherjee and V. K. Dhir. Study of lateral merger of vapor bubbles during nucleate pool boiling. *Journal of Heat Transfer*, 126:1023–1039, 2004.

[81] A. Mukherjee and S. G. Kandlikar. Numerical study of single bubbles with dynamic contact angle during nucleate pool boiling. *International Journal of Heat and Mass Transfer*, 50:127–138, 2007.

[82] J. G. Myers, V. K. Yerramilli, S. W. Hussey, G. F. Yee, and J. Kim. Time and space resolved wall temperature and heat flux measurements during nucleate boiling with constant heat flux boundary conditions. *International Journal of Heat and Mass Transfer*, 48:2429–2442, 2005.

[83] R. A. Nelson. Do we doubt too little? Examples from the thermal sciences. *Experimental Thermal and Fluid Science*, 25:255–267, 2001.

[84] S. Nukiyama. The maximum and minimum values of the heat Q transmitted from metal to boiling water under atmospheric pressure. *Journal of Japanese Society of Mechanical Engineers*, 37:367–374, 1934.

[85] S. Osher and J. A. Sethian. Fronts propagating with curvature dependent speed: Algorithms base on Hamilton-Jacobi formulations. *Journal of Computational Physics*, 79:12–49, 1988.

[86] J. L. Plawsky, A. Chatterjee, and P. C. Wayner. Modeling contact line dynamics in evaporating menisci. In *Proceedings of Comsol Users's conference*, 2009.

[87] M. S. Plesset and S. A. Zwick. The growth of vapor bubbles in superheated liquids. *Journal of Applied Physics*, 25:493–500, 1954.

[88] D. M. Qiu, V. K. Dhir, D. Chao, M. M. Hasan, E. Neumann, G. Yee, and A. Birchenough. Single-bubble dynamics during pool boiling under low gravity conditions. *Journal of Thermophysics and Heat Transfer*, 16:336–345, 2002.

[89] W. J. Rider and D. B. Kothe. Reconstructing volume tracking. *Journal of Computational Physics*, 141:112–152, 1998.

[90] H. Rusche. *Computational fluid dynamics of dispersed two-phase flows at high phase fraction*. PhD thesis, Imperial College of Science, Technology and Medicine, London, 2002.

[91] M. Schäfer. *Computational Engineering - Introduction to Numerical Methods*. Springer, 2006.

[92] R. W. Schrage. *A theoretical study of interphase mass transfer*. Columbia University Press, New York, 1953.

[93] N. Schweizer. *Multi-scale investigation of nucleate boiling phenomena in microgravity*. PhD thesis, Technische Universität Darmstadt (available at http://tuprints.ulb.tu-darmstadt.de/2377/), 2010.

[94] N. Schweizer and P. Stephan. Experimental study of bubble behavior and local heat flux in pool boiling under variable gravitational conditions. *Multiphase Science and Technology*, 21:329–350, 2009.

[95] L. E. Scriven. On the dynamics of phase growth. *Chemical Engineering and Science*, 10:1–13, 1959.

[96] B. Shu. *Numerische Simulation des Blasensiedens mit Volume-Of-Fluid- und Level-Set-Methode*. PhD thesis, Technische Universität Darmstadt, 2009.

[97] S. Siedel, S. Cioulachtjian, and J. Bonjour. Experimental analysis of bubble growth, departure and interactions during pool boiling on artificial nucleation sites. *Experimental Thermal and Fluid Science*, 32:1504–1511, 2008.

[98] C. Sodtke, J. Kern, N. Schweizer, and P. Stephan. High resolution measurements of wall temperature distribution underneath a single vapour bubble under low gravity conditions. *International Journal of Heat and Mass Transfer*, 49:1100–1106, 2006.

[99] G. Son and V. K. Dhir. Numerical simulation of saturated film boiling on a horizontal surface. *Journal of Heat Transfer*, 119:525–533, 1997.

[100] G. Son and V. K. Dhir. Numerical simulation of film boiling near critical pressures with a level set method. *Journal of Heat Transfer*, 120:183–192, 1998.

[101] G. Son and V. K. Dhir. A level set method for analysis of film boiling on an immersed solid surface. *Numerical Heat Transfer, Part B*, 52:153–177, 2007.

[102] G. Son, V. K. Dhir, and N. Ramanujapu. Dynamics and heat transfer associated with a single bubble during nucleate boiling on a horizontal surface. *Journal of Heat Transfer*, 121:623–631, 1999.

[103] K. Stephan and M. Abdelsalam. Heat-transfer correlations for natural convection boiling. *International Journal of Heat and Mass Transfer*, 23:73–87, 1980.

[104] P. Stephan. *Wärmedurchgang bei Verdampfung aus Kapillarrillen in Wärmerohren*. PhD thesis, Universität Stuttgart, 1992.

[105] P. Stephan and J. Hammer. A new model for nucleate boiling heat transfer. *Wärme- und Stoffübertragung*, 30:119–125, 1994.

[106] P. Stephan and J. Kern. Evaluation of heat and mass transfer phenomena in nucleate boiling. *International Journal of Heat and Fluid Flow*, 25:140–148, 2004.

[107] P. Stephan and F. Wondra. Nucleate pool boiling on tubes with subsurface mini and micro channels. In *Proceedings of the Sixth International ASME Conference on Nanochannels, Microchannels and Minichannels*, 2008.

[108] P. C. Stephan and C. A. Busse. Analysis of the heat transfer coefficient of grooved heat pipe evaporator walls. *International Journal of Heat and Mass Transfer*, 35:383–391, 1992.

[109] J. G. Truong and P. C. Wayner. Effects of capillary and van der Waals dispersion forces on the equilibrium profile of a wetting liquid: Theory and experiment. *Journal of Chemical Physics*, 87:4180–4188, 1987.

[110] G. Tryggvason, B. Bunner, A. Esmaeeli, D. Juric, N. Al-Rawahi, W. Tauber, J. Han, S. Nas, and Y.-J. Jan. A front-tracking method for the computations of multiphase flow. *Journal of Computational Physics*, 169:708–759, 2001.

[111] J. S. Turner. *Buoyancy effects in fluids*. Cambridge University Press, 1973.

[112] O. Ubbink. *Numerical prediction of two fluid systems with sharp interfaces*. PhD thesis, Imperial College of Science, Technology and Medicine, London, 1997.

[113] S. O. Unverdi and G. Tryggvason. A front-tracking method for viscous, incompressible, multi-fluid flows. *Journal of Computational Physics*, 100:25–37, 1992.

[114] E. A. T. van den Akker. *Particle-based evaporation models and wall interaction for microchannel cooling*. PhD thesis, Technische Universiteit Eindhoven, 2010.

[115] E. A. T. van den Akker, A. J. H. Frijns, C. Kunkelmann, P. A. J. Hilbers, P. Stephan, and A. A. van Steenhoven. Molecular dynamics simulation of the micro region. *Submitted to International Journal of Heat and Mass Transfer*, expected to be published in 2011.

[116] S. van Stralen and R. Cole. *Boiling phenomena*, volume 1. McGraw-Hill, 1979.

[117] E. Wagner. *Hochauflösende Messungen beim Blasensieden von Reinstoffen und binären Gemischen*. PhD thesis, Technische Universität Darmstadt, 2008.

[118] E. Wagner, C. Sodtke, N. Schweizer, and P. Stephan. Experimental study of nucleate boiling heat transfer under low gravity conditions using TLCs for high resolution temperature measurements. *Heat and Mass Transfer*, 42:875–883, 2006.

[119] E. Wagner and P. Stephan. High-resolution measurements at nucleate boiling of pure FC-84 and FC-3284 and its binary mixtures. *Journal of Heat Transfer*, 131:121008 (12 pages), 2009.

[120] E. Wagner, P. Stephan, O. Koeppen, and H. Auracher. High resolution temperature measurements at moving vapor/liquid and vapor/liquid/solid interfaces during bubble growth in nucleate boiling. In *Proc. 4th International Berlin Workshop on Transport Phenomena with Moving Boundaries*, pages 260–277. VDI Verlag, 2007.

[121] P. C. Wayner. Intermolecular forces in phase-change heat transfer: 1998 Kern Award Review. *AIChE Journal*, 45:2055–2068, 1999.

[122] J. J. Wei and H. Honda. Effects of fin geometry on boiling heat transfer from silicon chips with micro-pin-fins immersed in FC-72. *International Journal of Heat and Mass Transfer*, 46:4059–4070, 2003.

[123] S. W. J. Welch. Local simulation of two-phase flows including interface tracking with mass transfer. *Journal of Computational Physics*, 121:142–154, 1995.

[124] S. W. J. Welch. Direct simulation of vapor bubble growth. *International Journal of Heat and Mass Transfer*, 41:1655–1666, 1998.

[125] S. W. J. Welch and T. Radichi. Numerical computation of film boiling including conjugate heat transfer. *Numerical Heat Transfer, Part B*, 42:35–53, 2002.

[126] S. W. J. Welch and J. Wilson. A volume of fluid based method for fluid flows with phase change. *Journal of Computational Physics*, 160:662–682, 2000.

[127] H. G. Weller, G. Tabor, H. Jasak, and C. Fureby. A tensorial approach to computational continuum mechanics using object-oriented techniques. *Computers in Physics*, 12:620–631, 1998.

[128] F. Wondra, J. Dittmann, P. Stephan, and A. Beutler. Optimization of high performance evaporator tubes through structural modifications for pool boiling heat transfer. In *Proceedings of 5th European Thermal-Sciences Conference*, 2008.

[129] F. Wondra and P. Stephan. Pool boiling heat transfer from tubular micro structured surfaces in saturated FC-72. In *Proceedings of ECI International Conference on Boiling Heat Transfer*, 2006.

[130] J. Wu and V. K. Dhir. Numerical simulations of the dynamics and heat transfer associated with a single bubble in subcooled pool boiling. *Journal of Heat Transfer*, 132:11501 (15 pages), 2010.

[131] J. Wu, V. K. Dhir, and J. Qian. Numerical simulation of subcooled nucleate boiling by coupling level-set method with moving-mesh method. *Numerical Heat Transfer, Part B*, 51:535–563, 2007.

[132] Z. Yu, Y. Ge, and L.-S. Fan. Multi-scale simulation of oblique collisions of a droplet on a surface in the Leidenfrost regime. *Chemical Engineering and Science*, 62:3462–3472, 2007.

[133] L. Z. Zeng, J. F. Klausner, D. M. Bernhard, and R. Mei. A unified model for the prediction of bubble detachment diameters in boiling systems - II. Flow boiling. *International Journal of Heat and Mass Transfer*, 36:2271–2279, 1993.

[134] N. Zuber. Nucleate boiling. The region of isolated bubbles and the similarity with natural convection. *International Journal of Heat and Mass Transfer*, 6:53–78, 1963.

Curriculum vitae

Personal information

Name	Christian Kunkelmann
Date of birth	November 6, 1981
Place of birth	Erbach i. Odw.
Family status	Married, one child

Education

08/1988 - 07/1992	Elementary school (Grundschule Nieder-Ramstadt)
08/1992 - 06/2001	Secondary school (Georg-Büchner-Schule Darmstadt)

Studies of mechanical engineering

10/2002 - 07/2004	Basic studies of mechanical engineering at Technische Universität Darmstadt
08/2004 - 07/2005	Studies of mechanical engineering at Ecole Centrale de Lyon in France (emphasis on turbomachinery and computational fluid dynamics)
10/2005 - 12/2007	Advanced studies of mechanical engineering at Technische Universität Darmstadt (emphasis on thermodynamics, fluid mechanics and chemical engineering)

Professional career

01/2008 - 04/2011	Research and teaching assistant at the Institute of Technical Thermodynamics (Technische Universität Darmstadt) - Research topic: Numerical modeling and analysis of boiling phenomena
since 05/2011	Research engineer in the fluid dynamics team of BASF SE

Numerical Modeling and Investigation of Boiling Phenomena

Familie, Meiner

01 longkai guo Page 49
4/1/2019 16:21

02 longkai guo Page 51
4/1/2019 17:53

03 longkai guo Page 52
7/1/2019 9:36

04 longkai guo Page 52
7/1/2019 9:36

05 longkai guo Page 52
7/1/2019 9:37

06 longkai guo Page 54
7/1/2019 11:46

07 longkai guo Page 54
7/1/2019 11:49

08 longkai guo Page 55
7/1/2019 11:52

09 longkai guo Page 65
25/9/2018 6:26
temperature interface jump condition